

# **Role of transition metal ions in oxidative hair colouring**

**Kazim Raza Naqvi**

Doctor of Philosophy

University of York

Chemistry

March 2014

# Abstract

---

The objective of this Ph.D project was to study the role of transition metal ions in oxidative hair colouring. Model systems corresponding to real-life hair colouring conditions were designed to examine copper(II) and iron(III) catalysed decomposition of alkaline hydrogen peroxide and hydroxyl radical formation.

In a chelant-free system, copper(II) ions were more active in decomposing alkaline hydrogen peroxide compared to iron(III) ions. For copper(II) ions, the initial rate of decomposition of hydrogen peroxide and hydroxyl radical formation increased with an increase in initial concentration of copper(II) ions. Adding chelants to the reaction solution altered the catalytic activity of metal ions. EDTA and EDDS chelants with iron(III) generated more hydroxyl radical and decomposed higher amounts of hydrogen peroxide than the corresponding complexes of these chelants with copper(II) ions. Most studied chelants suppressed catalytic activity of copper(II) ions except HEDP chelant which rapidly decomposed hydrogen peroxide. The results highlight that different metal-chelant systems have different level of catalytic activity in the decomposition of hydrogen peroxide.

Adding large excess of calcium ions to the reaction solution influenced the binding of copper(II) ions. Unlike other chelants, only EDDS showed selective binding of copper(II) ions in the presence of calcium and suppressed the decomposition of hydrogen peroxide. Similar results were obtained for copper treated hair fibres, where EDDS again showed strong preference and selectivity for copper(II). This suggests that EDDS is the best chelant to control free radical mediated protein hair damage during oxidative hair colouring. The selectivity of EDDS chelant was explained using speciation plots.

Catalytic activity of copper(II) ions was also examined in the presence of aromatic dye precursors. PPD/MAP combination suppressed decomposition of alkaline hydrogen peroxide which suggests that oxidative hair dyeing is likely to induce less protein damage to hair as compared to the bleaching systems. It is believed that some unknown intermediates are formed which chelate copper catalysts changing their chemical activity.

Among the chelants examined in the current study, HEDP is an exception as its mixture with copper(II) ions led to rapid decomposition of alkaline hydrogen peroxide and showed a very unusual kinetic profile. A mechanistic study showed that the decomposition reaction proceeds via formation of an active catalyst that degrades the chelant and eventually seeds formation of catalytically-inactive basic copper phosphate/carbonate nanoparticles. The nanoparticles prevent any further catalytic reaction as freshly added  $\text{Cu}^{2+}$  ions quickly adsorb on their surface and do not form active catalyst.

In a separate study, human hair samples were analysed to quantify the amount of calcium carbonate present in the bubble shaped structures lying over the hair shaft. SEM Images were analysed to estimate the amount of material present while quantitative gas IR analysis showed that the amount of calcium carbonate increased with increasing bubble count level. Calcium carbonate found by IR analysis was less than the values estimated by image analysis which suggested that calcium carbonate may not be the only material present in the bubble and some other unknown material may also be present.

# Table of Contents

---

Abstract	ii
List of figures	xi
Acknowledgment	xxvi
Author's declaration	xxvii
<b>1 Introduction</b>	<b>2</b>
1.1 Human hair fibre	2
1.1.1 Metal contents of human hair fibre	3
1.2 Oxidative hair treatment	4
1.2.1 Chemistry of hair bleaching	6
1.2.2 Properties of bleached hair and the role of transition metal ions in bleaching	8
1.3 Metal catalysed decomposition of hydrogen peroxide	9
1.3.1 Fenton chemistry	9
1.3.1.1 Mechanism of Fenton Reaction	10
1.3.2 Copper catalysed decomposition of hydrogen peroxide	13
1.3.3 Introducing chelants in a Fenton reaction	14
1.4 Aims and objectives	15
<b>2 Monitoring hydroxyl radical formation in a Fenton- like reaction</b>	<b>19</b>
2.1 Hydroxyl radical	19
2.2 Monitoring hydroxyl radical formation	20
2.2.1 Electron spin resonance spectroscopy (ESR)	20
2.2.2 Aromatic probes	21
2.2.3 Colorimetric probe	23

2.2.3.1	Synthesis of NPGA probe	25
2.2.3.2	Electronic spectra of NPGA probe under alkaline pH conditions	26
2.2.3.3	Hydroxylation of NPGA probe in a Fenton-like reaction	27
2.2.3.4	LC-MS separation of H-NPGA/NPGA	29
2.2.3.5	$pK_a$ of H-NPGA	31
2.2.4	Conclusion	31

### **3 Decomposition of alkaline hydrogen peroxide catalysed by metal-chelant complexes 34**

3.1	Objective	36
3.2	Metal-ligand complexes	36
3.2.1	Crystal field theory	37
3.2.2	Consequences of metal-ligand binding	40
3.2.3	Stability of metal-ligand complex	41
3.2.4	HSAB concept	43
3.2.5	Metal speciation	44
3.3	Catalytic activity of metal-chelant complexes	48
3.4	Catalytic activity of iron(III) systems	49
3.4.1	Iron(III) chelant-free system	49
3.4.2	Catalytic activity of iron(III) chelant systems	50
3.4.2.1	Decomposition of hydrogen peroxide in Iron(III)–EDTA system	50
3.4.2.2	Catalytic activity of iron(III) complexes with other polyaminocarboxylate chelants	52
3.4.2.3	Catalytic activity of iron(III) phosphonate complexes	54
3.4.2.4	Hydroxyl radical formation in iron(III) – chelant systems	54
3.5	Conclusion	57
3.6	Catalytic activity of copper(II) systems	59
3.6.1	Catalytic activity of copper(II) in a chelant-free system	59

3.6.2	Catalytic activity of copper(II) chelant systems	62
3.6.2.1	Cu(II)-polyaminocarboxylate chelant systems	62
3.6.2.2	Catalytic activity of Cu(II)-phosphonate chelants	64
3.6.3	Hydroxyl radical formation in copper(II) – chelant systems	66
3.7	Iron(III) vs copper(II) and aminocarboxylate vs phosphonate chelants: Comparison of catalytic activity	68
3.8	Conclusion	69
<b>4</b>	<b>Binary metal systems</b>	<b>71</b>
4.1	Objectives	72
4.2	Changes in speciation plots in the presence of calcium	72
4.3	Decomposition of hydrogen peroxide in the binary system	77
4.3.1	Copper(II) – calcium binary system	77
4.3.2	Iron(III) – calcium binary system	80
4.3.3	Conclusion	81
4.4	Decomposition of hydrogen peroxide using hair fibers as a source of metal ions	82
4.4.1	Metal dosage and analysis of hair metal content	82
4.4.2	Decomposition of hydrogen peroxide by copper treated hair fibres in a chelant-free system	83
4.4.3	Decomposition of hydrogen peroxide by copper treated hair fibres in the presence of a chelant	85
4.4.4	Effect of changing metal-chelant ratio: EDDS vs EDTA	90
4.4.5	Selective binding of copper(II) ions by EDDS	93
4.5	Conclusion	95
<b>5</b>	<b>Copper(II)-HEDP system</b>	<b>97</b>

5.1	Objective	97
5.2	Decomposition of alkaline hydrogen peroxide in Cu <sup>2+</sup> -HEDP system	98
5.3	Influence of changing the reaction conditions	99
5.3.1	Attempt to restart the decomposition reaction	99
5.3.2	Increasing the initial concentration of the reaction components	100
5.4	Analysis of the decomposition reaction: HEDP chelant degradation	102
5.5	Formation of copper based nanoparticles	105
5.5.1	Chemical composition of nanoparticles	106
5.5.2	Oxidation state of copper in the nanoparticles	108
5.6	Role of hydrogen peroxide	110
5.7	Self-inhibiting behaviour of Cu(II) nanoparticles	111
5.8	Defeating the self-inhibiting effect	113
5.9	The nature of the active catalyst	114
5.10	Conclusion	116
<b>6</b>	<b>Permanent hair colouring</b>	<b>118</b>
6.1	Objective	121
6.2	Basic mechanism of permanent hair colouring	121
6.2.1	Oxidative coupling: coupling of <i>p</i> -phenylenediamine (PPD) and <i>m</i> -aminophenol (MAP)	122
6.3	Decomposition of alkaline hydrogen peroxide in a copper-dye precursor system	124

6.4	Monitoring hydroxyl radical formation in oxidative colouring	127
6.4.1	Reducing oxidative dyes using thioglycolic acid	128
6.4.2	Hydroxyl radical formation in copper- PPD/MAP system	131
6.5	Decomposition of alkaline hydrogen peroxide on adding pre-made oxidative dye	133
6.6	Hydrogen peroxide decomposition on adding PPD-MAP trinuclear dye	136
6.7	EPR study of copper-dye precursor mixture in the presence of alkaline hydrogen peroxide	137
6.8	Conclusion	140
<b>7</b>	<b>Calcium carbonate content in human hair fibre</b>	<b>143</b>
7.1	Hypothesis for “calcium carbonate” and objectives	145
7.2	Image analysis: Estimating amount of the bubble material	145
7.3	Quantitative chemical analysis of calcium carbonate in human hair fibres	149
7.3.1	Infrared spectroscopy of carbon dioxide	150
7.3.2	FT-IR method to quantify carbon dioxide gas	151
7.3.3	Method sensitivity	152
7.3.4	Determining the amount of carbonate in hair fibres	154
7.4	Defining the nature of bubble material	155
7.5	Conclusion	157
<b>8</b>	<b>General Conclusion and future work</b>	<b>159</b>

<b>9</b>	<b>Experimental procedures</b>	<b>163</b>
9.1	Materials and chemicals	163
9.2	Instrumentation	163
9.3	Experimental procedures for chapter 2	164
9.3.1	Synthesis of <i>N,N'</i> -(5-nitro-1,3-phenylene)bisglutaramide (NPGA) probe	164
9.3.1.1	Step A: Synthesis of 3,5-diaminonitrobenzene	164
9.3.1.2	Step B: Synthesis of NPGA	164
9.3.2	Monitoring hydroxyl radical formation with NPGA	165
9.3.3	LC-MS separation of H-NPGA/NPGA	165
9.4	Experimental procedures for chapters 3 & 4	166
9.4.1	Determination of hydrogen peroxide	166
9.4.2	Monitoring decomposition of hydrogen peroxide	166
9.4.3	Decomposition of hydrogen peroxide in a chelant-free system	167
9.4.4	Decomposition of hydrogen peroxide in the presence of a chelant	167
9.4.5	Decomposition of hydrogen peroxide in the presence of copper treated hair fibres	167
9.4.6	Hydrogen peroxide decomposition in binary metal system	168
9.5	Monitoring hydroxyl radical formation in binary metal system	168
9.6	Monitoring hydroxyl radical formation in the presence of copper treated hair fibres	168
9.7	Experimental procedures for chapter 5	169
9.7.1	Decomposition of hydrogen peroxide in Cu <sup>2+</sup> -HEDP systems	169
9.7.2	Isolation & purification of nanoparticles	169
9.7.3	Determination of copper and phosphorus	169

9.7.4	Determination of phosphate contents using molybdenum blue method	170
9.7.5	Analysing phosphate contents in the reaction solution	171
9.7.6	Analysing phosphate in nanoparticles	171
9.7.7	Determination of carbonate content in nanoparticles	171
9.7.8	Determining the oxidation state of copper in nanoparticles	172
9.7.9	EPR study of copper-HEDP catalysed decomposition of hydrogen peroxide	172
9.7.10	Identifying the active catalyst in copper-HEDP catalysed decomposition of hydrogen peroxide	172
<b>9.8</b>	<b>Experimental procedures for chapter 6</b>	<b>173</b>
9.8.1	Hydrogen peroxide decomposition the presence of dye primary/coupler or a combination of both	173
9.8.2	Hydrogen peroxide decomposition on adding pre-oxidised dye mixture	173
9.8.3	Reducing PPD-MAP oxidative dye using thioglycolic acid	173
9.8.4	Monitoring hydroxyl radical formation in the presence of dye precursors	174
9.8.5	Synthesis of PPD-MAP tri-nuclear dye	174
9.8.6	Monitoring decomposition of hydrogen peroxide on adding PPD-MAP trinuclear dye	176
<b>9.9</b>	<b>Experimental procedures for chapter 7</b>	<b>176</b>
9.9.1	Image analysis	177
9.9.2	Calculating mass of human hair fibre from its SEM image	177
9.9.3	Calculating volume of a single bubble from SEM images	178
9.9.4	Characterising various hair switches and counting the number of bubbles per hair fibre	178
9.9.5	Initial control experiments and designing new experimental setup	178
9.9.6	Recording IR spectra of atmospheric carbon dioxide	179
9.9.7	Control experiment without using hair fibres	179
9.9.7.1	Developing a standard curve	180
9.9.8	IR analysis of human hair fibres for calcium carbonate	181

9.9.9	IR analysis of pulverised human hair fibres for calcium carbonate	181
<b>10</b>	<b>Appendix</b>	<b>183</b>
10.1	Appendix I	183
10.2	Appendix II	185
10.3	Appendix III	196
10.4	Abbreviations	202
<b>11</b>	<b>References</b>	<b>203</b>

## List of figures

Figure 1-1: Structure of human hair fibre demonstrating cuticle, cortex and medulla. The scheme also shows the main chemical interactions between keratin fibres in human hair. ....	2
Figure 1-2: Proposed chemical structure of (a) eumelanin and (b) pheomelanin. ....	6
Figure 1-3: TEM images of melanin grains before and after oxidative bleaching. ....	7
Figure 1-4: Proposed mechanism for the oxidative degradation of dihydroxyindol dimer. ....	7
Figure 1-5: Cystine and its oxidation product cysteic acid. ....	8
Figure 1-6: Hydrogen peroxide decomposition in the presence of metal loaded human hair fibres. ....	9
Figure 1-7: Oxidation of tartaric acid in a Fenton reaction. ....	10
Figure 1-8: Iron(II) catalysed decomposition in a Fenton reaction. ....	11
Figure 1-9: Iron(III) catalysed decomposition in a Fenton reaction. ....	11
Figure 1-10: Formation of ferryl ion intermediate in a Fenton reaction. ....	12
Figure 1-11: Possible mechanistic pathways of the Fenton reaction. ....	13
Figure 1-12: Copper(II) catalysed decomposition of hydrogen peroxide in a Fenton-like reaction. ....	14
Figure 1-13: Hydrogen peroxide decomposition in a metal-ligand ( $L_n$ ) system. ....	14
Figure 1-14: The hydroxyl radical formation in metal catalysed decomposition of hydrogen peroxide. ....	15
Figure 2-1: Photolysis of water and hydrogen peroxide generating hydroxyl radicals. ....	20
Figure 2-2: DMPO spin trap for ESR study of hydroxyl radical formation. ...	21
Figure 2-3: Hydroxylation of phenol with hydroxyl radical. ....	22
Figure 2-4: Hydroxylation of salicylic acid in monitoring hydroxyl radical formation. ....	22
Figure 2-5: Hydroxylation of terephthalic acid. ....	23
Figure 2-6: Chemical structure of N, N'-(5-nitro-1,3-phenylene)bisglutaramide (NPGA) molecule. ....	24
Figure 2-7: Hydroxyl radical analysis using NPGA colorimetric probe. ....	25
Figure 2-8: Synthesis of NPGA probe. ....	26

Figure 2-9: Electronic spectra of NPGA probe at various pH levels. NPGA (0.02 mM) was dissolved in various buffer systems. pH 4.0 and 6.0 were 20 mM phosphate buffer solutions while pH 8.0, 9.0 & 10.0 were 20 mM ammonia/ammonium chloride buffer systems. Spectra were recorded against buffer blank.....	27
Figure 2-10: Hydroxylation of NPGA probe in a Fenton-like reaction. Reaction solution contained copper(II) sulfate (0.4 mM), NPGA probe (1.0 mM) in a chelant-free system at pH 10.0 using ammonia/ammonium chloride buffer (20 mM). Hydrogen peroxide (0.98 M) was added and spectra were recorded over time against reagent blank. ....	28
Figure 2-11: Hydroxylation of NPGA probe in iron(III) chloride-EDTA system. Reaction solution contained iron(III) chloride (0.18 mM), EDTA (1.3 mM), NPGA probe (1.0 mM) at pH 10.0 using ammonia/ammonium chloride buffer (20 mM). Hydrogen peroxide (0.98 M) was added and spectra were recorded over a period of 120 minutes against reagent blank.....	28
Figure 2-12: Analysing NPGA hydroxylation in a copper(II) catalysed Fenton-like reaction using HPLC after 90 minutes mixing of the reaction. Reaction solution contained 1 mM NPGA probe mixed with 0.18 mM copper (II) sulfate in 20 mM ammonia/ammonium chloride buffer with 0.98 M hydrogen peroxide. ...	30
Figure 2-13: Analysing NPGA hydroxylation in a copper(II) catalysed Fenton-like reaction using HPLC after 24 hours of the reaction. Reaction solution contained 1 mM NPGA probe mixed with 0.18 mM copper(II) sulfate in 20 mM ammonia/ammonium chloride buffer with 0.98 M hydrogen peroxide. ....	30
Figure 2-14: Titration curve for the determination of $pK_a$ of H-NPGA. ....	31
Figure 3-1: Chemical structure of some common polyaminocarboxylate and phosphonate ligands.....	36
Figure 3-2: A simple representation of octahedral metal aqua complex and metal EDTA complex. ....	37
Figure 3-3: Energy diagram of the $d$ orbitals in an octahedral crystal field. ....	38
Figure 3-4: Jahn-teller distortion in $d^9$ system of $Cu^{2+}$ complex. ....	40
Figure 3-5: List of hard and soft acids and bases according to HSAB concept. ....	43
Figure 3-6: Iron(III) speciation in a chelant-free system using 0.18 mM concentration of iron(III) chloride in 20 mM ammonia/ammonium chloride buffer solution. ....	45

Figure 3-7: Copper(II) speciation in a chelant-free system using 0.18 mM concentration of copper(II) sulfate in 20 mM ammonia/ammonium chloride buffer solution. ....	45
Figure 3-8: Iron(III) speciation in Fe <sup>3+</sup> -EDTA system using 0.18 mM concentration of iron(III) chloride and 1.3 mM tetrasodium EDTA in 20 mM ammonia/ammonium chloride buffer solution. ....	46
Figure 3-9: Copper(II) speciation in Cu <sup>2+</sup> -EDTA system using 0.18 mM concentration of copper(II) sulfate and 1.3 mM tetrasodium EDTA in 20 mM ammonia/ammonium chloride buffer solution. ....	47
Figure 3-10: Iron(III) catalysed decomposition of alkaline hydrogen peroxide in a chelant-free system at pH 10. The reaction solution contained 0.18 mM iron(III) chloride and 0.98 M hydrogen peroxide at pH 10 using 20 mM ammonia/ammonium chloride buffer. ....	49
Figure 3-11: Hydroxyl radical formation in Fe(III) chelant-free system at pH 10. The reaction solution contained 0.18 mM iron(III) chloride and 0.98 M hydrogen peroxide at pH 10 using 20 mM ammonia/ammonium chloride buffer. ....	50
Figure 3-12: Decomposition of hydrogen peroxide by Fe(III)-EDTA system at alkaline pH. The reaction contained 0.18 mM FeCl <sub>3</sub> and 1.3 mM EDTA.4Na and 0.98 M hydrogen peroxide in 20 mM ammonia/ammonium chloride buffer solution. ....	51
Figure 3-13: Decomposition of hydrogen peroxide in Fe <sup>3+</sup> -chelant systems at pH 8. The reaction solution contained 0.18 mM FeCl <sub>3</sub> , 1.3 mM of chelant and 0.98 M hydrogen peroxide in 20 mM ammonia/ammonium chloride buffer pH 8.0. ...	52
Figure 3-14: Decomposition of hydrogen peroxide in Fe <sup>3+</sup> -chelant systems at pH 9.0. The reaction solution contained 0.18 mM FeCl <sub>3</sub> , 1.3 mM of chelant and 0.98 M hydrogen peroxide in 20 mM ammonia/ammonium chloride buffer pH 9. ....	53
Figure 3-15: Decomposition of hydrogen peroxide in Fe <sup>3+</sup> -ligand systems at pH 10. The reaction solution contained 0.18 mM FeCl <sub>3</sub> , 1.3 mM of chelant and 0.98 M hydrogen peroxide in 20 mM ammonia/ammonium chloride buffer pH 10. ....	53
Figure 3-16: Hydroxyl radical formation in Fe <sup>3+</sup> -EDTA systems at alkaline pH. The reaction solution contained 0.18 mM FeCl <sub>3</sub> , 1.3 mM EDTA, 1.0 mM NPGA	

probe and 0.98 M hydrogen peroxide in 20 mM ammonia/ammonium chloride buffer. ....	55
Figure 3-17: Hydroxyl radical formation in Fe <sup>3+</sup> -ligand systems at pH 8. The reaction solution contained 0.18 mM FeCl <sub>3</sub> , 1.3 mM chelant, 1.0 mM NPGA probe and 0.98 M hydrogen peroxide in 20 mM ammonia/ammonium chloride buffer. ....	56
Figure 3-18: Hydroxyl radical formation in Fe <sup>3+</sup> - chelant systems at pH 9. The reaction solution contained 0.18 mM FeCl <sub>3</sub> , 1.3 mM chelant, 1.0 mM NPGA probe and 0.98 M hydrogen peroxide in 20 mM ammonia/ammonium chloride buffer. ....	56
Figure 3-19: Hydroxyl radical formation in various Fe <sup>3+</sup> - chelant systems at pH 10. The reaction solution contained 0.18 mM FeCl <sub>3</sub> , 1.3 mM chelant, 1.0 mM NPGA probe and 0.98 M hydrogen peroxide in 20 mM ammonia/ammonium chloride buffer. ....	57
Figure 3-20: Decomposition of hydrogen peroxide by copper(II) chelant -free system. The reaction solution contained 0.18 mM copper(II) sulfate in 20 mM ammonia/ammonium chloride buffer solution. ....	59
Figure 3-21: Effect of increasing initial copper(II) sulfate concentration in a chelant-free system on the decomposition of hydrogen peroxide at pH 10 using 20 mM ammonia/ammonium chloride buffer solution. The reaction solution contained copper(II) sulfate (0.18- 0.8 mM) and 0.98 M hydrogen peroxide. ....	60
Figure 3-22: Effect of increasing copper(II) sulfate concentration on the hydroxyl radical formation at pH 10. Each reaction solution contained copper(II) sulfate (0.18-1.0 mM), 1 mM NPGA probe and 0.98 M hydrogen peroxide in 20 mM ammonia/ammonium chloride buffer solution of pH 10. ....	61
Figure 3-23: Linear relationship between concentration of Cu <sup>2+</sup> ions and hydroxyl radical formation under alkaline reaction conditions. ....	61
Figure 3-24: Decomposition of hydrogen peroxide in Cu <sup>2+</sup> - chelant systems at pH 8. Each reaction solution contained 0.18 mM copper(II) sulfate, 1.3 mM chelant and 0.98 M hydrogen peroxide in 20 mM ammonia/ammonium chloride buffer. ....	63
Figure 3-25: Decomposition of hydrogen peroxide in Cu <sup>2+</sup> - chelant systems at pH 9. Reaction solution contained 0.18 mM copper(II) sulfate, 1.3 mM chelant and 0.98 M hydrogen peroxide in 20 mM ammonia/ammonium chloride buffer. ....	63

Figure 3-26: Decomposition of hydrogen peroxide in Cu <sup>2+</sup> - chelant systems at pH 10. Each reaction solution contained 0.18 mM copper(II) sulfate, 1.3 mM chelant and 0.98 M hydrogen peroxide in 20 mM ammonia/ammonium chloride buffer. ....	64
Figure 3-27: Decomposition of alkaline hydrogen peroxide in Cu(II) HEDP system. Each reaction solution contained 0.18 mM copper(II) sulfate, 1.3 mM HEDP chelant and 0.98 M hydrogen peroxide in 20 mM ammonia/ammonium chloride buffer. ....	65
Figure 3-28: Hydroxyl radical formation in Cu(II) – chelant systems at pH 8. Each reaction solution contained 0.18 mM copper(II) sulfate, 1.3 mM chelant, 1.0 mM NPGA probe and 0.98 M hydrogen peroxide in 20 mM ammonia/ammonium chloride pH 8.0.....	67
Figure 3-29: Hydroxyl radical formation in Cu(II) – chelant systems at pH 9. Each reaction solution contained 0.18 mM copper(II) sulfate, 1.3 mM chelant, 1.0 mM NPGA probe and 0.98 M hydrogen peroxide in 20 mM ammonia/ammonium chloride pH 9.....	67
Figure 3-30: Hydroxyl radical formation in Cu(II) – chelant systems at pH 10. Each reaction solution contained 0.18 mM copper(II) sulfate, 1.3 mM chelant, 1.0 mM NPGA probe and 0.98 M hydrogen peroxide in 20 mM ammonia/ammonium chloride pH 10.....	68
Figure 4-1: Copper speciation in the presence of calcium in a chelant-free system. ....	73
Figure 4-2: Copper speciation in the presence calcium ions and EDTA chelant in a 400 mM ammonia buffer. ....	74
Figure 4-3: EDTA speciation in copper-calcium system in a 400 mM ammonia buffer. ....	74
Figure 4-4: Copper(II) speciation in the presence of EDTA in a 400 mM ammonia buffer.....	75
Figure 4-5: Copper ion speciation in EDDS system in the presence of large excess of calcium ions. ....	76
Figure 4-6: EDDS speciation in copper-calcium binary system.....	76
Figure 4-7: Decomposition of alkaline hydrogen peroxide in copper-calcium binary system at pH 10 using 400 mM ammonia/ammonium chloride buffer solution. Each reaction solution contained 0.18 mM copper(II) sulfate, 125 mM calcium nitrate, 1.3 mM chelant and 0.98 M hydrogen peroxide.....	77

Figure 4-8: Control experiment at high ammonium concentration in the absence of calcium. Decomposition of alkaline hydrogen peroxide in copper(II) systems in the absence of calcium ions at pH 10 with 400 mM ammonia/ammonium chloride buffer solution. Each reaction solution contained 0.18 mM copper(II) sulfate, 1.3 mM chelant and 0.98 M hydrogen peroxide. ...78

Figure 4-9: Hydroxyl radical formation in Cu-Ca binary systems. Each reaction contained 0.18 mM copper(II) sulfate, 125 mM calcium nitrate, 1.3 mM chelant, 1.0 mM NPGA probe and 0.98 M hydrogen peroxide.....79

Figure 4-10: Decomposition of alkaline hydrogen peroxide in iron(III) - calcium binary system. Each reaction contained 0.18 mM iron(III) chloride, 125 mM calcium nitrate, 1.3 mM each chelant and 0.98 M hydrogen peroxide. ....81

Figure 4-11: Decomposition of alkaline hydrogen peroxide in a chelant-free model system using human hair fibres as a metal source. The reaction solution contained 100 mg of hair fibres and 0.98 M hydrogen peroxide at pH 10 using 400 mM ammonia/ammonium chloride buffer solution. ....84

Figure 4-12: Hydroxyl radical formation in copper treated hair fibres in a chelant-free system. The reaction solution contained 50 mg hair fibres, 1.0 mM NPGA and 0.98 M hydrogen peroxide at pH 10 using 400 mM ammonia/ammonium chloride buffer solution. The reaction solution was diluted by 10 times and analysed by UV-visible spectrophotometer. ....84

Figure 4-13: Decomposition of alkaline hydrogen peroxide by copper treated hair fibres in the presence of EDDS chelant at pH 10 using 400 mM ammonia/ammonium chloride buffer solution. The reaction solution contained 100 mg of hair fibres, 13.95 mM EDDS chelant and 0.98 M hydrogen peroxide. ....86

Figure 4-14: Hydroxyl radical formation by copper treated hair fibres in the presence of EDDS chelant at pH 10 using 400 mM ammonia/ammonium chloride buffer solution. Each reaction solution contained 50 mg of hair fibres, 1 mM NPGA, 13.95 mM EDDS and 0.98 M hydrogen peroxide. The reaction solution was diluted by 10 times and analysed by UV-visible spectrophotometer. ....86

Figure 4-15: Decomposition of alkaline hydrogen peroxide by copper treated hair fibres in the presence of EDTA chelant at pH 10 using 400 mM ammonia/ammonium chloride buffer solution. Each reaction solution contained 100 mg of hair fibres, 13.95 mM EDTA and 0.98 M hydrogen peroxide. ....88

Figure 4-16: Hydroxyl radical formation in hair-EDTA system at pH 10 using 400 mM ammonia/ammonium chloride buffer solution. The reaction solution contained 50 mg of hair fibres, 1 mM NPGA probe, 13.95 mM EDTA and 0.98 M hydrogen peroxide. The reaction solution was diluted by 10 times and analysed by UV-visible spectrophotometer. ....	88
Figure 4-17: Decomposition of alkaline hydrogen peroxide by copper treated hair fibres in the presence of DTPMP chelant at pH 10 using 400 mM ammonia/ammonium chloride buffer solution. The reaction solution contained 100 mg of hair fibres, 13.95 mM DTPMP and 0.98 M hydrogen peroxide. ....	89
Figure 4-18: Hydroxyl radical formation in hair-DTPMP system at pH 10 using 400 mM ammonia/ammonium chloride buffer solution. The reaction solution contained 50 mg of hair fibres, 1 mM NPGA probe, 13.95 mM DTPMP and 0.98 M hydrogen peroxide. The reaction solution was diluted by 10 times and analysed by UV-visible spectrophotometer. ....	90
Figure 4-19: Decomposition of alkaline hydrogen peroxide by copper treated hair fibres in the presence of EDDS chelant at pH 10 using 400 mM ammonia/ammonium chloride buffer solution. The reaction solution contained 100 mg of hair fibres, 0.94 mM EDDS and 0.98 M hydrogen peroxide. ....	91
Figure 4-20: Decomposition of alkaline hydrogen peroxide by copper treated hair fibres in the presence of EDTA chelant at pH 10 using 400 mM ammonia/ammonium chloride buffer solution. The reaction solution contained 100 mg of hair fibres, 0.94 mM EDTA and 0.98 M hydrogen peroxide. ....	92
Figure 4-21: Hydroxyl radical formation by copper treated hair fibres using low concentration of EDDS ligand at pH 10 using 400 mM ammonia/ammonium chloride buffer solution. ....	93
Figure 4-22: Molecular mechanics modelling for copper and calcium ions with EDTA and EDDS chelants. ....	94
Figure 5-1: Decomposition of alkaline hydrogen peroxide in copper-etidronic acid (HEDP) system. ....	97
Figure 5-2: Decomposition of alkaline hydrogen peroxide in Cu(II) HEDP system. The reaction solution contained 0.18 mM copper(II) sulfate, 1.3 mM HEDP chelant and 0.98 M hydrogen peroxide in 20 mM ammonia/ammonium chloride buffer. ....	98
Figure 5-3: Copper(II) speciation in Cu <sup>2+</sup> -HEDP system. ....	99

Figure 5-4: Effect of adding fresh metal ions and chelant in a stopped decomposition reaction containing 0.18 mM Cu<sup>2+</sup> ions and 1.3 mM HEDP chelant. (A) Bench mark reaction (B) more 1.3 mM HEDP chelant added at the 30<sup>th</sup> minute in an ongoing decomposition reaction (C) 0.18 mM Cu<sup>2+</sup> ions more added at the 30<sup>th</sup> minute. ....100

Figure 5-5: Effect of increasing copper ion concentration in Cu-HEDP catalysed decomposition of alkaline hydrogen peroxide containing different levels of copper(II) sulfate and HEDP chelant dissolved in 20 mM pH 10 ammonia/ammonium chloride buffer. ....101

Figure 5-6: Copper-HEDP catalysed decomposition of alkaline hydrogen peroxide at different ammonia levels. Reaction solution contained 0.18 mM of copper(II) sulfate, 1.3 mM of HEDP chelant dissolved in ammonia/ammonium chloride buffer pH 10 and mixed with 0.98 M of hydrogen peroxide. Hydrogen peroxide decomposition was monitored over time. (A) 400 mM ammonia/ammonium chloride buffer (B) 100 mM ammonia/ammonium chloride buffer (C) 20 mM ammonia/ammonium chloride buffer.....102

Figure 5-7: pH drop in Cu<sup>2+</sup>-HEDP decomposition system. Reaction solution contained 0.18 mM Cu<sup>2+</sup> ions and 1.3 mM HEDP chelant at pH 10 with 20 mM ammonia/ammonium chloride buffer. Hydrogen peroxide (0.98 M) was added to trigger the decomposition reaction. pH of the reaction solution monitored using a pH meter. The standard mean error for pH was 0.01 pH unit. ....103

Figure 5-8: Monitoring phosphate concentration in Cu<sup>2+</sup>-HEDP system of hydrogen peroxide decomposition at pH 10 using 20 mM ammonia/ammonium chloride buffer. The decomposition reaction solution contained 0.18 mM Cu(II) sulfate, 1.3 mM HEDP chelant and 0.98 M hydrogen peroxide. ....105

Figure 5-9: (A) UV-Vis spectra of Cu<sup>2+</sup>-HEDP reaction solution recorded over time showing absorption band for copper nanoparticles. Reaction solution contained 0.18 mM copper(II) sulfate, 1.3 mM HEDP and 0.98 M hydrogen peroxide (B) TEM image and size distribution of copper nanoparticles in Cu-HEDP reaction mixture.....106

Figure 5-10: FT-IR spectrum of carbon dioxide from isolated nanoparticles. ....108

Figure 5-11: TEM image and UV-Vis spectra of fabricated nanoparticles without using hydrogen peroxide (A) 12.5 μmol of copper(II) sulfate with 50 μmol

of  $(\text{NH}_4)_2\text{CO}_3$  in 25 mL of 20 mM phosphate buffer pH 10. (B) Fabricated nanoparticles after 10 days kept at lab bench. ....111

Figure 5-12: Fresh addition of Cu(II) sulfate to the nanoparticle solution in pH 10 ammonia/ammonium chloride buffer leads to an increased UV-Vis absorption. A reaction was carried out using 0.18 mM copper(II) sulfate, 1.3 mM HEDP chelant and 0.98 M hydrogen peroxide in 25 mL of buffer solution. Amount of  $\text{Cu}^{2+}$  added was 0.18 mM which gives total  $\text{Cu}^{2+}$  present in the solution as: (A) 0.72 mM; (B) 0.54 mM; (C) 0.36 mM; (D) 0.18 mM. ....112

Figure 5-13: Adding fresh HEDP chelant to an ongoing  $\text{Cu}^{2+}$ -HEDP catalysed hydrogen peroxide decomposition reaction just before it stops. Pre-neutralised HEDP (32.5  $\mu\text{mol}$  each time in 25 ml reaction solution) ligand was added at different time intervals. pH of the reaction solution was maintained by adding a few drops of 2 M sodium hydroxide.....113

Figure 5-14: EPR spectra of copper-HEDP reaction solution. Reaction solution contained  $\text{Cu}^{2+}$  (0.18 mM), HEDP (1.3 mM) in 20 mM pH 10 ammonia/ammonium chloride buffer with hydrogen peroxide (0.98 M), total reaction volume 25 mL. Aliquots (1.6 mL) were mixed with glycerol (0.4 mL) in a quartz EPR tube, and spectra were recorded at 120 K at the following times after the start of the reaction: (A) 2 min; (B) 8 min; (C) 15 min. ....114

Figure 5-15: UV-Vis spectra of Cu-HEDP reaction with hydrogen peroxide. Reaction solution contained 0.05 mM copper(II) sulfate, 0.05 mM HEDP ligand in 20 mM pH 10 ammonia/ammonium chloride buffer pH 10. Hydrogen peroxide 0.1 mM was added and spectra were recorded immediately against reagent blank. Reaction was carried out in UV-vis cell. Spectra obtained every 2 minutes over 120 minutes show changes in the reaction solution. ....115

Figure 5-16: (A) Formation of nanoparticles in a chelant-free system. The reaction solution contained 0.18 mM copper(II) sulfate dissolved in 20 mM ammonia/ammonium chloride buffer pH 10 with 0.98 M hydrogen peroxide TEM images showed large aggregates of nanoparticles. (B) Formation of copper based nanoparticles in Cu(II) chelant-free system in a 20 mM phosphate buffer pH 10 solution. TEM image of the reaction solution shows the presence of nanoparticles. ....116

Figure 6-1: Some examples of primary dye precursors.....120

Figure 6-2: Some examples of coupler dye precursors.....120

Figure 6-3: Schematic presentation of oxidative hair colouring demonstrating penetration of dye precursors and melanin bleaching. ....	122
Figure 6-4: Oxidation of <i>p</i> -phenylenediamine primary.....	123
Figure 6-5: Possible mechanism of oxidative coupling of <i>p</i> -phenylenediamine and <i>m</i> -aminophenol. ....	123
Figure 6-6: Decomposition of alkaline hydrogen peroxide in the presence of copper(II) sulfate and dye precursors at pH 10 using 400 mM ammonia/ammonium chloride buffer. Reaction solution contained 0.02 mM copper(II) sulfate with 1 mM dye precursor each and 0.98 M hydrogen peroxide. ....	124
Figure 6-7: Oxidative self-coupling of <i>p</i> -phenylenediamine.....	125
Figure 6-8: Copper catalysed decomposition of alkaline hydrogen peroxide in the presence of PPD primary and MAP coupler at pH 10 using 400 mM ammonia buffer with different concentration levels of copper(II) ions. Reaction solution contained 1 mM of each dye precursor and 0.98 M hydrogen peroxide. ....	126
Figure 6-9: Reducing PPD-MAP dye using TGA reduction method. Reaction solution contained 0.02 mM copper(II) sulfate, 1 mM PPD and 1 mM MAP mixed in 400 mM ammonia buffer. 0.98 M hydrogen peroxide was added to start the reaction. TGA (5%, 0.7 M) was added to reduce dye precursors and pH was adjusted back again using a few drops of ammonia. (A) PPD-MAP dye solution spectrum after 15 times dilution before adding TGA, (B) On adding TGA without any dilution, (C) pH adjusted back to alkaline 8.0, (D) After stirring for 60 minutes at alkaline pH. ....	130
Figure 6-10: Examining the stability of NPGA and its hydroxylated derivative in-situ using TGA reduction method. The reaction solution contained 0.18 mM Cu(II) sulfate, 1 mM NPGA with 0.98 M hydrogen peroxide in 400 mM ammonia/ammonium chloride buffer. (A) Hydroxylated derivative H-NPGA, (B) H-NPGA spectrum immediately after adding TGA at acidic pH, (C) H-NPGA spectrum after stirring with TGA for 30 min at acidic pH, (D) H-NPGA spectrum after adjusting pH back to alkaline, (E) 30 minutes under alkaline pH conditions, (F) 90 minutes under alkaline pH conditions. ....	131
Figure 6-11: Hydroxyl radical formation in various PPD only and PPD-MAP systems at different copper(II) levels using TGA reduction method. Apart from the	

copper and dye precursors, reaction solutions contained 0.98 M hydrogen peroxide in 400 mM ammonia buffer at pH 10.....132

Figure 6-12: Hydroxyl radical formation in 0.02 mM copper(II) sulfate in a chelant-free/dye-free system monitored over the course of reaction time using NPGA colorimetric probe. The reaction solution had pH 10 using 400 mM ammonia/ammonium chloride buffer. Hydrogen peroxide (0.98 M) was added to trigger the decomposition reaction. ....132

Figure 6-13: Impact of adding a pre-made dye solution to an ongoing copper(II) catalysed decomposition of alkaline hydrogen peroxide. Reaction solution contained copper(II) sulfate (0.02 mM) at pH 10 using 400 mM ammonia/ammonium chloride buffer. 1 mL of the dye solution was added to 25 mL reaction solution at 10<sup>th</sup> minute to give approximately 1 mM concentration of the dye. (A) Dye-free system (B) Pre-made PPD dye solution, (C) Pre-made PPD-MAP dye solution.....134

Figure 6-14: Hydrogen peroxide decomposition in copper catalysed system with added PPD-MAP pre-made dye at 10<sup>th</sup> min. Reaction solution contained 0.02 mM copper(II) sulfate at pH 10 using 400 mM ammonia/ammonium chloride buffer. ....135

Figure 6-15: Hydrogen peroxide decomposition in copper catalysed system with added pre-oxidised dye combination at 10<sup>th</sup> minute. (A) 0.02 mM copper(II) sulfate in a chelant/dye free system, (B) 0.02 mM copper(II) sulfate, 1 mM PPD-AHT dye, (C) 0.02 mM copper(II) sulfate, 1 mM PAP-MAP dye, (D) 0.02 mM copper(II) sulfate, 1 mM DTS-MAP dye. Reaction was carried out at pH 10 using 400 mM ammonia buffer. ....135

Figure 6-16: PPD-MAP oxidative trimer synthesised.....136

Figure 6-17: Impact of adding PPD-MAP trimer on copper catalysed decomposition of alkaline hydrogen peroxide. Reactions contained (A) 0.02 mM copper(II) sulfate in a chelant/dye-free system (B) 0.02 mM copper(II) sulfate, 0.25 mM PPD-MAP trimer. The reaction solution had pH 10.0 using 400 mM ammonia buffer. ....137

Figure 6-18: EPR spectra of copper(II) ions in a ligand-free system and along with PPD, MAP and PPD-MAP dye formed in-situ. Reaction solution contained 0.02mM copper(II) sulfate mixed with 0.98 M hydrogen peroxide in 400 mM ammonia/ammonium chloride buffer pH 10. The reaction mixture was stirred for 30 min and then mixed with glycerol (10%) and frozen in liquid nitrogen. The

spectra were recorded at 120 K. (A) Cu <sup>2+</sup> ions with hydrogen peroxide only in the absence of dye precursors (B) Cu <sup>2+</sup> with PPD-MAP dye formed in situ using hydrogen peroxide (C) Cu <sup>2+</sup> with PPD only without using hydrogen peroxide (D) Cu <sup>2+</sup> with MAP only without hydrogen peroxide.....	139
Figure 6-19: Metal binding with poly-phenylenediamine.....	140
Figure 7-1: SEM image of human hair fibre showing bubbles at hair shaft. .....	144
Figure 7-2: Cross section of human hair fibre showing material deposits underneath cuticles.....	144
Figure 7-3: Cross-sectional SEM image of a human hair showing bubble underneath the cuticles.....	146
Figure 7-4: Interaction of electromagnetic radiation with a molecule. <sup>211</sup> ...	150
Figure 7-5: Fundamental vibrations in a carbon dioxide molecule. <sup>213</sup> .....	151
Figure 7-6: FT-IR spectrum of air.....	152
Figure 7-7: Control experiment using phosphoric acid and stirring bar without hair fibres or carbonate showing low level of absorption for carbon dioxide. ...	153
Figure 7-8: IR spectra for various samples of human hair fibres showing the absorption band for carbon dioxide produced. ....	154
Figure 7-9: Comparing amount of calcium carbonate determined by image analysis and gas IR method.....	156
Figure 9-1: Synthesis of NPGA probe.....	165
Figure 9-2: Experimental setup to monitor decomposition of hydrogen peroxide.....	167
Figure 9-3: Cross-sectional SEM image of a human hair showing bubble underneath the cuticles.....	177
Figure 9-4: Schematic diagram of experimental setup for IR analysis of carbon dioxide. ....	179
Figure 9-5: IR spectra for carbon dioxide from various concentration levels of sodium carbonate to develop a standard curve.....	181
Figure 10-1: MS spectrum for H-NPGA in LC-MS analysis confirming the formation of H-NPGA derivative at 90 <sup>th</sup> minute of hydroxylation. MS-ESI m/z [M-H] <sup>+</sup> Found 396.1060 (Calculated for C <sub>16</sub> H <sub>18</sub> N <sub>3</sub> O <sub>9</sub> : 396.1049) .....	183
Figure 10-2: MS spectrum demonstrating presence of starting NPGA probe. MS-ESI m/z [M-H] <sup>+</sup> Found 380.1101 (Calculated for C <sub>16</sub> H <sub>18</sub> N <sub>3</sub> O <sub>8</sub> : 380.1099). .....	184
Figure 10-3: Iron(III) speciation in Fe <sup>3+</sup> -HEDTA system. ....	185

Figure 10-4: Iron(III) speciation in Fe <sup>3+</sup> -EDDS system. ....	185
Figure 10-5: Iron(III) speciation in Fe <sup>3+</sup> -DTPA system.....	186
Figure 10-6: Iron(III) speciation in Fe <sup>3+</sup> -HEDP system. ....	186
Figure 10-7: Iron(III) speciation in Fe <sup>3+</sup> -DTPMP system.....	187
Figure 10-8: Iron(III) speciation in Fe <sup>3+</sup> -EDDS/DTPMP mixed ligand system. .....	187
Figure 10-9: Copper(II) speciation in Cu <sup>2+</sup> -HEDTA system. ....	188
Figure 10-10: Copper(II) speciation in Cu <sup>2+</sup> -EDDS system. ....	188
Figure 10-11: Copper(II) speciation in Cu <sup>2+</sup> -DTPA system.....	189
Figure 10-12: Copper(II) speciation in Cu <sup>2+</sup> -HEDP system. ....	189
Figure 10-13: Copper(II) speciation in Cu <sup>2+</sup> -DTPMP system.....	190
Figure 10-14: Copper(II) ions speciation at high ammonia level (400 mM) in the absence of calcium ions.....	190
Figure 10-15: Iron(III) speciation in the presence of calcium in a chelant-free system. ....	191
Figure 10-16: Copper speciation in EDDS system at higher ammonia concentration level (400 mM).....	191
Figure 10-17: Copper ion speciation in DTPMP system in the presence of large excess of calcium ions. ....	192
Figure 10-18: DTPMP speciation in copper-calcium binary system.....	192
Figure 10-19: Copper speciation in DTPMP chelant system in the absence of calcium ions at higher ammonia level.....	193
Figure 10-20: Copper speciation in Hair-EDDS chelant system using copper treated hair fibres. ....	193
Figure 10-21: Copper speciation in Hair-EDTA chelant system using copper treated hair fibres. ....	194
Figure 10-22: Copper speciation in Hair-DTPMP chelant system using copper treated hair fibres. ....	194
Figure 10-23: Copper speciation in hair-EDDS system using a low concentration of EDDS ligand. ....	195
Figure 10-24: Copper speciation in hair-EDTA system using low concentration of EDTA ligand.....	195
Figure 10-25: pH drop in Cu <sup>2+</sup> -HEDP decomposition system. Reaction solution contained 0.18 mM Cu <sup>2+</sup> ions and 1.3 mM HEDP chelant at pH 10 with 20 mM ammonia/ammonium chloride buffer. Hydrogen peroxide (0.98 M) was	

added to trigger the decomposition reaction. (A) Bench mark reaction solution (B) initial pH of the reaction solution adjusted to 9.55 using few drops of dilute ammonia solution.....196

Figure 10-26: Monitoring HEDP degradation:  $^1\text{H}$  NMR of isolated nanoparticles. (A) HEDP ligand in  $\text{D}_2\text{O}$  (B) Cu/HEDP with glycerol (internal standard) in  $\text{D}_2\text{O}$ , 0.18 mM  $\text{Cu}^{2+}$ , 1.3 mM HEDP ligand dissolved in 20 mM pH 10 ammonia/ammonium chloride buffer (total reaction volume 25 mL). Solution was evaporated to remove buffer and solid residue was dissolved in  $\text{D}_2\text{O}$  with a few drops of concentrated nitric acid and glycerol. The proton NMR at 400 MHz showed a broadened (due to  $\text{Cu}^{2+}$ ) peak for HEDP ligand (C) 5 mg nanoparticles dissolved in 0.4 mL of concentrated nitric acid and subsequently dissolved in  $\text{D}_2\text{O}$ . Glycerol (0.1 g) was added and  $^1\text{H}$  NMR was obtained at 400 MHz machine. The spectrum did not show signal for HEDP ligand.....197

Figure 10-27: Colorimetric experiment to examine the oxidation state of copper in copper based nanoparticles.....198

Figure 10-28: Changes in copper speciation in 20 mM ammonia ammonia/ammonium chloride buffer and subsequent changes after complete degradation of HEDP ligand.....198

Figure 10-29: Changes in copper speciation in 20 mM ammonia ammonia/ammonium chloride buffer in the presence of HEDP chelant and phosphate & carbonate anions.....199

Figure 10-30: Hydrogen peroxide decomposition in  $\text{Cu}^{2+}$ -HEDP system with phosphate and carbonates added at the 6<sup>th</sup> minute to an ongoing decomposition reaction. (A) 0.18 mM of  $\text{Cu}(\text{II})\text{SO}_4$ , 1.3 mM of HEDP chelant dissolved in 20 mM pH 10 ammonia/ammonium chloride buffer with of hydrogen peroxide (0.98 M). Hydrogen peroxide decomposition was monitored over time. (B) To an ongoing reaction of A, 0.5 mL of 0.25 M phosphate buffer (disodium hydrogen phosphate-tri sodium phosphate) solution pH 10 was added at the 6<sup>th</sup> minute. (C) To another ongoing reaction A, 0.5 mL of 0.25 M ammonium carbonate was added at 6<sup>th</sup> minute using a syringe and hydrogen peroxide decomposition was monitored. ....199

Figure 10-31: Copper-HEDP catalysed hydrogen peroxide decomposition using different buffer composition. (A) 0.18 mM of copper(II) sulfate, 1.3 mM of HEDP chelant dissolved in 20 mM pH 10 ammonia/ammonium chloride buffer and mixed with 0.98 M hydrogen peroxide. Hydrogen peroxide decomposition

was monitored over time. (B) 0.18 mM of copper(II) sulfate, 1.3 mM of HEDP chelant dissolved in 20 mM pH 10 20 mM phosphate buffer with 0.98 M hydrogen peroxide. (C) 0.18 M of copper(II) sulfate in a chelant-free system dissolved in 20 mM pH 10 phosphate buffer with 0.98 M hydrogen peroxide. ....200

# Acknowledgment

---

I am heartily thankful to my supervisor, Dr. Victor Chechik for his encouragement, guidance and support. He was kind, friendly and forthcoming to me throughout my research. His help made my family life easy at York.

Many thanks to Dr Jennifer Marsh for her contribution and support throughout this project. I am also thankful to Dr Simon Godfery for valuable discussion and his permission to use scheme 3-1.

I am grateful to post doctorate fellows in our research group, Dr. Jamie Gould and Dr. Rob Thatcher for their valuable suggestions. I am thankful to my fellows, Thomas Newby, Chiara Baldassarri and Sindhu Krishna. Thanks to Rob Smith for a wonderful time together in the lab. I am grateful for his permission to use his data (Figure 6.12).

Thanks to The Procter and Gamble Company and Wild fund from University of York for funding this research.

Special thanks to Zhou Lu for submitting this thesis on my behalf and offering me valuable tips about life in China.

Lastly, I am immensely grateful to my mother, Kaneez Syeda Firdous for her huge contribution to my academic & professional career. I offer my regards to my beloved wife, Dr. Shazia Abarar. Surely, I cannot achieve my goals without her support. Welcome to our two new family members, Syeda Batool Naqvi and Muhammad Abbas Raza Naqvi who made my house “a sweet home”.

## **Declaration**

---

This research thesis is my original work carried out at The Department of Chemistry, The University of York, except where specific references have been made. I have not submitted this work neither as a part nor as a whole for a degree or diploma or other qualification at any other university.

**Kazim Raza Naqvi**

# Chapter 1: Introduction

---



The morphological structure of human hair fibre includes three major layers, the outermost layer is cuticle; the middle region is called cortex and the innermost region is medulla (Figure 1-1). These three layers differ slightly in their chemical composition.

The cuticle coats the fibre as “a tile on a roof”. Being the outermost layer, the cuticle plays an important role in controlling adsorption and diffusion of various active ingredients during bleaching, dyeing and fibre strengthening treatments (hair conditioning). It is also responsible for the shine, tactile properties, surface friction and wettability. The cuticle itself is made of various sub-layers. The outer hydrophobic covalently bonded layer is composed of an ester of 18-methyl-eicosanoic acid.<sup>12, 14</sup>

The cortex accounts for the major portion of the fibre and is largely responsible for its mechanical properties. It contains proteins that are termed keratinous or nonkeratinous according to their cystine content; nonkeratinous proteins contain less cystine. The consequently lower amount of disulfide crosslinks leaves nonkeratinous proteins more labile and less resistant to chemical attack than the cystine rich keratinous components of the fibre.<sup>13</sup>

In daily life, hair is subjected to various grooming treatments such as cleansing, conditioning, colouring and styling. The structure and chemical composition of hair plays an important role in these cosmetic treatments.<sup>15, 16</sup> The presence of lipids at the outermost layer and the extent of disulfide crosslinking offer resistance to the chemical treatments. Hence, different hair fibres may require different formulations for the same cosmetic treatment.

### **1.1.1 Metal contents of human hair fibre**

Human hair fibre may contain alkali, alkaline earth and transition metal ions.<sup>17</sup> Commonly observed metals are calcium, magnesium, iron, copper, zinc and lead.<sup>18-21</sup> There is a variety of both soft and hard chelating groups in the hair fibre. For instance, hair is rich in sulfur containing components, it is believed that metal ions are bonded through metal-sulfur interaction. Hydroxyl groups of serine and nitrogen groups may also provide metal binding sites. A recent EPR study also proposed nitrogen and oxygen binding sites for copper in hair fibre.<sup>22</sup> The carboxylate anions of dicarboxylic acids (aspartic acid and glutamic acid) can

also chelate metal ions. This fact is supported by the observation that hair absorbs more alkaline earth metals at neutral pH due to deprotonation of carboxylate.<sup>18, 23</sup> Oxidative hair treatment oxidises cystine to cysteic acid which can further enhance metal uptake by providing new binding sites.<sup>24-26</sup> Melanin pigment present in the hair fibre can also bind metal ions such as calcium, magnesium, iron and copper.<sup>27-29</sup>

Metal uptake in the hair fibre varies for different gender, age and is influenced by demographics and pollution. Inhabitant living in industrial zones may have high metal build up. Daily grooming which involves cleansing and styling contributes to the hair metal uptake.<sup>30</sup> Tap water contains a significant level of metal ions which get adsorbed on the fibre surface during washing. Calcium soap deposits have also been observed on the hair surface.<sup>31</sup> The presence of these metals changes the physicochemical characteristics of the hair fibre resulting in stiffness, difficulty in dry and wet combing and styling, less shine and large volume.<sup>25, 32</sup> This alters the response and behaviour of the hair fibre to different chemical treatments such as bleaching, permanent dyeing and straightening.

A quantitative analysis of American-Caucasian hair fibre by Procter & Gamble (P&G) found 10-20 ppm of iron and 100-200 ppm of copper. A large amount of calcium (1000–2000 ppm) and 150-300 ppm of magnesium ions was also observed.<sup>33</sup> These metal ions were extracted by fibre digestion and quantified by chromatographic and spectroscopic methods.<sup>34-37</sup>

## **1.2 Oxidative hair treatment**

Hair bleaching and permanent dyeing are chemical processes aimed at changing the hair colour.<sup>38</sup> The bleaching process is defined as “the lightening of natural hair colour”. The objective is to give hair a lighter look and prepare it for the subsequent dyeing steps. It is commonly used by both elderly people to conceal their grey hair and youth to achieve a new fashionable colour shade. The history of hair bleaching goes back to early Romans who first used plant ash to change their hair colour shade. The chemistry came to play a vital role with the application of hydrogen peroxide by the late 19<sup>th</sup> century. At an international exhibition in 1867, British chemist E. H. Thiellay demonstrated the benefits of

hydrogen peroxide for oxidative hair bleaching. His product was called *Eau de fontaine de Jouvence doree* (Golden water from the fountain of youth).<sup>39</sup>

Natural hair colour is due to small granules of polymeric pigment known as melanin.<sup>39-41</sup> Melanin is the main target site and component to be removed or degraded during the process of hair bleaching. Two types of melanin are found in human hair fibre, eumelanin and pheomelanin (Figure 1-2). Eumelanin provides brown to black colour shades while pheomelanin is responsible for yellow, blond and red colour shades. Hair colour is determined by the amount of melanin present, the ratio of the two types of melanin and their grain size. The melanin particles scatter light in addition to some absorption by the chromophores in the melanin structure, thus giving colour to the fibre. Melanin is relatively stable under acidic conditions and does not degrade or depolymerise, however, it can be depolymerised and bleached under alkaline conditions using an oxidising agent.<sup>41-47</sup>

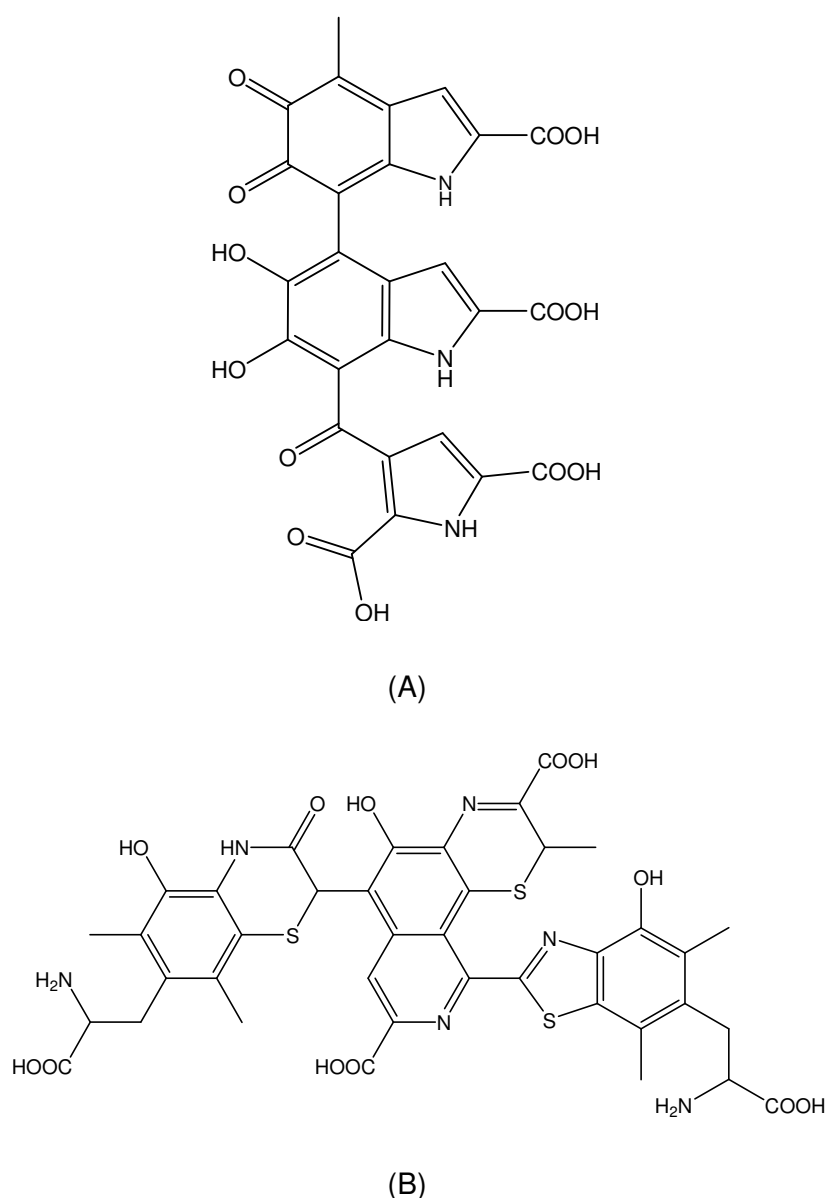


Figure 1-2: Proposed chemical structure of (a) eumelanin and (b) pheomelanin.<sup>47</sup>

### 1.2.1 Chemistry of hair bleaching

Hair bleaching involves oxidative degradation of melanin polymer (Figure 1-3). Hydrogen peroxide is commonly used in combination with ammonium hydroxide solution. Due to the complex structure of melanin, the reaction mechanism for bleaching is not fully known. It is believed that the bleaching process begins with the gradual solubilisation of the melanin in hydrogen peroxide at high pH which may detach pigment grains from the hair proteins. The dissolved melanin is fairly easily broken down or depolymerised to carboxylated

derivatives that are removed on rinse off.<sup>38, 39</sup> A model study has revealed that dihydroxyindol (DHI) and dihydroxyindol carboxylic acid dimer degrades at high pH via a repeated attack of nucleophilic peroxide anion. It involves breaking carbon-carbon bonds through various intermediates, eventually forming pyrrole acids (Figure 1-4).<sup>45</sup>

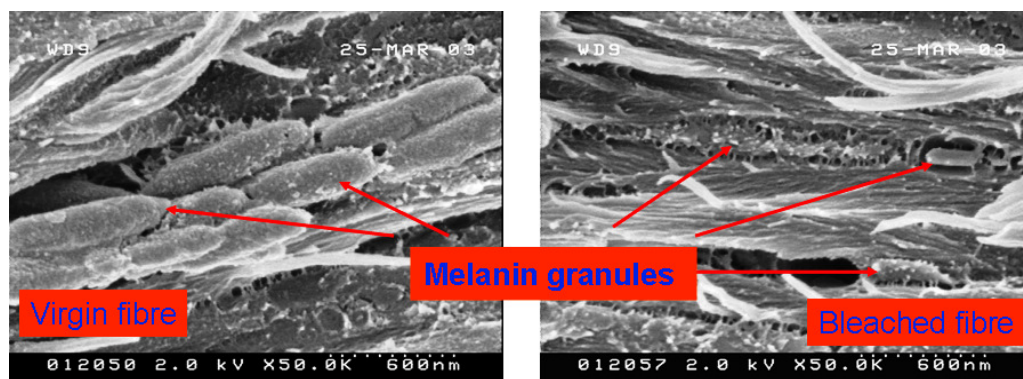


Figure 1-3: TEM images of melanin grains before and after oxidative bleaching.<sup>48</sup>

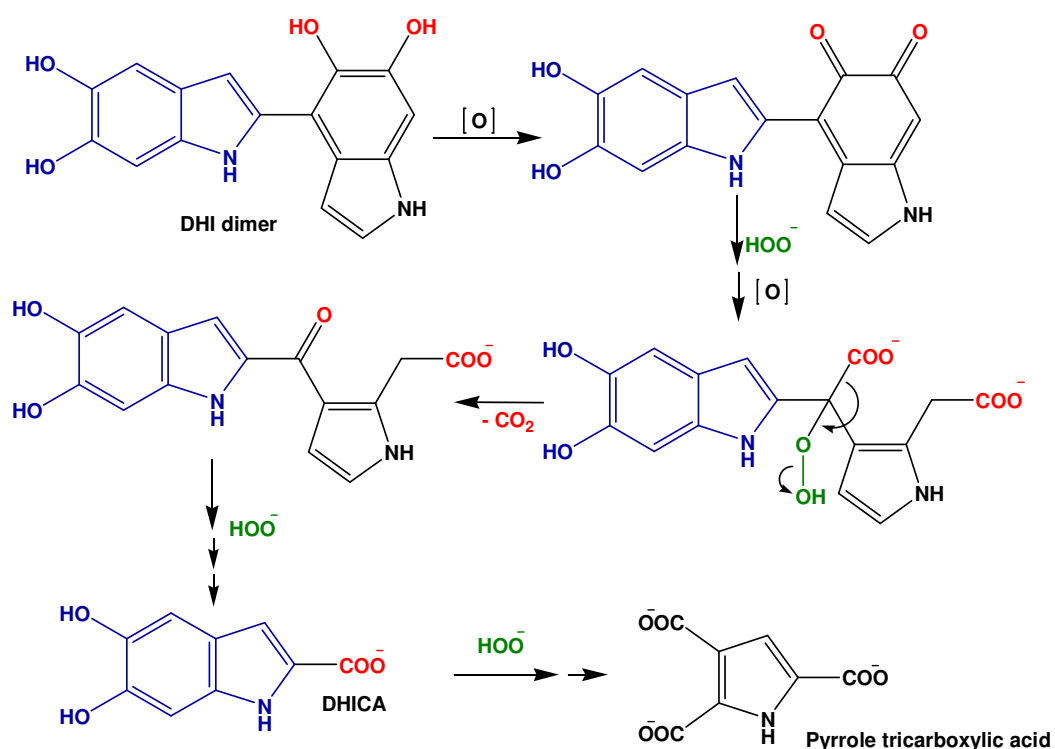


Figure 1-4: Proposed mechanism for the oxidative degradation of dihydroxyindol dimer.<sup>45</sup>

Apart from alkaline hydrogen peroxide, other oxidizing agents such as potassium permanganate, persulfates, peracetic acid and sodium hypochlorite have also been investigated for their ability to bleach melanin. Similarly, other alkalizing agents such as sodium hydroxide, sodium carbonate, monoethanolamine have also been studied. However, hydrogen peroxide & ammonia mixture is the best combination.<sup>49</sup> Ammonia has a special role in disintegrating melanin particles. The studies revealed that hair bleaching is not merely due to alkaline pH, but the ability of ammonia to partially solubilise the melanin particles.<sup>40</sup>

### 1.2.2 Properties of bleached hair and the role of transition metal ions in bleaching

In addition to bleaching melanin, oxidative treatment with alkaline hydrogen peroxide can induce various other chemical modifications in the hair fibre which can change its physicochemical and biological properties.<sup>50,51</sup> Bleaching can also lead to oxidation of protein components of the hair fibre. Oxidation of cystine cleaves disulfide linkage generating cysteic acid (Figure 1-5). This alters the electrostatic properties of fibre and creates anionic sites which can subsequently lead to higher metal uptake. As the disulfide bond contributes to the tensile properties of the fibre, its cleavage leaves hair fragile and damaged.<sup>52</sup> This is why bleached hair fibres present low tensile strength, high porosity and poor sensorial profile.<sup>53, 54</sup> This also alters the cosmetic attributes of the fibre and makes its manageability and styling difficult.<sup>55-58</sup>

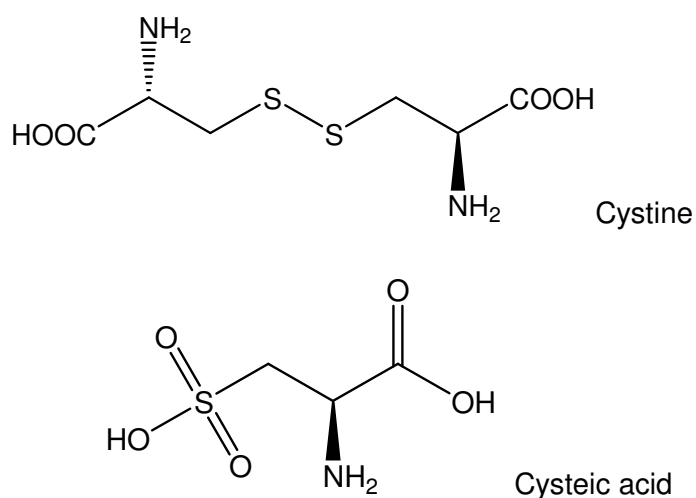


Figure 1-5: Cystine and its oxidation product cysteic acid.

As described earlier, hair contains a significant amount of iron and copper metal ions. These transition metals can catalyse decomposition of hydrogen peroxide during oxidative hair colouring through a Fenton-like reaction. During a preliminary experiment, bleaching hair fibres with alkaline hydrogen peroxide produced significant bubbles (Figure 1-6). This reaction may involve formation of highly reactive intermediates such as hydroxyl radicals or higher oxidation state metal intermediates. Free radical-mediated oxidation of proteins and lipids is well-known.<sup>59, 60</sup> Previous studies have reported a positive correlation of copper content in the hair and cysteine oxidation to form cysteic acid.<sup>61-63</sup> This metal-mediated free radical chemistry inside the hair fibre may cause significant damage to the hair fibre. This thesis reports our investigation of the role of iron and copper metal ions in oxidative hair colouring.

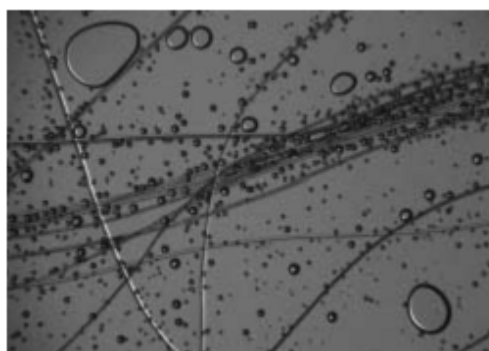


Figure 1-6: Hydrogen peroxide decomposition in the presence of metal loaded human hair fibres.<sup>63</sup>

## 1.3 Metal catalysed decomposition of hydrogen peroxide

### 1.3.1 Fenton chemistry

Metal catalysed decomposition of hydrogen peroxide has a long story extending over more than 100 years.<sup>64, 65</sup> H.J.H Fenton made exciting observations in 1876 when he was still an undergraduate student at Cambridge. He published his observations in *Chemical News*. A full paper was published later in 1894 where he described<sup>66</sup>

*“When tartaric acid in aqueous solution interacts with certain oxidizing agent in the presence of a trace of ferrous salt, a solution is obtained which gives a beautiful violet colour on the addition of a caustic alkali”.*

Fenton mentioned two important points in his findings essential for the reaction: (1) the presence of an oxidizing agent e.g. hydrogen peroxide or chlorine water, and (2) a small amount of a heavy metal such as iron(II) in its reduced form<sup>64-68</sup>. He isolated the product and determined its empirical formula. The product was dihydroxymaleic acid (Figure 1-7). The violet colour that Fenton observed is actually due to Fe complex of dihydroxymaleic acid.

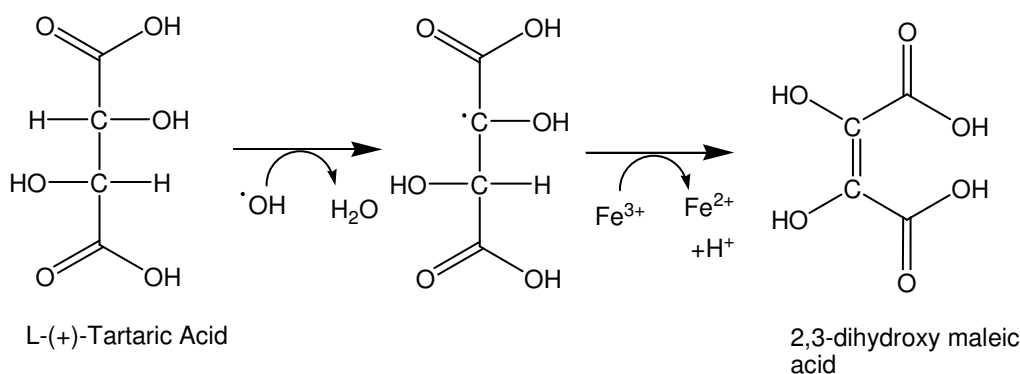


Figure 1-7: Oxidation of tartaric acid in a Fenton reaction.<sup>64</sup>

50 years later, Haber studied the iron catalysed decomposition of hydrogen peroxide and proposed the reaction mechanism. He proposed the formation of hydroxyl radical.<sup>65, 69</sup> There is a debate among researchers about the reaction mechanism and the formation of hydroxyl radical. Despite the controversy about its mechanism, the Fenton reaction has played an important role in organic synthesis, environmental processes and mechanistic studies.

### 1.3.1.1 Mechanism of Fenton Reaction

The metal catalysed decomposition of hydrogen peroxide has been the subject of numerous investigations. The chemistry of this reaction revolves around the transition metal in its lower oxidation state (reduced form such as  $\text{Fe}^{2+}$ ) which is oxidised to a higher oxidation state (oxidised form such as  $\text{Fe}^{3+}$ ) using an oxidizing agent, and then is reduced back to the original lower oxidation state. The important outcome of the reaction is the formation of new oxidizing species

which is far more powerful and reactive than the parent oxidizing agent.<sup>65</sup> The identification of this new oxidizing species was the point of interest for a series of investigations carried out over the years.

The earliest proposed mechanism for the decomposition of hydrogen peroxide in the presence of ferrous ion ( $\text{Fe}^{2+}$ ) is a chain reaction which describes the generation of hydroxyl radical. The hydroxyl radical is the new oxidant formed and is far more powerful than hydrogen peroxide.<sup>65</sup> It is a highly reactive and short lived species which may undergo a reaction with hydrogen peroxide yielding superoxide. The  $\text{Fe}^{2+}$  is oxidised to  $\text{Fe}^{3+}$  which in turn is reduced back to  $\text{Fe}^{2+}$  by superoxide to enter in a new cycle (Figure 1-8).

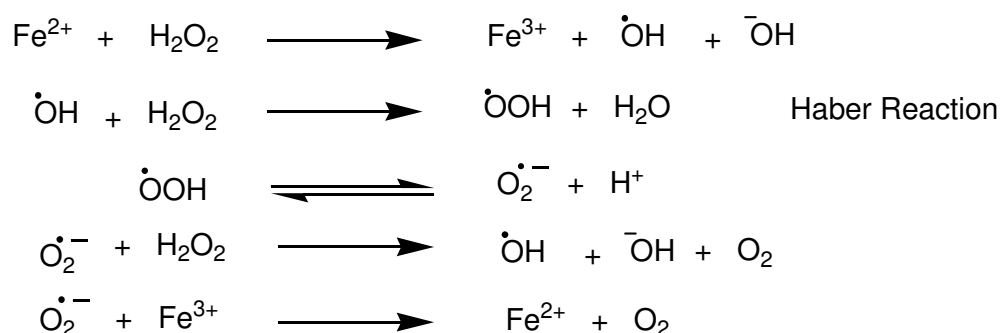


Figure 1-8: Iron(II) catalysed decomposition in a Fenton reaction.<sup>70</sup>

The ferric ion ( $\text{Fe}^{3+}$ ) decomposes hydrogen peroxide following a similar mechanism converting  $\text{Fe}^{3+}$  to  $\text{Fe}^{2+}$  generating superoxide. The  $\text{Fe}^{2+}$  and superoxide then enter the cycle for the decomposition of hydrogen peroxide.



Figure 1-9: Iron(III) catalysed decomposition in a Fenton reaction.

The activity of a metal in a Fenton reaction is related to its redox potential. The ability of the metal to cycle depends upon the ease of its switch over between the two oxidation states. The metal redox potential needs to be in a narrow window range which corresponds to  $\text{O}_2/\text{O}_2^-$  and  $\text{H}_2\text{O}_2/\dot{\text{O}}\text{H}$  conversions.<sup>70, 71</sup>

The formation of hydroxyl radical in the Fenton reaction has been an issue of debate over the years. Due to its high reactivity and short half-life, the detection

and analysis of hydroxyl radical by any direct method is extremely difficult. Various indirect methods were used to confirm the formation of hydroxyl radical.<sup>72</sup>

More or less at the same time as Haber proposed hydroxyl radical formation, the idea of formation of an iron-oxo intermediate or a complex in high oxidation state was also proposed.<sup>73</sup> In the excess of hydrogen peroxide, the oxygen evolution was explained by the formation of ferryl ion Fe(IV)=O (Figure 1-10).<sup>74-76</sup> Interestingly, the chemical reactivity of hydroxyl radical and ferryl ion is assumed to be very similar. This makes it extremely difficult to distinguish between the intermediates formed in the Fenton reaction.

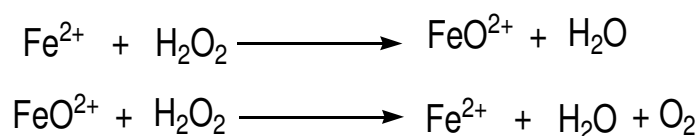


Figure 1-10: Formation of ferryl ion intermediate in a Fenton reaction.

The recent studies have demonstrated that the Fenton reaction may proceed through various pathways (Figure 1-11).<sup>77, 78</sup> The pathway in a given reaction depends on many factors such as: nature of the metal, nature of the ligand and solvent, the concentrations of the reactants, the nature and concentration of any substrate, the ratio of metal to hydrogen peroxide and pH of the reaction mixture. All these factors play a vital role in defining the mechanism of the Fenton reaction.<sup>65, 79</sup> The hydroxyl radical might be formed under the given reaction conditions, whereas ferryl ion may be the dominant intermediate under different conditions. The important point is that regardless of whether hydroxyl radical or iron-oxo complex is formed; the intermediate species is a powerful oxidant which has an important role in organic, medicinal chemistry and biochemistry.<sup>80</sup> In the rest of the thesis, hydroxyl radical is discussed as the main reactive intermediate involved, though the reaction may also involve formation of other reactive species with similar reactivity.

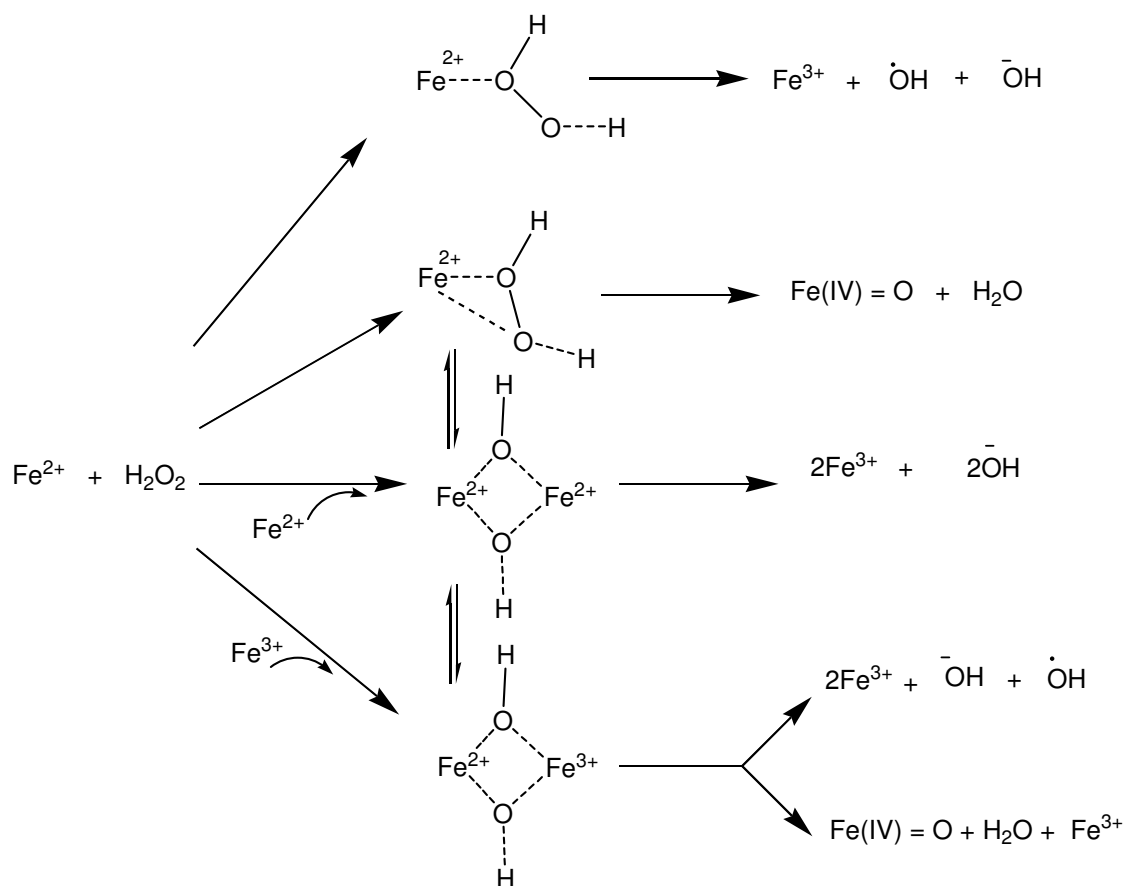


Figure 1-11: Possible mechanistic pathways of the Fenton reaction.<sup>77</sup>

### 1.3.2 Copper catalysed decomposition of hydrogen peroxide

Besides iron, several other transition metals in their low oxidation state can participate in a similar hydrogen peroxide decomposition mechanism.<sup>81</sup> Such reactions are generally known as Fenton like reactions. The kinetic data reveal that at ambient temperature,  $\text{Cu}^{2+}$  or  $\text{Cu}^+$  have high catalytic activity in the decomposition of hydrogen peroxide.<sup>65, 67</sup> The copper catalysed decomposition of hydrogen peroxide has also important implications for various biological systems.

Copper(II) catalyses the decomposition of hydrogen peroxide by following a mechanism similar to Fenton reaction (Figure 1-12).<sup>82-85</sup> It forms a complex with hydrogen peroxide which on decomposition gives  $\text{Cu}^+$  and superoxide. The reduced  $\text{Cu}^+$  decomposes hydrogen peroxide yielding hydroxyl radical and leading to oxidation of  $\text{Cu}^+$  back to  $\text{Cu}^{2+}$  which completes the cycle. Similarly, superoxide enters the cycle of hydrogen peroxide decomposition generating

hydroxyl radical. The superoxide also reduces  $\text{Cu}^{2+}$  to  $\text{Cu}^+$  to continue the metal recycling.<sup>86, 87</sup>

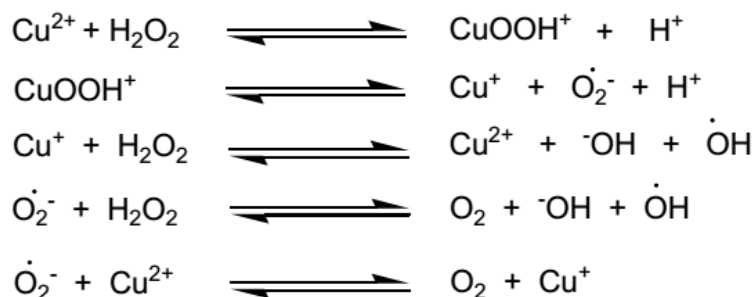


Figure 1-12: Copper(II) catalysed decomposition of hydrogen peroxide in a Fenton-like reaction.<sup>86, 87</sup>

### 1.3.3 Introducing chelants in a Fenton reaction

The Fenton reaction involves complex mechanistic pathways and introducing a ligand or other organic species may further complicate the reaction mechanism. Iron(II) or iron(III) systems with various ligands have been discussed extensively in the literature.<sup>88-92</sup> The ligands are employed with the aim to chelate metal in order to stabilise hydrogen peroxide. Metal complexation greatly influences the catalytic activity of central metal ions. The composition of the reaction solution, the nature of the donor atoms present in the chelant, steric hindrance and finally the stability of the metal-chelant complex under the experimental conditions alters the catalytic activity of metal ions.



Figure 1-13: Hydrogen peroxide decomposition in a metal-ligand ( $\text{L}_n$ ) system.

Generally a ligand is added to deactivate the metal ions; however some metal-ligand complexes may have high catalytic activity in the decomposition reaction. For example,  $\text{Fe}^{2+}/\text{Fe}^{3+}$  complexes with ethylenediaminetetraacetic acid (EDTA) and diethylenetriamine pentaacetic acid (DTPA) may act as pro-oxidants “increasing the activity for the formation of reactive oxygen species” as well as antioxidants “decreasing the formation of reactive oxygen species” solution depending upon the reaction conditions.<sup>92</sup> Koppenol also described that  $\text{Fe}^{2+}$ -

EDTA system might be 100 times more active than the corresponding  $\text{Fe}^{2+}$  aqua complex.<sup>82</sup>

In summary, different metal-ligand systems might have different catalytic activity in decomposing hydrogen peroxide depending upon the nature of the reaction system. The activity of iron(III) and copper(II) complexes with various chelants is discussed in chapter 3 of this thesis.

## 1.4 Aims and objectives

The aim of the current project is to investigate the catalytic activity of copper and iron metal ions in the decomposition of hydrogen peroxide under the alkaline conditions corresponding to oxidative hair colouring (pH 8-10). As mentioned earlier, transition metal ions in the hair fibre may catalyse the decomposition of hydrogen peroxide through a Fenton cycle. Previous investigations of the Fenton chemistry and hydroxyl radical formation have generally been carried out at acidic pH. Very little is known about the role of transition metals and their complexes in the decomposition of alkaline hydrogen peroxide. Also, most of the published work on the metal-catalysed decomposition of  $\text{H}_2\text{O}_2$  used metal/ligand concentrations, reaction conditions and the ligands which do not match the hair bleaching and dyeing system. The identification and quantification of the hydroxyl radical formation under realistic conditions have hardly been investigated. This provided the motivation for the current project which focuses on the investigation of the catalytic reactivity of these transition metals in the decomposition of hydrogen peroxide and hydroxyl radical formation at high pH.

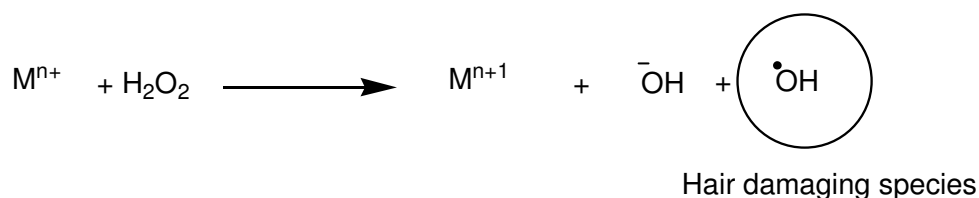


Figure 1-14: The hydroxyl radical formation in metal catalysed decomposition of hydrogen peroxide.

To achieve this goal, an analytical methodology for the analysis of hydroxyl radical needed to be developed. A colorimetric probe was used to monitor

hydroxyl radical formation in iron and copper catalysed decomposition of hydrogen peroxide which is discussed in chapter 2.

Various chelants were potential candidates for the current studies. The objective was to study the activity of various metal-ligand combinations in decomposition of alkaline hydrogen peroxide and generation of hydroxyl radicals. In this work, various chelants were screened for their efficacy and performance in preventing decomposition of alkaline hydrogen peroxide and suppressing hydroxyl radical formation. The criteria for choosing chelants for this study were based on their commercial availability and regulatory concerns for their usage in cosmetics. The chelants short listed for the current studies were ethylenediaminetetraacetic tetrasodium salt (EDTA), *N*-(hydroxyethyl)-ethylenediaminetriacetic trisodium salt (HEDTA), pentasodium diethylenetriaminepentaacetate (DTPA), ethylenediamine-*N,N'*-disuccinic acid (EDDS), 1-hydroxyethane 1,1-diphosphonic acid (HEDP) and diethylenetriamine penta(methylene phosphonic acid) (DTPMP). The results of our study of hydrogen peroxide decomposition and hydroxyl radical formation with copper and iron in the presence of these chelants are discussed in chapters 3, 4 & 5 of this thesis.

Apart from hair bleaching, oxidative hair dyeing using aromatic diamines and aminophenols may also be influenced by the presence of transition metal ions. Oxidative polymerisation of these dye precursors generates coloured species inside the hair fibre imparting new colour shades. Here, we report the results of our study on the effect of copper(II) ions in the decomposition of hydrogen peroxide in the presence of oxidative dye precursors e.g. *p*-phenylenediamine and *p*-aminophenol. The aromatic species may act as antioxidants and suppress the oxidation reaction; however, hardly any such study has been reported previously describing the influence of these oxidation dyes in catalysing or suppressing Fenton chemistry. This topic is discussed in chapter 6.

Chapter 7 discusses a quantitative analysis of calcium carbonate present in human hair fibres. As described earlier, human hair fibres contain high amounts of calcium. Oxidation (bleaching) and thermal treatments (daily grooming & blow drying) of hair fibre leaves hair fragile. Microscopic images of treated hair fibres show some bubbles lying over the hair shaft, however, the exact nature of the

bubble material was not known. In the current study, experiments were carried out to define the nature of the unknown bubble material.

## **Chapter 2: Monitoring hydroxyl radical formation in a Fenton-like reaction**

---

## 2 Monitoring hydroxyl radical formation in a Fenton-like reaction

The role of hydroxyl radical ( $\cdot\text{OH}$ ) in biology has been the focus of extensive research recently.<sup>80, 93</sup> It may cause oxidative stress, oxidation of lipid & protein and damage to natural fibres during chemical treatments.<sup>94</sup> Due to its high reactivity, detection and quantification of hydroxyl radical has been a challenge for scientists. The complex mechanism of Fenton-like reaction adds further complications to the detection and quantification of hydroxyl radicals. An absolute quantification is almost impossible. Various indirect methods have been utilised and reported in the literature.<sup>72</sup> The selectivity & sensitivity of the analytical method is an important aspect to be considered in choosing a particular method. This chapter describes our efforts to develop an experimental strategy to monitor hydroxyl radical formation in an alkaline pH media corresponding to hair bleaching and colouring. A colorimetric probe is discussed to monitor hydroxyl radical formation.

### 2.1 Hydroxyl radical

Hydroxyl radical is a highly reactive and short-lived species. An estimated value for its half-life is  $10^{-9}$  s.<sup>95, 96</sup> It is a strong oxidising agent ( $E^\circ \cdot\text{OH}/\text{H}_2\text{O} = 2.73\text{V}$ ) and can react with almost any molecule with rate constants approaching  $10^8 - 10^{10} \text{ M}^{-1} \text{ s}^{-1}$ .<sup>82</sup> It exhibits highly non-selective and indiscriminate behaviour in its reactivity.

Hydroxyl radicals can be generated via different pathways. One of them is Fenton and Fenton-like reactions where redox metal ions decompose hydrogen peroxide generating radical species. In the lab, it can be generated by photolysis of 1-hydroxy-2(1H)-pyridinethione.<sup>97, 98</sup> Other sources can be radiolysis of water<sup>99</sup> and UV-induced photolysis of hydrogen peroxide generating hydroxyl radicals (Figure 2-1).<sup>59, 100, 101</sup>

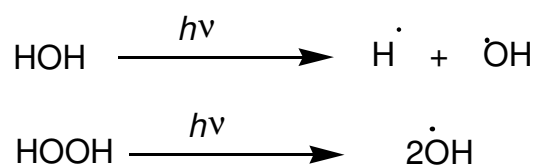


Figure 2-1: Photolysis of water and hydrogen peroxide generating hydroxyl radicals.

## 2.2 Monitoring hydroxyl radical formation

Quantification of hydroxyl radicals in a given system is important for defining mechanistic details about its formation and reactivity. Due to its high reactivity, it is extremely difficult to measure hydroxyl radical formation directly. Certain chemical and biological systems offer an even more difficult scenario due to the presence of natural anti-oxidants and radical scavengers. These species may interfere with the radical chemistry and make hydroxyl radical measurements more complicated.

Over the years, various methodological and technical improvements have been reported in the literature to monitor hydroxyl radical formation. Most of the previously reported studies rely on indirect methods employing a hydroxyl radical capturing probe that can be subsequently analysed by various chromatographic or spectroscopic techniques.

### 2.2.1 Electron spin resonance spectroscopy (ESR)

Electron spin resonance spectroscopy (ESR) is often employed to investigate free radical intermediates. ESR is a sensitive technique; however, a direct analysis of hydroxyl radical formation is impossible. It is due to its high mobility and reactivity especially in a liquid solution. The hydroxyl radical reacts with itself or other molecules very quickly and hence, its concentration never gets to a detectable level for an ESR analysis.<sup>102, 103</sup> An indirect approach is usually employed where a substance is added to the reaction system to trap highly reactive and short lived radicals. This is commonly known as spin trapping.<sup>104-107</sup>

Spin trap molecules react with short lived free-radicals to form relatively stable radical adducts which are stable enough to be detected and analysed by an ESR spectrometer. Common spin traps are nitrene and nitroso compounds



solution demonstrated the presence of oxidation products. It seems that the concentration of oxidised derivatives was low and could not be detected by NMR.

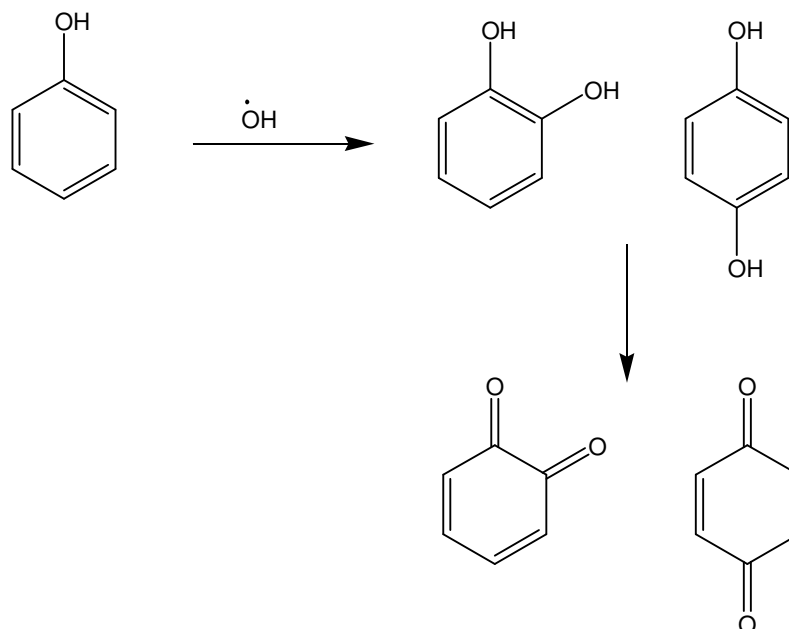


Figure 2-3: Hydroxylation of phenol with hydroxyl radical.

Another example of an aromatic probe is salicylic acid (Figure 2-4). Its hydroxylation gives three derivatives, 1,2-dihydroxybenzene (catechol), 2,5-dihydroxybenzoic acid (2,5-DHBA) and 2,3-dihydroxybenzoic acid (2,3-DHBA). These three derivatives can be separated and quantified using HPLC, GC or capillary electrophoresis techniques.<sup>110</sup> Though salicylic acid has been utilised extensively in biological systems, it suffers from some problems. Formation of three derivatives makes quantitative analysis difficult.

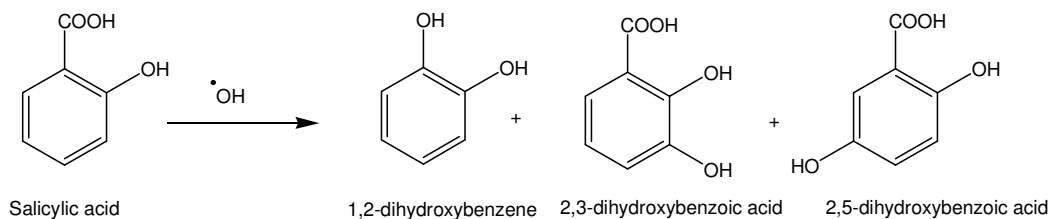


Figure 2-4: Hydroxylation of salicylic acid in monitoring hydroxyl radical formation.

Terephthalic acid (TPA) has also been utilised in various biological and Fenton-like systems (Figure 2-5). The hydroxylated terephthalic acid (H-TPA) is

fluorescent and hence can be monitored using fluorescence spectrophotometry.<sup>111-114</sup> The hydroxylation gives a single derivative which makes quantitative analysis easy. Although fluorescence spectroscopy is a sensitive technique, it also suffers from some drawbacks where fluorescence quenching may influence quantitative analysis and reproducibility.

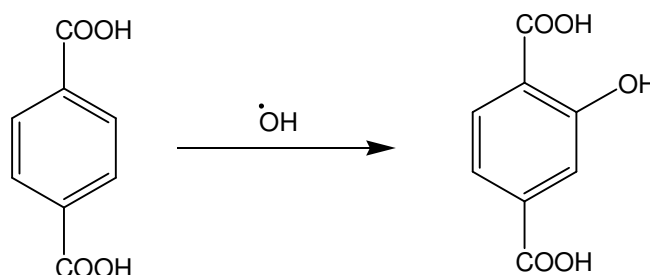


Figure 2-5: Hydroxylation of terephthalic acid.

Beside above mentioned probes and techniques, various other probes have been utilised to quantify hydroxyl radical formation. Reviews have summarised various analytical methods to quantify hydroxyl radical formation in chemical and biochemical processes.<sup>72, 115</sup> For example, oxidation of dimethylsulfoxide (DMSO) to give methanesulfinic acid can be monitored using UV-visible spectrophotometer<sup>116, 117</sup> and a chemiluminescence technique that uses luminol (3-aminophthalhydrazide) probe reports on a series of oxygen containing radical species.<sup>118-120</sup>

### 2.2.3 Colorimetric probe

Early experiments to quantify hydroxyl radical formation employing phenol and terephthalic acid probes using proton NMR could not detect hydroxylated derivatives. This was probably due to low concentration levels of the hydroxylated derivatives formed in the reaction solution. Under these circumstances, a sensitive analytical technique was required to quantify micro or even nano-molar concentration levels of the hydroxylated probe. Colorimetric analysis is a sensitive technique and easy to generate quantitative data. Its high sensitivity and simplicity in monitoring the chemical reaction can be exploited to quantify hydroxyl radical formation in a Fenton-like reaction using a suitable water soluble probe. R. C. Hider synthesised a colorimetric probe, *N,N'*-(5-nitro-1,3-phenylene)bisglutaramide (NPGA) to monitor hydroxyl radical formation which yields a coloured derivative on oxidation (Figure 2-6).<sup>121</sup>

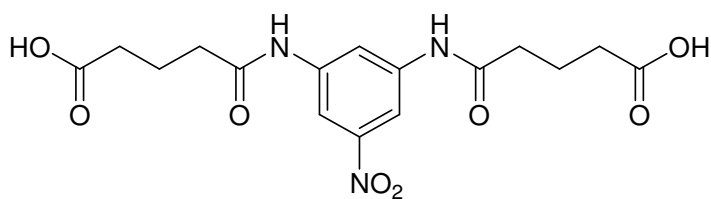


Figure 2-6: Chemical structure of N,N'-(5-nitro-1,3-phenylene)bisglutaramide (NPGA) molecule.

N,

The probe molecule contains an aromatic centre with side chain substituents. In a Fenton reaction, NPGA undergoes hydroxylation at its *ortho* or *para* position to give hydroxy NPGA (H-NPGA). The hydroxylated derivative is a nitrophenol which dissociates to a nitrophenolate ion under the alkaline conditions. The probe absorbs in the UV region with  $\lambda_{\max}$  292 nm while its hydroxylation causes a red shift and the nitrophenolate absorbs at 400 – 450 nm in the visible region.

In the NPGA molecule, the position of the side chain substituents and nitro group directs the attack of hydroxyl group at specific positions. Tri-substitutions at 1, 3 and 5 positions help to avoid multiple hydroxy derivatives and subsequent oxidation step observed for other phenolic probes. Position of the nitro group offers resonance stability to the phenolate anion which results in an increased spectral sensitivity and extinction coefficient (Figure 2-7).

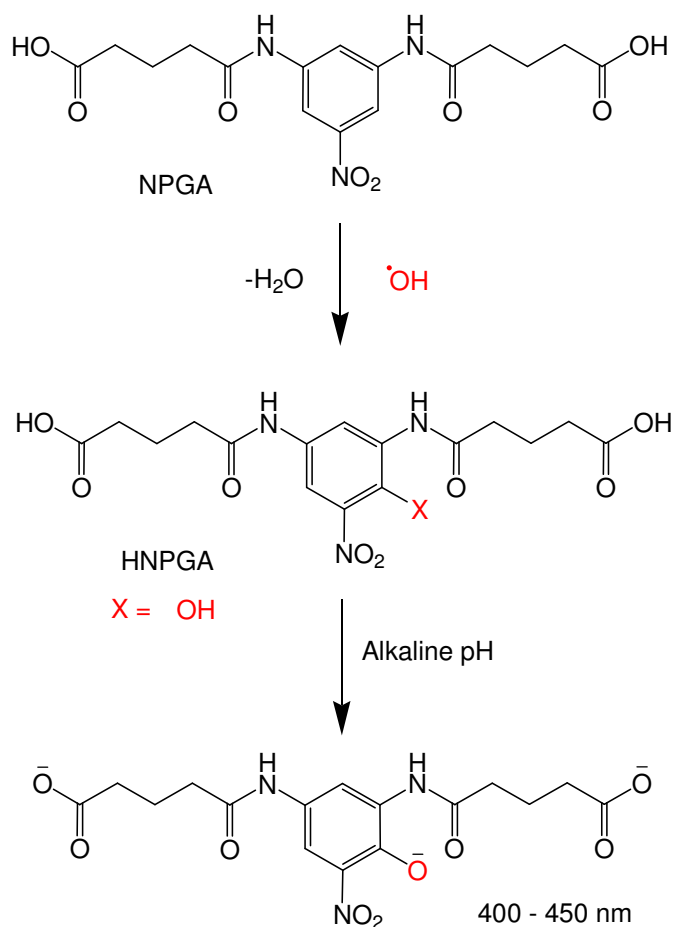


Figure 2-7: Hydroxyl radical analysis using NPGA colorimetric probe.

### 2.2.3.1 Synthesis of NPGA probe

The NPGA probe was synthesised following the literature procedure (Figure 2-8).<sup>121</sup> The synthesis involves two steps. In the first step, one of the nitro groups in 3,5-dinitroaniline was reduced to 3,5-diaminonitrobenzene using the Zinin reduction method. Zinin reduction employs sulfide, disulfide or polysulfide to reduce nitroarenes to aromatic amines. The reaction was first reported by Zinin in 1842 and has been utilised for the synthesis of aromatic amines.<sup>122</sup> The exact mechanism of Zinin reduction is not known, however, it is believed to form nitroso species which is further reduced to hydroxylamine and amine. An advantage of Zinin reduction is the selective reduction of a single nitro group in a dinitro or trinitro system as was the case here in the synthesis of 3,5-diaminonitrobenzene. Due to mild reduction conditions, functional groups other than nitro groups are less likely to undergo reduction reaction.

In the second step, glutaric anhydride was used to add hydrophilic substituents. R. C. Hider initially synthesised the acetylated version, however this was found to be water insoluble and hence was not suitable for practical applications. The choice of glutaric acid was to make sure that the final NPGA probe is water soluble in a typical Fenton-like reaction.

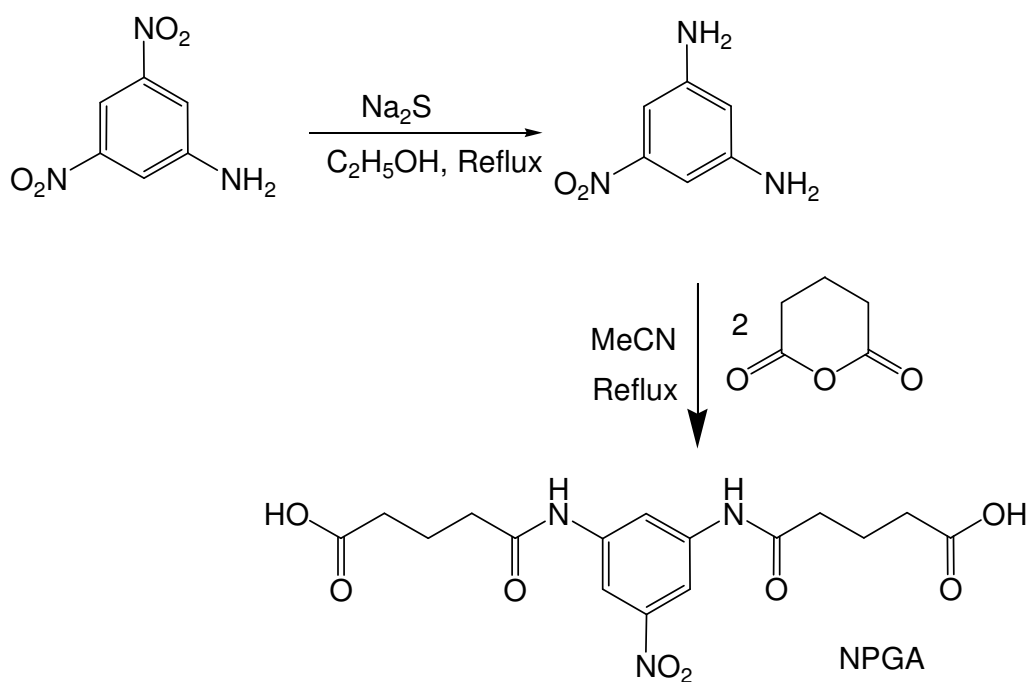


Figure 2-8: Synthesis of NPGA probe.<sup>121</sup>

### 2.2.3.2 Electronic spectra of NPGA probe under alkaline pH conditions

As the current study mainly deals with the alkaline conditions, it is important for the chosen probe to be stable under the alkaline reaction conditions. To examine stability of the NPGA probe, its electronic spectra were recorded at various pH levels using different buffer compositions. The results (Figure 2-9) show that NPGA probe did not show any change in its electronic spectra and was stable under alkaline conditions.

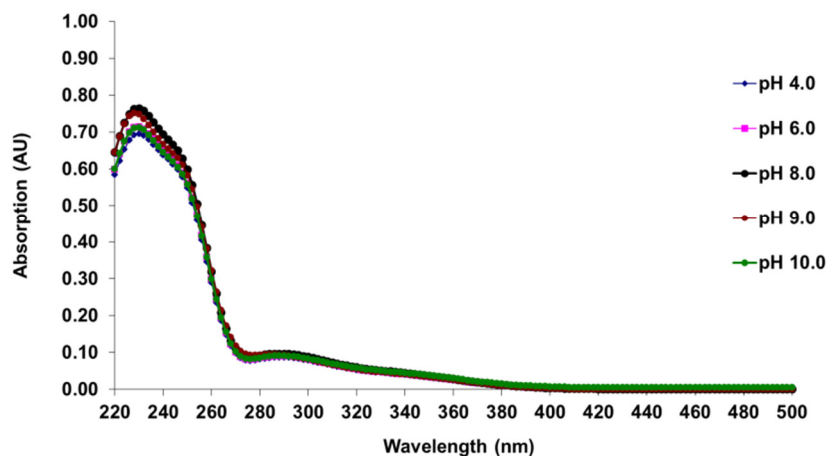


Figure 2-9: Electronic spectra of NPGA probe at various pH levels. NPGA (0.02 mM) was dissolved in various buffer systems. pH 4.0 and 6.0 were 20 mM phosphate buffer solutions while pH 8.0, 9.0 & 10.0 were 20 mM ammonia/ammonium chloride buffer systems. Spectra were recorded against buffer blank.

### 2.2.3.3 Hydroxylation of NPGA probe in a Fenton-like reaction

To examine the hydroxylation of NPGA probe in a Fenton-like reaction, the NPGA probe was added to a copper(II) sulfate catalysed decomposition of hydrogen peroxide. The reaction was carried out at pH 10 using 20 mM ammonia/ammonium chloride buffer in a chelant free system. The electronic spectra were recorded immediately after adding hydrogen peroxide using a UV-visible spectrophotometer. The blank solution had the same composition except for hydrogen peroxide. The results (Figure 2-10) showed an absorption band forming immediately on mixing with hydrogen peroxide in 400-450 nm region. The absorption level increased with the reaction time.

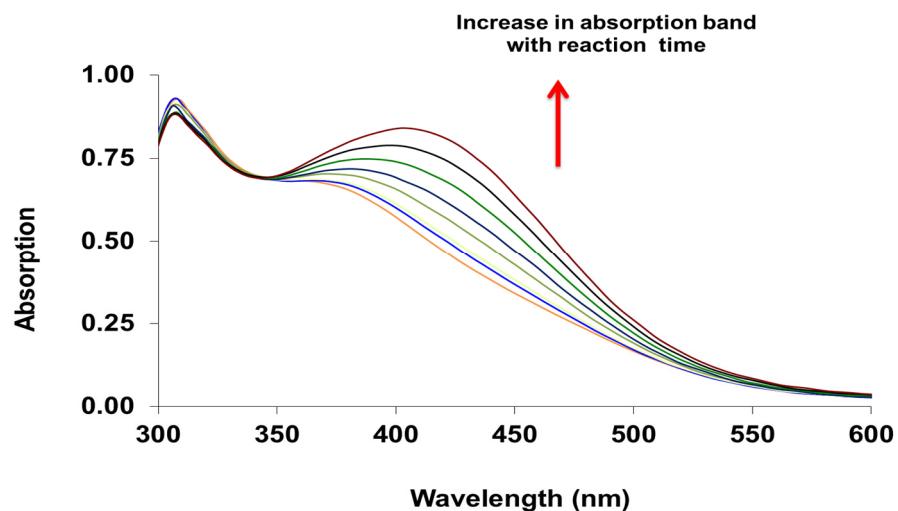


Figure 2-10: Hydroxylation of NPGA probe in a Fenton-like reaction. Reaction solution contained copper(II) sulfate (0.4 mM), NPGA probe (1.0 mM) in a chelant-free system at pH 10.0 using ammonia/ammonium chloride buffer (20 mM). Hydrogen peroxide (0.98 M) was added and spectra were recorded over time against reagent blank.

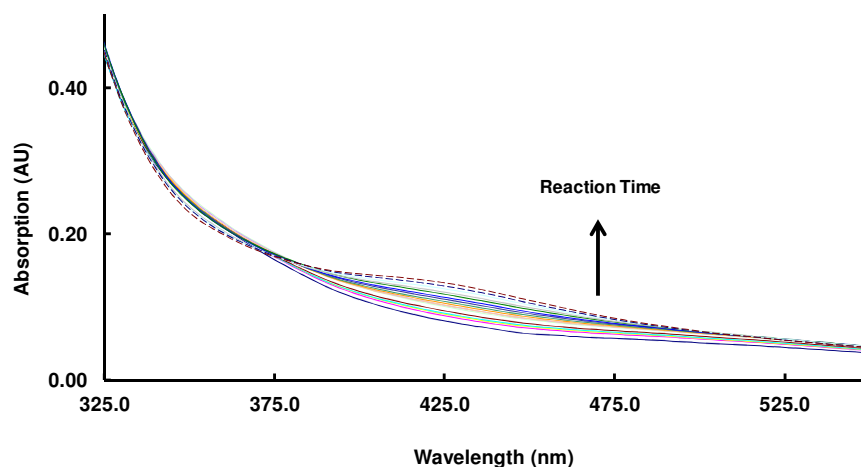


Figure 2-11: Hydroxylation of NPGA probe in iron(III) chloride-EDTA system. Reaction solution contained iron(III) chloride (0.18 mM), EDTA (1.3 mM), NPGA probe (1.0 mM) at pH 10.0 using ammonia/ammonium chloride buffer (20 mM). Hydrogen peroxide (0.98 M) was added and spectra were recorded over a period of 120 minutes against reagent blank.

The presence of an organic substrate in a Fenton-like reaction system may interfere with the probe and complicate monitoring hydroxyl radical. To examine

NPGA probe in a metal-chelant system, another experiment was carried out with added EDTA chelant. Iron(III) chloride was mixed with EDTA chelant and hydrogen peroxide in a buffer solution (pH 10). UV-visible spectra of the reaction solution were recorded immediately against reagent blank. The electronic spectrum showed absorption band for the hydroxylated NPGA derivatives (Figure 2-11).

These experiments demonstrate the performance of NPGA in capturing hydroxyl radical and monitoring its formation in a Fenton-like reaction. The presence of chelants does not interfere with the absorption bands.

#### **2.2.3.4 LC-MS separation of H-NPGA/NPGA**

Hydroxyl radicals can oxidise and degrade almost any chemical compound. NPGA and its hydroxylated derivatives (H-NPGA) are also prone to such degradation. Hence, it is important to study their stability in a strongly oxidising alkaline media. For this reason, hydroxylation of the NPGA probe in a Fenton-like reaction and formation of its hydroxylated H-NPGA derivative were analysed using reverse phase liquid chromatography coupled with mass spectrometer (LC-MS). A separation method and experimental conditions were developed and optimised using reverse phase HPLC. A sample analysed after 90 minutes of the hydroxylation reaction showed two well resolved peaks in the chromatogram (Figure 2-12). The H-NPGA molecule eluted first at 17<sup>th</sup> minute while the other peak at 49<sup>th</sup> minute was the unreacted NPGA probe. The assignment of peaks was confirmed by MS-ESI spectrometry (Figure 10-1 & Figure 10-2). On hydroxylation, the NPGA probe would form two hydroxylated derivatives (*ortho* & *para* substituted). However, LC-MS experiments could not resolve these two derivatives. R. C. Hider approximated the ratio of *ortho* to *para* isomers as 6:1.<sup>121</sup> Further optimisation of experimental conditions is required to improve hydroxylation yield and separation of two isomers. The same reaction solution was analysed again after overnight mixing which also showed two peaks (Figure 2-13).

These experiments offer evidence for NPGA hydroxylation and formation of the hydroxylated derivatives in-situ in a metal catalysed decomposition of alkaline

hydrogen peroxide. They also demonstrate the stability of NPGA probe under the experimental conditions.

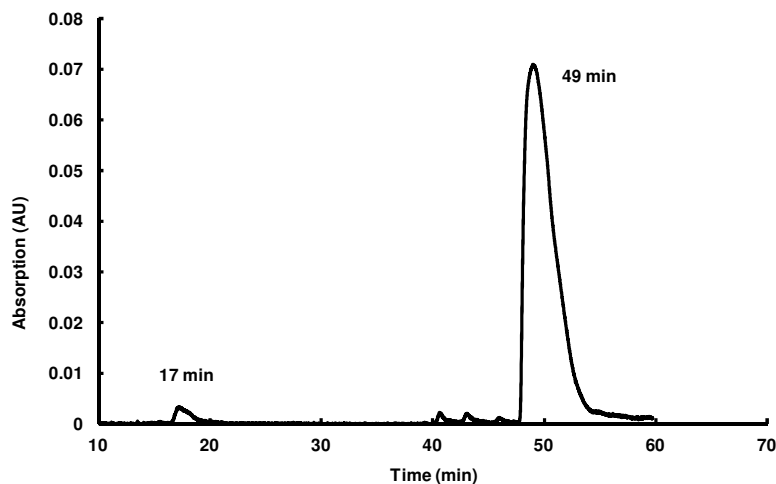


Figure 2-12: Analysing NPGA hydroxylation in a copper(II) catalysed Fenton-like reaction using HPLC after 90 minutes mixing of the reaction. Reaction solution contained 1 mM NPGA probe mixed with 0.18 mM copper (II) sulfate in 20 mM ammonia/ammonium chloride buffer with 0.98 M hydrogen peroxide.

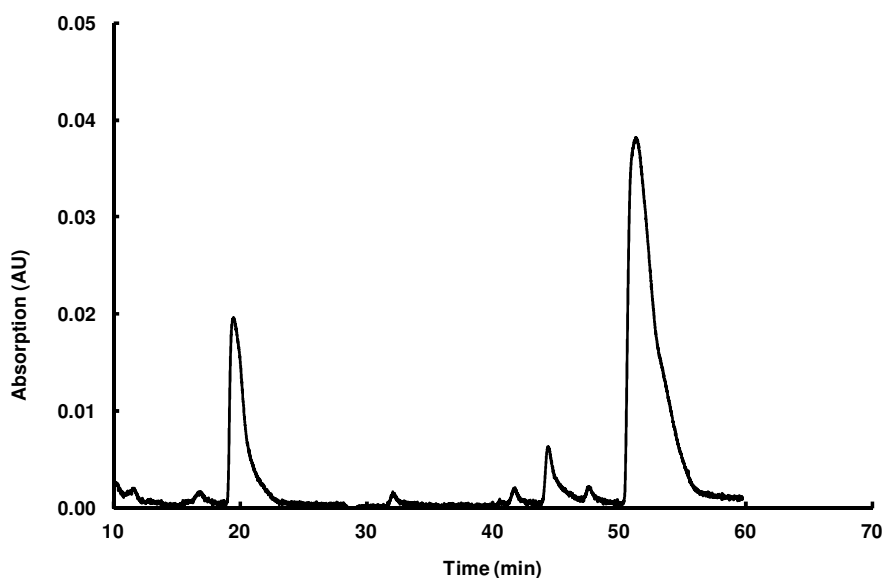


Figure 2-13: Analysing NPGA hydroxylation in a copper(II) catalysed Fenton-like reaction using HPLC after 24 hours of the reaction. Reaction solution contained 1 mM NPGA probe mixed with 0.18 mM copper(II) sulfate in 20 mM ammonia/ammonium chloride buffer with 0.98 M hydrogen peroxide.

Further isolation of H-NPGA derivatives was carried out using preparative TLC ( $R_f$ : 0.35, solvent: dichloromethane and methanol (4:1)). However, the isolated material was insufficient to carry out further characterisation.

### 2.2.3.5 $pK_a$ of H-NPGA

Hydroxylated derivative, H-NPGA, is a nitrophenol which undergoes dissociation to a nitro-phenolate ion under alkaline conditions. This anion is responsible for the absorption in the visible region. As the current study deals with the alkaline pH, a  $pK_a$  value for the hydroxylated derivative should be determined. H-NPGA is required to be completely dissociated under alkaline conditions. To determine the  $pK_a$  values, isolated H-NPGA was titrated against standard sodium hydroxide solution. The volume of the titrant was plotted against the pH and a titration curve was produced (Figure 2-14). The curve was fitted using CurTiPot software.<sup>123</sup> Three  $pK_a$  values obtained were 5.21, 5.69 and 6.19 which were in good agreement with the estimated figures. The results suggest that under the alkaline hair colouring conditions (pH 8-10), the H-NPGA would be fully deprotonated to give phenolate ion which is required for its spectrophotometric analysis.

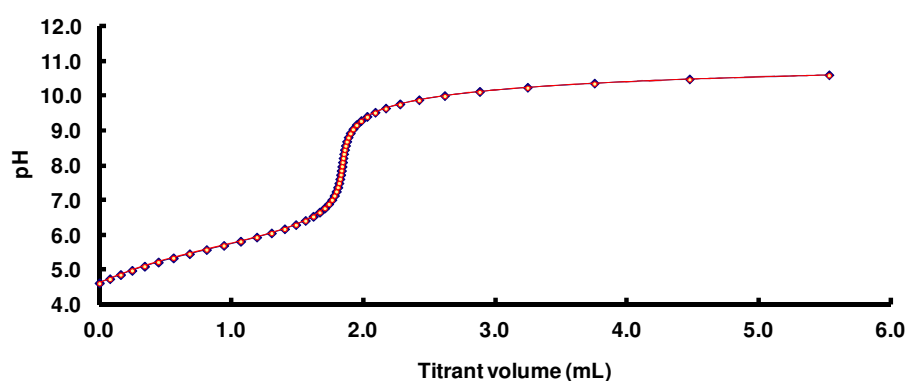


Figure 2-14: Titration curve for the determination of  $pK_a$  of H-NPGA.

## 2.2.4 Conclusion

NPGA colorimetric probe was used to monitor hydroxyl radical formation in a Fenton-like reaction. Its hydroxylated derivatives (H-NPGA) were analysed by

LC-MS. Both NPGA and H-NPGA were stable at alkaline pH and in the oxidizing conditions. UV-visible spectrophotometric analysis suggests that the absorbance of H-NPGA at 430 nm could be used to monitor hydroxyl radical formation.

It is important to mention that an absolute quantification of hydroxyl radicals is very difficult. Various methods and probes reported in the literature provide only a relative quantification of radical species in a given model system. NPGA probe does not react with the hydroxyl radicals stoichiometrically. The hydroxyl radicals may also react with other species present in the reaction mixture. Therefore, NPGA hydroxylation under the Fenton reaction conditions would only provide a relative concentration of hydroxyl radical.

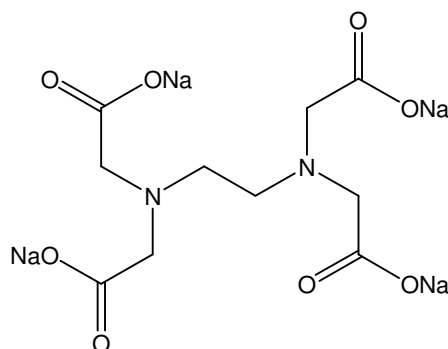
Despite the concerns about the selectivity of hydroxyl radical and qualitative nature of the hydroxylation reaction, the NPGA colorimetric probe can provide a valuable comparison of the hydroxyl radical formation in different chemical models. The important feature of using NPGA is the high sensitivity of UV-visible spectroscopy and its simplicity for monitoring the chemical reaction. Previous studies have employed NPGA probe to monitor hydroxyl radicals in biological systems and cellulose bleaching in textile systems.<sup>121, 124, 125</sup> With these reasons in mind, the NPGA probe was chosen for the current study to monitor hydroxyl radical formation in different metal-ligand catalysed Fenton-like reaction & hair colouring systems.

## **Chapter 3: Decomposition of alkaline hydrogen peroxide catalysed by metal-chelant complexes**

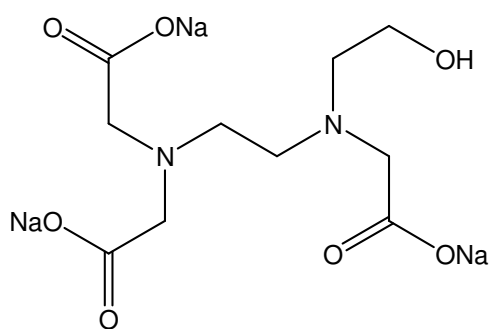
---

### 3 Decomposition of alkaline hydrogen peroxide catalysed by metal-chelant complexes

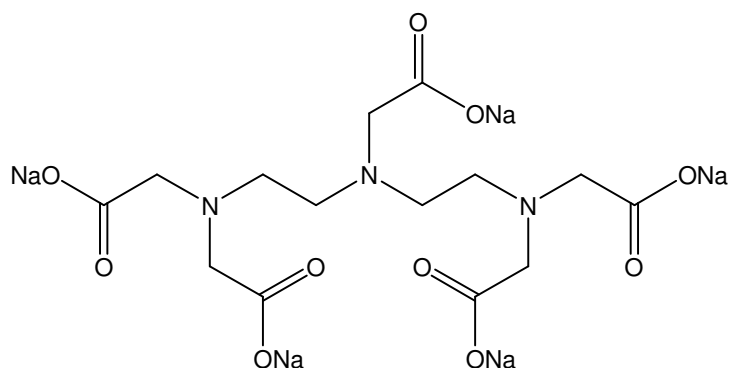
Chelants are often used to bind metal ions with the objective to stabilise hydrogen peroxide. Over the years, various chelants have been studied to control the catalytic activity of iron and copper ions in the decomposition of hydrogen peroxide. Two main classes of chelants commonly employed are polyaminocarboxylates e.g. ethylenediaminetetraacetic acid (EDTA) and phosphonates, e.g. diethylenetriamine penta(methylene phosphonic acid) (DTPMP). The main criteria for choosing a particular chelant in hair colouring formulation are based on the regulatory concerns, commercial availability, binding strength with the metal and stability of the metal-chelant complex under the reaction conditions. This chapter describes the catalytic activity of copper(II) and iron(III) mixed with various chelants in the alkaline medium using ammonia/ammonium chloride buffer system. Metal-chelant speciation plots were developed using Medusa software.<sup>126</sup> The following chelants were used in the current study



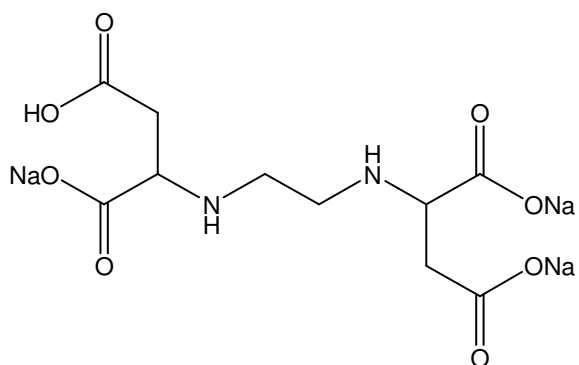
Ethylenediaminetetraacetic acid tetrasodium salt (EDTA. 4Na)



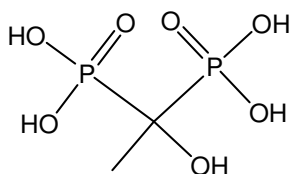
*N*-(Hydroxyethyl)-ethylenediaminetriacetic acid trisodium salt (HEDTA. 3Na)



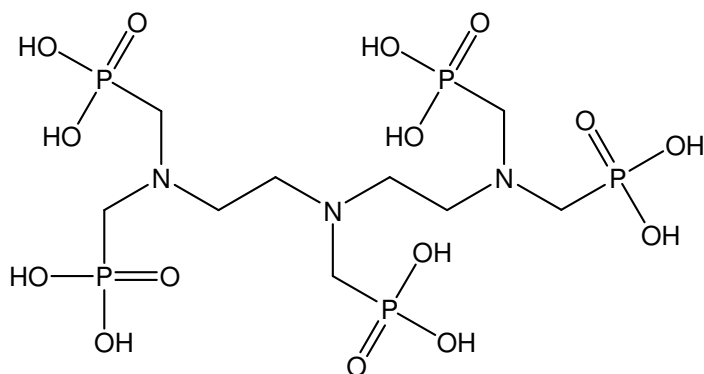
Pentasodium diethylenetriaminepentaacetate (DTPA. 5Na)



Ethylenediamine-*N,N'*-disuccinic acid trisodium salt (EDDS. 3Na)



1-Hydroxyethylidene 1,1-diphosphonic acid (HEDP)



Diethylenetriamine penta(methylene phosphonic acid) (DTPMP)

Figure 3-1: Chemical structure of some common polyaminocarboxylate and phosphonate ligands.

### 3.1 Objective

The aim of this chapter is to describe the catalytic activity of iron(III) and copper(II) metal ions in a Fenton-like reaction under the alkaline conditions. Various chelants are added to the metal systems to explore the activity of these metal-chelant complexes in the decomposition of alkaline hydrogen peroxide. The chapter discusses the influence of the chelant on the metal speciation in the reaction solution and rate of decomposition of alkaline hydrogen peroxide. We also describe screening of various chelants for their performance in suppressing hydrogen peroxide decomposition and hydroxyl radical formation.

### 3.2 Metal-ligand complexes

Copper and iron both belong to *d*-block metals in the periodic table with  $[Ar]3d^{10}4s^1$  and  $[Ar]3d^64s^2$  electronic configuration, respectively. They exhibit a range of oxidation states. Copper mostly occurs as  $Cu^{2+}$  though  $Cu^+$  and  $Cu^{3+}$  also exist. Iron has two common oxidation states,  $Fe^{2+}$  and  $Fe^{3+}$  while compounds with further higher oxidation states are also present. A characteristic feature of transition metal ions is the formation metal-ligand complexes e.g.  $[Cu(H_2O)_6]^{2+}$  and  $[Fe(H_2O)_6]^{3+}$ . A complex is a combination of a Lewis acid (central metal atom) and Lewis bases (the ligand). The central metal atom ( $Cu^{2+}$  and  $Fe^{3+}$  in the above examples) and electron rich ligand ( $H_2O$ ) are bonded via a coordinative bond. The ligand can be a monoatomic species (monodentate e.g.  $F^-$ ) or as large as a

polymer (multi-dentate). The ligands attached directly to the metal atom define the primary coordination sphere and the numbers of ligands attached give the coordination number of the complex. A ligand employing multiple donors to attach to the central metal ion is called a chelant. A good example is EDTA chelant complex with  $\text{Fe}^{3+}$  or  $\text{Cu}^{2+}$  metal ions (Figure 3-2).

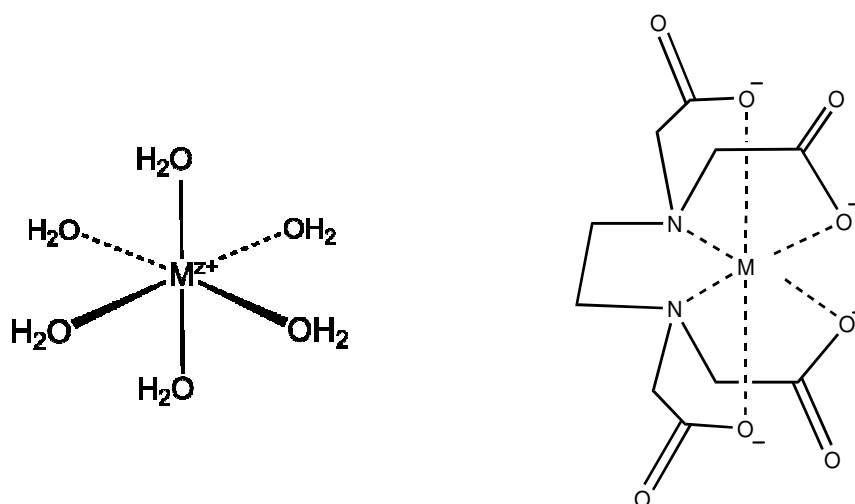


Figure 3-2: A simple representation of octahedral metal aqua complex and metal EDTA complex.

### 3.2.1 Crystal field theory

The bonding between a central metal ion and a ligand can be explained by crystal field theory where ligand lone pair is described as a point negative charge. The ligand lone electrons repel  $d$ -electrons of the metal and this repulsion results in the splitting of the  $d$  orbitals. The splitting pattern accounts for the electrons of the metal and explains the stability and spectroscopic and magnetic properties of complex.<sup>127-130</sup>

An octahedral  $[\text{Fe}(\text{H}_2\text{O})_6]^{3+}$  is a  $d^5$  complex. The  $d_{z^2}$  and  $d_{x^2-y^2}$  orbitals ( $e_g$ ) have electrons pointing along the axes and hence they are repelled more strongly by negative charges of the ligands than the electrons in the other three  $d$ -orbitals,  $d_{xy}$ ,  $d_{yx}$  and  $d_{zy}$  ( $t_{2g}$ ) which point between the ligands. This results in a splitting where triply degenerating orbitals  $t_{2g}$  lie lower than the doubly degenerating  $e_g$  orbitals (Figure 3-3). This splitting is called crystal field splitting parameter ( $\Delta_{\text{oct}}$ ).

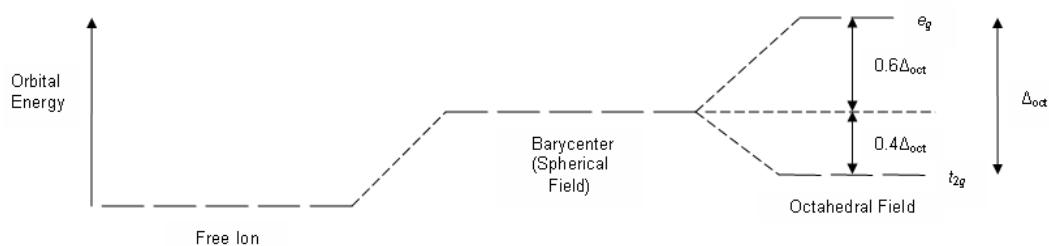
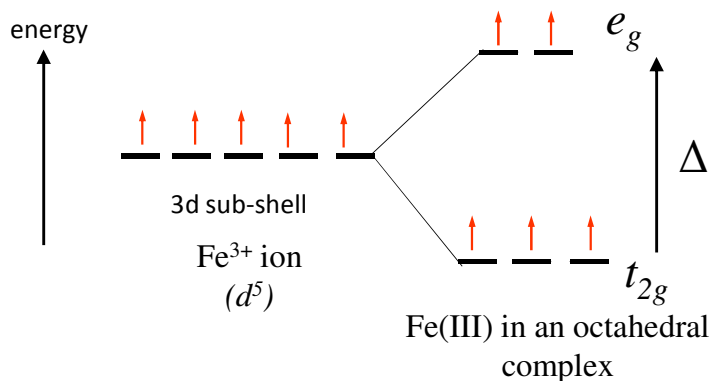


Figure 3-3: Energy diagram of the  $d$  orbitals in an octahedral crystal field.

In the above octahedral model, because there are three  $t_{2g}$  and two  $e_g$ , the  $t_{2g}$  orbitals lie  $2/5\Delta_o$  lower than the average energy level while  $e_g$  orbitals lie  $3/5\Delta_o$  above the average energy. The occupation of the lower energy  $t_{2g}$  level by electrons causes a stabilization of the complex, whereas occupation of the  $e_g$  level causes a rise in energy. The net energy of  $t_{2g}$   $e_g$  is called crystal field stabilisation energy (CFSE) which can be written as

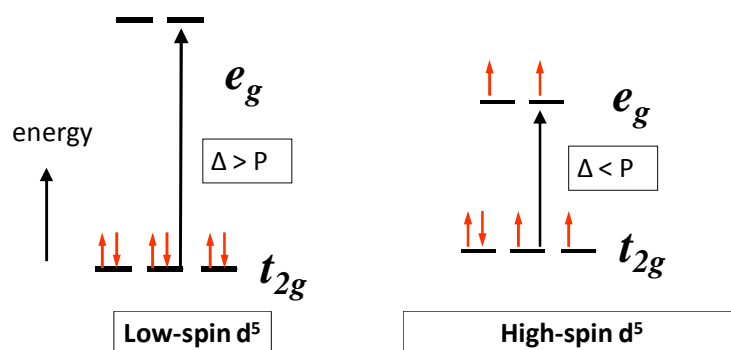
$$\text{CFSE} = (-2/5x + 3/5y) \Delta_o$$

For  $\text{Fe}^{3+}$  with  $d^5$  system, the electronic configuration and energy diagram can be presented as



The pattern of electron filling may depend upon the ligands attached and require considering strong coulombic repulsion known as *pairing energy*. A  $\Delta_o$  more than pairing energy will give strong field case with a low spin configuration where more electron reside in the lower  $t_{2g}$  state with paired electron spin which eventually imparts a diamagnetic behaviour. On other hand, when pairing energy is more than  $\Delta_o$ , a weak field complex with more unpaired electrons is preferred known as high spin complex presenting paramagnetic behaviour. In the above

example of  $[\text{Fe}(\text{H}_2\text{O})_6]^{3+}$ , water ligand leads to a high spin complex while the same  $d^5$  system of  $\text{Fe}^{3+}$  with  $\text{CN}^-$  ligand gives a low spin complex due to a different  $\Delta_o$ . The electronic configuration for a typical high and low spin systems are shown here



Complex  $[\text{Cu}(\text{H}_2\text{O})_6]^{2+}$  of  $d^9$  system, does not show regular octahedral geometry. This is explained by *Jahn-Teller (J-T) effect* which describes that when orbitals in the same level are occupied by different numbers of electrons, this will lead to distortion of the molecular structure. In other words, if the ground state electronic configuration is degenerate, the molecule will distort to remove degeneracy.  $\text{Cu}(\text{II})$  with its  $d^9$  configuration is degenerate and has J-T distortion. In an octahedral system, this distortion may involve elongation of two axial bonds or the compression of the four bonds that lie in the line of a plane. An alternative can be compression along the axis and elongation in the plane. The  $d$ -orbitals aligned with the two more distant donor atoms along the  $z$ -axis experience less repulsion and so drop in energy ( $d_{xz}$ ,  $d_{yz}$ , and  $d_{z^2}$ ), while those closer to the in-plane donor atoms ( $d_{xy}$ ,  $d_{x^2-y^2}$ ) rise in energy. This explains additional stability of  $\text{Cu}^{2+}$  complexes and its distorted geometry.

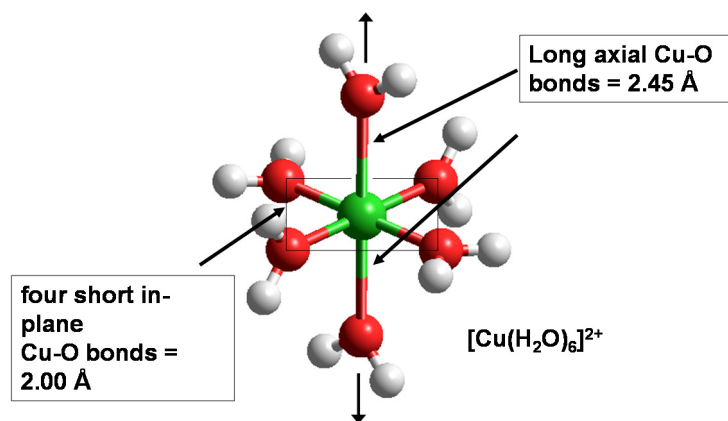
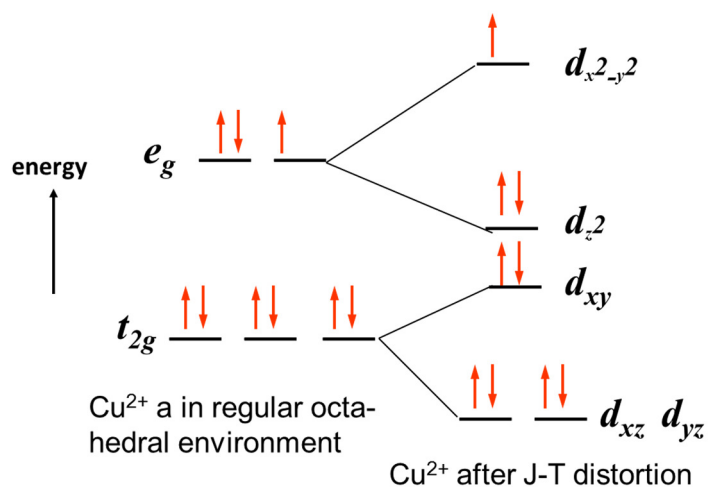


Figure 3-4: Jahn-teller distortion in  $d^9$  system of Cu<sup>2+</sup> complex.

### 3.2.2 Consequences of metal-ligand binding

Metal-ligand interaction may bring significant consequences for the new complex. This may bring structural changes and alter physical & chemical properties of the individual components. Changing the central metal ion or the ligand may lead to easily observable features such as colour of the complex solution. It can also greatly influence the fate and catalytic activity of transition metal ions in decomposing hydrogen peroxide via a Fenton-like reaction. Various multi-dentate ligands called chelants have been studied in a Fenton-like reaction. One common example of such molecules is EDTA.

### 3.2.3 Stability of metal-ligand complex

The stability of metal-ligand complex can be assessed by the equilibrium constant. A simple chemical reaction for a metal-aqua complex can be seen in equation below.

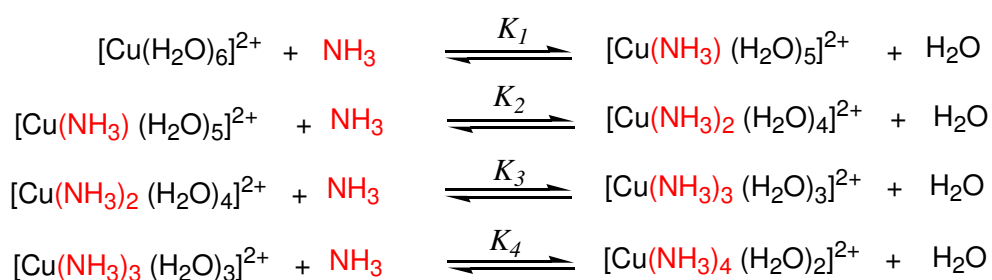


$$K = \frac{[\text{M}(\text{OH}_2)_{(x-1)}\text{L}^{n+}][\text{H}_2\text{O}]}{[\text{M}(\text{OH}_2)_x^{n+}][\text{L}]}$$

As water is in large excess, this equation can be simplified to

$$K = \frac{[\text{ML}^{n+}]}{[\text{M}^{n+}][\text{L}]}$$

A common example is addition of ammonia to a hexaaquacopper(II) complex which immediately gives a blue coloured solution. Here, ammonia is replacing four molecules which can be called a ligand-exchange process. The reaction proceeds step by step and can be written as

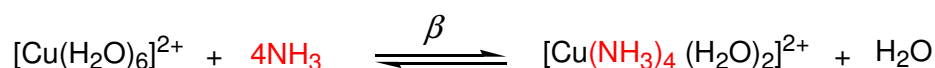


The stability constant values for each are found in the literature.<sup>132</sup>

<b>Complex Ion</b>	<b>K (mol<sup>-1</sup> dm<sup>3</sup>)</b>	<b>Log K</b>
[Cu(NH <sub>3</sub> )(H <sub>2</sub> O) <sub>5</sub> ] <sup>2+</sup>	K <sub>1</sub> = 1.78 x 10 <sup>4</sup>	4.25
[Cu(NH <sub>3</sub> ) <sub>2</sub> (H <sub>2</sub> O) <sub>4</sub> ] <sup>2+</sup>	K <sub>2</sub> = 4.07 x 10 <sup>3</sup>	3.61
[Cu(NH <sub>3</sub> ) <sub>3</sub> (H <sub>2</sub> O) <sub>3</sub> ] <sup>2+</sup>	K <sub>3</sub> = 9.55 x 10 <sup>2</sup>	2.98
[Cu(NH <sub>3</sub> ) <sub>4</sub> (H <sub>2</sub> O) <sub>2</sub> ] <sup>2+</sup>	K <sub>4</sub> = 1.74 x 10 <sup>2</sup>	2.24

Table 3-1: Stability constants for each individual copper-ammonia complex.

Overall reaction scheme and equilibrium constant can be written as



$$\beta = \frac{[\text{Cu}(\text{NH}_3)_4(\text{H}_2\text{O})_2]^{2+}}{[\text{Cu}(\text{H}_2\text{O})_6]^{2+} [\text{NH}_3]^4}$$

$$\beta = K_1 \times K_2 \times K_3 \times K_4$$

$$\log \beta = \log K_1 + \log K_2 + \log K_3 + \log K_4$$

Here  $\beta$  is called the stepwise stability constant and its value for the copper-ammonia reaction is 13.1 suggesting a greater tendency for ammonia to replace water molecules forming a relatively more stable copper-ammonia complex.

Various factors influence metal-ligand stability. They include size and charge density (size to charge ratio) of the central metal ion, size of the ligand and geometry of the complex. Polydentate ligands make a more stable complex compared to corresponding monodentate ligands (chelate effect). These factors will come into discussion in the current study to explain the formation of various copper and iron complexes and their activity in decomposing hydrogen peroxide.

### 3.2.4 HSAB concept

Metal ion interaction with a ligand (Lewis acid – Lewis base interaction) can be split into two classes of metals i.e. *class a* and *class b*. This was first defined by analysing stability constants of a metal for halides.

Class *a* binds  $I^- < Br^- < Cl^- < F^-$  and      Class *b* binds  $F^- < Cl^- < Br^- < I^-$

The stability values decrease for  $Al^{3+}$  from  $F^-$  to  $I^-$  and increase for  $Hg^{2+}$  which was used to assign  $Al^{3+}$  to class *a* while  $Hg^{2+}$  lies in class *b*. The relationship was further generalised by Pearson by classifying Lewis acids and ligands (Lewis bases) as 'hard' or 'soft'. The theory of hard and soft acids and bases (HSAB) is used to rationalize observed patterns in complex stability. Class *a* members are called "hard" while class *b* members are known as "soft" acids or bases.<sup>127, 128</sup>

The concept describes the polarisabilities of the metal ions. Hard acids are generally small monocations with high charge density and low polarizability. These metal ions show preference for similar low polarisable donor species which are called hard bases. Opposite to this, soft acids are bigger in size with low charge density and high polarizability. They prefer to bind with donors who are also highly polarisable, e.g., soft bases. These correlations suggest that hard acids form complexes predominantly by columbic interaction while for soft acids covalent bonding is more important.

Hard Acids $H^+, Li^+, Na^+, K^+,$ $Mg^{2+}, Ca^{2+}, Cr^{2+},$ $Cr^{3+}, Al^{3+}$	Borderline Acids $Fe^{2+}, Co^{2+}, Ni^{2+},$ $Cu^{2+}, Zn^{2+}, Pb^{2+}$	Soft Acids $Cu^+, Ag^+, Au^+, Ti^+,$ $Hg^+, Pd^{2+}, Cd^{2+},$ $Pt^{2+}, Hg^{2+}$
Hard Bases $F^-, OH^-, H_2O, NH_3,$ $CO_3^{2-}, SO_4^{2-}, PO_4^{3-}$	Borderline Bases $NO_2^-, SO_3^{2-}, Br^-,$	Soft Bases $H^-, R^-, CN^-, I^-$

Figure 3-5: List of hard and soft acids and bases according to HSAB concept.

### 3.2.5 Metal speciation

A solution containing metal ions and different ligands may contain various metal-ligand complexes. Their formation may depend upon solution composition, pH of the reaction solution and strength of metal-ligand interactions. The chemical speciation of a metal describes its distribution in the solution. It gives the concentrations of different chemical forms of the metal which together make up the total concentration of metal in the reaction solution. Metal speciation can be determined using various analytical techniques. It can also be modelled using known stability constants of the possible metal-ligand complexes in a model system.

There are two major reference databases for the stability constants of the metal-ligand complex. The first is the IUPAC-published “Critical evaluation of metal complexes in aqueous solutions” and the second database is the “Critical stability constants of metal complexes database, National Institute of Standards & Technology (NIST)”. In the current study, chemical speciation for  $\text{Fe}^{3+}$  and  $\text{Cu}^{2+}$ , in the presence of different chelants was modelled using the NIST database. Procter & Gamble generously provided the database and Medusa software to model the speciation plots.<sup>126</sup>

The speciation of iron(III) and copper(II) in a chelant-free system with 20 mM ammonia shows that metal oxide is the dominant species in the reaction mixture (Figure 3-6 & Figure 3-7). At high pH both copper and iron form insoluble hydroxides which the database calls “oxides”. Throughout the thesis, the term “oxide” is used to imply formation of metal hydroxide under alkaline conditions. The formation of metal oxide creates a heterogeneous system which may influence the decomposition of hydrogen peroxide. Despite high stability of the copper-ammonia complexes, they do not form to an appreciable extent in a 20 mM ammonia buffer.

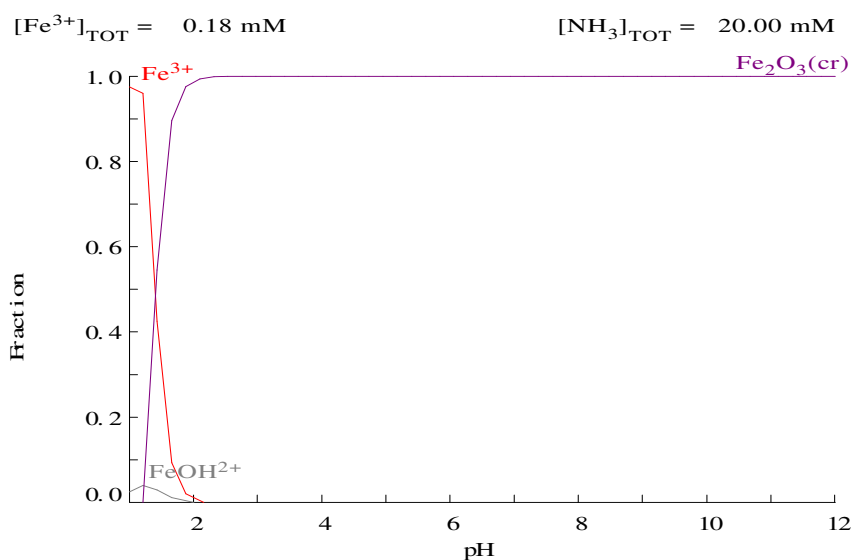


Figure 3-6: Iron(III) speciation in a chelant-free system using 0.18 mM concentration of iron(III) chloride in 20 mM ammonia/ammonium chloride buffer solution.

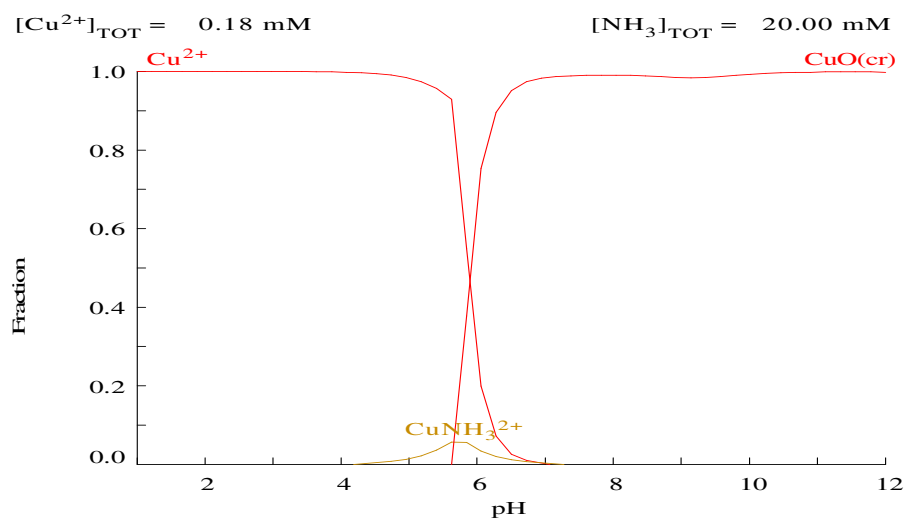


Figure 3-7: Copper(II) speciation in a chelant-free system using 0.18 mM concentration of copper(II) sulfate in 20 mM ammonia/ammonium chloride buffer solution.

Addition of hexadentate EDTA chelant (1.3 mM) changes the metal speciation (Figure 3-8 & Figure 3-9). Iron is complexed with EDTA chelant and Fe-EDTA complex is the dominant species in the solution. At pH 8–9, Fe(EDTA)(OH)<sup>2-</sup> complex is formed while at even higher pH, metal oxide is the main species. These changes in speciation may lead to a variation in activity of

$\text{Fe}^{3+}$ -EDTA system in the alkaline media. The  $\text{Cu}^{2+}$ -EDTA complex is stable over a wide range of pH and no metal oxide is formed under the reaction conditions. These plots demonstrate that different metals differ in their tendency to bind the same chelant.

According to HSAB concept,  $\text{Fe}^{3+}$  ion is harder than  $\text{Cu}^{2+}$  and hydroxyl anion ( $\text{OH}^-$ ) is harder than EDTA chelant. Hence,  $\text{Fe}^{3+}$  ions prefer to bind hydroxyl anion to give iron hydroxide at pH 10. Similarly EDTA chelant and other aminocarboxylates being softer than hydroxyl anion form stronger complexes with  $\text{Cu}^{2+}$  than with  $\text{Fe}^{3+}$ . This explains why copper(II) systems with most ligands stay soluble in the reaction solution at higher pH than Fe(III) which forms iron hydroxide precipitates.

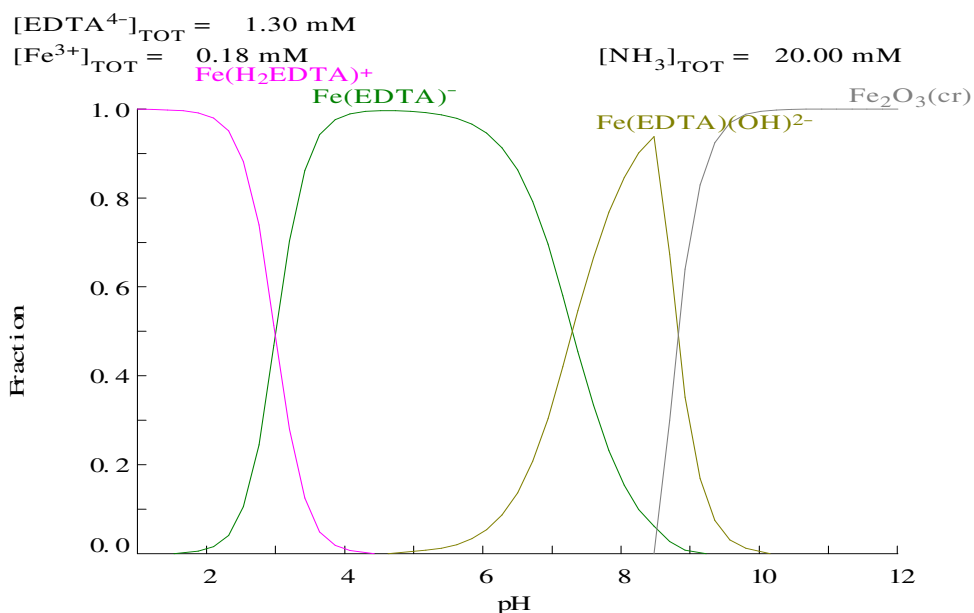


Figure 3-8: Iron(III) speciation in  $\text{Fe}^{3+}$ -EDTA system using 0.18 mM concentration of iron(III) chloride and 1.3 mM tetrasodium EDTA in 20 mM ammonia/ammonium chloride buffer solution.

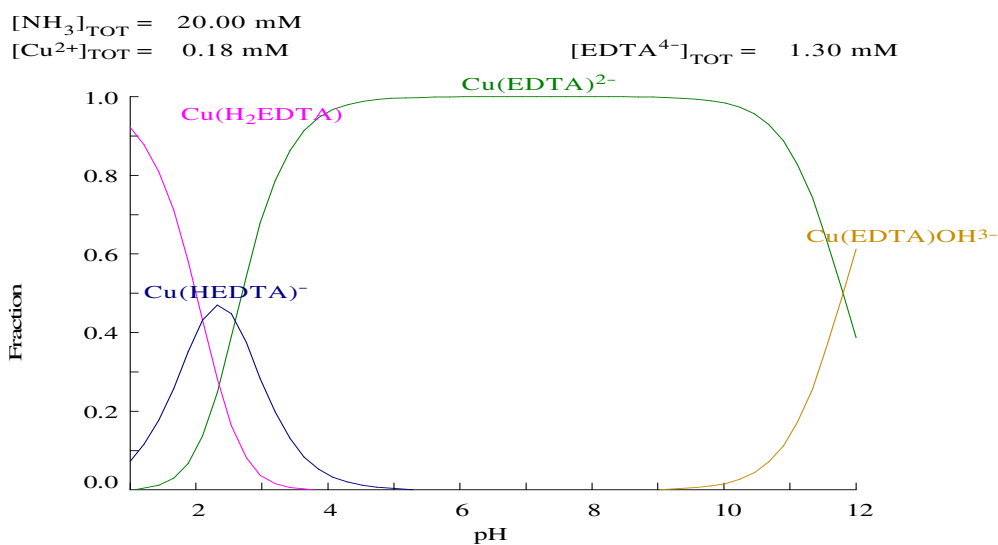


Figure 3-9: Copper(II) speciation in  $\text{Cu}^{2+}$ -EDTA system using 0.18 mM concentration of copper(II) sulfate and 1.3 mM tetrasodium EDTA in 20 mM ammonia/ammonium chloride buffer solution.

The  $\text{Fe}^{3+}$  speciation follows the similar trends with HEDTA, DTPA and EDDS chelants at 1.3 mM concentration level where metal oxide is formed under alkaline conditions (Figure 10-3 to Figure 10-5). As discussed earlier, iron(III) does not bind strongly with aminocarboxylate chelants, it may require significantly higher concentration of the chelant to prevent formation of iron hydroxide. Copper(II) exhibits stronger affinity for aminocarboxylates and its complex with HEDTA is stable at high pH while in  $\text{Cu}^{2+}$ -EDDS system, metal speciation exhibits changes from pH 8.0 to 10.0 (Figure 10-9 & Figure 10-10).

For HEDP and DTPMP phosphonate chelants, speciation plots for  $\text{Fe}^{3+}$  show that metal oxide is the major species present at alkaline pH for both chelants (Figure 10-6 & Figure 10-7). Copper(II) ions with these phosphonate chelants offer a different scenario. In the  $\text{Cu}^{2+}$ -DTPMP system, the metal-ligand complex is stable and is the dominant species under alkaline conditions while for the  $\text{Cu}^{2+}$ -HEDP system, copper(II) speciation changes under the alkaline pH conditions and metal oxide is formed (Figure 10-12 & Figure 10-13).

These speciation plots highlight that  $\text{Fe}^{3+}$  and  $\text{Cu}^{2+}$  have different binding strengths for the same chelant. Most of chelants are unable to chelate  $\text{Fe}^{3+}$  ions at high pH. An important feature of the metal speciation under the alkaline conditions is the formation of metal oxide which changes the nature of the

reaction solution making it heterogeneous. These metal oxide particles have the tendency to aggregate and form bigger particles which may ultimately cause precipitation. This may greatly change the kinetics of a decomposition reaction. Insoluble metal hydroxides may be active in hydrogen peroxide decomposition; however, their activity may depend upon diffusion/mass transfer due to the heterogeneous nature of the system. It is also clear from the speciation plots that changing the pH of the reaction solution changes the metal speciation which may influence the decomposition of hydrogen peroxide.

### **3.3 Catalytic activity of metal-chelant complexes**

A series of experiments were carried out to study the catalytic activity of iron(III) and copper(II) complexes with EDTA, HEDTA, DTPA, EDDS, HEDP and DTPMP ligands in decomposing alkaline hydrogen peroxide. The hydroxyl radical formation was monitored using NPGA colorimetric probe while the gasometric method was employed to determine the overall decomposition of hydrogen peroxide.

### 3.4 Catalytic activity of iron(III) systems

#### 3.4.1 Iron(III) chelant-free system

The first experiment in the current studies was carried out for iron(III) in a chelant-free system.

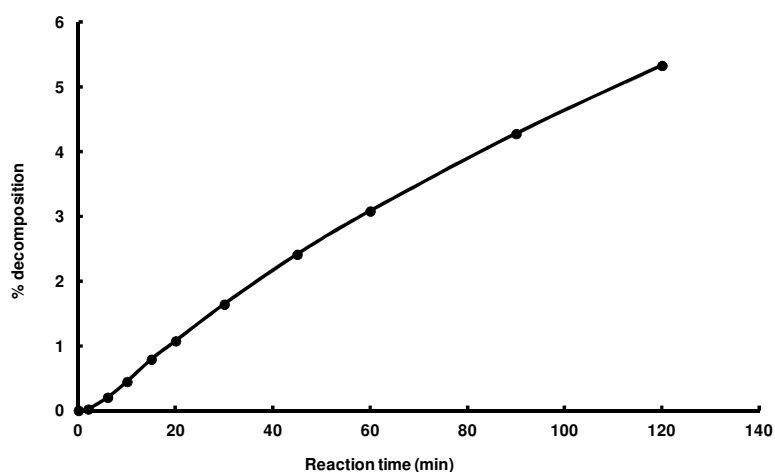


Figure 3-10: Iron(III) catalysed decomposition of alkaline hydrogen peroxide in a chelant-free system at pH 10. The reaction solution contained 0.18 mM iron(III) chloride and 0.98 M hydrogen peroxide at pH 10 using 20 mM ammonia/ammonium chloride buffer.

The result shows a steady increase in the decomposition of hydrogen peroxide (Figure 3-10). The metal speciation shows that iron(III) oxide is the only species under the reaction conditions which is insoluble at high pH.

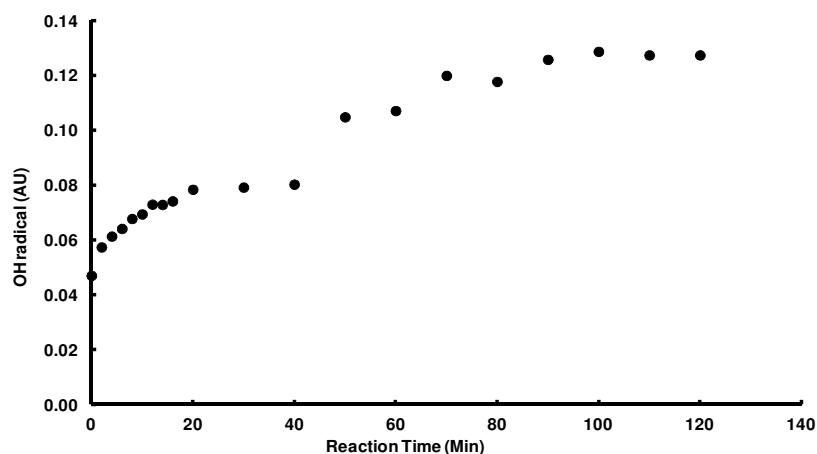


Figure 3-11: Hydroxyl radical formation in Fe(III) chelant-free system at pH 10. The reaction solution contained 0.18 mM iron(III) chloride and 0.98 M hydrogen peroxide at pH 10 using 20 mM ammonia/ammonium chloride buffer.

The result for the hydroxyl radical formation shows significant scatter (Figure 3-11). It is due to the aggregation and precipitation of the metal oxide particles with particles interfering with the passage of incident light from the spectrophotometer and thus producing scatter. Due to this interference, the iron(III) chelant-free system was not studied further at other pH levels.

### 3.4.2 Catalytic activity of iron(III) chelant systems

#### 3.4.2.1 Decomposition of hydrogen peroxide in Iron(III)–EDTA system

The Fe<sup>3+</sup>-EDTA system showed high catalytic activity in the decomposition of alkaline hydrogen peroxide. The results show that the catalytic activity of the Fe<sup>3+</sup>-EDTA complex decreased with increasing the pH of the reaction solution (Figure 3-12).

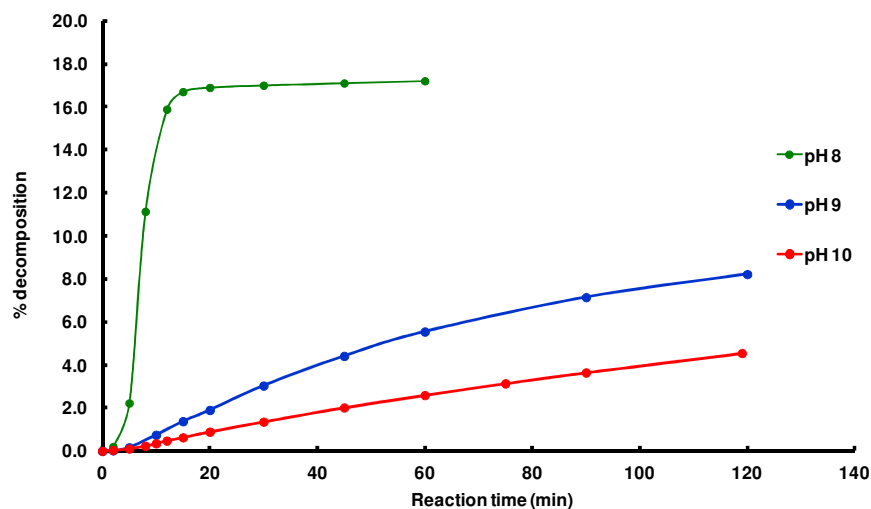


Figure 3-12: Decomposition of hydrogen peroxide by Fe(III)-EDTA system at alkaline pH. The reaction contained 0.18 mM FeCl<sub>3</sub> and 1.3 mM EDTA.4Na and 0.98 M hydrogen peroxide in 20 mM ammonia/ammonium chloride buffer solution.

At pH 8, the reaction exhibited a high initial rate of decomposition which later on changed and reaction almost stopped. The speciation plot (Figure 3-8) shows the presence of Fe(EDTA)(OH)<sup>2-</sup> complex at pH 8.0 as the main species present in the reaction conditions. Reaction solution turned purple coloured immediately on adding hydrogen peroxide. The formation of this coloured complex has been the subject of numerous previous investigations.<sup>133, 134</sup> The spectroscopic characterisation suggests that the coloured species is a peroxy complex Fe(EDTA)O<sub>2</sub><sup>3-</sup>. Previous studies have characterised this complex and concluded that it accelerates the decomposition reaction.<sup>88, 134</sup> This explains the high rate of decomposition of hydrogen peroxide observed at pH 8. Previously published studies discussed the degradation of the EDTA chelant at this stage.<sup>88, 134</sup> It is believed that once the chelant was fully degraded, decomposition reaction stopped due to deactivation of the catalyst on forming iron hydroxide. This is further discussed later in section 3.5.

An increase to pH 9.0 and 10.0 changes the metal speciation and iron oxide is now the dominant species present in the reaction solution. Insoluble iron hydroxide particles have the tendency to aggregate and grow in size. This eventually leads to precipitation of brown coloured iron hydroxide which changes the nature of the reaction solution to a heterogeneous system. As long as the

particles stay suspended in the reaction matrix, they have the ability to decompose hydrogen peroxide. The kinetics of such catalysis may depend upon the particle size of the metal oxide, the presence of other organic substrates e.g. chelant, pH and ionic strength of the reaction solution. Finally, complete precipitation of iron(III) hydroxide would almost stop the decomposition reaction. This explains variation in the activity of Fe<sup>3+</sup>-EDTA system on changing the pH of the reaction solution.

### 3.4.2.2 Catalytic activity of iron(III) complexes with other polyaminocarboxylate chelants

The different complexes exhibited different catalytic behaviour in the H<sub>2</sub>O<sub>2</sub> decomposition reaction and the pH of the reaction solution greatly influenced their activity due to changes in metal speciation.

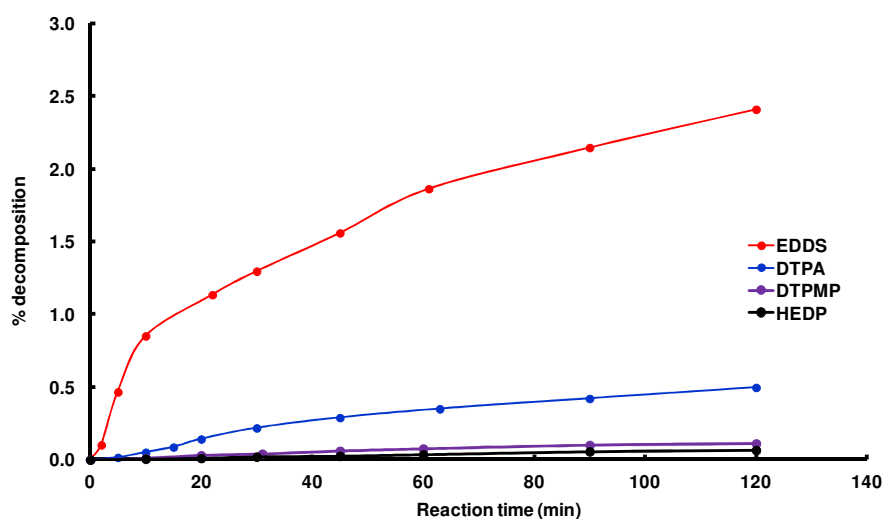


Figure 3-13: Decomposition of hydrogen peroxide in Fe<sup>3+</sup>-chelant systems at pH 8. The reaction solution contained 0.18 mM FeCl<sub>3</sub>, 1.3 mM of chelant and 0.98 M hydrogen peroxide in 20 mM ammonia/ammonium chloride buffer pH 8.0.

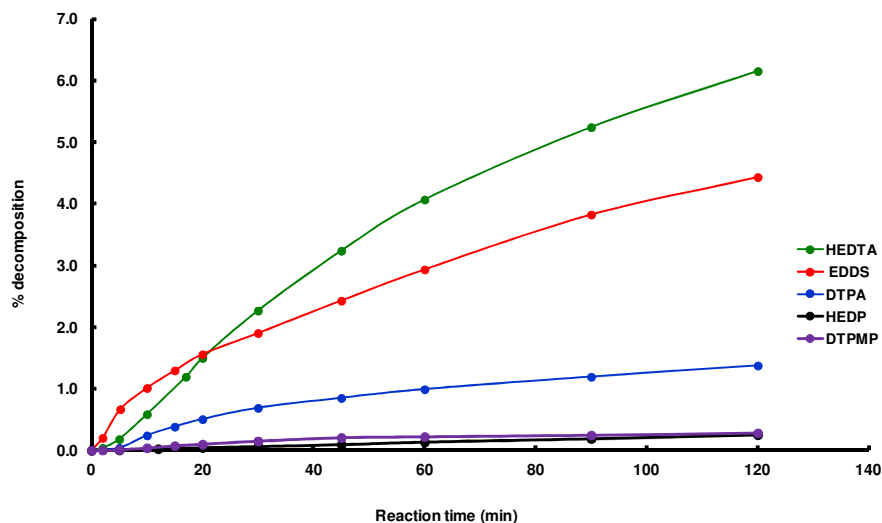


Figure 3-14: Decomposition of hydrogen peroxide in  $\text{Fe}^{3+}$ -chelant systems at pH 9.0. The reaction solution contained 0.18 mM  $\text{FeCl}_3$ , 1.3 mM of chelant and 0.98 M hydrogen peroxide in 20 mM ammonia/ammonium chloride buffer pH 9.

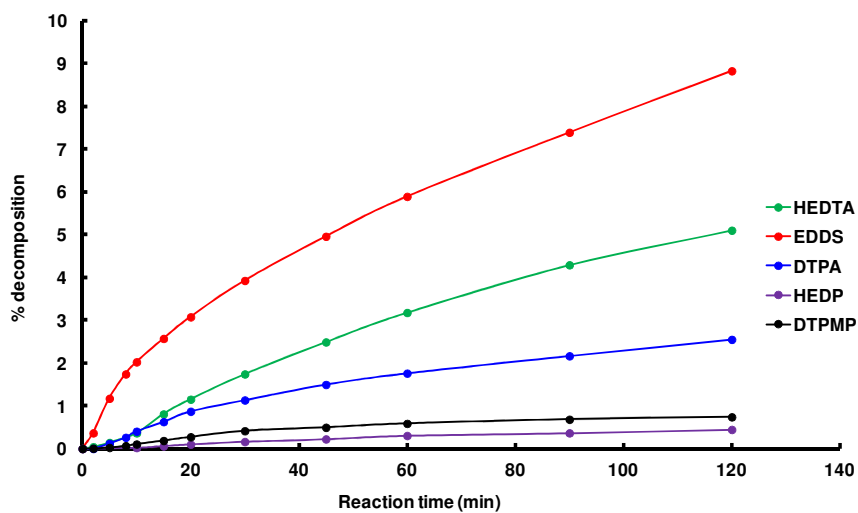


Figure 3-15: Decomposition of hydrogen peroxide in  $\text{Fe}^{3+}$ -ligand systems at pH 10. The reaction solution contained 0.18 mM  $\text{FeCl}_3$ , 1.3 mM of chelant and 0.98 M hydrogen peroxide in 20 mM ammonia/ammonium chloride buffer pH 10.

At pH 8 and 10, the  $\text{Fe}^{3+}$ -EDDS system showed high catalytic activity. As EDDS chelant does not chelate  $\text{Fe}^{3+}$  ions under the alkaline conditions and iron oxide is the only species present in the reaction solution, brown precipitates were

observed in the reaction solution overnight. These particles decompose hydrogen peroxide in a heterogeneous system. The  $\text{Fe}^{3+}$ -HEDTA system is a similar case where metal oxide is the dominant species present in the reaction solution. The results show that the catalytic activity of the complex varied very little from pH 9 to 10. Although, both EDDS and EDTA systems contain iron oxide particles, they exhibited slightly different activity in the decomposition reaction. It seems that the presence of chelant may influence the surface induced activity of insoluble particles. Different chelants may adsorb on the surface of insoluble particles and modify their chemical properties.

The  $\text{Fe}^{3+}$ -DTPA system exhibited a similar trend. At pH 8, a major fraction of metal is effectively chelated (Figure 10-5) which showed low decomposition of hydrogen peroxide. The decomposition reaction accelerated on raising the pH of the reaction solution due to the formation of  $\text{Fe}(\text{DTPA})(\text{OH})^{3-}$  complex. At pH 10, iron(III) oxide and  $\text{Fe}(\text{DTPA})(\text{OH})^{3-}$  are the main species present under the reaction conditions which increased the decomposition of hydrogen peroxide as previously observed in  $\text{Fe}^{3+}$ -EDTA system.

#### **3.4.2.3 Catalytic activity of iron(III) phosphonate complexes**

The  $\text{Fe}^{3+}$  complexes with phosphonate chelants (HEDP and DTPMP) showed low activity in decomposing hydrogen peroxide under the alkaline conditions (Figure 3-13 to Figure 3-15). Interestingly, the speciation models for  $\text{Fe}^{3+}$  with HEDP and DTPMP chelants show that neither chelant complexes metal ions and iron(III) oxide is the only species present under the reaction conditions (Figure 10-6 & Figure 10-7). As discussed earlier, the chelant adsorption on the metal oxide particle may vary depending upon the chelant and pH of the reaction solution. This chelant adsorption may thus decrease the catalytic activity of the iron(III) oxide particles leading to low decomposition of hydrogen peroxide.

#### **3.4.2.4 Hydroxyl radical formation in iron(III) – chelant systems**

Hydroxyl radical formation in the  $\text{Fe}^{3+}$ -EDTA system is also influenced by the pH of the reaction solution due to changes in metal speciation as was observed earlier for overall hydrogen peroxide decomposition.

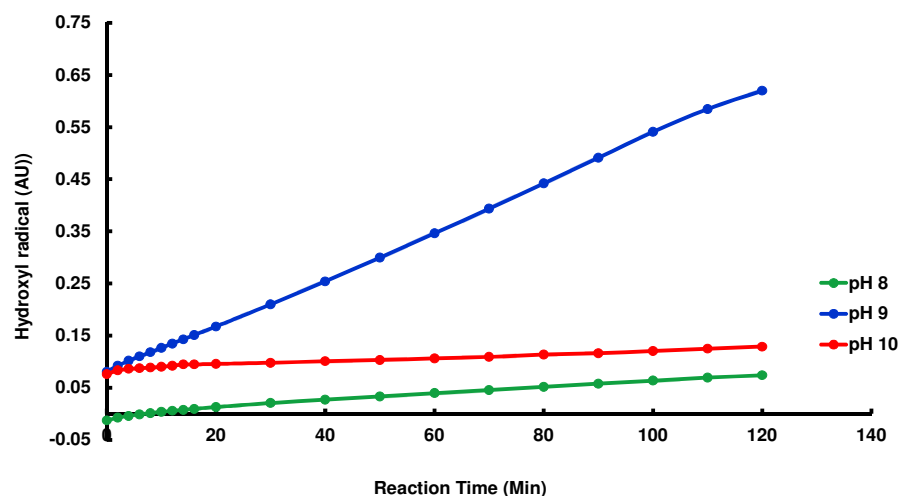


Figure 3-16: Hydroxyl radical formation in Fe<sup>3+</sup>-EDTA systems at alkaline pH. The reaction solution contained 0.18 mM FeCl<sub>3</sub>, 1.3 mM EDTA, 1.0 mM NPGA probe and 0.98 M hydrogen peroxide in 20 mM ammonia/ammonium chloride buffer.

At pH 8, relatively low concentration of hydroxyl radical was detected despite a high overall decomposition observed in the gasometric analysis. Also, the hydrogen peroxide decomposition shows a change in kinetics after a brief initial reaction time. However, no such change in reaction kinetics was observed in hydroxyl radical formation. As discussed earlier, the purple coloured peroxy complex is likely to be responsible for the high level of peroxide decomposition. There might be different mechanisms for the decomposition of hydrogen peroxide, they may involve either free radical or higher oxidation state iron intermediates (or both), and hence a correlation between hydrogen peroxide decomposition and hydroxyl radical formation may not always be observed. At pH level 9 & 10, iron hydroxide particles are present which decomposed alkaline hydrogen peroxide and generated hydroxyl radicals.

In Fe<sup>3+</sup>-EDDS system, the reaction initially exhibited rapid formation of hydroxyl radicals which suddenly stopped and no further increase in H-NPGA absorption was observed (Figure 3-18 & Figure 3-19). EDDS does not chelate the metal ions at pH 9 & 10 and metal oxide is the only species present in the reaction solution. The brown precipitates of iron oxide were observed in the quartz cell which confirmed the precipitation of metal oxide and deactivation of the metal ion catalyst.

For other aminocarboxylate chelants, HEDTA and DTPA, initial rate of hydroxyl radical formation changed with the change in pH of the reaction solution, however, the overall amount of radical formed was almost the same.

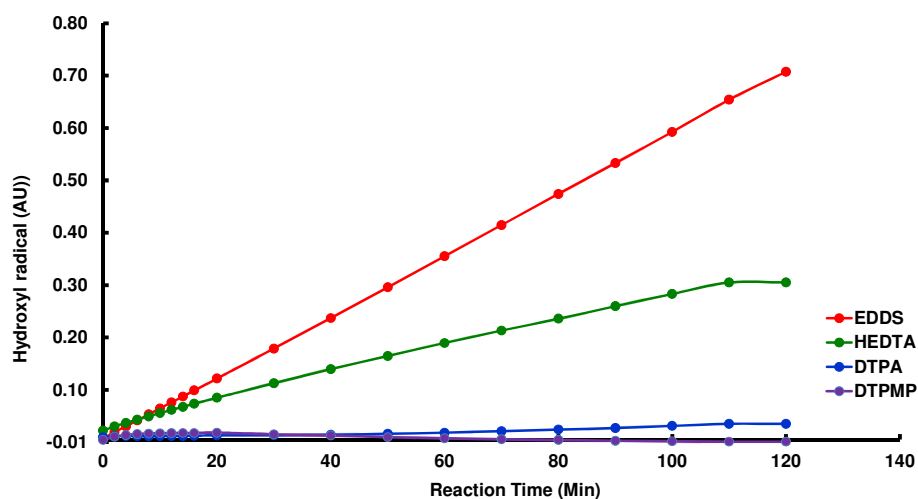


Figure 3-17: Hydroxyl radical formation in  $\text{Fe}^{3+}$ -ligand systems at pH 8. The reaction solution contained 0.18 mM  $\text{FeCl}_3$ , 1.3 mM chelant, 1.0 mM NPGA probe and 0.98 M hydrogen peroxide in 20 mM ammonia/ammonium chloride buffer.

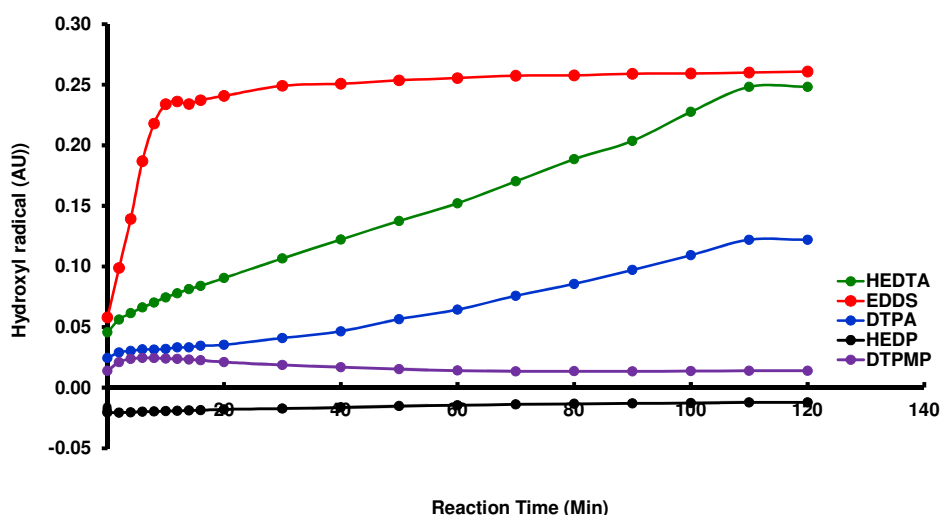


Figure 3-18: Hydroxyl radical formation in  $\text{Fe}^{3+}$ -chelant systems at pH 9. The reaction solution contained 0.18 mM  $\text{FeCl}_3$ , 1.3 mM chelant, 1.0 mM NPGA probe and 0.98 M hydrogen peroxide in 20 mM ammonia/ammonium chloride buffer.

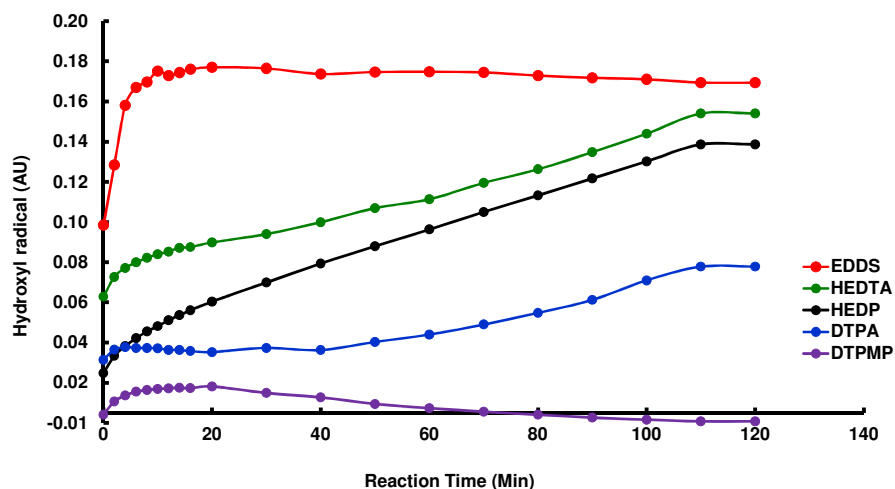


Figure 3-19: Hydroxyl radical formation in various  $\text{Fe}^{3+}$ -chelant systems at pH 10. The reaction solution contained 0.18 mM  $\text{FeCl}_3$ , 1.3 mM chelant, 1.0 mM NPGA probe and 0.98 M hydrogen peroxide in 20 mM ammonia/ammonium chloride buffer.

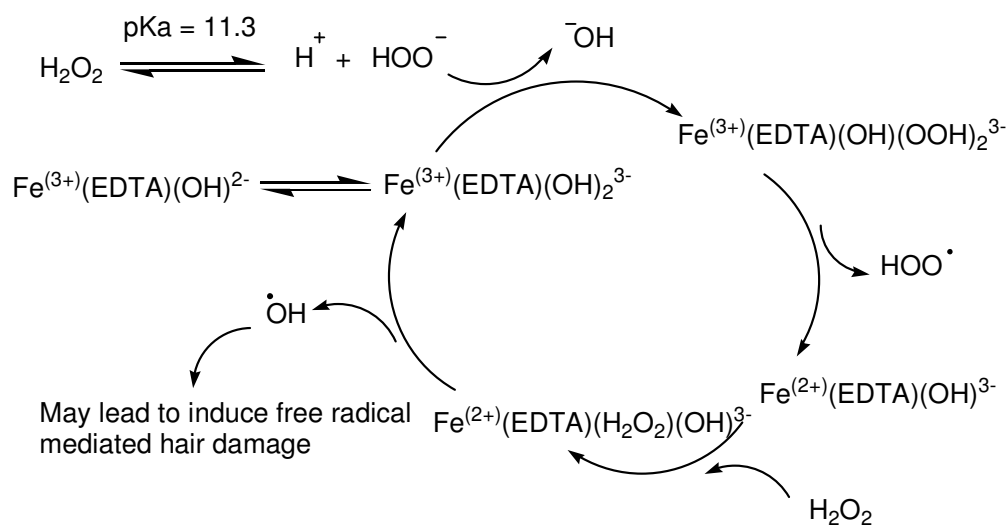
Iron(III) with phosphonate chelants (HEDP & DTPMP) generated a low level of hydroxyl radicals. A similar trend was observed earlier for the overall decomposition of hydrogen peroxide. Although the phosphonate chelants do not complex the iron(III) ions at high pH, they are superior in suppressing the hydroxyl radical formation as compared to the aminocarboxylate-based chelants.

### 3.5 Conclusion

In summary, most of chelants studied here do not complex iron(III) metal ions at high pH conditions. Phosphonate chelants were superior in suppressing hydrogen peroxide decomposition and hydroxyl radical formation. Aminocarboxylate chelants e.g EDTA, accelerated the decomposition reaction and rapidly decomposed alkaline hydrogen peroxide. This highlights an important feature of the current study that metal-chelant systems behave differently under alkaline pH conditions and hence a comprehensive study is required to screen their catalytic activity and effectiveness in stabilising alkaline hydrogen peroxide.

Iron-EDTA system is a typical example of a Fenton-like reaction which has been studied extensively.<sup>134</sup> At pH 8, it promoted hydrogen peroxide decomposition. At alkaline pH level, iron-EDTA speciation shows the presence of

$\text{Fe}(\text{EDTA})(\text{OH})^{2-}$  where hydroxyl group is coordinated with the central metal ion. The formation of peroxy complex involves a ligand exchange, the  $\text{OOH}^-$  replaces  $\text{OH}^-$  (Scheme 3-1). This substitution depends upon the concentration of hydrogen peroxide utilised and pH of the reaction solution.<sup>133</sup> An increase in pH increases the dissociation of hydrogen peroxide to give the  $\text{OOH}^-$  anion and thus contributes to the formation of peroxy complex. Similar peroxy complexes with other chelants such as HEDTA, 1,2-cyclohexanediaminetetracetic acid (CDTA) and nitrilotriacetic acid (NTA) have also been cited in the literature.<sup>134</sup>



Scheme 3-1: Schematic diagram of the formation of peroxy complex in iron(III) EDTA/EDDS systems under alkaline pH conditions.<sup>135</sup>

Hydroxyl radicals formed during the decomposition reaction may attack the EDTA molecule. This may cleave a carbon-nitrogen linkage or removal of an acidic group initiating EDTA degradation. As chelant is in excess, another molecule of EDTA binds to the metal ions and the cycle goes on until the complete degradation of the chelant.<sup>135</sup> The complete degradation of peroxy complex changes the purple colour of the reaction solution to light yellow. The decomposition reaction almost stops at this point because of the precipitation of iron hydroxide. This explains high amounts of hydrogen peroxide decomposition in  $\text{Fe}^{3+}$ -EDTA at pH 8 in the current study.

At even higher pH iron(III) hydroxide is the main species present in the reaction solution which eventually leads to precipitation of iron hydroxide. This precipitation explains the change in kinetic curve for the hydroxyl radical

generation in EDTA & EDDS systems at pH 9 and 10. Similarly the large scatter observed for hydroxyl radical formation in iron(III) chelant-free system is due to precipitation.

### 3.6 Catalytic activity of copper(II) systems

#### 3.6.1 Catalytic activity of copper(II) in a chelant-free system

Copper(II) ions showed high catalytic activity in the decomposition of hydrogen peroxide. The speciation plots suggest that copper(II) oxide is the main species under the alkaline reaction conditions (Figure 3-7) which decomposed alkaline hydrogen peroxide. The activity of copper(II) hydroxide increased from pH 8 to 10 (Figure 3-20).

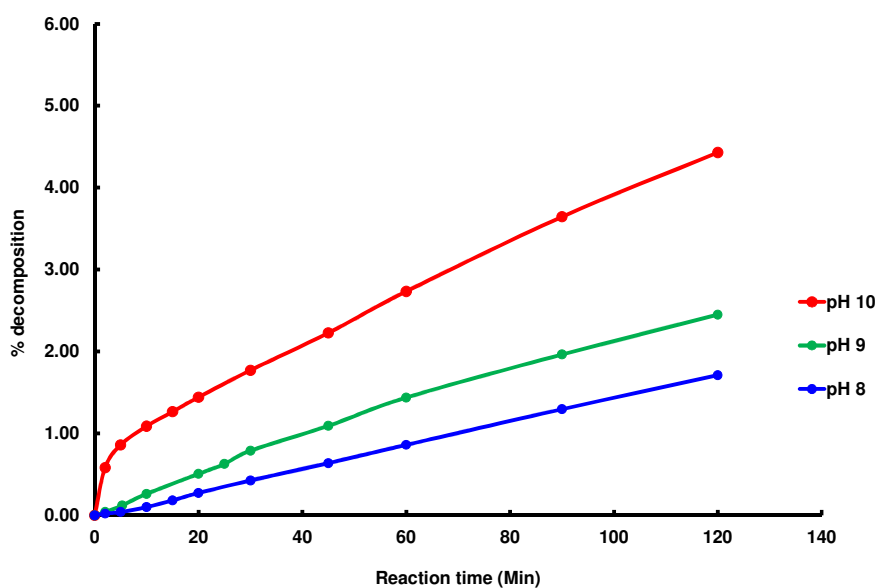


Figure 3-20: Decomposition of hydrogen peroxide by copper(II) chelant-free system. The reaction solution contained 0.18 mM copper(II) sulfate in 20 mM ammonia/ammonium chloride buffer solution.

Further experiments were carried out by increasing the initial concentration of copper(II) ions. The objective was to observe a relationship between initial concentration of copper(II) ions and amount of hydrogen peroxide decomposed and hydroxyl radicals formed. The results suggest an increase in copper(II) ions concentration increases the decomposition of hydrogen peroxide (Figure 3-21)

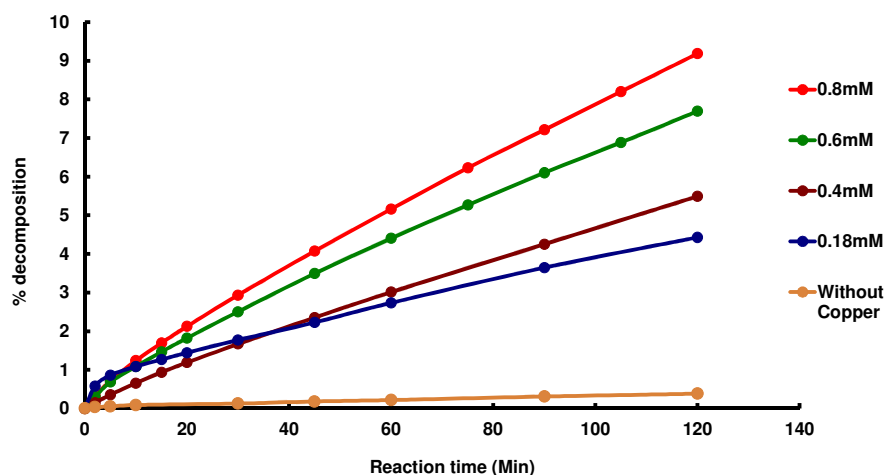


Figure 3-21: Effect of increasing initial copper(II) sulfate concentration in a chelant-free system on the decomposition of hydrogen peroxide at pH 10 using 20 mM ammonia/ammonium chloride buffer solution. The reaction solution contained copper(II) sulfate (0.18- 0.8 mM) and 0.98 M hydrogen peroxide.

A similar trend was observed for the hydroxyl radical formation (Figure 3-22). The reactions demonstrated a rapid initial increase in absorption for H-NPGA probe which subsequently slowed down and a steady increase in hydroxyl radical formation was observed. Fenton-reaction requires a switchover between  $\text{Cu}^{2+}$  and  $\text{Cu}^+$  oxidation states. It is possible that initially the reaction proceeds rapidly until  $\text{Cu}^{2+}$  is reduced to  $\text{Cu}^+$  before slowing down as the oxidation of  $\text{Cu}^+$  to  $\text{Cu}^{2+}$  becomes rate-determining. Interestingly, plotting initial concentration of copper(II) ions against initial amount of hydroxyl radicals formed showed a linear relationship. A deviation was observed at longer reaction times and at a higher concentration level of copper(II) ions (1 mM) where a brown precipitate was observed in the quartz cell.

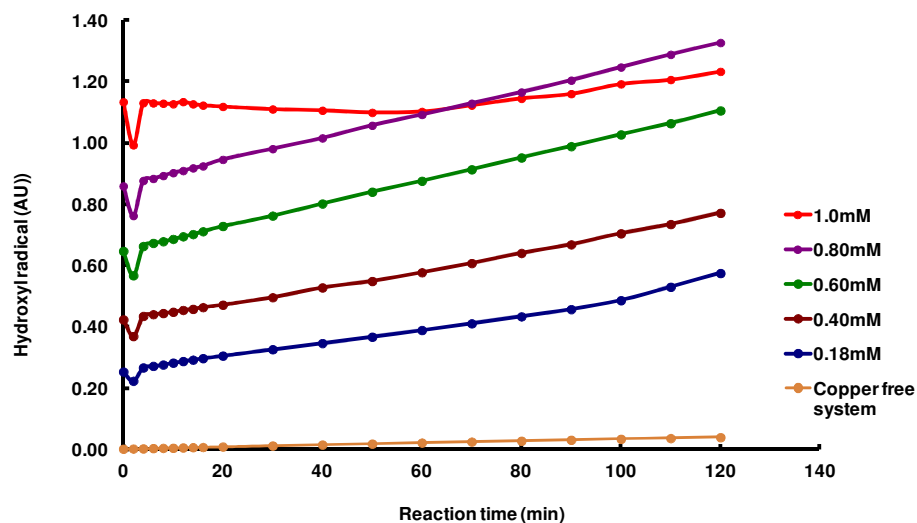


Figure 3-22: Effect of increasing copper(II) sulfate concentration on the hydroxyl radical formation at pH 10. Each reaction solution contained copper(II) sulfate (0.18-1.0 mM), 1 mM NPGA probe and 0.98 M hydrogen peroxide in 20 mM ammonia/ammonium chloride buffer solution of pH 10.

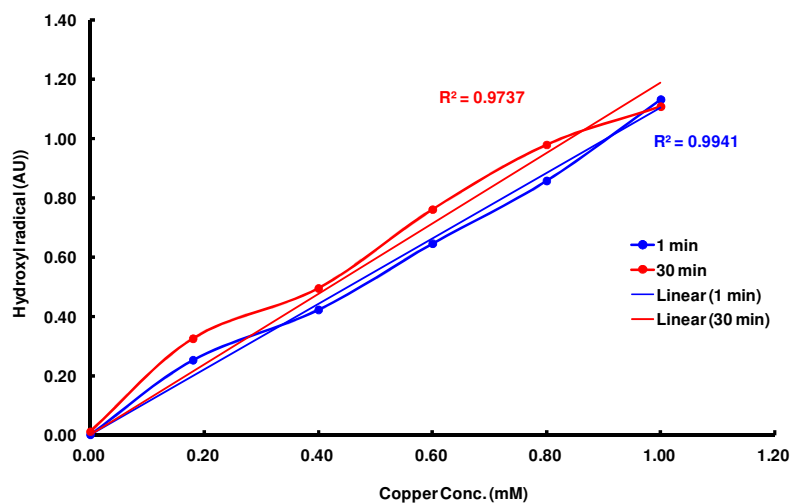


Figure 3-23: Linear relationship between concentration of  $\text{Cu}^{2+}$  ions and hydroxyl radical formation under alkaline reaction conditions.

In summary for the copper chelant-free system, copper(II) ions decomposed alkaline hydrogen peroxide rapidly. Copper(II) and iron(III) ions show different catalytic activity under the alkaline conditions in a chelant-free system. Iron precipitates quickly even at low concentration leading to deactivation of the

catalyst while copper(II) ions stay in solution. Copper(II) ions also eventually precipitate at a higher concentration level e.g. a system with 1.0 mM concentration precipitated quickly. It seems Cu(II) ions are active in the decomposition reaction until their concentration reaches a threshold level where precipitation occurs.

### **3.6.2 Catalytic activity of copper(II) chelant systems**

Further work was carried out to investigate the catalytic activity of copper(II) ions mixed with various chelants in the decomposition of hydrogen peroxide.

#### **3.6.2.1 Cu(II)-polyaminocarboxylate chelant systems**

Copper(II) complexes with EDTA and HEDTA chelants showed low catalytic activity in decomposing alkaline hydrogen peroxide (Figure 3-24) and it varied slightly with the pH which is due to changes in copper speciation. The speciation plots for these copper-chelant systems (Figure 3-9 and Figure 10-9) show that copper(II) ions are complexed by the chelants at all reaction conditions studied. These complexes decompose hydrogen peroxide slowly. The DTPA chelant similarly showed low activity with copper(II) ions. These three chelants exhibited almost identical behaviour at all pH levels and hence are preferred in stabilising hydrogen peroxide on industrial scale.

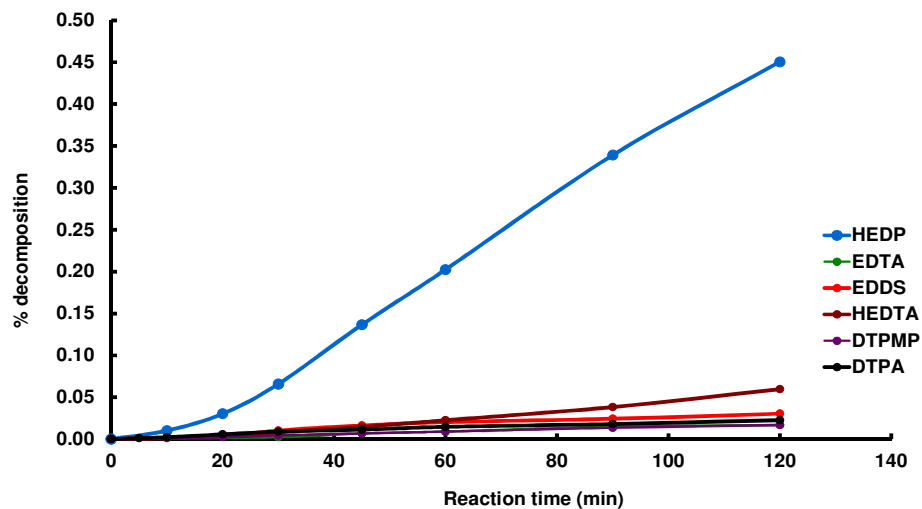


Figure 3-24: Decomposition of hydrogen peroxide in  $\text{Cu}^{2+}$ -chelant systems at pH 8. Each reaction solution contained 0.18 mM copper(II) sulfate, 1.3 mM chelant and 0.98 M hydrogen peroxide in 20 mM ammonia/ammonium chloride buffer.

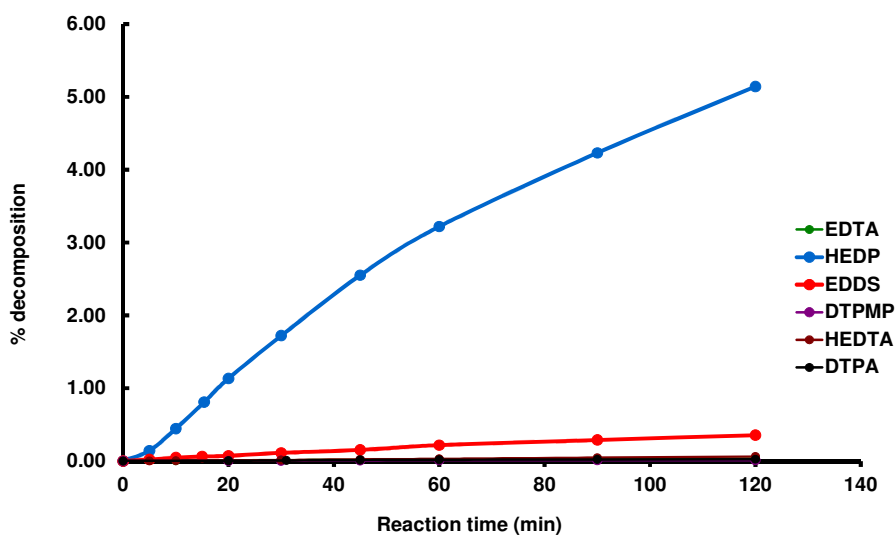


Figure 3-25: Decomposition of hydrogen peroxide in  $\text{Cu}^{2+}$ -chelant systems at pH 9. Reaction solution contained 0.18 mM copper(II) sulfate, 1.3 mM chelant and 0.98 M hydrogen peroxide in 20 mM ammonia/ammonium chloride buffer.

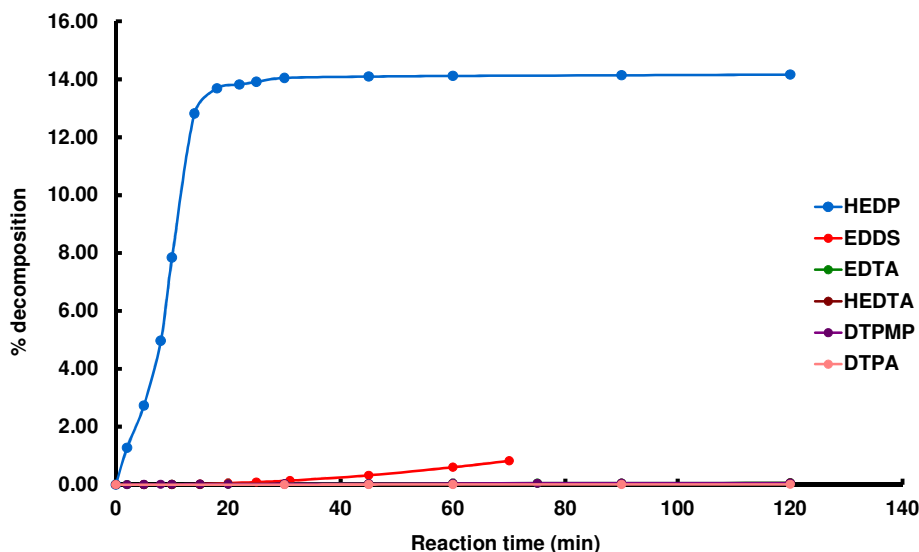


Figure 3-26: Decomposition of hydrogen peroxide in  $\text{Cu}^{2+}$ -chelant systems at pH 10. Each reaction solution contained 0.18 mM copper(II) sulfate, 1.3 mM chelant and 0.98 M hydrogen peroxide in 20 mM ammonia/ammonium chloride buffer.

Interestingly,  $\text{Cu}^{2+}$ -EDDS system exhibited relatively high activity among other aminocarboxylate chelants. The results show that its activity increased on increasing the pH of the reaction solution (pH 8 to 10). At pH 8 & 9, copper speciation shows that  $\text{Cu}(\text{EDDS})^{2-}$  complex is the dominant species present in the reaction solution (Figure 10-10) which suppressed the decomposition reaction. The metal speciation changes at pH 10 and apart from the  $[\text{Cu}(\text{EDDS})]^{2-}$  complex, the reaction mixture contains a  $[\text{Cu}(\text{OH})\text{EDDS}]^{3-}$  complex with a hydroxyl group coordinated to the central metal atom which resulted in accelerating the hydrogen peroxide decomposition.

### 3.6.2.2 Catalytic activity of $\text{Cu}(\text{II})$ -phosphonate chelants

The DTPMP chelant effectively chelates the copper(II) ions and the different complexes are present in the alkaline reaction solution (Figure 10-13). The results for the overall decomposition show that  $\text{Cu}^{2+}$ -DTPMP complex has low activity in the decomposition reaction (Figure 3-24 to Figure 3-26). At pH 10,  $\text{Cu}(\text{OH})\text{DTPMP}^{9-}$  is the predominant species. Although for aminocarboxylate chelants, coordination of hydroxyl group have been observed to accelerate the decomposition reaction, the  $\text{Cu}(\text{OH})\text{DTPMP}^{9-}$  did not influence the decomposition

reaction. This again suggests that complexes of different chelants exhibit different catalytic activity.

The  $\text{Cu}^{2+}$ -HEDP system showed a very different behaviour in the decomposition kinetics with the highest level of hydrogen peroxide decomposition observed. The copper speciation in the presence of HEDP chelant varies significantly with the pH (Figure 10-12). Different Cu-HEDP complexes are present at pH 8 & 9 while copper(II) oxide is the main species at pH 10. This explains variation in catalytic activity of the Cu-HEDP system at different pH levels (Figure 3-27).

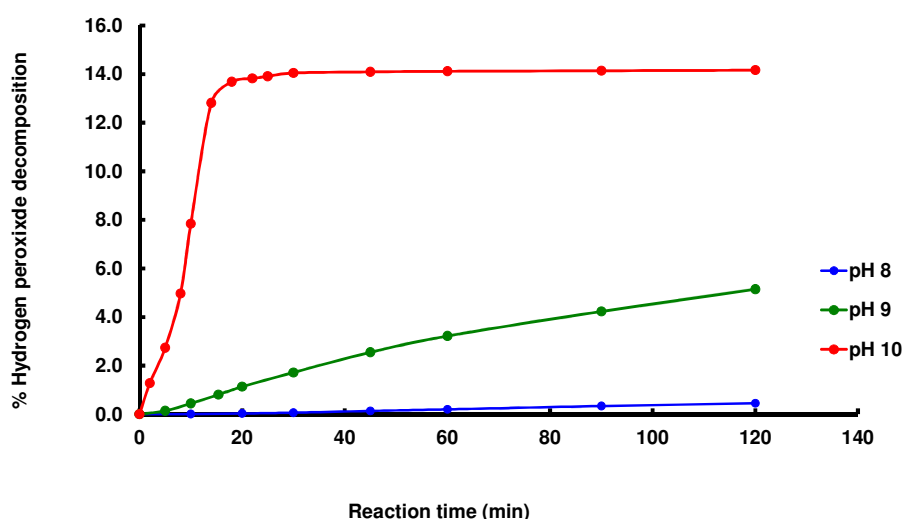


Figure 3-27: Decomposition of alkaline hydrogen peroxide in Cu(II) HEDP system. Each reaction solution contained 0.18 mM copper(II) sulfate, 1.3 mM HEDP chelant and 0.98 M hydrogen peroxide in 20 mM ammonia/ammonium chloride buffer.

At pH 10, the  $\text{Cu}^{2+}$ -HEDP system decomposed almost 14%  $\text{H}_2\text{O}_2$  in the first 16-18 minutes. This is the highest decomposition rate observed among all chelant systems studied. After the rapid initial decomposition, an abrupt change in the decomposition curve was observed and reaction almost stopped. No such change in the decomposition curve has been observed for other chelants discussed earlier with both copper(II) or iron(III) metal ions. This stimulated us to carry out a further investigation to understand the activity of  $\text{Cu}^{2+}$ -HEDP system. The topic is discussed later in chapter 5.

The activity of  $\text{Cu}^{2+}$ -HEDP complex decreased at pH levels of 8 & 9 and no abrupt change in its kinetic behaviour was observed. This is due to changes in copper speciation. At pH 9, the complex  $\text{Cu}(\text{HEDP})(\text{OH})^{3-}$  is contributing to the copper speciation which is possibly responsible for decomposition of hydrogen peroxide. At pH 8, copper(II) ions are effectively complexed by the chelant which results in the least activity among other pH levels. These results again suggest that the catalytic activity is greatly influenced by the pH of the reaction solution. The changes in pH of the reaction solution change the metal speciation and thus change the catalytic activity in the decomposition reaction.

### **3.6.3 Hydroxyl radical formation in copper(II) – chelant systems**

The hydroxyl radical formation in copper(II) chelant systems showed almost the same trend as was observed in the decomposition of hydrogen peroxide. A low level of hydroxyl radical was detected in most of the systems suggesting the low catalytic activity in the reaction except  $\text{Cu}^{2+}$ -HEDP (Figure 3-28). Some trends were negative which is probably due to a drift in spectrophotometer during the data acquisition. However, the results clearly suggest the low catalytic activity of  $\text{Cu}^{2+}$ -chelant systems in the generation of hydroxyl radical.

The  $\text{Cu}^{2+}$ -HEDP chelant system is an exception and the hydroxyl radical formation increased on increasing the pH of the reaction solution. At pH 10, a change in absorption curve was observed which corresponds to the similar observation for the overall decomposition.

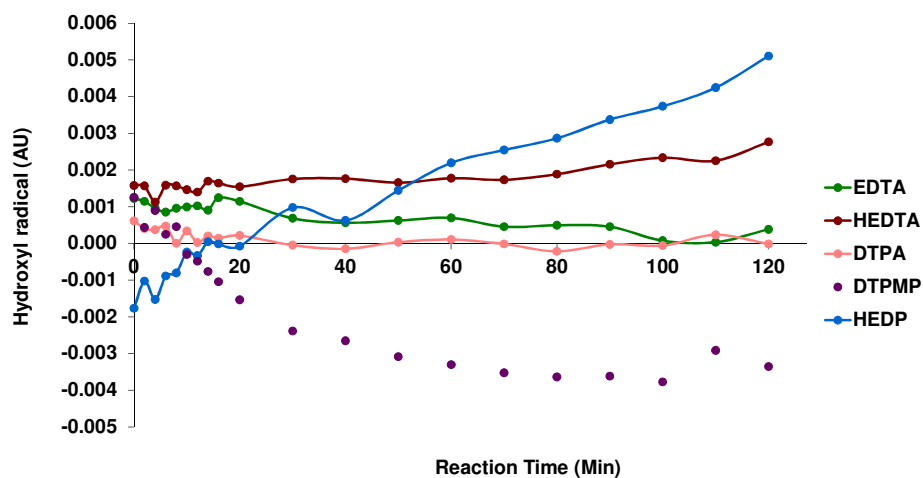


Figure 3-28: Hydroxyl radical formation in Cu(II) – chelant systems at pH 8. Each reaction solution contained 0.18 mM copper(II) sulfate, 1.3 mM chelant, 1.0 mM NPGA probe and 0.98 M hydrogen peroxide in 20 mM ammonia/ammonium chloride pH 8.0.

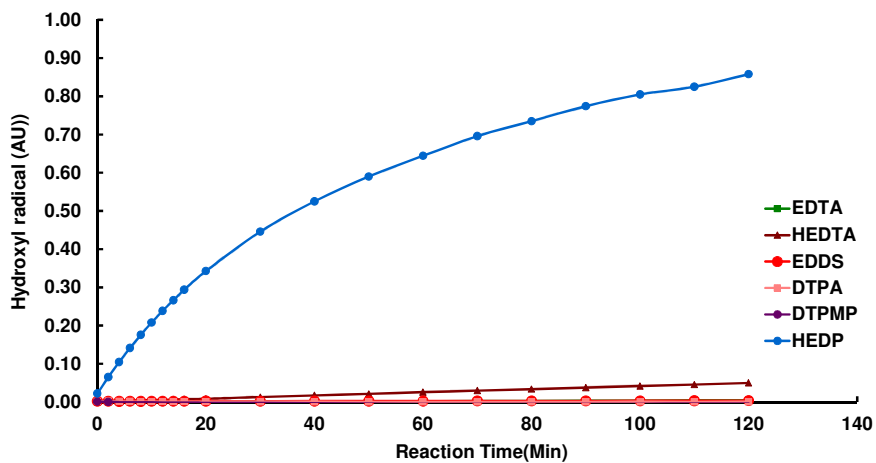


Figure 3-29: Hydroxyl radical formation in Cu(II) – chelant systems at pH 9. Each reaction solution contained 0.18 mM copper(II) sulfate, 1.3 mM chelant, 1.0 mM NPGA probe and 0.98 M hydrogen peroxide in 20 mM ammonia/ammonium chloride pH 9.

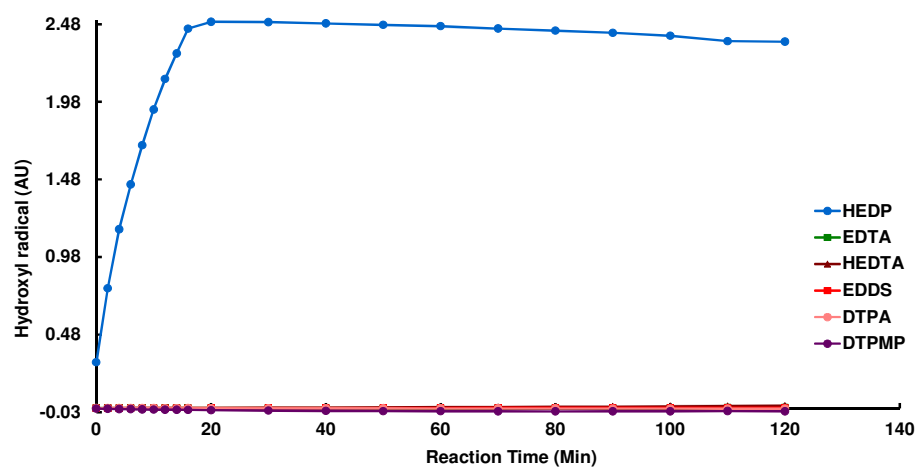


Figure 3-30: Hydroxyl radical formation in Cu(II) – chelant systems at pH 10. Each reaction solution contained 0.18 mM copper(II) sulfate, 1.3 mM chelant, 1.0 mM NPGA probe and 0.98 M hydrogen peroxide in 20 mM ammonia/ammonium chloride pH 10.

### 3.7 Iron(III) vs copper(II) and aminocarboxylate vs phosphonate chelants: Comparison of catalytic activity

In a chelant-free system, copper(II) ions are more active in decomposing alkaline hydrogen peroxide compared to iron(III) ions. Both metals ions form metal oxides which aggregate and eventually precipitate in the reaction solution. Iron(III) oxide is observed to have higher tendency for precipitation. This is clearly demonstrated in the colorimetric analysis for hydroxyl radical formation at pH 10 where the precipitation resulted in large scatter in the data. For copper(II) ions, the initial rate of decomposition and hydroxyl radical formation is high and it increases with an increase in initial concentration of copper(II) ions.

Aminocarboxylate chelants such as EDTA and EDDS combined with iron(III) ions generated more hydroxyl radical and decomposed higher amounts of hydrogen peroxide than the corresponding complexes with copper(II) ions. Usually chelants are added to minimise hydrogen peroxide decomposition, however, in some case (depending upon pH of the reaction solution), addition of

the chelant may form a pro-oxidant system which actually accelerates hydrogen peroxide decomposition. On the other hand, most aminocarboxylate and phosphonate chelants are effective in chelating copper(II) ions and suppressing hydrogen peroxide decomposition except HEDP chelant.

The DTPMP was the best chelant for suppressing both copper(II) and iron(III) catalysed hydrogen peroxide decomposition.

### **3.8 Conclusion**

Copper(II) ions can decompose hydrogen peroxide and generate hydroxyl radicals under the alkaline hair colouring conditions. Commonly employed chelants such as EDTA and EDDS are effective in suppressing copper(II) activity and slow down hydrogen peroxide decomposition. Copper-HEDP is an exception where rapid hydrogen peroxide decomposition is observed and a significant amount of peroxide is decomposed. The same chelants complexed with iron(III) ions accelerate the decomposition of alkaline hydrogen peroxide while iron(III) in a chelant-free system leads to iron oxide/hydroxide precipitation. Iron oxide particles are capable of catalysing hydrogen peroxide decomposition. These results guide us in choosing the right chelant combination in hair colouring formulation for an improved and superior colouring application.

Beside copper and iron, hair contains a large amount of calcium and magnesium metal ions. These alkaline earth metal ions compete with transition metal ions for the added chelant which may greatly influence the catalytic activity of the transition metal ions in the decomposition reaction. This new dimension is studied and discussed in the next chapter.

## **Chapter 4: Decomposition of alkaline hydrogen peroxide in a binary metal system**

---

# Chapter 4: Decomposition of alkaline hydrogen peroxide in a binary metal system

---

## 4 Binary metal systems

The previous chapter discussed copper(II) and iron(III) catalysed decomposition of hydrogen peroxide at high pH. The results reveal that copper(II) ions decompose hydrogen peroxide under alkaline conditions while iron(III) ions precipitate quickly leading to catalyst deactivation. Also, copper is the most abundant transition metal in human hair. This suggests that copper is the main metal responsible for the decomposition of alkaline hydrogen peroxide and hydroxyl radical formation. Chelants e.g. EDTA, EDDS and DTPMP suppressed the catalytic activity of copper(II) ions in solution model systems. These experiments were comprised of relatively a simple model system containing a single metal and only one chelant. However, a real-life system for hair permanent colouring is much more complex.

Beside copper and iron, human hair fibre contains different other metals e.g. calcium, magnesium, sodium and potassium.<sup>18</sup> A recent quantitative study reports 1000–2000 ppm of calcium and 150-300 ppm of magnesium ions in natural non-chemically treated American-Caucasian hair fibres.<sup>24</sup> These values are even higher for chemically treated hair fibres where 5000-6000 ppm of calcium and 500-800 ppm of magnesium are present.<sup>24, 25</sup> Calcium is the most abundant metal in hair fibre. The presence of large amounts of calcium ions in a hair colouring system complicates the situation, calcium and copper ions may compete for the chelant. This may influence the metal ion speciation and the activity of transition metal ions in the decomposition of hydrogen peroxide. Therefore it is important to study a two metal model system (binary metal system) where copper or iron ions are present along with a large excess of calcium. This chapter discusses a two metal system containing copper–calcium and iron–calcium mixture under alkaline conditions. The first set of experiments was performed in a chelant-free solution while further experiments were carried out by adding EDTA, EDDS or DTPMP chelants. These three chelants were chosen due to their performance observed in the previous chapter.

A further, more realistic model was designed using human hair fibres as a source of metal ions. Their metal content was determined prior to employing them in the current study.

## **4.1 Objectives**

The aim here is to study the catalytic activity of transition metal ions in a Fenton-like reaction in the presence of a large excess of calcium ions. The target was to investigate the selectivity of various chelants in chelating metal ions and subsequent influence on the decomposition of hydrogen peroxide.

Further experiments are carried out using human hair fibres as a source of metal ions. The objective is to evaluate the performance of selected chelants in suppressing free radical formation in the presence of metal treated hair fibres.

## **4.2 Changes in speciation plots in the presence of calcium**

Copper speciation plots were simulated by adding a relatively large excess of calcium ions (125 mM). The concentration of ammonia in the reaction solution was also increased to 400 mM to make it more comparable to a real-life hair colouring application. The increase in ammonia concentration greatly influenced the copper speciation in a chelant-free system and copper-ammonia  $[\text{Cu}(\text{NH}_3)_4]^{2+}$  complex was observed (Figure 4-1). The iron(III) system with added calcium ions expectedly showed iron(III) oxide as the main species present in the reaction solution (Figure 10-15).

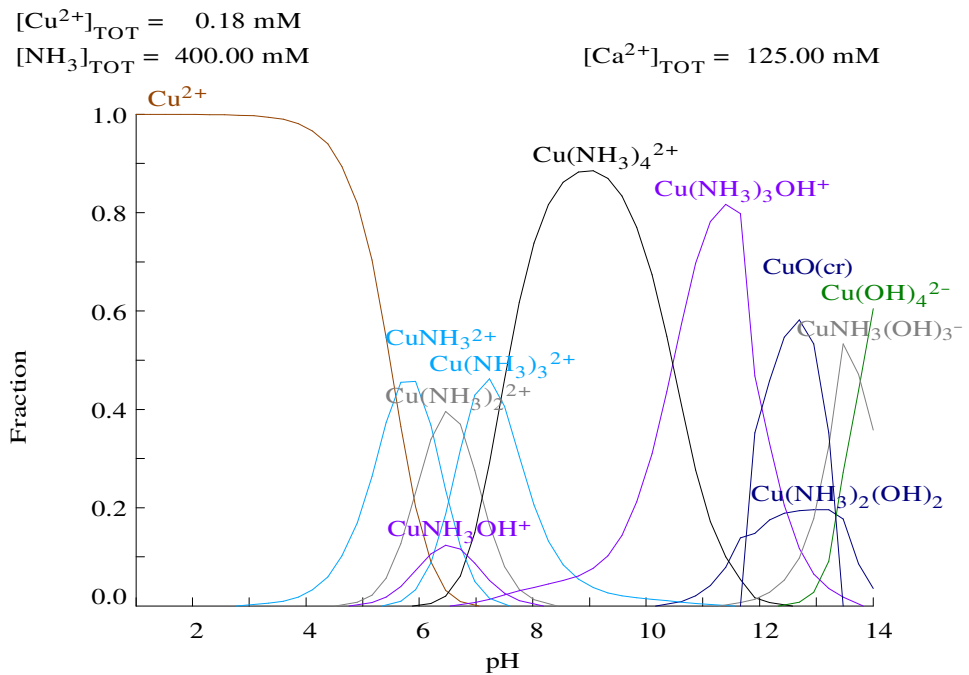


Figure 4-1: Copper speciation in the presence of calcium in a chelant-free system.

Addition of EDTA chelant to the copper-calcium system demonstrated an interesting scenario. The speciation plots suggest that at high pH level,  $[\text{Cu}(\text{NH}_3)_4]^{2+}$  complex is the predominant species in the reaction solution and the chelant does not seem to complex copper(II) ions (Figure 4-2). The EDTA speciation shows that most of EDTA is associated with Ca-EDTA complex and no copper-EDTA complex is present at pH 10 (Figure 4-3). However, the speciation plot in the absence of calcium ions did not show any copper-ammonia complex and only copper-EDTA complex was present in the reaction solution (Figure 4-4). These plots demonstrate the impact of calcium in the reaction system on copper speciation where calcium ions are competing for the EDTA chelant. These changes in copper speciation suggest a high rate of decomposition of hydrogen peroxide for copper-calcium EDTA system.

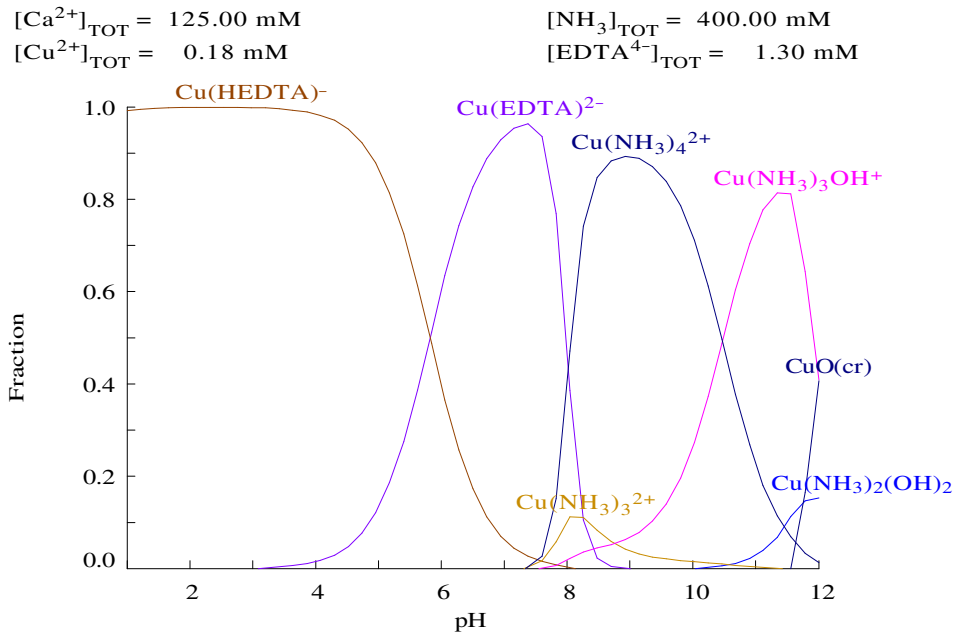


Figure 4-2: Copper speciation in the presence calcium ions and EDTA chelant in a 400 mM ammonia buffer.

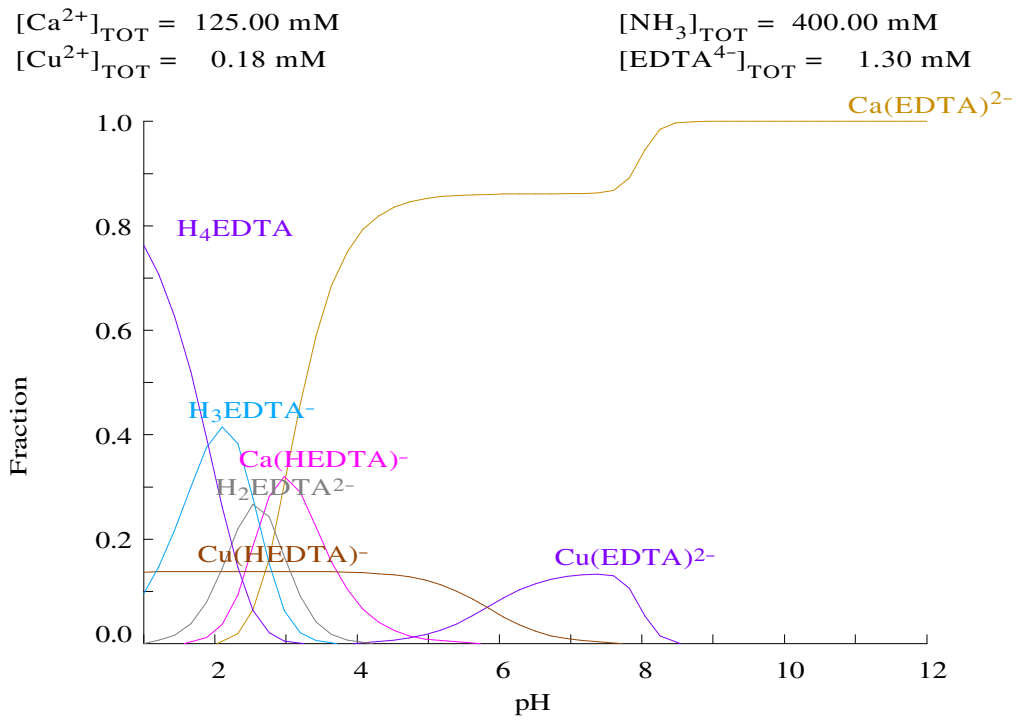


Figure 4-3: EDTA speciation in copper-calcium system in a 400 mM ammonia buffer.

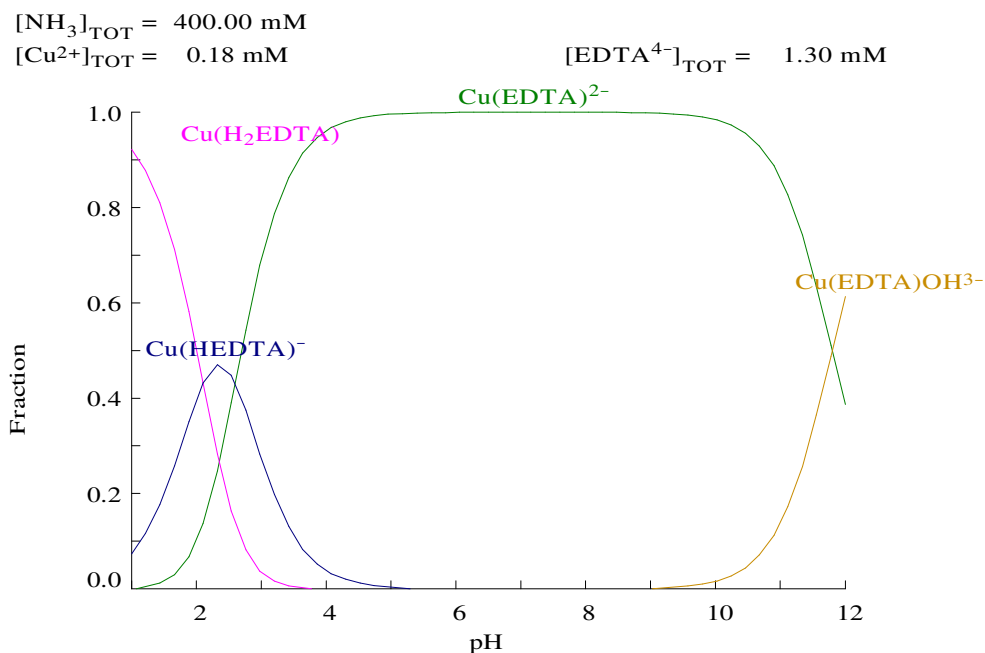


Figure 4-4: Copper(II) speciation in the presence of EDTA in a 400 mM ammonia buffer.

A different scenario was observed for the EDDS chelant system. Despite the presence of the large excess of calcium ions, EDDS chelant showed preference for copper(II) ions and copper-EDDS complex  $[\text{Cu}(\text{EDDS})]^{2-}$  was present in the reaction solution along with a small fraction of  $[\text{Cu}(\text{NH}_3)_4]^{2+}$  complex (Figure 4-5 & Figure 4-6). Here, EDDS chelant behaves differently compared to the EDTA system which suggests a different catalytic activity for copper-EDTA and copper-EDDS systems in the presence of calcium ions.

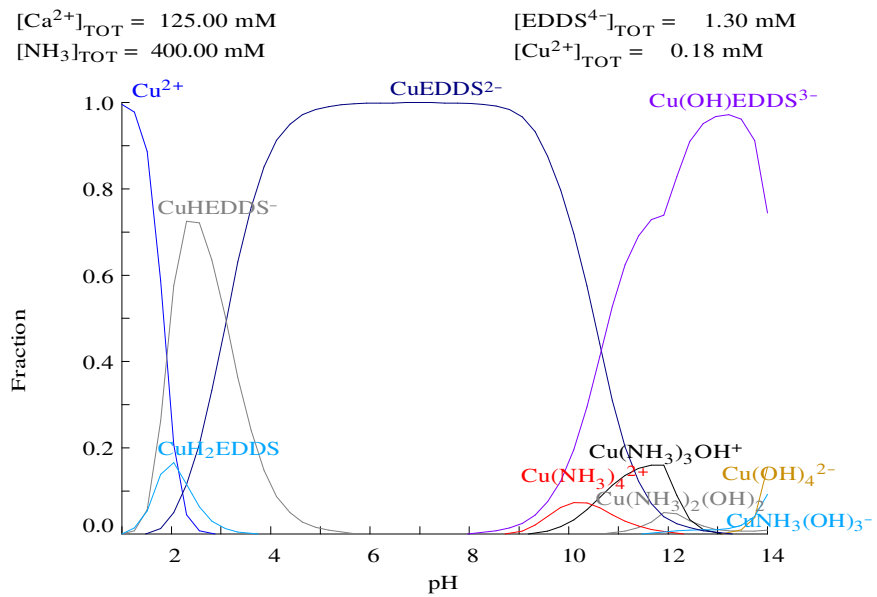


Figure 4-5: Copper ion speciation in EDDS system in the presence of large excess of calcium ions.

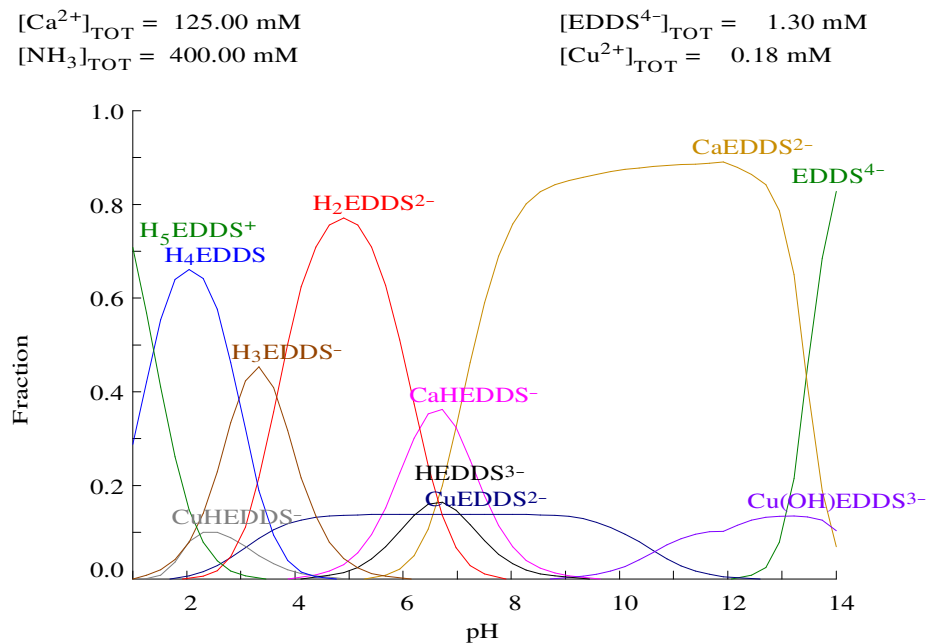


Figure 4-6: EDDS speciation in copper-calcium binary system.

A similar scenario was observed for copper speciation in the presence of DTPMP chelants (Figure 10-17 & Figure 10-18) where copper-DTPMP complex was present in the reaction solution.

## 4.3 Decomposition of hydrogen peroxide in the binary system

### 4.3.1 Copper(II) – calcium binary system

The first binary combination studied was copper-calcium in a chelant-free solution at pH 10. The results showed a very rapid decomposition for alkaline hydrogen peroxide (Figure 4-7). All of the hydrogen peroxide was decomposed within the first 2-5 minutes. In the previous chapter, the same amount of copper(II) ions in the absence of calcium using 20 mM ammonia/ammonium chloride buffer showed a relatively slow rate of decomposition. An increase in ammonia concentration in the reaction solution facilitates the formation of  $[\text{Cu}(\text{NH}_3)_4]^{2+}$  complex which in turn activates the copper(II) ions accelerating the decomposition reaction. As calcium is a harder acid than copper(II), only copper(II) ions bind with ammonia to form a copper-ammonia complex.

A control experiment in the absence of calcium ions also showed a high rate of hydrogen peroxide decomposition (Figure 4-8).

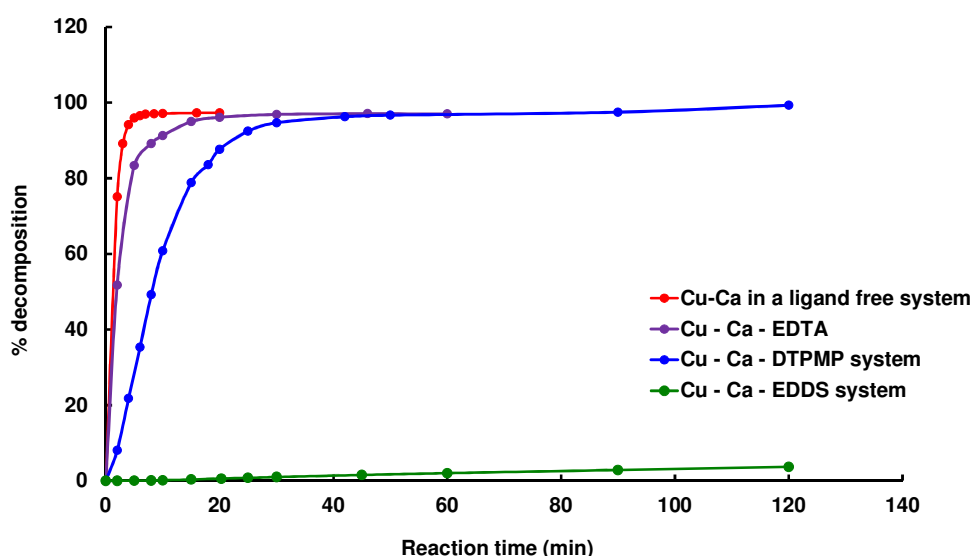


Figure 4-7: Decomposition of alkaline hydrogen peroxide in copper-calcium binary system at pH 10 using 400 mM ammonia/ammonium chloride buffer solution. Each reaction solution contained 0.18 mM copper(II) sulfate, 125 mM calcium nitrate, 1.3 mM chelant and 0.98 M hydrogen peroxide.

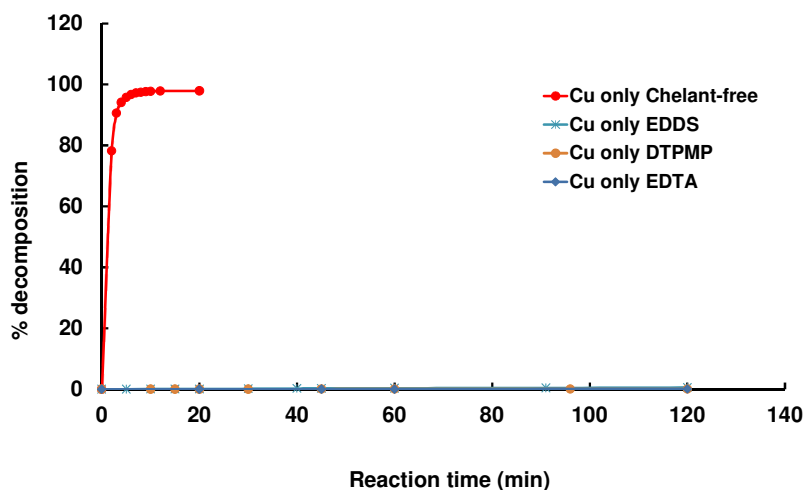


Figure 4-8: Control experiment at high ammonium concentration in the absence of calcium. Decomposition of alkaline hydrogen peroxide in copper(II) systems in the absence of calcium ions at pH 10 with 400 mM ammonia/ammonium chloride buffer solution. Each reaction solution contained 0.18 mM copper(II) sulfate, 1.3 mM chelant and 0.98 M hydrogen peroxide.

Further experiments were carried out by adding chelants to the copper-calcium system. The results show that EDDS is the only chelant that suppressed the decomposition reaction. Addition of EDTA and DTPMP chelants had almost no influence on the rate of the reaction (Figure 4-7). Interestingly, a control experiment in the absence of calcium ions showed an opposite effect where addition of EDTA and DTPMP chelants suppressed the decomposition of alkaline hydrogen peroxide (Figure 4-8). These results clearly demonstrate the effect of calcium ions competing for the chelant at high pH of the reaction solution. EDDS chelant selectively binds to copper(II) ions in the presence of calcium ions. This phenomenon is explained by the speciation plots as discussed earlier. The selectivity of EDDS chelant is further examined in the next sections.

The speciation plots for EDTA showed that calcium ions are strongly competing for the EDTA chelant and copper(II) ions bind with ammonia. EDTA is a hard base compared to ammonia as nitrogen-based bases are softer than oxygen based ones due to lower electronegativity and higher polarisability. As calcium is harder than copper(II), calcium binds EDTA stronger than copper(II) ions and copper(II) ions bind ammonia stronger than calcium ions. This leads to

the formation of  $[\text{Cu}(\text{NH}_3)_4]^{2+}$  complex that catalyse hydrogen peroxide decomposition and explains the high rate of the decomposition reaction.

Although the DTPMP chelant forms copper-chelant complexes at high pH along with the presence of a small fraction of a copper-ammonia complex (Figure 10-17), the system showed high activity in the decomposition reaction. A control experiment in the absence of calcium showed suppression in the rate of hydrogen peroxide decomposition and only small amount of hydrogen peroxide was decomposed. Here again, the presence of calcium demonstrated its influence on the decomposition reaction. This can be explained by the precipitation of calcium-DTPMP complex. On addition of DTPMP chelant to the copper-calcium solution, a white precipitate was observed immediately. A control experiment in the absence of copper(II) ions also showed the same precipitation. It is possible that the surface of insoluble calcium-DTPMP complex acts as a heterogeneous catalyst for hydrogen peroxide decomposition.

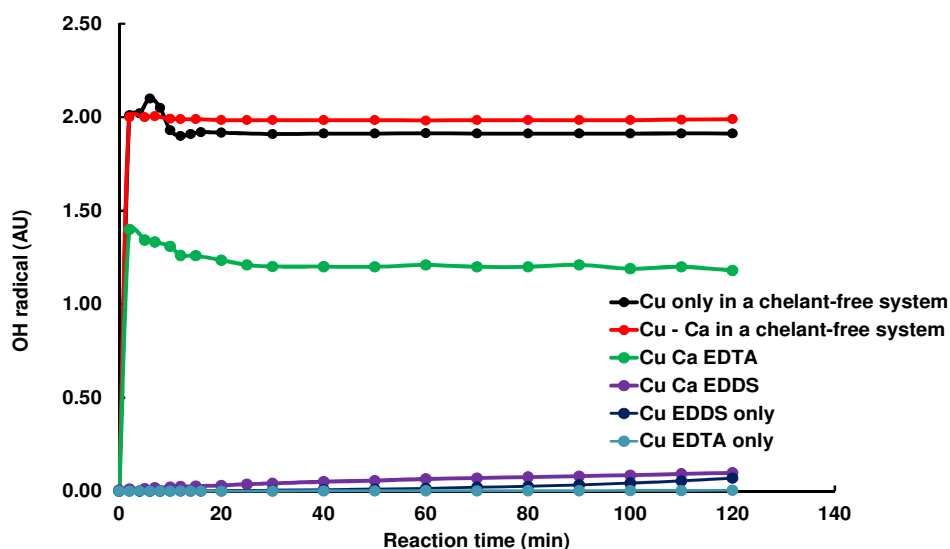


Figure 4-9: Hydroxyl radical formation in Cu-Ca binary systems. Each reaction contained 0.18 mM copper(II) sulfate, 125 mM calcium nitrate, 1.3 mM chelant, 1.0 mM NPGA probe and 0.98 M hydrogen peroxide.

The hydroxyl radical formation in the binary systems also showed a similar pattern of catalytic activity (Figure 4-9). The chelant-free system produced a high level of hydroxyl radical immediately on mixing with the hydrogen peroxide. EDDS chelant suppressed hydroxyl radical formation both in the presence and absence

of calcium ions. This is consistent with the results of overall hydrogen peroxide decomposition and again shows that EDDS is the only chelant that is able to suppress the catalytic activity of copper(II) ions in the presence of calcium.

In the EDTA system, high hydroxyl radical flux was observed in the presence of calcium ions. The control experiment in the absence of calcium showed that EDTA was able to suppress hydroxyl radical formation. This matches the results for overall  $\text{H}_2\text{O}_2$  decomposition and demonstrates the effect of calcium ions. The DTPMP system could not be studied due to the precipitation of calcium-DTPMP complex in the quartz cell.

In summary, the above experiments and speciation plots provide an interesting insight about the selectivity and superior performance of EDDS chelant in chelating copper(II) ions in preference to calcium ions. EDDS is the only chelant able to suppress free radical chemistry under the alkaline hair colouring conditions. The selectivity of chelants is further examined in the next sections.

### **4.3.2 Iron(III) – calcium binary system**

Similarly, iron-calcium binary system was studied. Ferric ions in a chelant-free system exhibited high catalytic activity in the decomposition reaction (Figure 4-10). The speciation plot for the chelant-free system describes the presence of insoluble iron hydroxide present in the reaction responsible for the hydrogen peroxide decomposition. Activity of metal oxide/hydroxide particles has already been discussed in the previous chapter describing the surface catalysed decomposition of hydrogen peroxide by suspended particles.

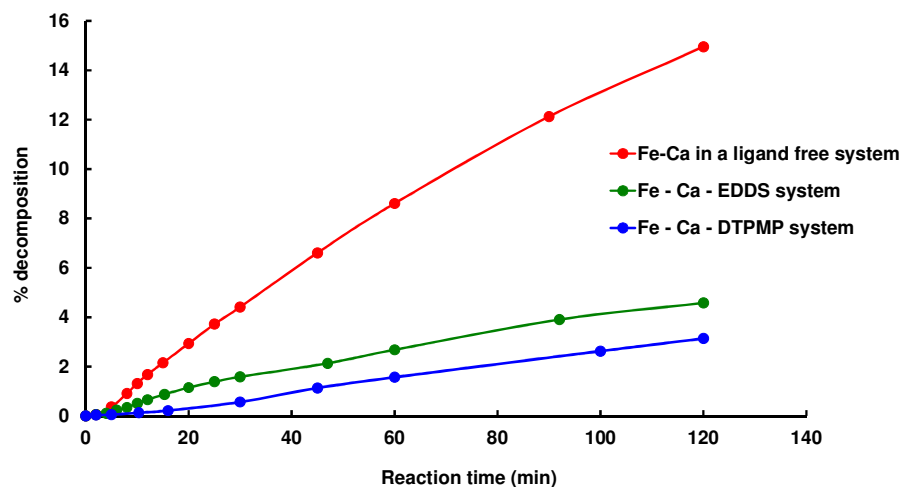


Figure 4-10: Decomposition of alkaline hydrogen peroxide in iron(III) - calcium binary system. Each reaction contained 0.18 mM iron(III) chloride, 125 mM calcium nitrate, 1.3 mM each chelant and 0.98 M hydrogen peroxide.

Introducing EDDS and DTPMP chelants changed the kinetics of decomposition of hydrogen peroxide. Although speciation plots for both EDDS and DTPMP chelants show that they do not complex iron ions at high pH, they were effective in stabilising hydrogen peroxide. As discussed earlier, iron(III) is a hard acid which binds hydroxyl anion ( $\text{OH}^-$ ) under the alkaline conditions in preference to softer ammonia, EDDS and DTPMP. Hence ammonia or chelants do not form strong complexes with iron(III) ions. Similar behaviour was observed in the earlier solution model system. It is believed that low catalytic activity of iron hydroxide in the presence of chelant is due to the chelant adsorption on the metal hydroxide particles.

### 4.3.3 Conclusion

These experiments describe the catalytic activity of transition metal ions in a model system containing relatively large amounts of calcium ions. Among the chelants studied here, EDDS displayed preference for binding copper(II) ions and hence was the best chelant to prevent the decomposition of hydrogen peroxide and hydroxyl radical formation. These experiments highlight the advantage of using the EDDS chelant under the alkaline hair colouring conditions. Further work

is carried out later in the chapter to explain EDDS binding copper ions preferentially.

#### **4.4 Decomposition of hydrogen peroxide using hair fibers as a source of metal ions**

The work described in this section was carried out using human hair fibres as a source of metal ions. The objective was to examine the activity of deposits of transition metals on the hair fibres in decomposition of alkaline hydrogen peroxide and generation of hydroxyl radicals. This is the next step in designing a real-life hair colouring model with the aim to further enhance our understanding of the activity of these metal ions and the effect of various chelants on the decomposition of hydrogen peroxide.

##### **4.4.1 Metal dosage and analysis of hair metal content**

Virgin human hair fibres were treated with copper(II) sulfate solution in a P&G lab in USA.<sup>136</sup> The metal treatment involved soaking virgin natural Caucasian hair fibres in a standard aqueous solution of copper(II) sulfate (1000 ppm). The different level of metal uptake was obtained by varying treatment time. Hair fibres were dried in air at room temperature. Metal composition of hair fibres was determined by digesting small samples of hair fibres in concentrated nitric acid. The metal content was subsequently analysed using inductively coupled plasma–atomic emission spectroscopy (ICP-AES). The hair samples contain large amounts of calcium and magnesium along with copper, zinc, iron and manganese (Table 4-1). The large amount of alkaline earth metal ions along with copper and iron presents a real-life picture of the level of metals present in human hair.

<i>Metal contents in hair fibre samples (ppm)</i>					
<i>Treatment</i>	<i>Mg</i>	<i>Ca</i>	<i>Mn</i>	<i>Fe</i>	<i>Cu</i>
<i>Level</i>					
Level 1	720	6577	8	15	40
Level 2	742	6756	8	14	58
Level 3	735	6726	8	14	68
Level 4	736	6807	8	15	81

Table 4-1: Metal content in hair fibres after copper treatment. A “level” defines different amounts of metal concentration present on the hair fibre.

#### **4.4.2 Decomposition of hydrogen peroxide by copper treated hair fibres in a chelant-free system**

The copper treated hair fibres were used as source of metal ions to decompose hydrogen peroxide. The decomposition reaction was monitored by the gasometric method. The results (Figure 4-11) demonstrate that copper deposits in the hair fibre decompose alkaline hydrogen peroxide. Increase in copper contents on the fibre increased the rate of reaction and overall level of hydrogen peroxide decomposed. The same set of hair fibres was analysed for hydroxyl radical formation using the NPGA colorimetric probe. Copper deposits generated hydroxyl radicals under the alkaline conditions. The rate of hydroxyl radical formation also increased with the increase in copper level (Figure 4-12). This proposes a direct relationship between metal content of the hair fibre and the free radical formation which is consistent with our earlier results in the solution model.

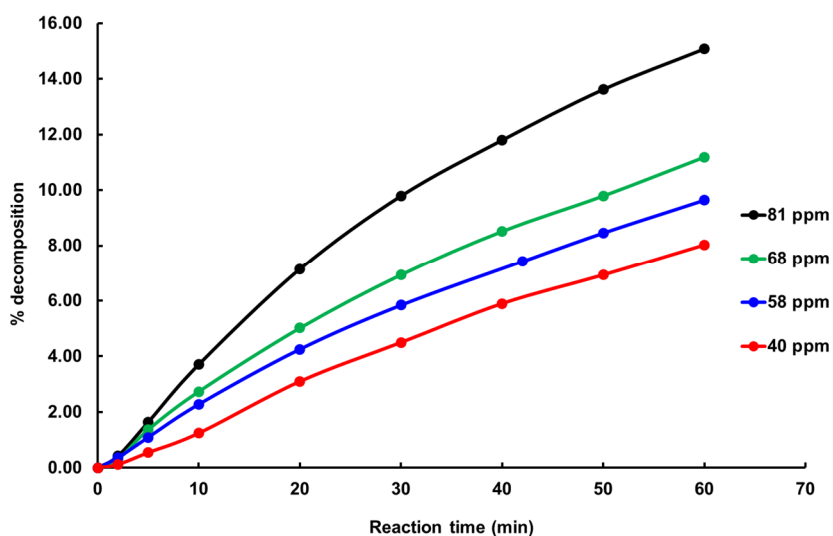


Figure 4-11: Decomposition of alkaline hydrogen peroxide in a chelant-free model system using human hair fibres as a metal source. The reaction solution contained 100 mg of hair fibres and 0.98 M hydrogen peroxide at pH 10 using 400 mM ammonia/ammonium chloride buffer solution.

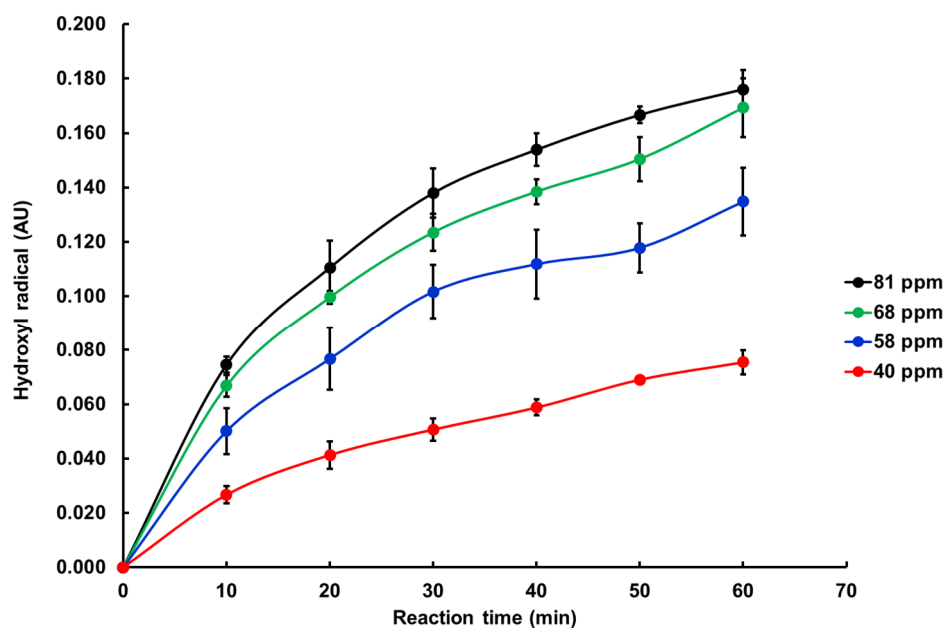


Figure 4-12: Hydroxyl radical formation in copper treated hair fibres in a chelant-free system. The reaction solution contained 50 mg hair fibres, 1.0 mM NPGA and 0.98 M hydrogen peroxide at pH 10 using 400 mM ammonia/ammonium chloride buffer solution. The reaction solution was diluted by 10 times and analysed by UV-visible spectrophotometer.

Comparison of these results with the previous data on copper–calcium binary solution systems shows that less hydroxyl radical is detected in the hair experiments as compared to the model solutions containing a similar amount of copper. This discrepancy can be explained by the low penetration of NPGA probe inside the hair fibre and hence lower efficiency of radical capture. Alternatively, copper ions adsorbed inside the hair shaft may have limited accessibility and may not leach into the bulk solution. Recent studies reports that calcium is mainly present in the outer layer of cuticles while copper is abundant in the cortex of hair fibre.<sup>24</sup> The location of metal ions may influence their diffusion into the reaction solution. As a result, the actual amount of accessible copper ions might be less than the total copper present on the hair fibre. In any case, our results suggest that the NPGA colorimetric probe can be successfully employed to monitor hydroxyl radical formation in the hair fibre.

#### **4.4.3 Decomposition of hydrogen peroxide by copper treated hair fibres in the presence of a chelant**

The same set of hair samples was analysed in the presence of EDTA, EDDS and DTPMP chelants in the reaction solution. The chelant concentration (13.95 mM) used here corresponded to an approximate amount of chelant used in a typical hair colouring formulation. The speciation plots were developed using the amount of metals determined by the ICP-OES technique (Table 4-1). The results for oxygen evolution demonstrate that chelants greatly influenced the overall decomposition of hydrogen peroxide.

EDDS chelant stabilised alkaline hydrogen peroxide and only a small amount of hydrogen peroxide was decomposed (Figure 4-13). An increase in copper concentration showed very little effect on the overall decomposition which is probably due to a relatively large concentration of chelant employed where copper is complexed with the chelant. Earlier results for calcium-copper binary system in the solution model system showed the same results where EDDS slowed down the rate of decomposition reaction. The speciation plot shows EDDS preference for copper(II) ions despite the presence of large excess of calcium and magnesium ions present in the reaction solution (Figure 10-20).

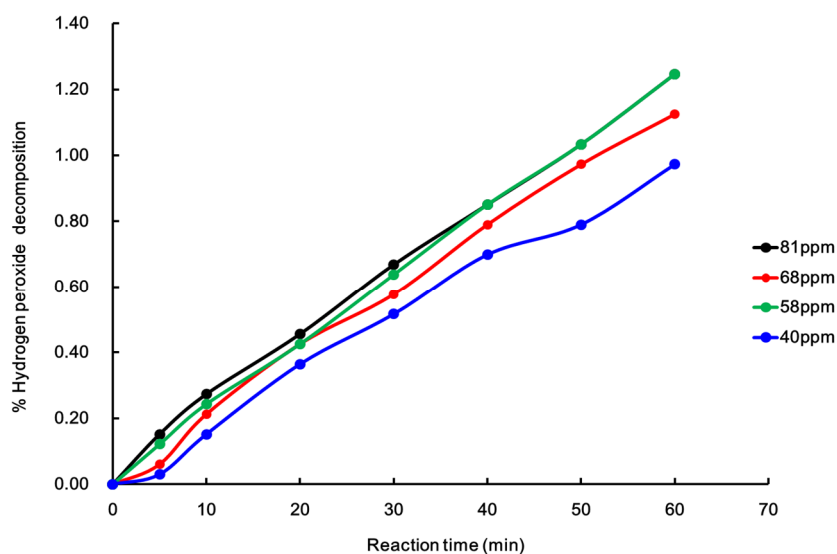


Figure 4-13: Decomposition of alkaline hydrogen peroxide by copper treated hair fibres in the presence of EDDS chelant at pH 10 using 400 mM ammonia/ammonium chloride buffer solution. The reaction solution contained 100 mg of hair fibres, 13.95 mM EDDS chelant and 0.98 M hydrogen peroxide.

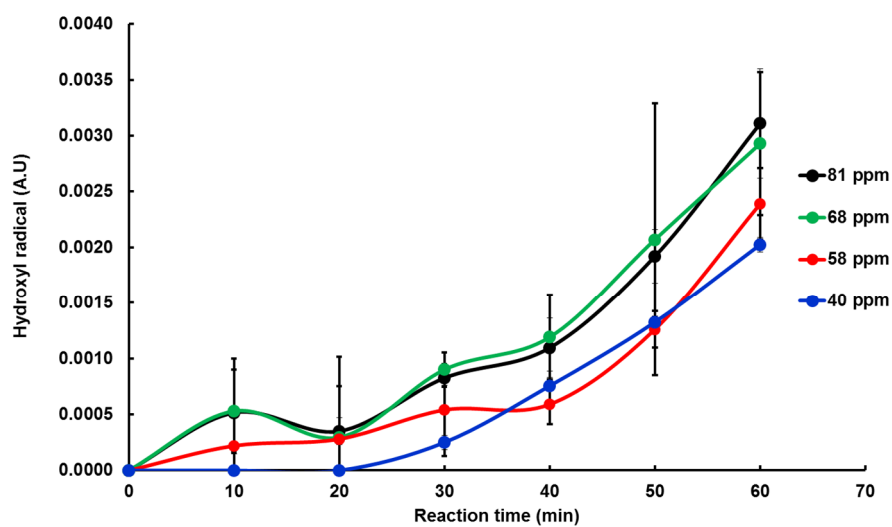


Figure 4-14: Hydroxyl radical formation by copper treated hair fibres in the presence of EDDS chelant at pH 10 using 400 mM ammonia/ammonium chloride buffer solution. Each reaction solution contained 50 mg of hair fibres, 1 mM NPGA, 13.95 mM EDDS and 0.98 M hydrogen peroxide. The reaction solution was diluted by 10 times and analysed by UV-visible spectrophotometer.

As discussed earlier, virgin non-chemically treated human hair contains small amount of copper bound to melanin and protein residues which may not be accessible to EDDS chelant and may be active in decomposition reaction. This amount of copper might be similar in all copper-treated hair samples and hence leads to almost same rate of decomposition.

A similar trend was observed for hydroxyl radical formation for the same hair samples (Figure 4-14). Absorption intensity observed was very low compared to the chelant-free system highlighting a significant decrease in hydroxyl radical formation in the presence of EDDS chelant.

Although the speciation plots suggested the presence of copper-ammonia complex in the reaction solution, EDTA chelant suppressed the decomposition reaction. The rate of hydrogen peroxide decomposition in this case was slower than that in the EDDS chelant system; however, it generated more hydroxyl radicals (Figure 4-15 &

Figure 4-16). This difference might be due to metal distribution inside hair cortex. Also, calcium in the hair is not free but is complexed with some protein residues e.g. carboxylic acid. Therefore, the speciation may depend not only on the Cu/Ca competition for EDTA but also on the competitive binding of calcium and copper to the chelating groups in the hair fibre.

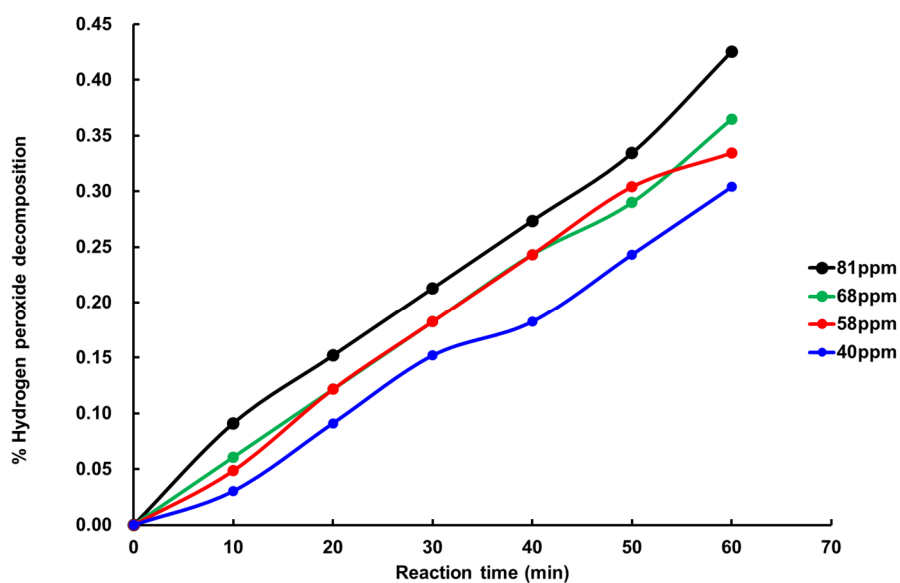


Figure 4-15: Decomposition of alkaline hydrogen peroxide by copper treated hair fibres in the presence of EDTA chelant at pH 10 using 400 mM ammonia/ammonium chloride buffer solution. Each reaction solution contained 100 mg of hair fibres, 13.95 mM EDDS and 0.98 M hydrogen peroxide.

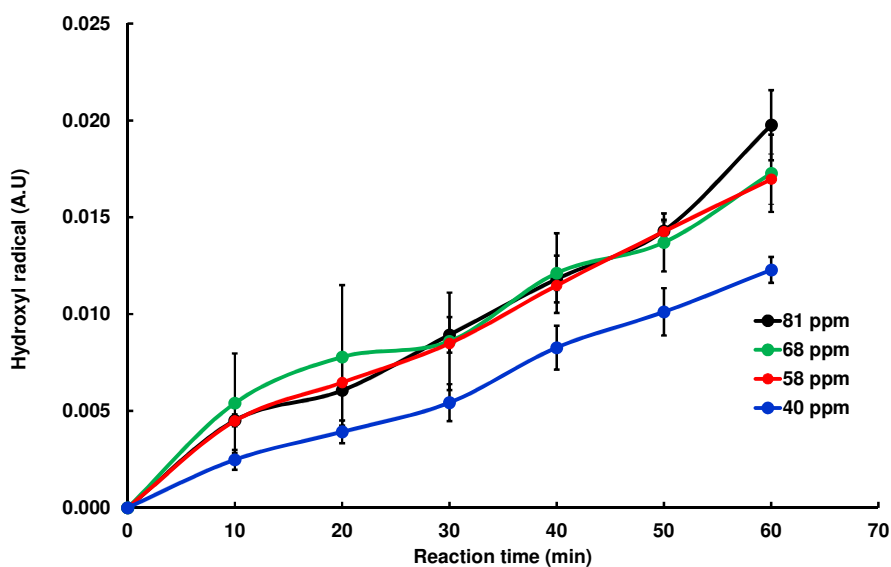


Figure 4-16: Hydroxyl radical formation in hair-EDTA system at pH 10 using 400 mM ammonia/ammonium chloride buffer solution. The reaction solution contained 50 mg of hair fibres, 1 mM NPGA probe, 13.95 mM EDTA and 0.98 M hydrogen peroxide. The reaction solution was diluted by 10 times and analysed by UV-visible spectrophotometer.

DTPMP chelant was also studied under the same experimental conditions and it also suppressed the decomposition reaction (Figure 4-17). The speciation model shows that copper-DTPMP complex is the main species present in the reaction which is consistent with the earlier solution model system (Figure 10-22).

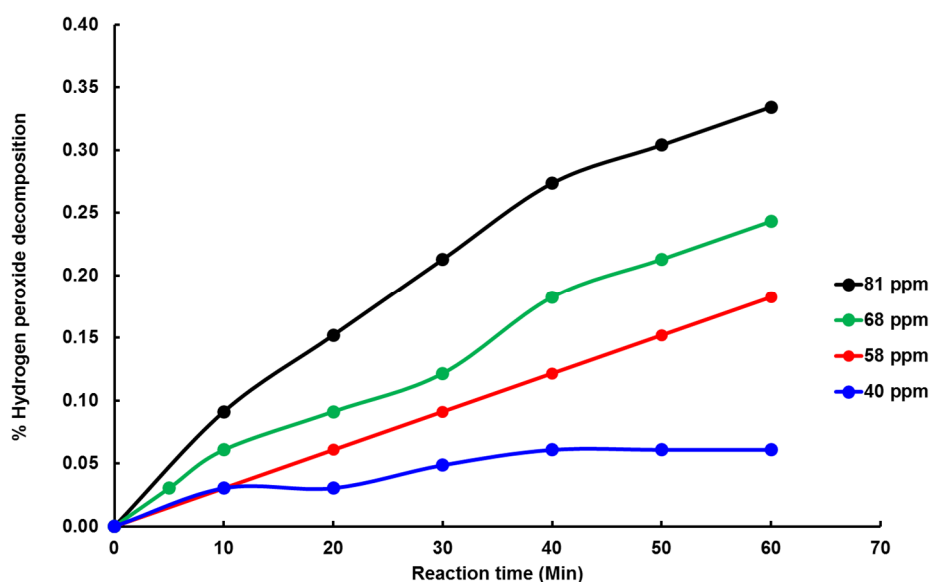


Figure 4-17: Decomposition of alkaline hydrogen peroxide by copper treated hair fibres in the presence of DTPMP chelant at pH 10 using 400 mM ammonia/ammonium chloride buffer solution. The reaction solution contained 100 mg of hair fibres, 13.95 mM DTPMP and 0.98 M hydrogen peroxide.

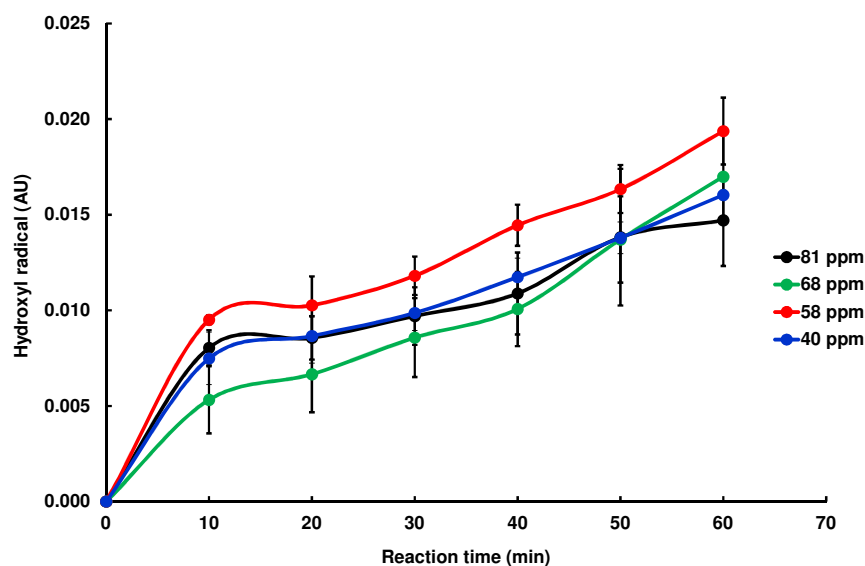


Figure 4-18: Hydroxyl radical formation in hair-DTPMP system at pH 10 using 400 mM ammonia/ammonium chloride buffer solution. The reaction solution contained 50 mg of hair fibres, 1 mM NPGA probe, 13.95 mM DTPMP and 0.98 M hydrogen peroxide. The reaction solution was diluted by 10 times and analysed by UV-visible spectrophotometer.

The above experiments demonstrate the performance of each chelant in suppressing hydrogen peroxide decomposition and free radical chemistry under the alkaline pH conditions.

Due to the complex nature of the reaction solution, the effectiveness of a chelant depends on its penetration inside hair fibre and leaching of transition metal ions into the reaction solution. Although relatively large amount of hydrogen peroxide decomposed in the presence of EDDS, this reaction mixture generated very small amount of hydroxyl radicals. This highlights its performance in suppressing free radical chemistry under the alkaline hair colouring conditions and suggests that it can be used to control free radical induced-protein damage to hair fibre.

#### 4.4.4 Effect of changing metal-chelant ratio: EDDS vs EDTA

In the above experiments, the amount of chelant was almost 10 times higher than the amount of copper present in the hair fibre. The actual metal-chelant ratio might be different due to the slow rate of diffusion across the hair. Further experiments were carried out with the same set of hair samples and different

metal-chelant ratios. The objective was to assess the EDDS and EDTA performance at low concentration. The chelant concentration was decreased from 13.95 mM to 0.94 mM concentration level.

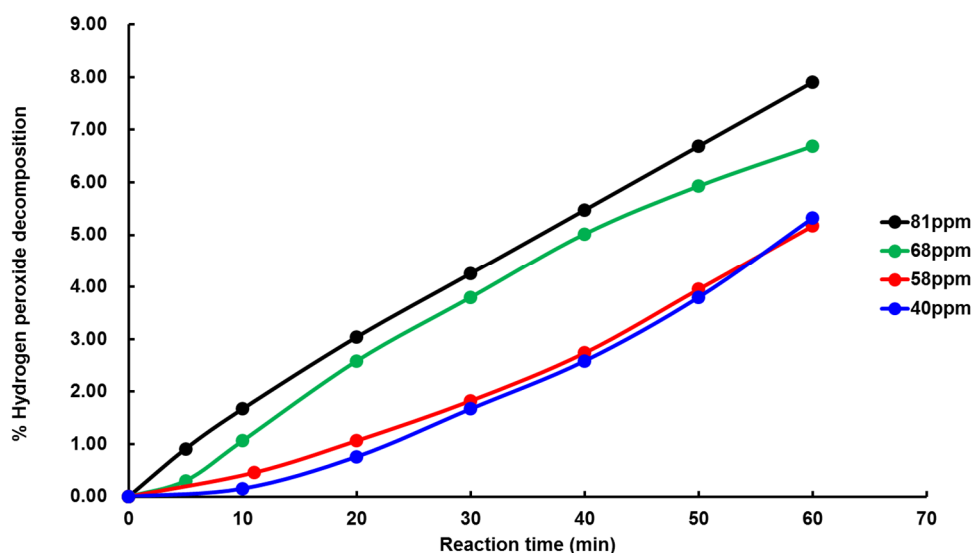


Figure 4-19: Decomposition of alkaline hydrogen peroxide by copper treated hair fibres in the presence of EDDS chelant at pH 10 using 400 mM ammonia/ammonium chloride buffer solution. The reaction solution contained 100 mg of hair fibres, 0.94 mM EDDS and 0.98 M hydrogen peroxide.

A decrease in concentration of both chelants resulted in an increase in hydrogen peroxide decomposition due to a change in metal-chelant ratio (Figure 4-19). As described earlier, hair experiments offer a complex system with copper and calcium ions bound to different functional groups in the hair. Some may be bound weakly and can leach into solution. However, other fraction of metal ions may stay complexed by the hair functionalities. The speciation of metal ions in this complex system depends on the competitive binding of different metals by the chelants and the binding sites in the hair.

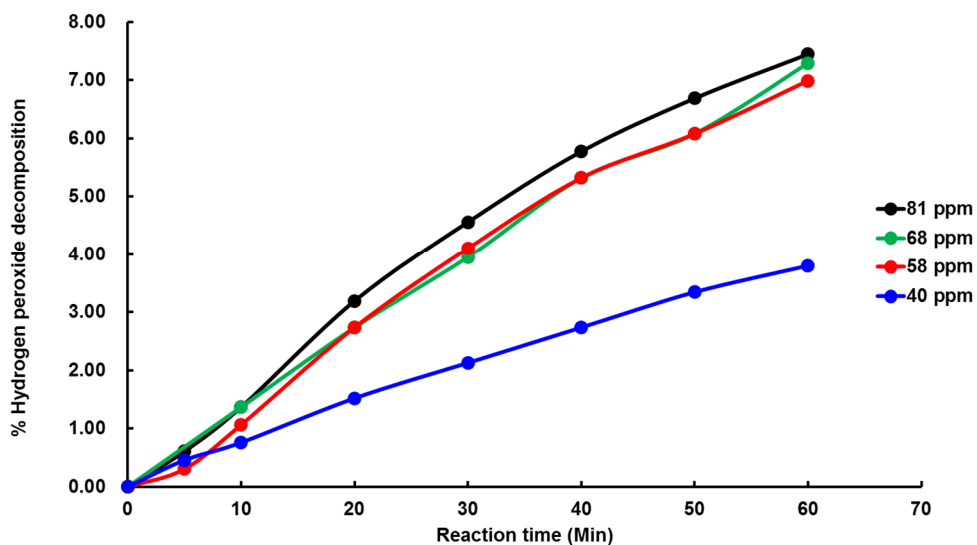


Figure 4-20: Decomposition of alkaline hydrogen peroxide by copper treated hair fibres in the presence of EDTA chelant at pH 10 using 400 mM ammonia/ammonium chloride buffer solution. The reaction solution contained 100 mg of hair fibres, 0.94 mM EDTA and 0.98 M hydrogen peroxide.

Although both EDDS and EDTA decomposed almost same amount of hydrogen peroxide, they showed a significant difference in the amount of hydroxyl radical generated in the reaction solution (Figure 4-21). At lower chelant concentration, hydroxyl radical flux in the EDTA system was still significantly higher than that observed for the EDDS reaction solution. EDDS chelant suppressed the hydroxyl radical formation. This highlights mechanistic differences involved in the two chelant systems. The Cu-EDTA complex seems to decompose hydrogen peroxide via a radical mechanism while the EDDS complex decomposes via a non-radical mechanism.

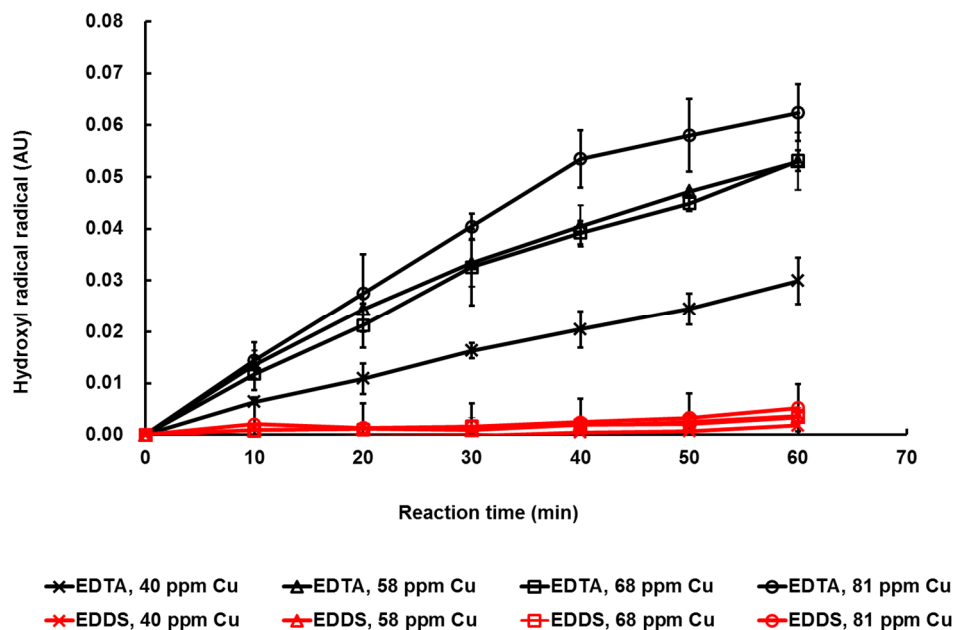


Figure 4-21: Hydroxyl radical formation by copper treated hair fibres using low concentration of EDDS ligand at pH 10 using 400 mM ammonia/ammonium chloride buffer solution.

These experiments show the advantage of EDDS chelant compared to EDTA in controlling copper induced free radical chemistry at high pH level. The speciation model showed that even at lower concentration, EDDS chelant had high selectivity for copper ions (Figure 10-23 & Figure 10-24). This is an important result suggesting that despite the presence of a large excess of alkaline earth metal ions, EDDS chelant has a strong preference for copper ions and is superior in suppressing copper catalysed free radical chemistry under the alkaline conditions.

#### 4.4.5 Selective binding of copper(II) ions by EDDS

The above experiments showed selective interaction between EDDS chelant and copper(II) ions at high pH. The selectivity can be explained by the geometry of the metal-chelant complex. Both EDTA and EDDS chelate copper ion forming an octahedral complex and the stability constants for Cu-EDDS and Cu-EDTA complexes are also similar. However, the two chelants have significantly different stability constants for calcium (Table 4-2).

Chelant	log <i>K</i>	
	Cu	Ca
EDDS	18.4	4.58
EDTA	18.78	10.65

Table 4-2: Stability constant for EDTA & EDDS chelants for calcium and copper(II) ions.<sup>132, 137</sup>

This difference in stability constant and higher affinity of EDDS for copper can be explained by molecular modelling which suggests that the selectivity is driven by the ionic radius of the central metal atom (Figure 4-22).<sup>138</sup> The calcium ion is larger (1.0 Å) than the copper(II) ion (0.73 Å).<sup>139</sup> EDTA chelates both copper(II) and calcium ions with all its carboxylate groups which fits around the central metal ions comfortably. However, EDDS is not flexible enough and does not fit around the calcium ion due to its bigger ionic radius while it fits very well around the copper ion. Therefore, the geometrical strain in the EDDS-calcium complex leads to the low stability constant. This explains the selectivity and preferential behaviour of EDDS chelant for copper(II) ions.

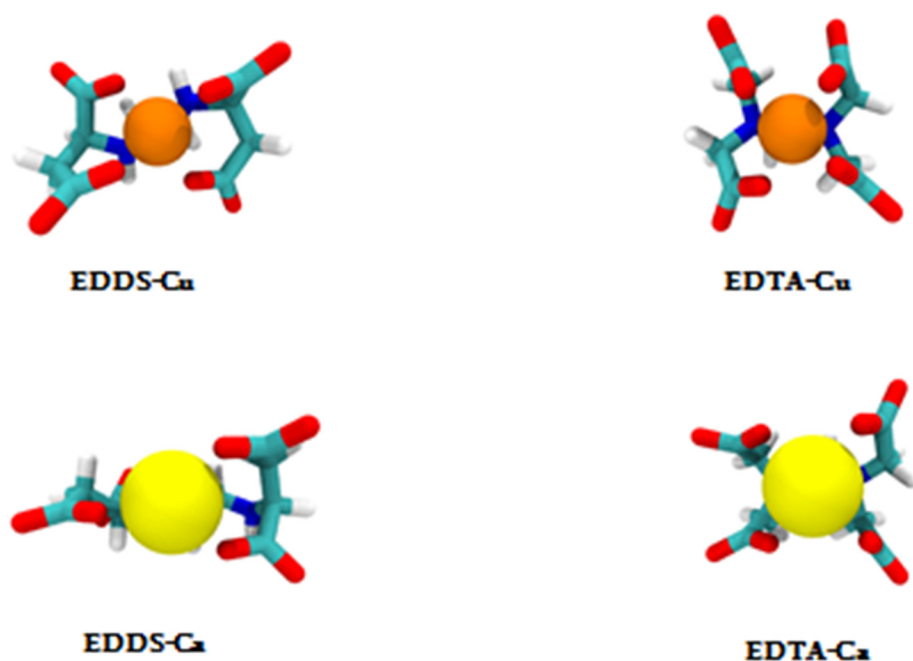


Figure 4-22: Molecular mechanics modelling for copper and calcium ions with EDTA and EDDS chelants.<sup>138</sup>

## 4.5 Conclusion

The NPGA colorimetric probe was successfully used to monitor hydroxyl radical formation in the presence of hair fibres. The transition metal ions present on hair shaft or inside hair fibre decompose alkaline hydrogen peroxide via a Fenton-like reaction generating hydroxyl radical. Among various chelants studied, EDDS showed strong preference and selectivity for copper(II) in the presence of large excess of calcium and magnesium ions both in a solution model as well as in the presence of hair fibres. This resulted in suppressing the hydroxyl radical formation suggesting that EDDS is superior compared to chelants e.g. EDTA and DTPMP. The low level of hydroxyl radical formation in the EDDS system can be exploited to minimise free radical induced protein hair damage during permanent hair colouring.

## **Chapter 5: Formation of copper(II) nanoparticles in Cu<sup>2+</sup>-HEDP system**

---

## 5 Copper(II)-HEDP system

In the first phase of current project, the catalytic activity of various metal chelant mixtures in the decomposition of alkaline hydrogen peroxide was studied (Chapters 3, 4). One of the systems studied was  $\text{Cu}^{2+}$ -etidronic acid (HEDP) in 20 mM ammonia/ammonium chloride buffer at pH 10. The  $\text{H}_2\text{O}_2$  decomposition reaction showed unusual behaviour in the  $\text{Cu}^{2+}$ -HEDP chelant system in alkaline solutions. It was found that copper-HEDP catalysed reaction exhibited self-accelerated, rapid initial hydrogen peroxide decomposition that terminated abruptly long before its completion. A similar profile was observed for the hydroxyl radical formation in this system (Figure 3-30). The HEDP chelant is often employed in stabilising hydrogen peroxide at industrial scale and has been used in oxidative hair colouring formulations to prevent its decomposition.<sup>39</sup> The unusual kinetics of the decomposition stimulated our efforts to investigate the reaction mechanism for the decomposition of alkaline hydrogen peroxide. A series of experiments were carried out to understand the change in reaction kinetics.

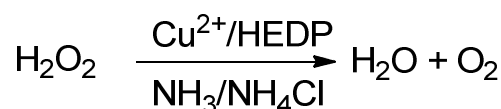
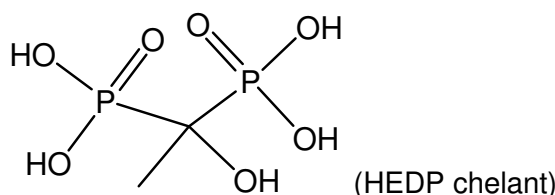


Figure 5-1: Decomposition of alkaline hydrogen peroxide in copper-etidronic acid (HEDP) system.

### 5.1 Objective

The focus of this chapter is to uncover the roots of the self-inhibiting behaviour in the autocatalytic  $\text{Cu}^{2+}$ -HEDP system at high pH. The aim is to study the nature of the decomposition mechanism. This would broaden the scope of

our understanding of the general mechanistic approach to copper based Fenton-like reactions.

## 5.2 Decomposition of alkaline hydrogen peroxide in Cu<sup>2+</sup>-HEDP system

In a typical reaction, copper(II) sulfate (0.18 mM), HEDP chelant (1.3 mM) and hydrogen peroxide (0.98 M) were mixed with 20 mM pH 10 ammonia/ammonium chloride buffer. The profile for oxygen evolution during the decomposition reaction showed a sigmoid trend typical of an auto-catalytic reaction. However, only a small amount of oxygen evolved and no further oxygen evolution was observed after 16-18 min of the reaction (Figure 5-2). A substantial quantity of hydrogen peroxide was still present at the end of decomposition, as shown by the addition of catalase which led to further peroxide decomposition and oxygen evolution. Changing the pH of the reaction solution greatly influenced the decomposition kinetics where the decomposition reaction at pH 8 & 9 did not show the high rate of decomposition and did not terminate abruptly.

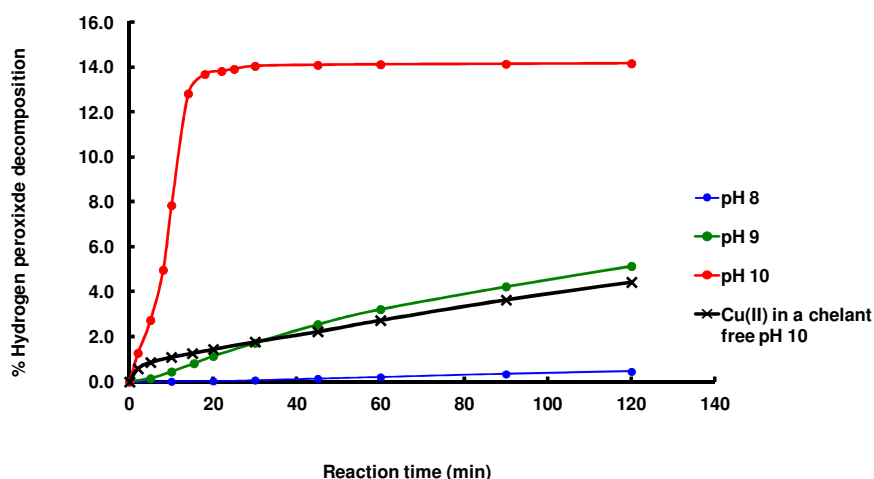


Figure 5-2: Decomposition of alkaline hydrogen peroxide in Cu(II) HEDP system. The reaction solution contained 0.18 mM copper(II) sulfate, 1.3 mM HEDP chelant and 0.98 M hydrogen peroxide in 20 mM ammonia/ammonium chloride buffer.

The copper speciation in the presence of HEDP chelant varies significantly with the changes in pH of the reaction solution (Figure 5-3). Different Cu-HEDP

complexes are present at pH 8 & 9 while copper(II) hydroxide is the main species at pH 10. This explains variation in catalytic activity of the Cu-HEDP system at different pH levels shown in Figure 5-2.

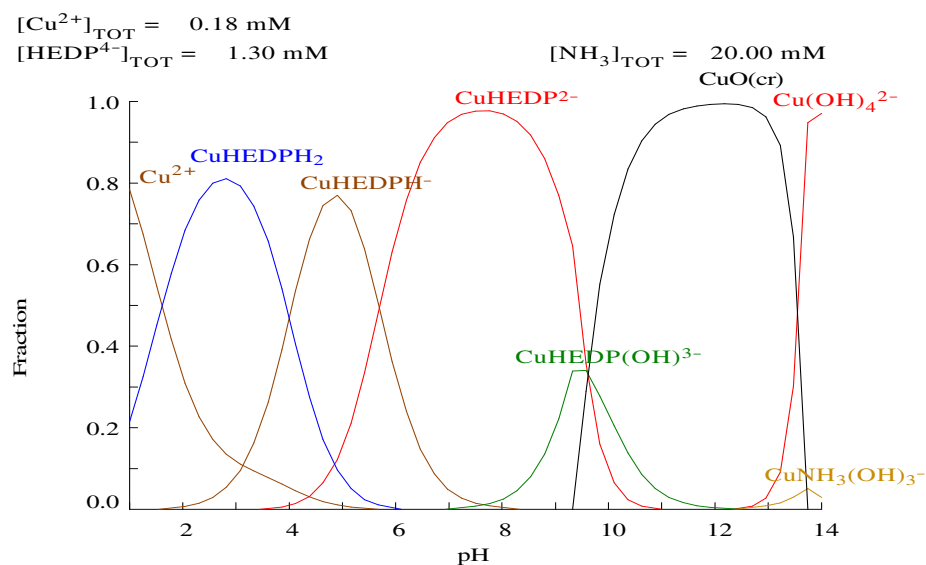


Figure 5-3: Copper(II) speciation in  $Cu^{2+}$ -HEDP system.

### 5.3 Influence of changing the reaction conditions

A series of experiments were conducted by varying the concentration of  $Cu^{2+}$  ions and HEDP chelant or changing the composition of buffer solution to examine the impact of these changes on the kinetics of the decomposition reaction.

#### 5.3.1 Attempt to restart the decomposition reaction

A reaction was carried out using  $Cu(II)$  sulfate (0.18 mM), HEDP (1.3 mM) and hydrogen peroxide (0.98 M) in 20 mM ammonia buffer solution at pH 10. The reaction followed the same kinetics and stopped after rapid initial decomposition of the hydrogen peroxide. After 30 minutes, fresh  $Cu^{2+}$  (0.18 mM) ions were added to the reaction solution. The objective was to see if this addition can restart the decomposition reaction. The result shows that adding fresh  $Cu^{2+}$  ions did not induce any further  $H_2O_2$  decomposition (Figure 5-4).

In a separate experiment, fresh HEDP (1.3 mM) was added after 45 minutes of the start of the decomposition reaction. Adding fresh chelant also did not restart the decomposition reaction (Figure 5-4).

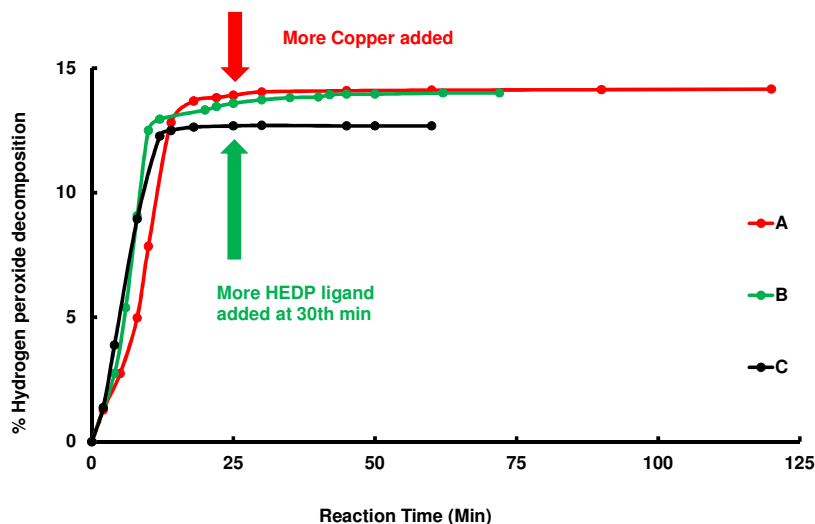


Figure 5-4: Effect of adding fresh metal ions and chelant in a stopped decomposition reaction containing 0.18 mM  $\text{Cu}^{2+}$  ions and 1.3 mM HEDP chelant. (A) Bench mark reaction (B) more 1.3 mM HEDP chelant added at the 30<sup>th</sup> minute in an ongoing decomposition reaction (C) 0.18 mM  $\text{Cu}^{2+}$  ions more added at the 30<sup>th</sup> minute.

It seems that once the decomposition stopped, the reaction intermediates undergo some irreversible changes which deactivate the freshly-added copper ions and/or inhibit the decomposition of hydrogen peroxide.

### 5.3.2 Increasing the initial concentration of the reaction components

Further experiments were carried out by increasing the initial concentration of  $\text{Cu}^{2+}$  ions while keeping the chelant concentration constant at 1.3 mM. The result (Figure 5-5) shows that increasing the initial concentration of metal ions increased the initial rate of decomposition reaction. This is consistent with our previous results where the rate of decomposition directly depends upon the initial concentration of metal ions (Section 3.6.1). However, the overall amount of hydrogen peroxide decomposed was almost same despite the increase in  $\text{Cu}^{2+}$  ions concentration.

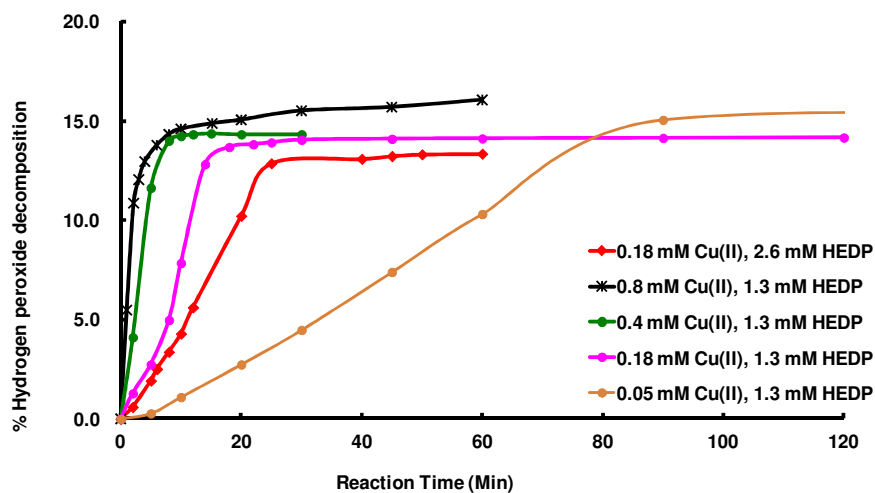


Figure 5-5: Effect of increasing copper ion concentration in Cu-HEDP catalysed decomposition of alkaline hydrogen peroxide containing different levels of copper(II) sulfate and HEDP chelant dissolved in 20 mM pH 10 ammonia/ammonium chloride buffer.

Changes in the concentration of base strongly influenced the reaction kinetics. Reaction proceeded rapidly to completion at high ammonia concentration (Figure 5-6). This matches with the earlier experiments with  $\text{Cu}^{2+}$  ions at high ammonia concentration levels (Figure 4-8). This was expected due to changes in copper speciation which suggests that high ammonia levels lead to the formation of copper-ammonia complex responsible for the rapid decomposition of hydrogen peroxide (Figure 10-14).

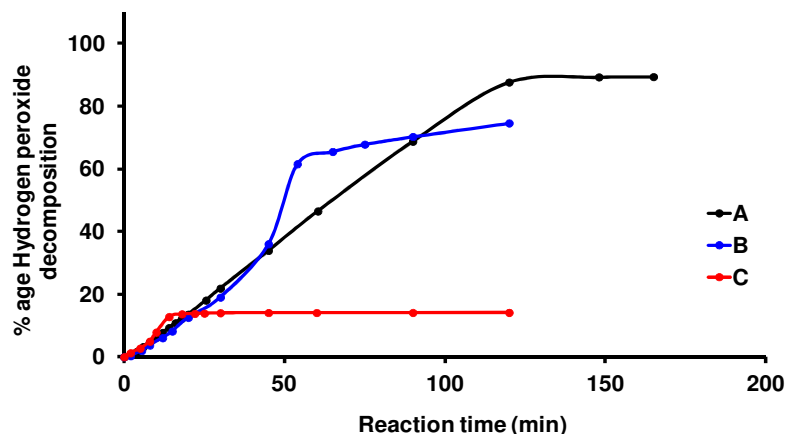


Figure 5-6: Copper-HEDP catalysed decomposition of alkaline hydrogen peroxide at different ammonia levels. Reaction solution contained 0.18 mM of copper(II) sulfate, 1.3 mM of HEDP chelant dissolved in ammonia/ammonium chloride buffer pH 10 and mixed with 0.98 M of hydrogen peroxide. Hydrogen peroxide decomposition was monitored over time. (A) 400 mM ammonia/ammonium chloride buffer (B) 100 mM ammonium/ammonium chloride buffer (C) 20 mM ammonia/ammonium chloride buffer.

The abrupt termination of the catalytic decomposition could be caused by either degradation of the catalyst, or formation of a self-poisoning species. As addition of either fresh metal ions or chelant did not restart peroxide decomposition, the catalyst degradation alone cannot be responsible for the premature reaction end, and some sort of self-inhibiting products must be formed. In order to determine the structure of these reaction products, we analysed the composition of the reaction mixture at the end of hydrogen peroxide decomposition.

#### 5.4 Analysis of the decomposition reaction: HEDP chelant degradation

The first experiment carried out was to monitor the changes in the pH of the reaction solution during hydrogen peroxide decomposition. The results (Figure 5-7) showed that pH of the reaction mixture changed from 10.0 to 9.18 upon mixing the reagents. This is consistent with the value calculated by taking into account  $pK_a$  of hydrogen peroxide and HEDP chelant. The pH of the reaction solution however continued to drop during the course of decomposition and was

only stable when the oxygen evolution stopped. Overall, the pH dropped from 9.18 to 8.92. No further pH drop was observed afterwards. This small change of pH, however, cannot account for the abrupt end of the reaction.

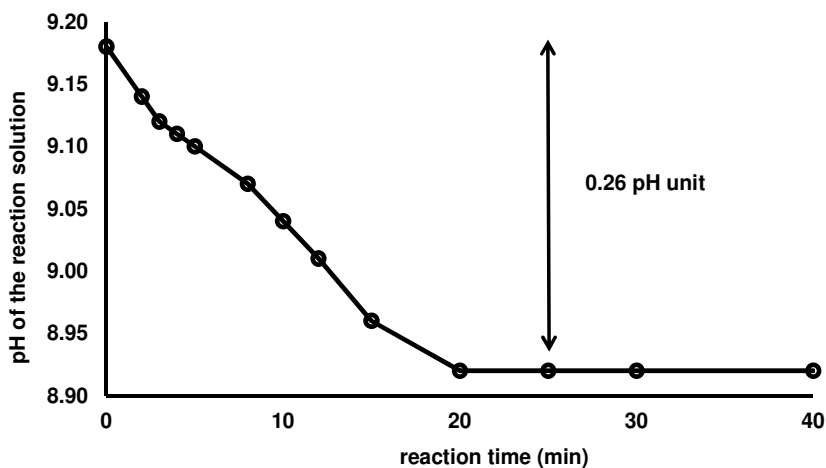


Figure 5-7: pH drop in  $\text{Cu}^{2+}$ -HEDP decomposition system. Reaction solution contained 0.18 mM  $\text{Cu}^{2+}$  ions and 1.3 mM HEDP chelant at pH 10 with 20 mM ammonia/ammonium chloride buffer. Hydrogen peroxide (0.98 M) was added to trigger the decomposition reaction. pH of the reaction solution monitored using a pH meter. The standard mean error for pH was 0.01 pH unit.

A similar experiment was carried out by adjusting the initial pH of the reaction mixture to 9.55 by adding a few drops of ammonia. The pH dropped during the decomposition reaction to 9.33 (Figure 10-25), but the reaction profile was essentially identical to that of the original reaction and decomposition of hydrogen peroxide stopped abruptly after 16-18 min.

The pH drop during the reaction is unexpected as the decomposition of slightly acidic hydrogen peroxide should lead to the increased pH. The observed pH change can be explained by oxidation of either ammonia or HEDP chelant to form acidic products. Ammonia in the strongly oxidising Fenton-like system would be expected to produce nitric acid. However, nitrate analysis by ion exchange chromatography gave negative result. Other possibility can be the oxidation of HEDP chelant to form phosphate and carbonate ions. Degradation of organic substrates in a Fenton-like reaction has been reported in literature.<sup>140, 141</sup> For instance, aminocarboxylate ligands such as EDTA and ethylenediamine-*N,N'*-

disuccinic acid (EDDS) are prone to complete degradation *via* a radical mediated mechanism.<sup>134, 142</sup> Organic phosphates and phosphonates have also been reported to undergo degradation.<sup>143, 144</sup> Here, the Cu<sup>2+</sup>-HEDP system also produced a significant level of hydroxyl radicals which may degrade HEDP chelant. Oxidation of phosphonate chelant may form phosphate and carbonate ions in the reaction solution. To confirm the chelant degradation, phosphate content in the reaction solution was monitored during the hydrogen peroxide decomposition reaction.

The molybdenum blue colorimetric method was used to measure the amount of phosphate in the reaction solution. This method has been utilised to quantify phosphate contents in water samples<sup>145-147</sup> and has been recommended by the US and European water agencies to measure phosphate.<sup>148</sup> It was employed here as an indirect approach to determine phosphate concentration in the reaction solution. The phosphate analysis of the reaction mixture showed immediate release of phosphate ions on mixing with hydrogen peroxide. This suggests an immediate start of chelant degradation. The phosphate release profile (Figure 5-8) closely mirrored that for the oxygen evolution and phosphate concentration increased over time until hydrogen peroxide decomposition stopped. To explain the pH drop quantitatively, complete ligand degradation at the end of reaction must be assumed. This is consistent with the <sup>1</sup>H and <sup>13</sup>P NMR results which showed no HEDP signals for the reaction product.

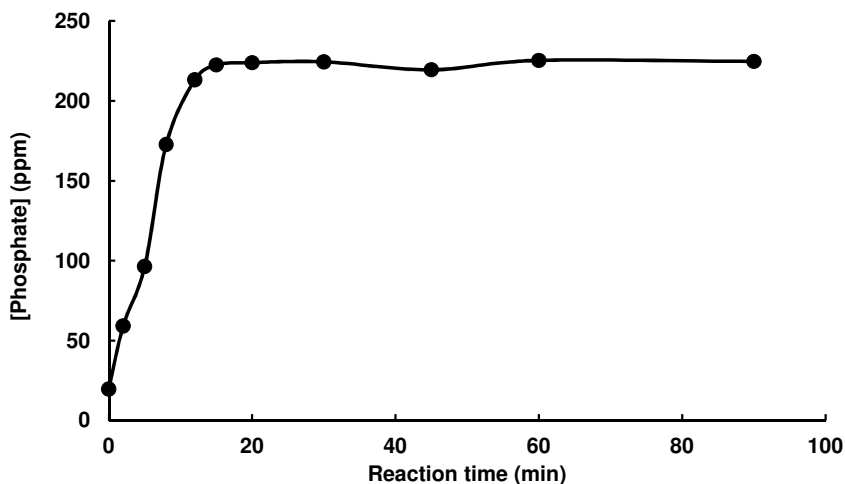


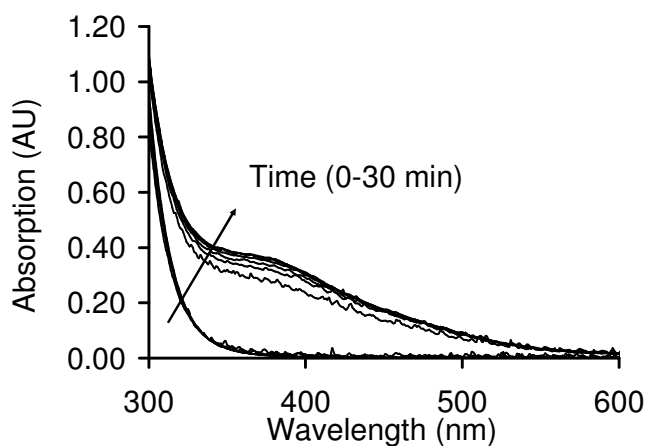
Figure 5-8: Monitoring phosphate concentration in Cu<sup>2+</sup>-HEDP system of hydrogen peroxide decomposition at pH 10 using 20 mM ammonia/ammonium chloride buffer. The decomposition reaction solution contained 0.18 mM Cu(II) sulfate, 1.3 mM HEDP chelant and 0.98 M hydrogen peroxide.

In summary so far, Cu<sup>2+</sup>-HEDP catalysed decomposition of hydrogen peroxide depends upon the pH of the reaction solution. Once stopped, the decomposition reaction could not be triggered again. Hydrogen peroxide decomposition is accompanied by HEDP degradation to give carbonate and phosphate. Complete degradation of HEDP coincides with the abrupt end of the peroxide decomposition.

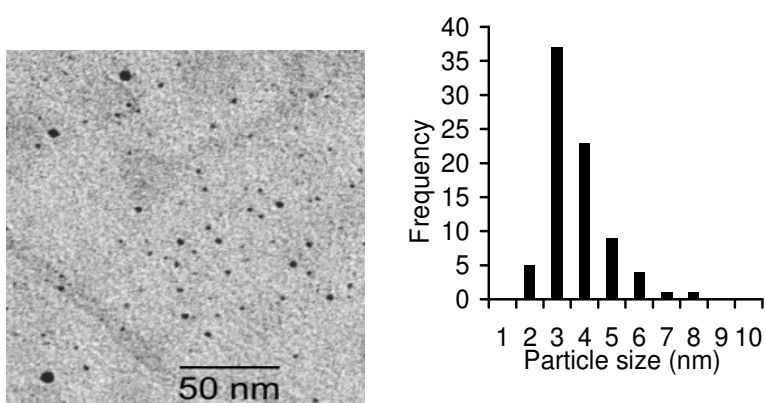
## 5.5 Formation of copper based nanoparticles

Interestingly, the reaction solution became brown coloured at the end of the reaction. The UV-Vis analysis of the reaction mixture at the end of decomposition revealed a broad featureless spectrum (Figure 5-9 A). This absorption is typical of inorganic nanoparticles. For instance, ligand-protected copper(II) oxide nanoparticles show similar UV spectra and hence similar colour.<sup>149, 150</sup> TEM images confirmed the formation of small nanoparticles with average diameter 3.0±1.0 nm (Figure 5-9 B). The nanoparticles were purified by dialysis against water. Interestingly, the nanoparticles showed remarkable stability as no aggregation was observed upon storage in solution for 4 weeks at room temperature. The experiments using a higher concentration level of ammonia did

not show any brown coloured solution or the absorption band in the UV-visible analyses suggesting that no such nanoparticles are formed in those systems.



A



B

Figure 5-9: (A) UV-Vis spectra of  $\text{Cu}^{2+}$ -HEDP reaction solution recorded over time showing absorption band for copper nanoparticles. Reaction solution contained 0.18 mM copper(II) sulfate, 1.3 mM HEDP and 0.98 M hydrogen peroxide (B) TEM image and size distribution of copper nanoparticles in Cu-HEDP reaction mixture.

### 5.5.1 Chemical composition of nanoparticles

To establish the chemical composition of nanoparticles, they were isolated, purified by dialysis and characterized. Their elemental composition was determined by combustion analysis and ICP-OES techniques.

The elemental composition of nanoparticles showed the presence of carbon (1.53%) along with hydrogen (1.25%). ICP-OES results gave copper (53.5%) and phosphorus (5.35%) content (Table 5-1). The C/H ratio is inconsistent with HEDP chelant. The  $^1\text{H}$  and  $^{31}\text{P}$  NMR spectra of acid-degraded nanoparticles also did not show any signals of HEDP chelant (Figure 10-26). As we observed formation of inorganic phosphate in the reaction mixture at the end of decomposition, we propose that the presence of C and P can be due to carbonate and phosphate ions.

<i>Element</i>	<i>%W/W</i>
Carbon	1.535
Hydrogen	1.25
Nitrogen	-
Copper	53.5
Phosphorus	5.35

Table 5-1: Elemental composition of purified nanoparticles isolated from  $\text{Cu}^{2+}$ -HEDP decomposition reaction.

To confirm the presence of phosphate in nanoparticles, a molybdenum blue colorimetric method was employed. The results for the acid-degraded nanoparticles indeed confirmed the presence of phosphate at significant level ( $13 \pm 1$ ) % which agrees with the amount of phosphorus found in ICP-OES results.

The amount of carbonate present in nanoparticles was determined using a quantitative IR method. Nanoparticles were mixed with phosphoric acid and the gas evolved was collected and the amount of  $\text{CO}_2$  was determined. A series of control experiments using pre-dried sodium carbonate were carried out to optimise experimental conditions. The IR spectrum of gas evolved on dissolving these nanoparticles in a strong acid confirmed the presence of carbon dioxide gas (Figure 5-10). A quantitative analysis gave ( $7.7 \pm 0.2$ ) % of carbonate content in the nanoparticles which matches with the amount of carbon found in the elemental analysis.

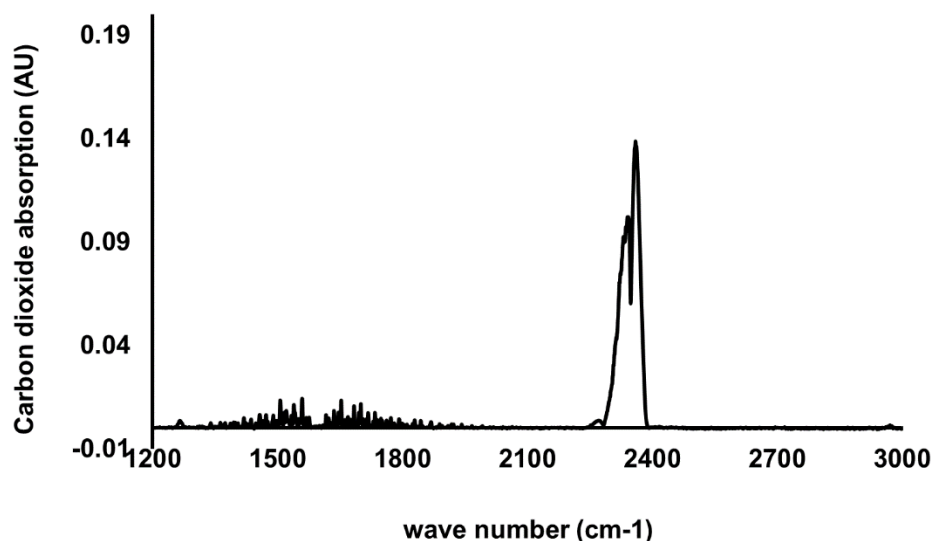


Figure 5-10: FT-IR spectrum of carbon dioxide from isolated nanoparticles.

The data from elemental analysis, ICP-OES, phosphate and carbonate analysis were modelled together to obtain the composition of nanoparticles. The results suggest that the nanoparticles are a mixture of basic copper phosphate and carbonate. The nanoparticles also contained ca. 6% of strongly adsorbed water that cannot be removed by keeping the nanoparticles under vacuum (Table 5-2).

<i>Compound</i>	<i>W/W %</i>
$\text{Cu}_2(\text{OH})_2\text{CO}_3$	34
$\text{Cu}_3(\text{OH})_3\text{PO}_4$	60
$\text{H}_2\text{O}$	6.0

Table 5-2: Chemical composition of Cu(II) nanoparticles isolated from  $\text{Cu}^{2+}$ -HEDP catalysed decomposition of alkaline hydrogen peroxide.

### 5.5.2 Oxidation state of copper in the nanoparticles

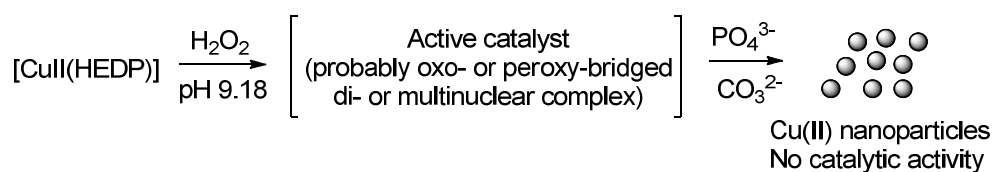
The oxidation state of copper in the nanoparticles can conceivably be 0, +1, +2 or +3. Formation of copper metal in the strongly oxidising medium is highly unlikely, and is inconsistent with the results of elemental analysis. In order to confirm the oxidation state of copper in the nanoparticles, they were dissolved in

concentrated hydrochloric acid under inert atmosphere. UV-Vis spectra of the resultant solution showed quantitative formation of Cu(II) chloride ( $\text{CuCl}_4^{2-}$ ). As UV spectra clearly differentiate Cu(I) and Cu(II) chlorides (Figure 10-27), this experiment makes it possible to rule out Cu(I) as the nanoparticle constituent. Formation of Cu(III) species in Fenton-like reaction would be a tantalising possibility, and some Cu(III) compounds have UV-Vis spectra similar to that recorded for the nanoparticles.<sup>151</sup> However, most Cu(III) compounds are very unstable<sup>152</sup> and while Cu(III) could be an intermediate in the reaction, it is highly unlikely to form very stable nanoparticles as the reaction product. In addition, Cu(III) nanoparticles are inconsistent with the elemental analysis. All these arguments are consistent with the nanoparticle composition given in Table 5-2.

Formation of basic copper(II) phosphate/carbonate is in reasonable agreement with the copper speciation plots calculated for the experimental conditions (Figure 10-28) and literature binding constants.<sup>153</sup> The accuracy of the data for copper phosphate is uncertain, and in any case the binding constants will be strongly affected by the nanoscopic size of the particles. Nonetheless, speciation plots clearly suggest formation of basic copper phosphate under reaction conditions.

Variation of reaction conditions also leads to results consistent with the speciation plots. Adding phosphate and carbonate to an ongoing hydrogen peroxide decomposition reaction mixture does not change the overall reaction profile (Figure 10-30). Carrying out the reaction in a 20 mM phosphate buffer slows the reaction down but also does not change the decomposition profile (Figure 10-31).

On the basis of the above observations, we can explain the course of the reaction (Scheme 5-1). The reaction involves formation of a highly reactive intermediate, probably an HEDP-containing oxo- or peroxy bridged copper complex. Formation of di, tri- and multinuclear copper-oxo bridged species has been proposed and observed previously.<sup>85, 154, 155</sup> In particular, several multinuclear copper-HEDP complexes have been reported in the literature<sup>100, 156</sup> These layered materials, prepared by a hydrothermal method, have phosphate and oxo bridges as revealed from the XRD data.



Scheme 5-1: Proposed pathway for the formation of copper nanoparticles in Cu(II)-HEDP catalysed decomposition of alkaline hydrogen peroxide.

Formation of an active complex in our system explains the sigmoid profile of the reaction kinetics. The reactive intermediates lead not only to hydrogen peroxide decomposition, but also HEDP degradation. Monomeric and dimeric copper oxygen complexes have been reported to possess high catalytic activity for oxidizing organic molecules with hydrogen peroxide.<sup>157-162</sup> Once all HEDP ligand has been degraded, the HEDP-free copper intermediates act as seeds to nucleate formation of basic copper phosphate/carbonate nanoparticles which have no catalytic activity. Nanoparticle formation is irreversible; hence addition of more HEDP chelant at the end of reaction does not result in further decomposition of hydrogen peroxide. In order to test the proposed pathway, additional experiments were carried out.

## 5.6 Role of hydrogen peroxide

Upon inspection of speciation plots (Figure 10-28 & Figure 10-29), one should notice that Cu(II) oxide is the predominant species formed under reaction conditions. Copper(II)-based nanoparticles would therefore be expected to form even in the absence of hydrogen peroxide. However no nanoparticle formation was observed in the absence of hydrogen peroxide under these conditions, even in the presence of HEDP and/or phosphate/carbonate ions. The formation of copper(II) oxide is presumably limited by kinetic factors. We therefore hypothesise that the role of hydrogen peroxide in the nanoparticle formation is to generate an active catalyst, probably an oxo- or peroxy-bridged complex which upon oxidation of the stabilising chelant (HEDP) acts as a seed for the nanoparticle formation thus overcoming the kinetic barrier to nucleation. This unusual role of hydrogen peroxide in nanoparticle nucleation is consistent with the proposed mechanism and experimental observations.

By carefully varying the reaction conditions, we were able to form copper phosphate/carbonate nanoparticles in the absence of hydrogen peroxide with the properties nearly identical to those of the nanoparticles formed in peroxide decomposition reaction (Table 10-1); however this required much higher temperature and long reaction time (Figure 5-11). Nonetheless, this experiment further supports the proposed composition of the nanoparticles.

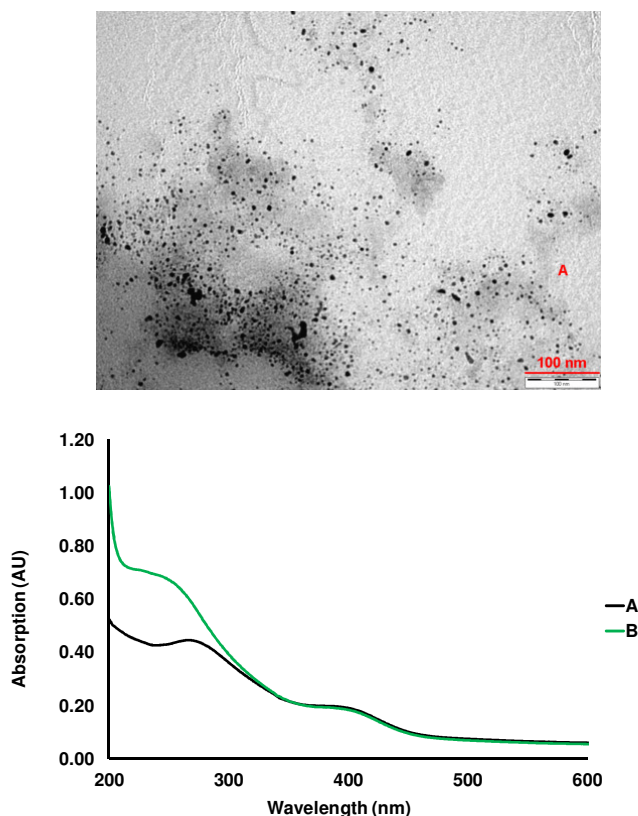


Figure 5-11: TEM image and UV-Vis spectra of fabricated nanoparticles without using hydrogen peroxide (A) 12.5  $\mu\text{mol}$  of copper(II) sulfate with 50  $\mu\text{mol}$  of  $(\text{NH}_4)_2\text{CO}_3$  in 25 mL of 20 mM phosphate buffer pH 10. (B) Fabricated nanoparticles after 10 days kept at lab bench.

## 5.7 Self-inhibiting behaviour of Cu(II) nanoparticles

As the copper phosphate/carbonate nanoparticles are the main product of the reaction, they must possess self-inhibiting properties observed in the overall process of hydrogen peroxide decomposition. This can be understood if we assume that nanoparticle surface provides seeds for further nanoparticle growth upon addition of extra Cu(II) at the end of reaction. Any added Cu(II) ions get

immediately adsorbed on the nanoparticle surface. Therefore, no reactive intermediates are formed and the hydrogen peroxide decomposition is not observed.

In order to test this hypothesis, we carried out a series of control experiments. Variable amounts of fresh Cu(II) sulfate were added to the nanoparticle solution at the end of hydrogen peroxide decomposition and the reaction mixtures were examined using UV-Vis spectroscopy. Instant and almost linear increase in the absorption was consistent with the nanoparticle growth (Figure 5-12). The nanoparticle solution remained stable and no precipitation was observed until Cu(II) concentration reached 0.8 mM, at which point a brown precipitate was found. Thus, the experimentally observed inability of freshly added Cu(II) to restart the hydrogen peroxide decomposition can be attributed to the rapid adsorption of Cu(II) on the nanoparticle surface leading to the growth of catalytically inactive particles and thus self-poisoning.

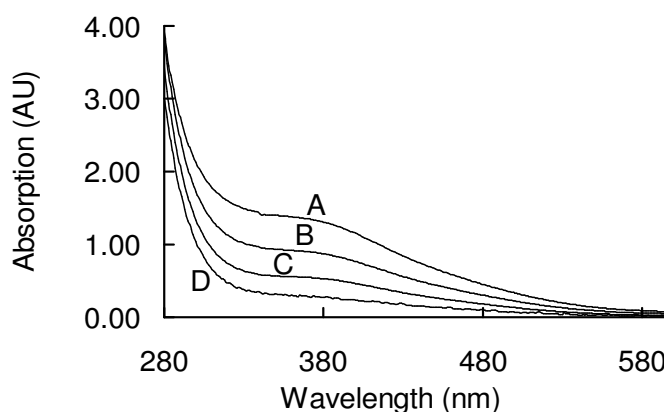


Figure 5-12: Fresh addition of Cu(II) sulfate to the nanoparticle solution in pH 10 ammonia/ammonium chloride buffer leads to an increased UV-Vis absorption. A reaction was carried out using 0.18 mM copper(II) sulfate, 1.3 mM HEDP chelant and 0.98 M hydrogen peroxide in 25 mL of buffer solution. Amount of  $\text{Cu}^{2+}$  added was 0.18 mM which gives total  $\text{Cu}^{2+}$  present in the solution as: (A) 0.72 mM; (B) 0.54 mM; (C) 0.36 mM; (D) 0.18 mM.

The observed effect of changing the metal to ligand ratio on the kinetic profile of the decomposition reaction (Figure 5-5) can now be explained in terms of the proposed reaction pathway. Increased Cu(II) concentration leads to a faster hydrogen peroxide decomposition (presumably due to the higher concentration of the active catalyst) and also to a faster nanoparticle formation (due to faster nucleation/growth). Increased concentration of HEDP stabilizes the initial

complex and hence slows down the formation of the active catalyst and decreases the rate of hydrogen peroxide decomposition.

## 5.8 Defeating the self-inhibiting effect

In the proposed reaction mechanism, the nanoparticle nucleation only occurs after complete degradation of HEDP which presumably is involved in the structure of the active catalyst. This conclusion makes it possible to rationally design reaction conditions that would not exhibit self-poisoning effect. Continuous addition of HEDP chelant to an ongoing hydrogen peroxide decomposition reaction should prevent the active catalyst from nucleating the nanoparticles. In a control experiment, we added HEDP in three batches at different reaction times before the nanoparticle formation was observed. As HEDP decomposition gives acidic products and hence leads to pH drop, we re-adjusted the pH with NaOH half way through the reaction to maintain the reaction conditions unchanged. This simple procedure indeed prevented the nanoparticle formation and induced continuous decomposition of hydrogen peroxide with no sign of self-inhibition (Figure 5-13). This experiment strongly suggests that the trigger for nanoparticle nucleation is complete oxidation of HEDP which is consistent with the proposed mechanism.

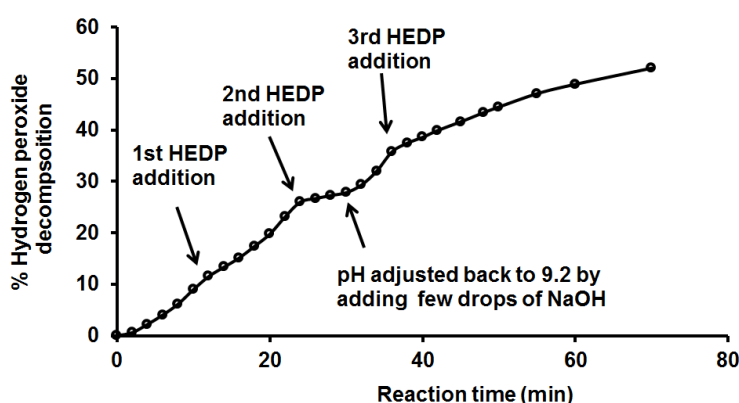


Figure 5-13: Adding fresh HEDP chelant to an ongoing  $\text{Cu}^{2+}$ -HEDP catalysed hydrogen peroxide decomposition reaction just before it stops. Pre-neutralised HEDP ( $32.5 \mu\text{mol}$  each time in  $25 \text{ ml}$  reaction solution) ligand was added at different time intervals. pH of the reaction solution was maintained by adding a few drops of  $2 \text{ M}$  sodium hydroxide.

## 5.9 The nature of the active catalyst

The proposed reaction mechanism involves formation of a highly active copper based catalyst. A series of experiments were carried out to define the exact nature of the catalysts. Unfortunately, our attempts were unsuccessful. EPR spectra of reaction solutions crash-frozen at different time intervals showed complex pattern due to the presence of several Cu(II) species (consistent with the speciation predictions) but neither the lineshape nor the intensity changed up until the end of hydrogen peroxide decomposition, at which point EPR signal abruptly disappeared which is consistent with the nanoparticle formation (Figure 5-14). Mass spectroscopic (ESI) investigation also did not show any new Cu(II) complexes.

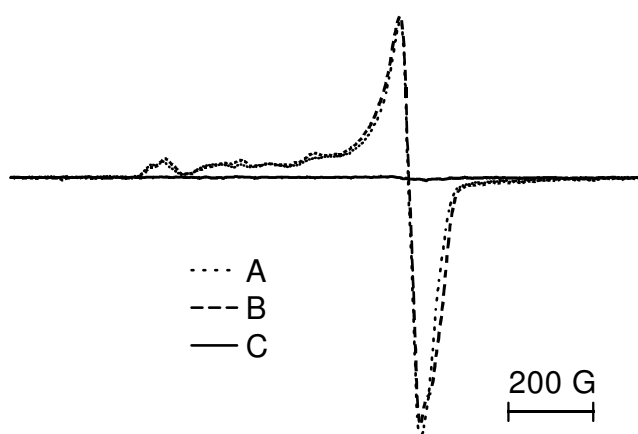


Figure 5-14: EPR spectra of copper-HEDP reaction solution. Reaction solution contained  $\text{Cu}^{2+}$  (0.18 mM), HEDP (1.3 mM) in 20 mM pH 10 ammonia/ammonium chloride buffer with hydrogen peroxide (0.98 M), total reaction volume 25 mL. Aliquots (1.6 mL) were mixed with glycerol (0.4 mL) in a quartz EPR tube, and spectra were recorded at 120 K at the following times after the start of the reaction: (A) 2 min; (B) 8 min; (C) 15 min.

UV-Vis spectra analysis at low concentration of copper and chelant showed some small changes in the line-shape consistent with the changes in the copper speciation during the course of hydrogen peroxide decomposition (Figure 5-15). Taken together, these data suggest that the concentration of the active catalyst is very low throughout the reaction, and complete degradation of HEDP ligand triggers very fast nucleation and growth of the nanoparticles.

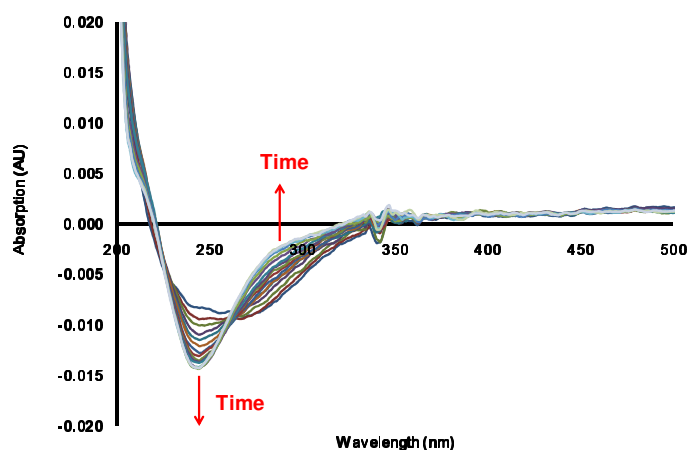


Figure 5-15: UV-Vis spectra of Cu-HEDP reaction with hydrogen peroxide. Reaction solution contained 0.05 mM copper(II) sulfate, 0.05 mM HEDP ligand in 20 mM pH 10 ammonia/ammonium chloride buffer pH 10. Hydrogen peroxide 0.1 mM was added and spectra were recorded immediately against reagent blank. Reaction was carried out in UV-vis cell. Spectra obtained every 2 minutes over 120 minutes show changes in the reaction solution.

Despite the failure to characterise the active catalyst, it is clear that the HEDP chelant is essential for its generation. No nanoparticle formation was observed when the reactions were repeated in the presence of other ligands [EDTA, EDDS, DTPMP, DTPA], phosphate ion, and in the absence of any chelant. One can hypothesise that strongly coordinating hexa- and octadentate chelants do not favour formation of bridged copper dimers/oligomers which are likely to be the active species in the hydrogen peroxide decomposition reaction.

The reaction in a chelant-free system in an ammonia buffer showed immediate nanoparticle formation upon addition of hydrogen peroxide as evidenced by the UV spectra; however these materials were unstable and quickly precipitated from solution (Figure 5-16). Carrying out the reaction in a ligand-free 20 mM phosphate buffer also resulted in the immediate formation of somewhat more stable nanoparticles which showed very little catalytic activity (Figure 5-16). The presence of phosphate thus seems critical for the formation of stable nanoparticles.

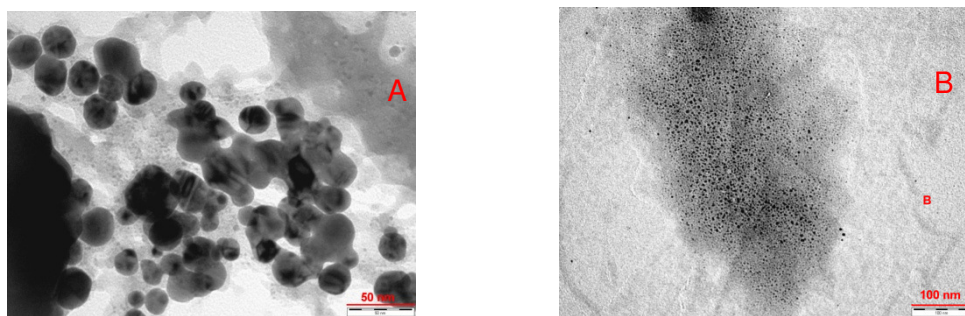


Figure 5-16: (A) Formation of nanoparticles in a chelant-free system. The reaction solution contained 0.18 mM copper(II) sulfate dissolved in 20 mM ammonia/ammonium chloride buffer pH 10 with 0.98 M hydrogen peroxide. TEM images showed large aggregates of nanoparticles. (B) Formation of copper based nanoparticles in Cu(II) chelant-free system in a 20 mM phosphate buffer pH 10 solution. TEM image of the reaction solution shows the presence of nanoparticles.

## 5.10 Conclusion

The  $\text{Cu}^{2+}$ -HEDP system decomposes hydrogen peroxide at alkaline pH rapidly, however, the reaction stops abruptly. The decomposition of hydrogen peroxide proceeds via formation of an active catalyst that degrades the chelant and eventually seeds formation of catalytically-inactive basic copper phosphate/carbonate nanoparticles. The nanoparticles prevent any further catalytic reaction as freshly added  $\text{Cu}^{2+}$  ions quickly adsorb on their surface and do not form active catalyst.

This is a rather unusual scenario for the Fenton-like chemistry; however it is perhaps not so uncommon in other areas. For instance, many Pd-catalysed cross-coupling reactions proceed via formation of an active catalyst. There is evidence that at least in some cases multinuclear clusters possess high catalytic activity. At the end of the reaction, the active catalyst nucleates formation of bigger particles which eventually precipitate to form Pd black which is usually catalytically inactive. The lability of the active catalyst in this type of reaction is essential for the high catalytic activity; yet it facilitates eventual nucleation to form inactive larger particles. We believe Cu-HEDP catalyzed degradation of hydrogen peroxide follows the same principles.

## **Chapter 6: Hydrogen peroxide decomposition in the presence of oxidative dye precursors**

---

## 6 Permanent hair colouring

Hair dyeing is chemical processing of human hair fibres to provide complete cover-up of the grey fibres with a variety of shades for an adequate long-lasting effect. It's history dates back to early Roman era when people started using various vegetable, mineral and animal derived substances to change their hair colour.<sup>15, 163</sup> Modern hair colouration is mainly divided into two groups, oxidative and non-oxidative hair colouring. This classification is based on the type of colourant used, their chemistry and their affinity for the hair fibre.<sup>164, 165</sup>

Non-oxidative coloration is further divided into two groups, temporary and semi-permanent colorants. Temporary colorants offer instant colour shades and do not involve any chemical processing. They are popular among youth to colour their hair for a particular event and then wash off with a single shampoo application. Semi-permanent colorants also do not involve any chemical processing. The product usually contains nitro-aromatic molecules sometimes mixed with inorganic pigments under neutral or slightly alkaline pH conditions. They last for 5-6 shampoo washings and thus require a reapplication. A characteristic point of semi-permanent coloration is zero or minimum hair damage to hair fibre as it does not involve any harsh chemical processing.<sup>164, 166, 167</sup>

Oxidative colouring is also divided into three groups, permanent, demi-permanent and auto-oxidation dyeing. In demi-permanent dyeing, melanin is bleached to a lesser extent. This product utilises a small amount of monoethanolamine as an alkaliser to get a pH level of 7-8. As demi-permanent dyeing does not involve high level of melanin bleaching and it may offer superior hair quality. However, it gives very few colour shades and exhibits poor colour retention. Auto-oxidation colouring is popular among male consumers and develops colour with time using atmospheric oxygen. Few examples are reported in the literature using 1,2,4-trihydroxybenzene molecules.<sup>164, 168</sup>

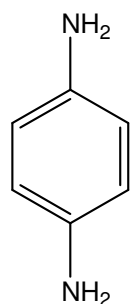
Permanent dyeing accounts for the major share of hair colour market. It is popular among consumers due to its superior grey hair coverage, wide range of colour shades available and better wash and light fastness properties offering a long lasting colour. Permanent dyeing involves a diffusion controlled process where active ingredients penetrate the hair first and then react to form a new

chromophore inside hair fibre. Dyeing application comprises two components, a colour gel or cream and an oxidising developer lotion. Colour cream contains dye precursors which are organic aromatic molecules formulated at high alkaline pH of 9-10. Ammonia is the common choice of an alkaliser. Developer lotion contains an oxidising agent such as hydrogen peroxide stabilised at acidic pH. Two components are mixed together just before the application. High ammonia content in the colouring cream ensures alkaline pH (9.0 – 10.0) of the final mixture which activates hydrogen peroxide to oxidise dye precursors. Beside oxidation of dye precursors, hydrogen peroxide bleaches naturally occurring melanin pigment inside hair fibre and its decomposition products are subsequently removed during rinse off.

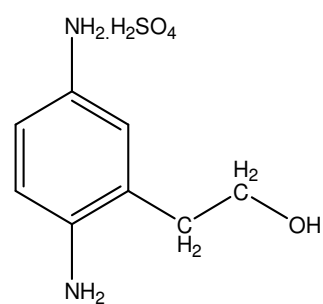
A range of dye precursors is available which are utilised to develop various colour shades.<sup>169</sup> They are aromatic molecules generally classified as primaries and couplers in hair colour industry. Primary precursors are aromatic diamines or aminophenols with amino (-NH<sub>2</sub>) or hydroxy (-OH) group in the *ortho* or *para* positions of the aromatic ring. These groups and their positions on benzene ring are important in determining the reactivity and rate of reaction for these molecules. The nature of these groups may also influence the colour shade development.<sup>164, 170, 171</sup> The couplers are also aromatic diamines or amino phenols with a similar structure though with substitution at the *meta* position. They don't develop significant colour themselves, however, when mixed with primary precursors, they develop intense colour shades. Hydrogen peroxide oxidises the primary to a highly electrophilic intermediate which then couples with the coupler. Some examples of primaries and couplers are presented below (Figure 6-1 &

Figure 6-2).

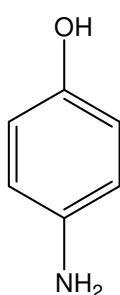
### Primary molecules



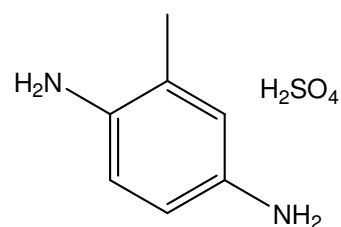
*p*-phenylenediamine (PPD)



Hydroxyethyl-*p*-phenylenediamine sulfate



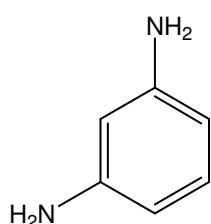
4-aminophenol (PAP)



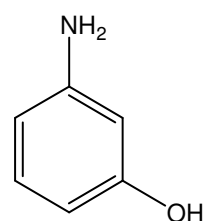
2,5-toluenediamine sulfate (DTS)

Figure 6-1: Some examples of primary dye precursors.

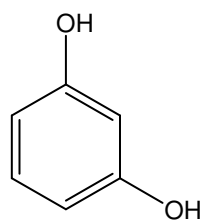
### Couplers



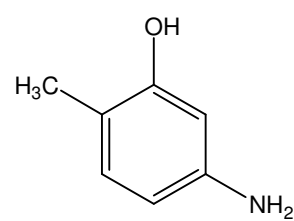
*m*-phenylenediamine



*m*-aminophenol (MAP)



1,3-dihydroxybenzene



4-amino-2-hydroxytoluene (AHT)

Figure 6-2: Some examples of coupler dye precursors.

## 6.1 Objective

Previous chapters have described the role of transition metal ions in decomposing alkaline hydrogen peroxide in the presence of various chelants. The chelants influence the metal activity by changing metal speciation. In oxidative dyeing where aromatic dye precursors are also present, these metal ions may influence colour development. Published literature reported this as “green hair problem” associated with copper deposits on the hair fibre.<sup>172</sup> However, the potential involvement of these transition metal ions in the oxidative permanent colouring of hair has not been explored before.

This chapter investigates the role of added aromatic dye precursors in a copper catalysed decomposition of alkaline hydrogen peroxide. The dye precursors themselves or their oxidation products may alter catalytic activity of copper ions in decomposing hydrogen peroxide and generating hydroxyl radicals. This may lead to a new dimension in controlling free radical chemistry in oxidative hair colouring and minimising hair damage. Hydrogen peroxide decomposition was monitored using gasometric assembly while a modified approach was adapted to monitor formation of hydroxyl radicals using NPGA colorimetric probe.

## 6.2 Basic mechanism of permanent hair colouring

Small molecules of dye precursors can diffuse into the hair fibre. Alkaline media with ammonia facilitates their diffusion by opening cuticle pores of the hair fibre. Primaries are oxidised inside the hair to give reactive intermediates which then react with the couplers. This reaction yields a new chromophore imparting a new colour shade to the fibre. The new chromophore is bigger in size than the starting precursors and thus cannot diffuse out of the fibre easily (Figure 6-3). The desired colour shade is achieved by mixing 5-10 dye precursors in a suitable delivery system e.g. emulsion or gel.

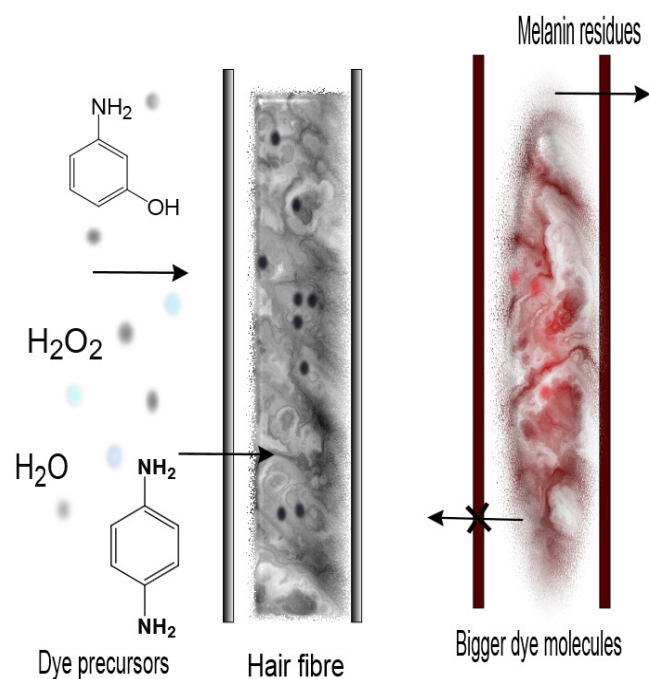


Figure 6-3: Schematic presentation of oxidative hair colouring demonstrating penetration of dye precursors and melanin bleaching.

### 6.2.1 Oxidative coupling: coupling of *p*-phenylenediamine (PPD) and *m*-aminophenol (MAP)

The mechanism of oxidative hair dyeing has been reviewed previously.<sup>173-175</sup> The first step is the oxidation of primary to give a reactive intermediate. A common primary employed is *p*-phenylenediamine. Under alkaline conditions in the presence of hydrogen peroxide, *p*-phenylenediamine is oxidised to give quinone diimine (QDI<sup>+</sup>) (Figure 6-4). This electrophilic intermediate reacts with the coupler such as *m*-aminophenol at its most nucleophilic carbon position to give binuclear leuco dye which in turn is further oxidised to form indophenol. In some cases, depending upon the primary used, this binuclear dye reacts with another QDI<sup>+</sup> molecule to give a trinuclear dye. In case of *p*-phenylenediamine (PPD) and *m*-aminophenol (MAP), chain polymerisation continues and forms polynuclear dark reddish brown colorant (Figure 6-5).

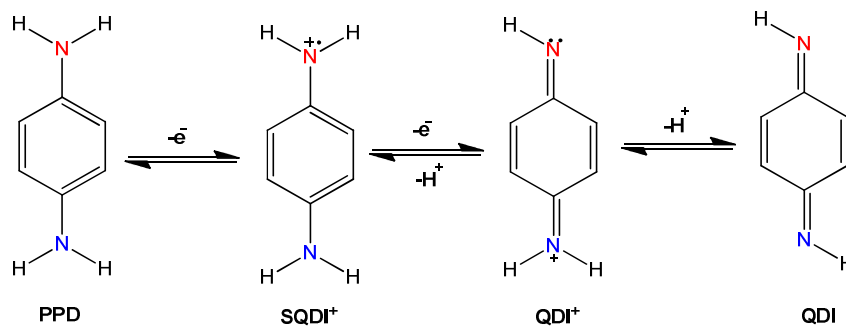


Figure 6-4: Oxidation of *p*-phenylenediamine primary.

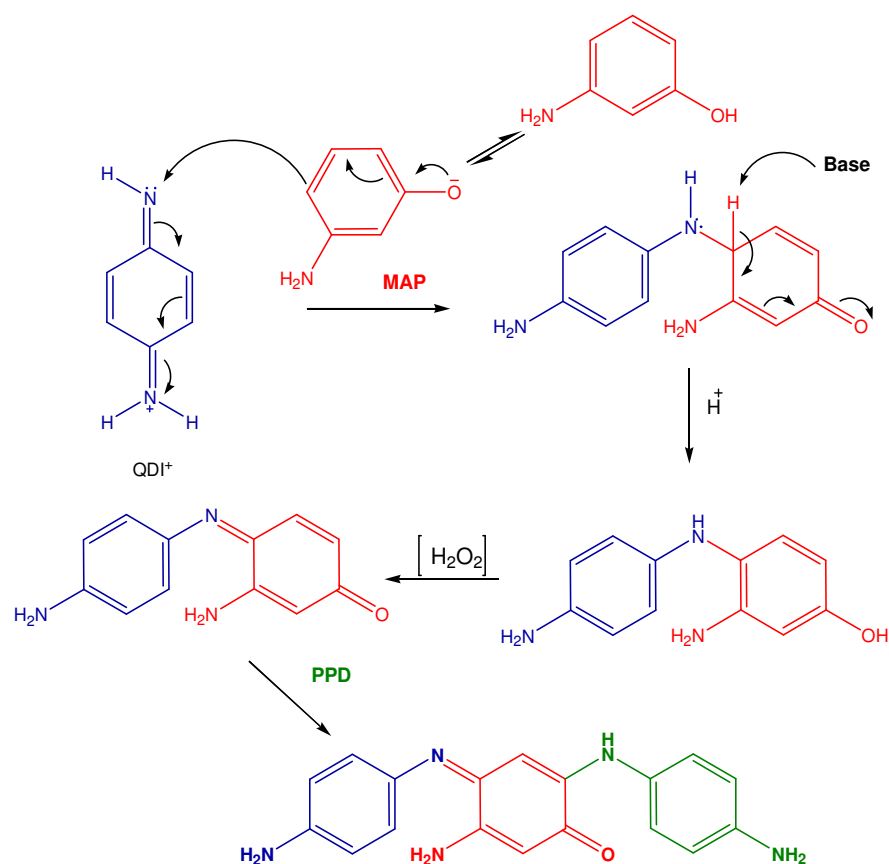


Figure 6-5: Possible mechanism of oxidative coupling of *p*-phenylenediamine and *m*-aminophenol.

These binuclear and trinuclear (trimer) molecules are formed inside the hair fibre and are trapped there because of their large size ensuring that the dye colour achieved is permanent and cannot be washed out easily.

### 6.3 Decomposition of alkaline hydrogen peroxide in a copper-dye precursor system

In order to study the role of these organic dye precursors in a Fenton-like reaction, a series of experiments were carried out by adding dye precursors in the hydrogen peroxide decomposition solution under alkaline pH conditions using ammonia/ammonium chloride buffer. A first set of experiments was carried out by employing a single aromatic molecule system such as phenol. Similarly, other dye primaries and couplers were also examined under similar experimental conditions.

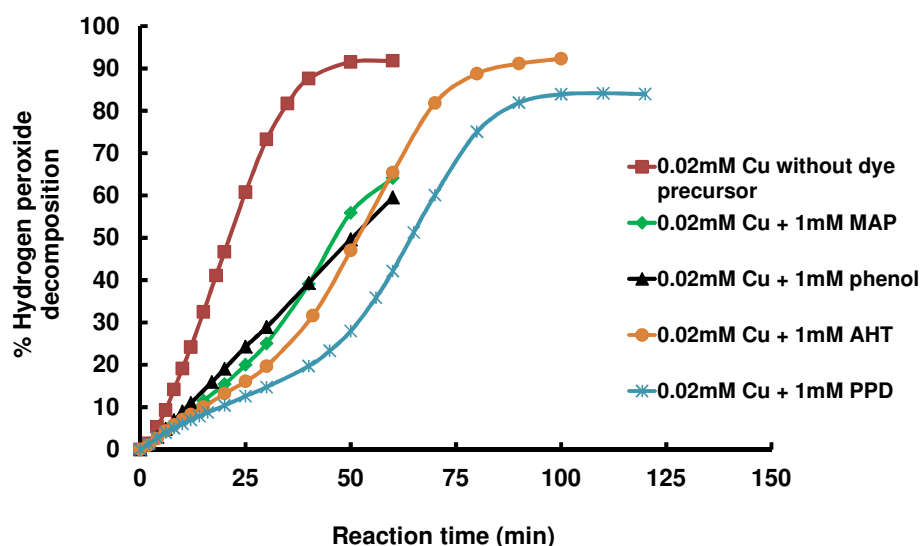


Figure 6-6: Decomposition of alkaline hydrogen peroxide in the presence of copper(II) sulfate and dye precursors at pH 10 using 400 mM ammonia/ammonium chloride buffer. Reaction solution contained 0.02 mM copper(II) sulfate with 1 mM dye precursor each and 0.98 M hydrogen peroxide.

Control experiment containing copper(II) ions without added dye precursors decomposed hydrogen peroxide rapidly. However, the addition of dye precursors suppressed the decomposition of alkaline hydrogen peroxide significantly (Figure 6-6). Even simple phenol had influence over decomposition kinetics. PPD addition demonstrated a higher effect suppressing hydrogen peroxide decomposition. The reaction solution turned coloured on introducing hydrogen

peroxide. PPD is a commonly employed primary in hair colouring that undergoes oxidation producing coloured intermediate species which subsequently undergoes self-coupling reaction to generate multi-nuclear dark black coloured material (Figure 6-7). Different dye precursors exhibited different activity in the decomposition reaction which could be due to their different rates of oxidation.

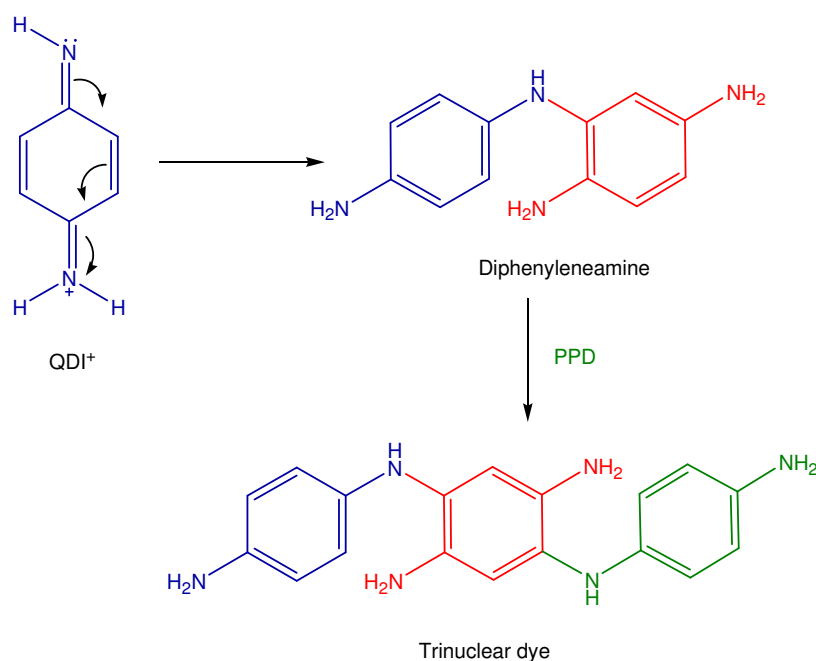


Figure 6-7: Oxidative self-coupling of *p*-phenylenediamine.

Further experiments were carried out by adding *meta*-substituted coupler along with a primary in an equal molar ratio in the reaction solution. MAP coupler was mixed with copper(II) sulfate and PPD in an alkaline buffer solution (pH 10). The results reveal that in-situ coupling of PPD and MAP has pronounced impact in suppressing decomposition of alkaline hydrogen peroxide (Figure 6-8). Even at relatively higher level of copper(II) ions (0.18 mM) in 400 mM ammonia/ammonium chloride buffer where copper(II) ions in a dye-free system decomposed alkaline hydrogen peroxide rapidly, PPD-MAP system slowed down the decomposition reaction. Also, this PPD-MAP system exhibited greater suppression compared to single PPD self-coupling system (Figure 6-6) which suggests that different couplers may lead to different kinetics in the decomposition reaction.

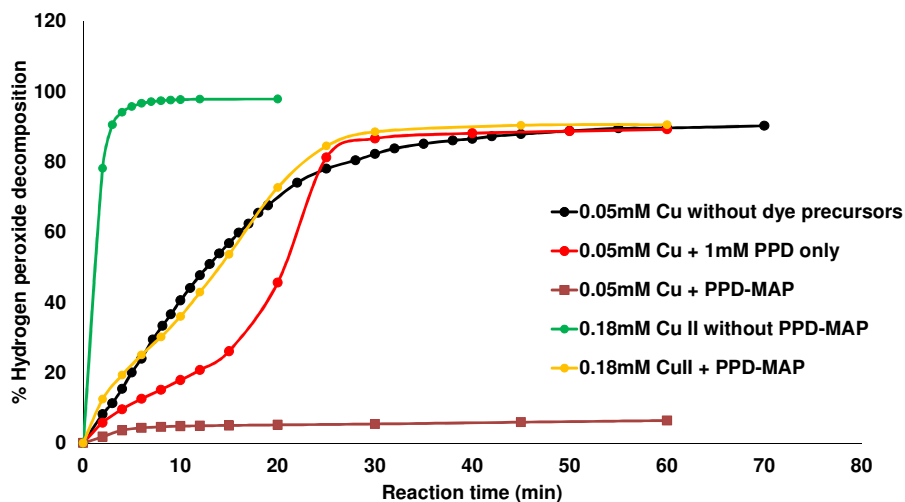


Figure 6-8: Copper catalysed decomposition of alkaline hydrogen peroxide in the presence of PPD primary and MAP coupler at pH 10 using 400 mM ammonia buffer with different concentration levels of copper(II) ions. Reaction solution contained 1 mM of each dye precursor and 0.98 M hydrogen peroxide.

The above experiments show that the presence of aromatic dye precursors suppressed the decomposition of alkaline hydrogen peroxide. Addition of a *meta*-substituted coupler e.g. MAP alongside PPD has a very profound influence on the decomposition reaction. In a copper-PPD reaction solution, addition of a coupler and hydrogen peroxide immediately forms a coloured solution. Interestingly, most of the systems exhibited a self-accelerating behaviour in hydrogen peroxide decomposition when the colour of the reaction solution had faded.

Phenols and nitrophenols demonstrate anti-oxidant activity by capturing free radical species and disrupting free radical chain mechanism. Here, Fenton-like reaction in the presence of dye precursors may also form hydroxyl radicals. It is possible that these dye precursors and their oxidation products interfere and break free radical chain mechanism of Fenton reaction which hence influences the overall hydrogen peroxide decomposition.

An alternative explanation would consider chelation of copper ions by dye precursors which were used as starting materials. Oxidation of these dye precursors forms multinuclear larger molecules which may also chelate copper

ions. This metal-dye complexation might be responsible for the suppression of hydrogen peroxide decomposition.

These hypotheses required further experimentation to define the mechanism of the dye induced suppression of hydrogen peroxide decomposition. It was important to identify the species responsible for suppressing the catalytic activity of copper(II) ions in decomposing alkaline hydrogen peroxide. We have therefore carried out experiments quantifying hydroxyl radical formation using NPGA probe while different metal-dye systems were examined to study metal-dye interaction.

## **6.4 Monitoring hydroxyl radical formation in oxidative colouring**

Earlier studies with added aminocarboxylate or phosphonate chelants altered copper activity in hydrogen peroxide decomposition and hydroxyl radical formation. Some systems e.g. Fe(III)-EDTA (pH 8.0) and Cu(II)-HEDP (pH 10.0) rapidly decomposed hydrogen peroxide and produced hydroxyl radicals while others e.g. Cu(II)-EDDS suppressed the decomposition reaction and formation of radical species. So, different metal chelant systems behave differently under different experimental conditions. We reasoned that the same might be true for the copper-dye precursor systems. Hence, it was important to monitor hydroxyl radical formation in the presence of these dye precursors.

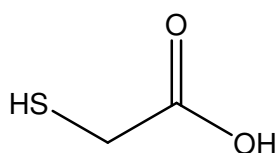
In the previous chapters, NPGA colorimetric probe was employed to monitor hydroxyl radical formation in a metal or metal-chelant system under various reaction conditions. For those experiments, monitoring hydroxylated NPGA (H-NPGA) in-situ was relatively easy as no other coloured species was present in the system. However, copper-dye precursor system generates deeply coloured solution immediately on adding hydrogen peroxide. These intensely coloured species may interfere in quantitative H-NPGA analysis. Therefore a slightly modified experimental set-up was adapted here while using the same NPGA probe to monitor hydroxyl radical formation. The experimental design was to remove or decolourise dark coloured dye species and selectively monitor H-NPGA using UV-visible spectrophotometer. Oxidative hair dyes can be reduced using a reducing agent such as ascorbic acid. H-NPGA is a nitrophenolate and

is stable to mild reducing agents whereas indo dyes can be reduced easily. Interestingly, some products are available in the market to remove colour stains from the consumer skin following an oxidative colour application.<sup>39</sup> Such formulations usually employ ascorbic acid, sodium sulfite or thioglycolic acid.

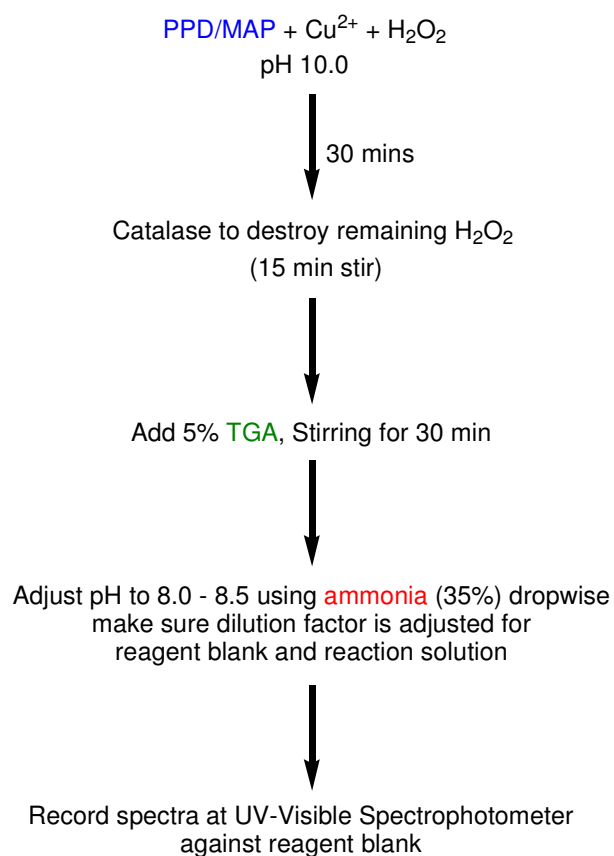
In early experiments, reducing agents such as sodium sulfite, ascorbic acid and sodium dithionite were tested to reduce dye; however, they were not able to decolourise deeply coloured solution completely. Sodium borohydride was also used, however, its poor stability in aqueous solution was a concern and gas evolution was strongly interfering with UV-visible analysis.

#### 6.4.1 Reducing oxidative dyes using thioglycolic acid

Adding thioglycolic acid immediately decolourised the deeply coloured dye solution. Reaction solution contained copper(II) sulfate, NPGA probe, dye precursors and hydrogen peroxide in ammonia/ammonium chloride buffer solution (400 mM, pH 10). The experiment was conducted following a stepwise scheme (Scheme 6-1). Addition of thioglycolic acid (TGA, 5%, 0.7 M) ( $pK_a$  3.76) caused a pH change which was dropped to acidic (pH 3.50). To analyse H-NPGA, pH was adjusted back to alkaline using ammonia solution to make sure the nitrophenolate is completely deprotonated.



Thioglycolic acid (TGA),  $pK_a=3.76$



Scheme 6-1: Stepwise schematic methodology to reduce PPD-MAP oxidative dye using thioglycolic acid under alkaline oxidative permanent colouring conditions.

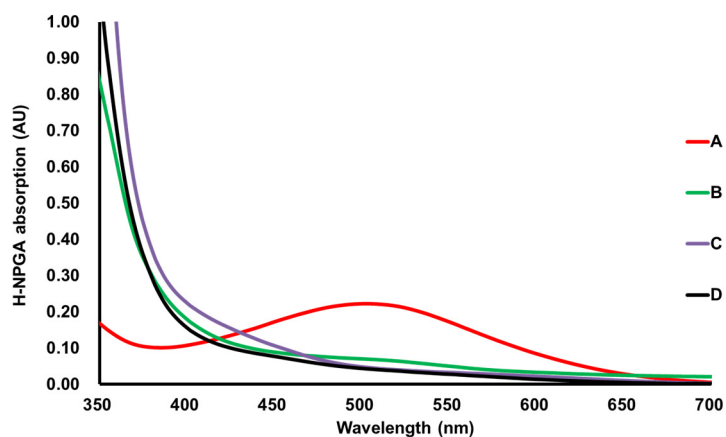


Figure 6-9: Reducing PPD-MAP dye using TGA reduction method. Reaction solution contained 0.02 mM copper(II) sulfate, 1 mM PPD and 1 mM MAP mixed in 400 mM ammonia buffer. 0.98 M hydrogen peroxide was added to start the reaction. TGA (5%, 0.7 M) was added to reduce dye precursors and pH was adjusted back again using a few drops of ammonia. (A) PPD-MAP dye solution spectrum after 15 times dilution before adding TGA, (B) On adding TGA without any dilution, (C) pH adjusted back to alkaline 8.0, (D) After stirring for 60 minutes at alkaline pH.

The results (Figure 6-9) show that the TGA method effectively reduced PPD-MAP dye. Adjusting pH back to alkaline did not lead to the coloured solution demonstrating the irreversible reduction and efficacy of TGA as a reducing agent under experimental conditions

An important concern was the stability of NPGA colorimetric probe under the reducing conditions. To examine its stability, a control experiment was carried out in the absence of dye precursors with added NPGA following TGA reduction method (Scheme 6-1). The spectra below (Figure 6-10) demonstrate that on adding TGA there is an immediate change in absorption spectrum of the reaction solution for H-NPGA. This change in electronic spectrum was pH dependent and subsequent addition of ammonia reproduced the H-NPGA spectrum which was stable for over the period of at least 90 minutes. As observed from UV-visible data, the addition of thioglycolic acid under the experimental conditions did not reduce H-NPGA derivative and the probe was stable suggesting that H-NPGA can be analysed selectively using the TGA reduction method.

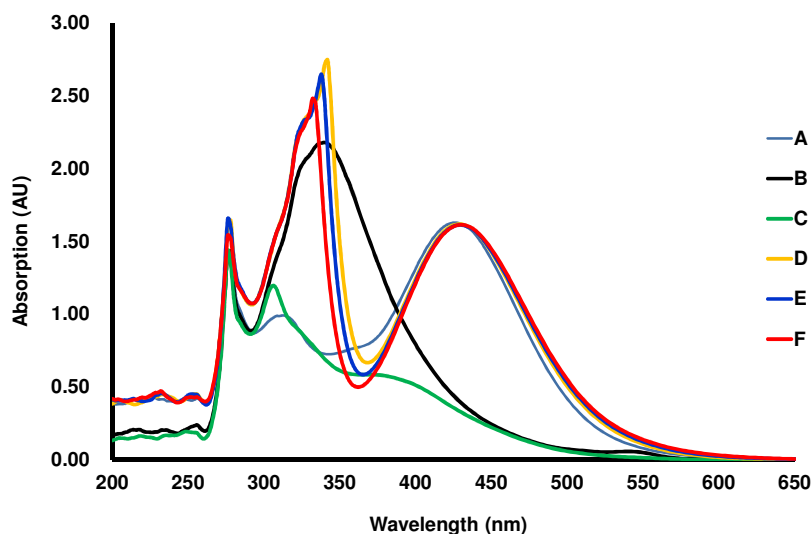


Figure 6-10: Examining the stability of NPGA and its hydroxylated derivative in-situ using TGA reduction method. The reaction solution contained 0.18 mM Cu(II) sulfate, 1 mM NPGA with 0.98 M hydrogen peroxide in 400 mM ammonia/ammonium chloride buffer. (A) Hydroxylated derivative H-NPGA, (B) H-NPGA spectrum immediately after adding TGA at acidic pH, (C) H-NPGA spectrum after stirring with TGA for 30 min at acidic pH, (D) H-NPGA spectrum after adjusting pH back to alkaline, (E) 30 minutes under alkaline pH conditions, (F) 90 minutes under alkaline pH conditions.

#### 6.4.2 Hydroxyl radical formation in copper- PPD/MAP system

Following the method described in the previous section, hydroxyl radical formation was monitored in a PPD-MAP reaction mixture at different copper concentration levels (Scheme 6-1).

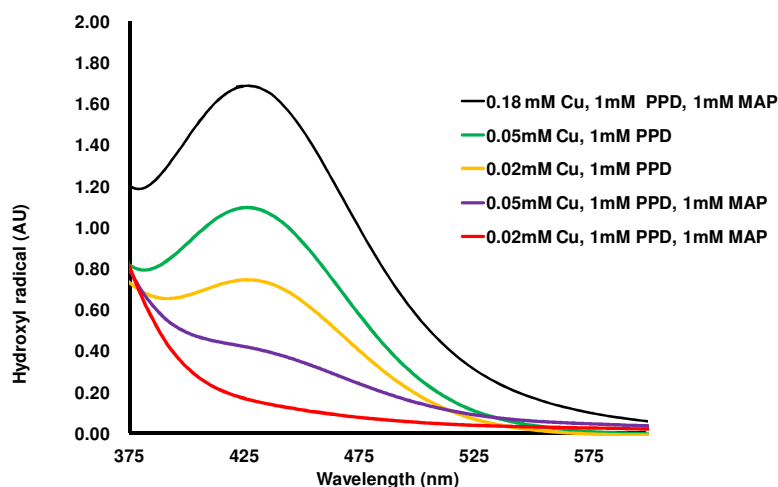


Figure 6-11: Hydroxyl radical formation in various PPD only and PPD-MAP systems at different copper(II) levels using TGA reduction method. Apart from the copper and dye precursors, reaction solutions contained 0.98 M hydrogen peroxide in 400 mM ammonia buffer at pH 10.

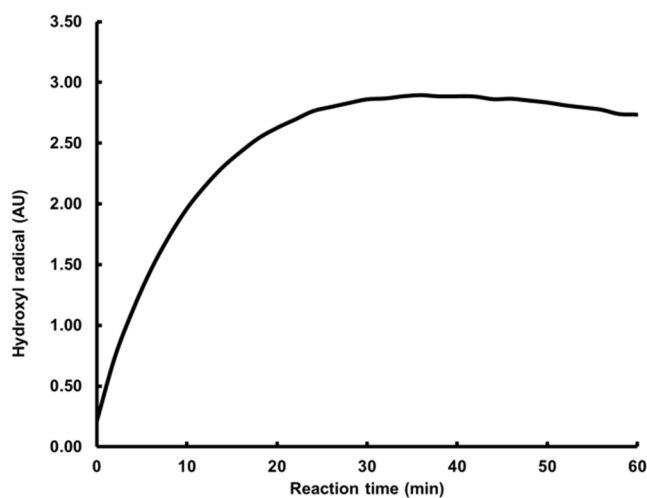


Figure 6-12: Hydroxyl radical formation in 0.02 mM copper(II) sulfate in a chelant-free/dye-free system monitored over the course of reaction time using NPGA colorimetric probe. The reaction solution had pH 10 using 400 mM ammonia/ammonium chloride buffer. Hydrogen peroxide (0.98 M) was added to trigger the decomposition reaction.<sup>176</sup>

The results demonstrate low level of hydroxyl radical being formed in the presence of PPD-MAP dye precursors (Figure 6-11). It should be recalled here that NPGA probes does not offer absolute quantification of hydroxyl radical formation in a given reaction solution. Especially in the presence of multinuclear dye molecules, it is possible that the system might have higher hydroxyl radical

formation and NPGA probe might have been unable to compete with the dye precursors for the reaction with the hydroxyl radical. However, in a model experimental system, our data suggest that the presence of dye molecules suppressed hydroxyl radical formation.

Copper(II) ions are highly active in a chelant-free/dye-free system under similar experimental conditions. Dye-free systems generated significant level of hydroxyl radicals (Figure 6-12).<sup>176</sup> Comparison of these results with those obtained in the presence of dye precursors suggest that the oxidative dye precursors clearly slowed down the decomposition reaction and hydroxyl radical formation.

## **6.5 Decomposition of alkaline hydrogen peroxide on adding pre-made oxidative dye**

To investigate the role of oxidative intermediates/products in suppressing hydrogen peroxide decomposition, pre-made dye solution was added to an ongoing copper catalysed decomposition reaction. Dye precursors were mixed in ammonia/ammonium chloride buffer (pH 10, 400 mM) and hydrogen peroxide was added to initiate the oxidation reaction. No metal ions were added to this reaction solution. The reaction solution turned dark coloured immediately on adding hydrogen peroxide which was stirred for 30 min. This coloured dye solution was then added to a separately ongoing copper(II) catalysed decomposition reaction and impact of this dye addition was monitored on the hydrogen peroxide decomposition.

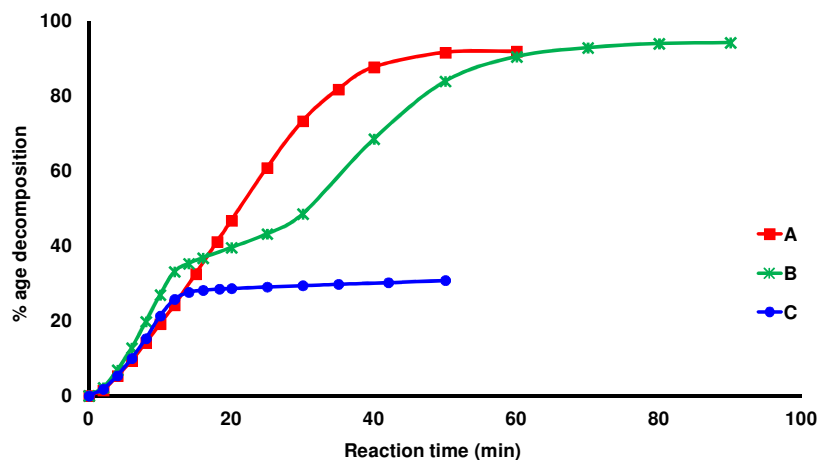


Figure 6-13: Impact of adding a pre-made dye solution to an ongoing copper(II) catalysed decomposition of alkaline hydrogen peroxide. Reaction solution contained copper(II) sulfate (0.02 mM) at pH 10 using 400 mM ammonia/ammonium chloride buffer. 1 mL of the dye solution was added to 25 mL reaction solution at 10<sup>th</sup> minute to give approximately 1 mM concentration of the dye. (A) Dye-free system (B) Pre-made PPD dye solution, (C) Pre-made PPD-MAP dye solution

The results (Figure 6-13) show that addition of the dye prepared by self-coupling of PPD only slightly slowed hydrogen peroxide decomposition while addition of PPD-MAP dye solution abruptly stopped the decomposition reaction. However, at very long reaction times the reaction gradually accelerated and eventually all hydrogen peroxide was decomposed (Figure 6-14). At this point the dark coloured reaction solution was completely decolourised thus suggesting that the increase in decomposition rate is largely due to the degradation of the inhibitor (e.g., a dye present in the MAP-PPD mixture).

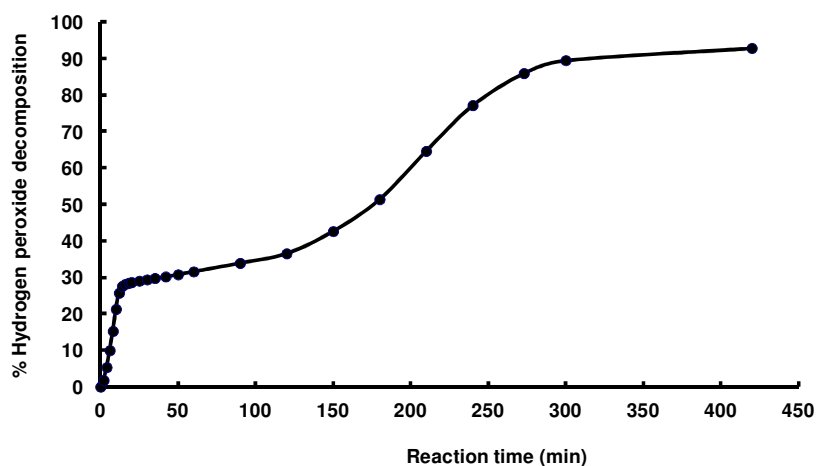


Figure 6-14: Hydrogen peroxide decomposition in copper catalysed system with added PPD-MAP pre-made dye at 10<sup>th</sup> min. Reaction solution contained 0.02 mM copper(II) sulfate at pH 10 using 400 mM ammonia/ammonium chloride buffer.

Similar experiments were carried out with other dye precursor combinations. Their addition also demonstrated an immediate impact on the decomposition kinetics (Figure 6-15). However, none exhibited such profound influence as observed in the PPD-MAP system.

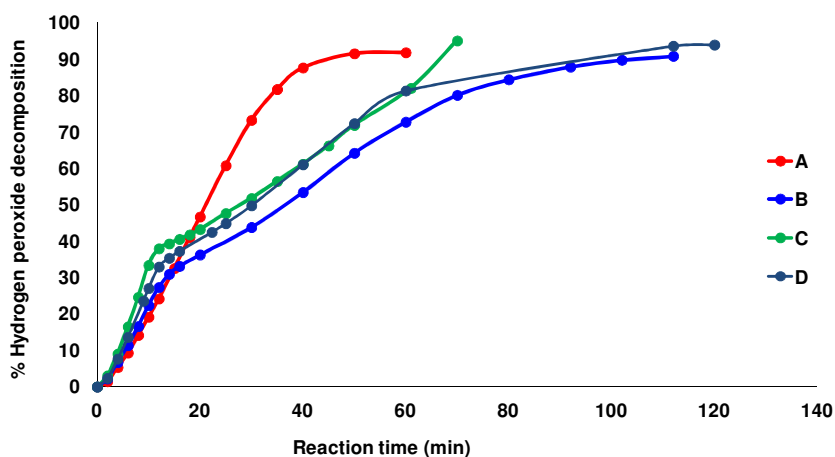


Figure 6-15: Hydrogen peroxide decomposition in copper catalysed system with added pre-oxidised dye combination at 10<sup>th</sup> minute. (A) 0.02 mM copper(II) sulfate in a chelant/dye free system, (B) 0.02 mM copper(II) sulfate, 1 mM PPD-AHT dye, (C) 0.02 mM copper(II) sulfate, 1 mM PAP-MAP dye, (D) 0.02 mM copper(II) sulfate, 1 mM DTS-MAP dye. Reaction was carried out at pH 10 using 400 mM ammonia buffer.

In summary, all dye precursors–coupler mixtures slow down the decomposition of alkaline hydrogen peroxide. PPD-MAP system showed the most profound effect and almost stopped the decomposition reaction. The experiments with the pre-made PPD-MAP dye suggest that starting material is not responsible in suppressing the decomposition reaction and some intermediates or oxidation products may be involved.

## 6.6 Hydrogen peroxide decomposition on adding PPD-MAP trinuclear dye

The oxidation of PPD and MAP gives a mixture of binuclear, trinuclear and multinuclear dye species. The results of the previous section suggest that dye precursors taken individually do not have strong effect on suppressing the hydrogen peroxide decomposition and postulate a potential involvement of a multinuclear dye. To examine its role in the decomposition reaction, a PPD-MAP trimer was synthesised, isolated and subsequently added to a copper catalysed decomposition of alkaline hydrogen peroxide (Figure 6-16). The trimer was dissolved in ammonia/ammonium chloride buffer and mixed with copper(II) sulfate. Hydrogen peroxide was added to the reaction solution and its decomposition was monitored.

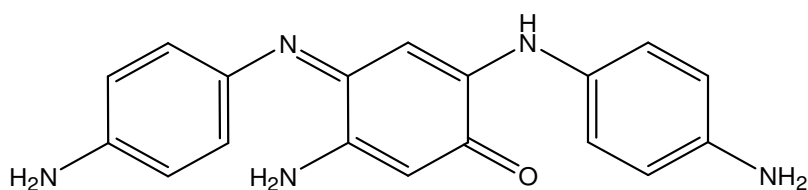


Figure 6-16: PPD-MAP oxidative trimer synthesised.

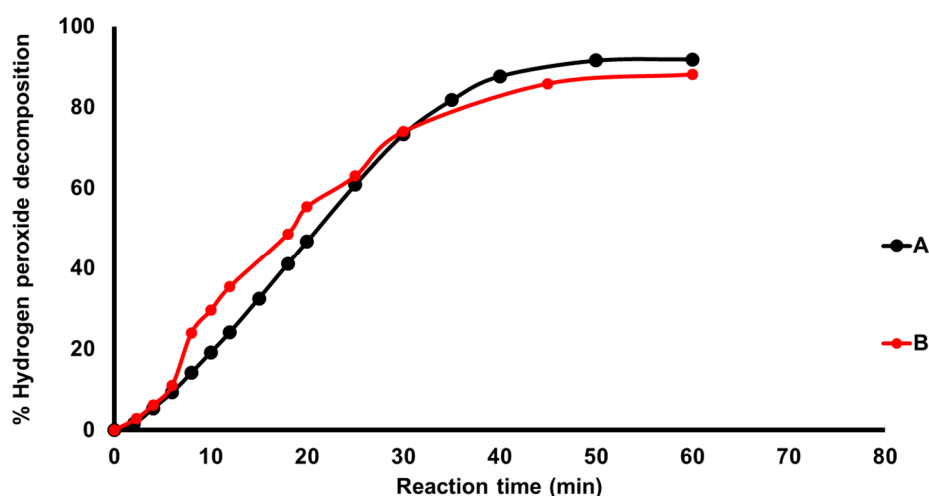


Figure 6-17: Impact of adding PPD-MAP trimer on copper catalysed decomposition of alkaline hydrogen peroxide. Reactions contained (A) 0.02 mM copper(II) sulfate in a chelant/dye-free system (B) 0.02 mM copper(II) sulfate, 0.25 mM PPD-MAP trimer. The reaction solution had pH 10.0 using 400 mM ammonia buffer.

Addition of PPD-MAP trimer did not change the kinetics of hydrogen peroxide decomposition (Figure 6-17). Control experiment with copper(II) ions in a dye-free system also showed rapid evolution of oxygen gas in the gasometric setup and all hydrogen peroxide was decomposed. This suggests that the PPD-MAP trimer is not responsible for suppressing hydrogen peroxide decomposition. PPD and MAP individually slow down the decomposition; however the effect is much weaker than that of the PPD-MAP dye (Figure 6-6). This excludes the trimer and starting dye precursors from being responsible for suppressing the copper activity in decomposing hydrogen peroxide. It seems that some other unknown species is involved in suppressing the copper(II) ions activity.

## 6.7 EPR study of copper-dye precursor mixture in the presence of alkaline hydrogen peroxide

PPD-MAP oxidative coupling involves formation of various intermediate species. As discussed earlier (Section 6.2.1), the first step is the oxidation of primary to give quinone imine which then undergoes electrophilic addition to the coupler. The coupling reaction generates leuco intermediates that further oxidise to give the dyes. So, in a reaction where various intermediate species are formed

in-situ, it is difficult to identify the species responsible for suppressing the decomposition reaction.

To further look into this matter, low temperature EPR experiments were carried out. EPR features of copper(II) ions strongly depend on the coordination environment. The spectra for the reaction solution containing copper(II) ions in the absence of PPD/MAP did not change much on adding MAP or PPD individually, however, it changes dramatically upon formation of the PPD-MAP dye in situ using hydrogen peroxide (Figure 6-18).

The broad almost featureless spectrum suggests either formation of polynuclear copper complexes or a mixture of several complexes. Due to high concentration level of ammonia used, the spectra in the absence of MAP/PPD are those of the copper-ammonia complex. The changes in spectra with PPD-MAP dye suggest that oxidative dye formed has strong affinity for  $\text{Cu}^{2+}$  ions. It seems that some unknown compound is formed during PPD coupling (other than the trimer) which interacts with the copper ions. A change in the copper environment leads to the loss of catalytic activity in decomposing alkaline hydrogen peroxide.

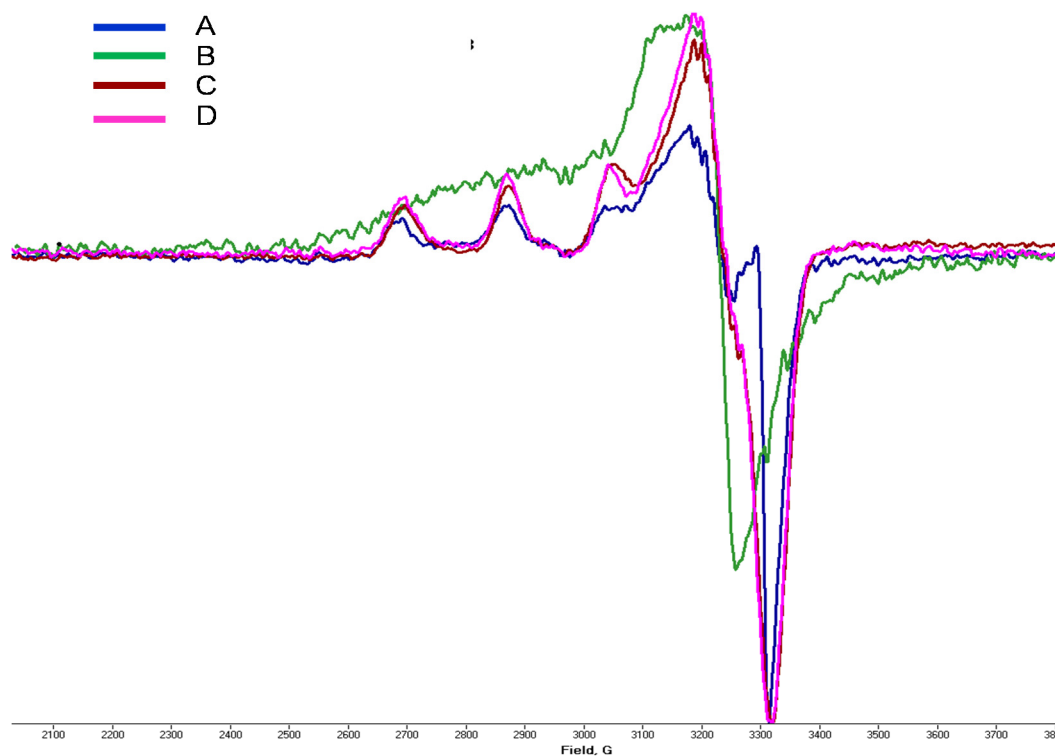


Figure 6-18: EPR spectra of copper(II) ions in a ligand-free system and along with PPD, MAP and PPD-MAP dye formed in-situ. Reaction solution contained 0.02mM copper(II) sulfate mixed with 0.98 M hydrogen peroxide in 400 mM ammonia/ammonium chloride buffer pH 10. The reaction mixture was stirred for 30 min and then mixed with glycerol (10%) and frozen in liquid nitrogen. The spectra were recorded at 120 K. (A)  $\text{Cu}^{2+}$  ions with hydrogen peroxide only in the absence of dye precursors (B)  $\text{Cu}^{2+}$  with PPD-MAP dye formed in situ using hydrogen peroxide (C)  $\text{Cu}^{2+}$  with PPD only without using hydrogen peroxide (D)  $\text{Cu}^{2+}$  with MAP only without hydrogen peroxide.

Metal coordination with aminocarboxylate and phosphonate chelants has been discussed in previous chapters. Metal-ligand binding may change the metal speciation leading to an altered catalytic activity of metal ions in a Fenton-like reaction. Dye precursors studied above also contain amino and hydroxyl substituents on the benzene ring. Their oxidation forms bigger multinuclear dye molecules with amine and imine groups which actually may have higher affinity for binding copper ions.

Syntheses of some polyphenol, poly-aniline and poly-phenylenediamine polymers and their chelating properties have been reported in the literature (Figure 6-19).<sup>177-180</sup> Similar chemistry may be involved here in the copper-PPD-MAP system where large polymeric dye molecules chelate active copper(II)

changing its chemical activity. However, it should be remembered that different dye combinations would exhibit different capacity for binding copper(II) ions as observed earlier for different metal-ligand systems. This variation in copper binding capacity will influence the catalytic activity of copper(II) ions in a Fenton-like reaction.

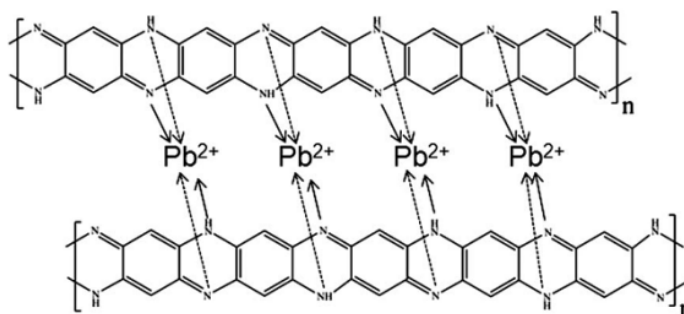


Figure 6-19: Metal binding with poly-phenylenediamine.<sup>179</sup>

## 6.8 Conclusion

Copper(II) ions are active in decomposing alkaline hydrogen peroxide in an oxidative permanent hair dyeing mixture via a Fenton-like reaction. However, the presence of aromatic primaries and couplers such as PPD/MAP suppress hydrogen peroxide decomposition. It is believed that their oxidation reaction forms some unknown compounds which chelate copper catalysts changing their chemical activity. EPR study confirms a change in copper environment during the decomposition reaction. Unfortunately, it was difficult to identify the nature of these compounds at this stage.

These results have important implications for oxidative hair dyeing. The previous chapters discussed activity of copper(II) ions rapidly decomposing alkaline hydrogen peroxide. Addition of chelants such as EDTA and EDDS were required to stabilise hydrogen peroxide and control free radical chemistry. These systems correspond to a real-life hair bleaching systems. Here in the permanent hair dyeing systems, it seems that the presence of dye precursors themselves stabilises the alkaline hydrogen peroxide. This means that due to a higher flux of hydroxyl radical, bleaching systems (which lack inhibiting dye precursors) could lead to more protein loss from the hair fibre than the oxidative dyeing systems.

This agrees with the hair protein loss data for the hair bleaching and dyeing systems where P&G observed lower protein damage in oxidative colouring compared to the bleaching system.<sup>181</sup>

## **Chapter 7: Calcium carbonate content in human hair fibre**

---

## 7 Calcium carbonate content in human hair fibre

Human hair may contain alkali, alkaline earth and transition metal ions.<sup>18</sup> Redox metals such as copper and iron may participate in a Fenton-like reaction causing hair damage as discussed in chapters 3 & 4. Most abundant metals present in hair fibre are calcium and magnesium.<sup>17, 24, 35, 182</sup> The main source of these metal ions is regular hair cleansing with tap water and subsequent usage of various grooming and styling products. Metal ions bind with carboxylate and sulfonate residues of the protein fibre. Calcium and magnesium being hard can bind with carboxylate while copper being relatively softer may go for aromatic heterocycles e.g. melanin and sulfonate. As described earlier, the metal uptake may change the physiochemical characteristics and health of hair fibre perceived by the final consumer.<sup>25</sup>

In recent work at P&G, scanning electron microscope (SEM) images of human hair fibres revealed deposits of calcium salts over the hair shaft (Figure 7-1). They appear as small bubbles (less than 100  $\mu\text{m}$ ) in the images. The bubble size increases with repeated cleansing treatments which is potentially due to more exposure to hard water.<sup>183</sup> However, no attempt has been made to determine the nature of these bubbles. They have been described to induce physical cracks along the hair shaft causing significant damage to hair fibre. Establishing the chemistry of the unknown material in a bubble is important. It may lead to develop technology preventing the bubble formation or removing them from hair to minimise hair damage and improve hair health.

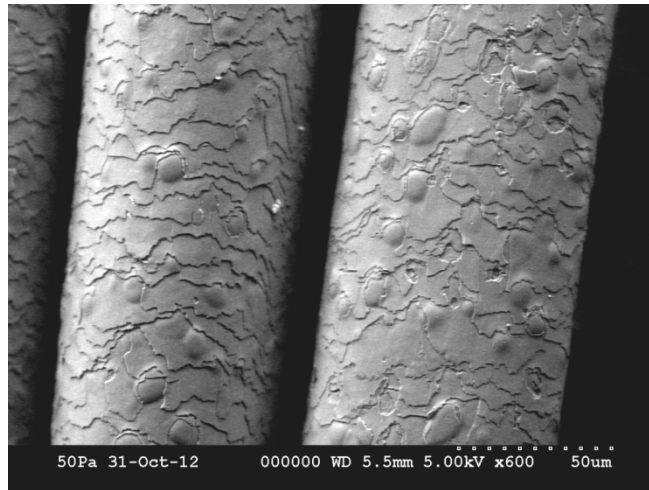


Figure 7-1: SEM image of human hair fibre showing bubbles at hair shaft.

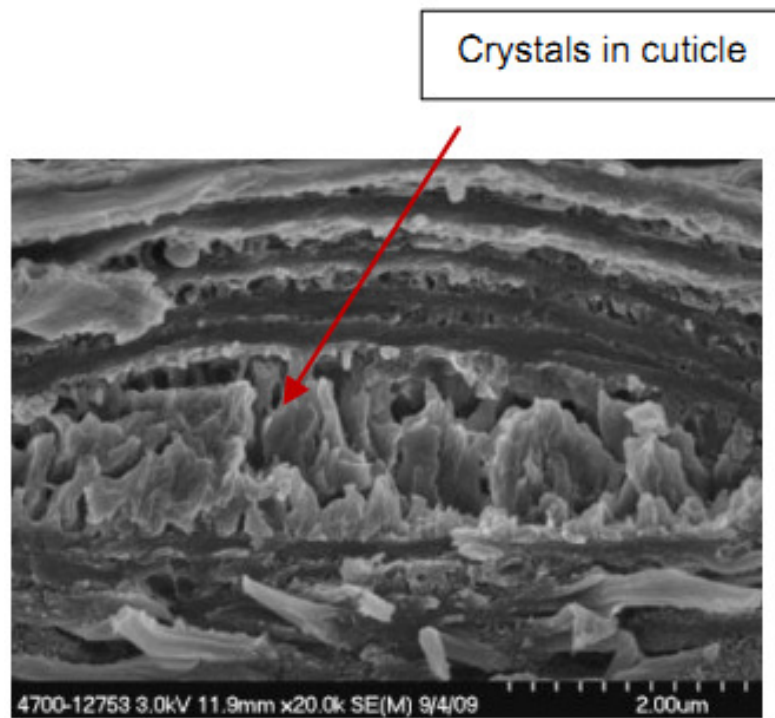


Figure 7-2: Cross section of human hair fibre showing material deposits underneath cuticles.

## **7.1 Hypothesis for “calcium carbonate” and objectives**

Consumer living in high water hardness area exhibited more bubbles. Images of hair cross section showed the presence of some unknown disc shaped material underneath the cuticles layer. SEM-EDX results show the presence of calcium material. However, the exact nature of calcium could not be established. We hypothesised that the bubbles consist of insoluble calcium carbonate deposited over time with repeated hair washing. In an early study, fibres containing large number of bubbles were treated with an acid formulations (pH, 4.0-4.5) containing citric acid. SEM images after the acid treatment shows the removal of bubbles.<sup>183</sup> This early result supported the presence of calcium carbonate.

This chapter describes an attempt to define the nature of the unknown bubble material. A quantitative analysis is carried out to determine the amount of calcium carbonate present in human hair fibre. As these bubbles are very small in size, a sensitive analytical methodology is required for accurate measurement. A new image analysis method was employed to estimate amount of material present in bubbles.

## **7.2 Image analysis: Estimating amount of the bubble material**

Digital image analysis is a process of obtaining valuable information from an image. It generally involves a computer assisted approach where customised software collects empirical data which is subsequently processed to generate quantitative information. This technique is becoming increasingly popular among scientists finding application in wide range of scientific disciplines.<sup>184, 185</sup> Recent examples have been observed with biological, archaeological and ecosystem monitoring using digital images.<sup>186-188</sup> Hair care industry has also been using this technique to examine surface properties of human hair fibre. Hair growth and hair fall has been examined using digital image processing.<sup>189-191</sup> Hair health<sup>192</sup>, shine<sup>193</sup> and customer perception about their hair health<sup>194</sup> has also been studied using image analysis. Atomic force microscopy (AFM) and scanning electron imaging has been employed to quantify surface hair damage and evaluating the efficacy of various hair care formulations.<sup>195-197</sup> Following similar approach here,

SEM images of human hair fibre are used to estimate the amount of calcium carbonate present in hair fibres.

SEM images of hair cross section for different hair switches were taken at P&G. Google image program “Picasa” version 3.0 was used to analyse image data to calculate the volume and mass of a bubble present in a hair fibre. Further details are discussed in experimental section 9.9.1.

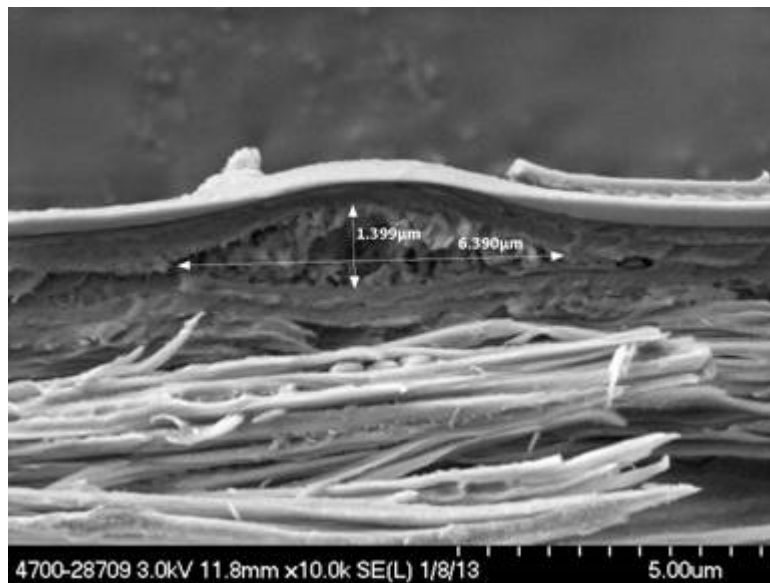
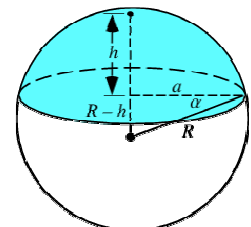


Figure 7-3: Cross-sectional SEM image of a human hair showing bubble underneath the cuticles.

Cross sectional hair SEM images (Figure 7-3) show the bubbles are a disc shaped material lying underneath the cuticle layer. The volume of a single bubble was calculated assuming a spherical disc cap shape using the following equation.

$$\text{Volume of disc cap} = \frac{1}{6} \pi h (3a^2 + h^2)$$



Here  $a$  is radius and  $h$  is the height.

Ten SEM images were processed and the data are presented in Table 7-1. The data exhibit significant variation in volume of individual bubbles suggesting a wide range of bubble sizes.

<i>Samples ID</i>	<i>volume of individual bubble (<math>\mu\text{m}^3</math>)</i>
B1	91.24
B2	108.79
B3	23.85
B4	31.23
B5	30.57
JM-1	17.09
JM-2	38.99
JM-3	27.78
JM-4	39.43
JM-5	17.10
Average	42.61 $\pm$ 31

Table 7-1: Average volume of an individual bubble calculated using SEM data.

Further in the study, the sample size was increased by obtaining more SEM images for five sets of hair switches. Each switch contained fifty hair fibres. The image data characterised hair switches with different levels of bubbles and defined “hair bubble count” which is the number of hair fibres containing bubbles out of fifty fibres analysed under SEM. Number of bubbles in a given hair fibre were counted using SEM images from each switch. The data are presented in Table 7-2.

<i>Sample</i>	<i>Bubble count level</i>	<i>Total number of bubbles</i>
Control	Non-chemically treated fibres	

Ponytail 53	Zero	
Ponytail 59	19	80 (n=14)
Ponytail 50	33	55 (n=8)
Ponytail 104	41	51 (n=7)
Ponytail 69	46	199 (n=19)

Table 7-2: Ponytail fibre characterisation by SEM imaging. Number of fibres with bubbles observed in a ponytail fibre switches (n represents the number of fibres).

The volume of individual bubbles, total number of bubbles and bubble count level were employed to calculate the total volume of all bubbles present in the fibre using the following equation. The results are presented in Table 7-3.

$$\text{Total volume of bubble material in a hair switch} = \text{Average volume of bubbles} \times \text{total of number of bubbles in a fibre} \times \text{bubble count factor}$$

Here

$$\text{Bubble count factor} = \frac{\text{Number of fibres containing bubbles}}{\text{Total No. of fibres analysed under SEM}}$$

<i>Samples</i>	<i>Average estimated bubble material (%)</i>
Ponytail 53	
Ponytail 59	0.030% ± 0.01
Ponytail 50	0.084% ± 0.02
Ponytail 104	0.075% ± 0.02
Ponytail 69	0.109% ± 0.01

Table 7-3: Estimated level of bubble material present in human hair fibre using image analysis method with SEM data assuming spherical cap bubble shape.

SEM images show an increase in the number of bubbles with increasing bubble count level. This is potentially due to hair ageing factor where repeated hair cleansing induce more bubble formation. The above results show that overall

these hair samples contain very small amount of the bubble material (sub-ppm level) and it makes only a small fraction of the total mass of a fibre. Here, image analysis offered a reasonable approximation for the amount of material present in the bubbles.

The volume of an individual bubble was calculated from only one set of hair fibres. Early observations under SEM show that bubble size increases with more exposure to hard water. In that case, using a single bubble volume value was not a realistic approach to estimate total volume of all bubbles. A large number of cross-sectional images would have been required to verify this which was not feasible.

The results also suggest that a sensitive analytical technique is required to accurately determine small (sub-ppm) level bubble material in these hair samples. As the bubble material is hypothesised to be calcium carbonate, a sensitive technique for carbonate detection in heterogeneous solid samples was sought.

### **7.3 Quantitative chemical analysis of calcium carbonate in human hair fibres**

Quantitative analysis for carbonate content can be carried out using various techniques. The choice of an analytical methodology depends upon method sensitivity and its detection limit. A titrimetric method can be used to determine calcium carbonate in eggshell while the amount of carbonate in soil samples has been determined using a gas the volumetric method measuring volume of carbon dioxide gas evolved upon treatment with acid.<sup>198, 199</sup> However, more sensitive techniques are required to analyse sub-ppm levels of carbonate. Separation techniques such as ion chromatography and capillary electrophoresis have been employed to analyse inorganic anions in biological and soil samples.<sup>200-202</sup> Infrared<sup>203, 204</sup> and Raman spectroscopic<sup>205</sup> methods have also been reported to determine carbonate directly. Attempts were also made at P&G Cincinnati to measure carbonate level in hair fibre directly, however, it did not work out successfully.

An indirect method is measuring carbon dioxide gas evolved via thermal decomposition of carbonate or with strong acid treatment. Carbon dioxide gas then can be quantified in situ or with suitable sampling method using infrared spectroscopic<sup>204, 206, 207</sup> or gas chromatographic techniques.<sup>208, 209</sup> Environmental studies to monitor greenhouse gases such as carbon dioxide (CO<sub>2</sub>), methane (CH<sub>4</sub>) and nitrous oxide (N<sub>2</sub>O) have extensively utilised infrared spectroscopy.<sup>210</sup> Previously in chapter 5, a quantitative gas IR method has been used to quantify carbonate content in copper based nanoparticles. A similar FT-IR approach was adapted here to quantify calcium carbonate in human hair fibres.

### 7.3.1 Infrared spectroscopy of carbon dioxide

A hetero-atomic molecule held together with a chemical bond, forms an electric dipole that oscillates with a specific frequency. If this non-symmetrical bond is irradiated with light, the electrical component of the electromagnetic radiation can transfer its energy to the bond provided that mechanical frequency of bond matches the frequency of electromagnetic radiation (Figure 7-4). This interaction causes energy absorption which provides valuable information about the molecule. In the absence of a change in dipole moment which is the case in non-polar bonds such as O=O in oxygen, no interaction of electromagnetic radiation with the molecule takes place and thus no absorption is observed. The radiations from the infrared region (10000 – 100 cm<sup>-1</sup> and more precisely mid-infrared region ranging 4000-400 cm<sup>-1</sup>) possess low energy, which causes vibrational and rotational excitation.

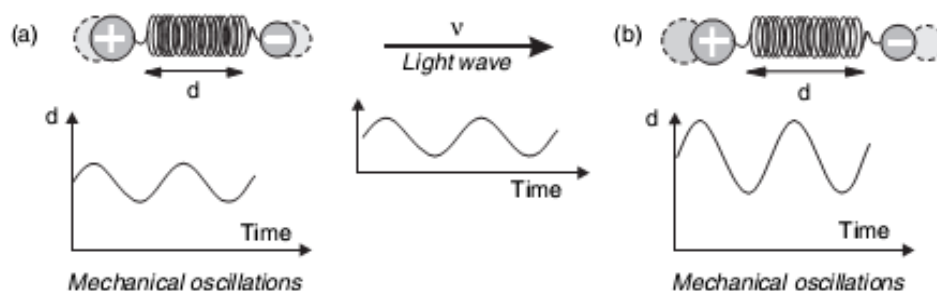


Figure 7-4: Interaction of electromagnetic radiation with a molecule.<sup>211</sup>

A non-linear molecule with N numbers of atoms has 3N degrees of freedom of which three are translational and another three are rotational. The remaining 3N - 6 describes its vibrational motion. Vibrational motion may be stretching or

bending. A stretching vibration is a rhythmical movement along the bond axis changing the inter-atomic distance while a bending vibration involves a change in bond angle. However, in a linear molecule of carbon dioxide, rotation of atoms along the bond axis does not involve displacement of atoms. It thus loses one of its rotational degree of freedom. That's why the total number of degrees of freedom for linear carbon dioxide molecule is  $3N - 5$ . This gives carbon dioxide four fundamental vibrational modes ( $(3 \times 3) - 5 = 4$ ). There are two stretching vibrations while the other two are bending. In an asymmetrical vibration, one carbon-oxygen bond stretches out of phase while the other contracts producing a change in dipole moment inducing absorption around  $2350 \text{ cm}^{-1}$ . As both oxygen atoms share the same carbon centre, it causes a strong mechanical coupling displaying a significant shift in absorption frequency from the carbon-oxygen (C=O) bond of ketones (which absorbs around  $1715 \text{ cm}^{-1}$ ). The symmetrical stretching does not produce any change in dipole moment and hence no absorption can be observed. Two bending vibrations are equivalent and thus have same frequency absorbing around  $665 \text{ cm}^{-1}$ .<sup>212-215</sup>

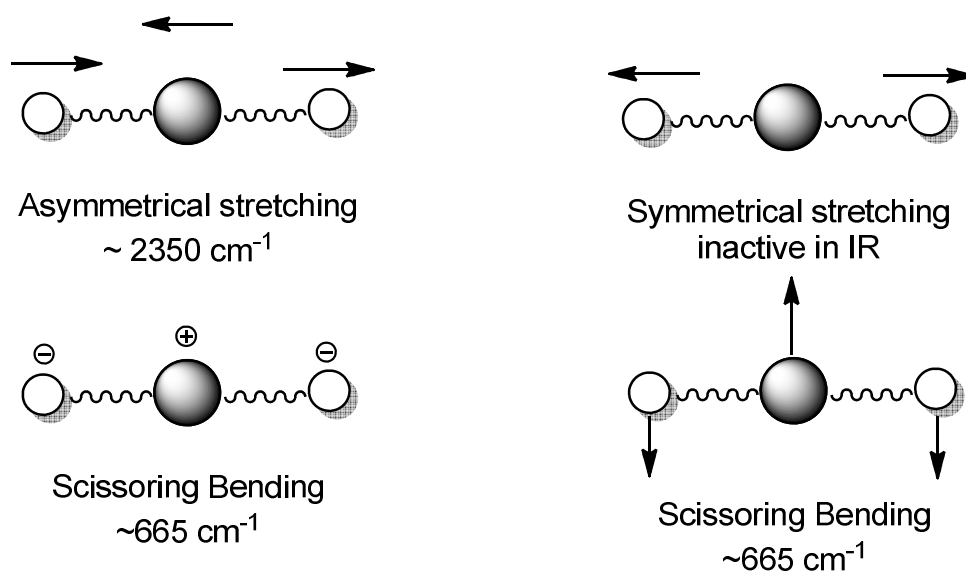


Figure 7-5: Fundamental vibrations in a carbon dioxide molecule.<sup>213</sup>

### 7.3.2 FT-IR method to quantify carbon dioxide gas

Air contains 394 ppm (0.039% v/v) carbon dioxide and it absorbs strongly in the mid-IR region.<sup>216</sup> A quantitative measurement of carbon dioxide below its atmospheric level requires minimising background interference. A series of

control experiments were carried to develop an optimised control reaction setup to minimise this background interference. An experimental setup connecting the reaction vessel and gas IR cell was designed. Hair fibres in a sealed reaction vessel were treated with concentrated inorganic acid and the evolved carbon dioxide was quantified. Phosphoric acid was a preferred choice over other acids due to its low volatility and lack of oxidising power.

### 7.3.3 Method sensitivity

An IR spectrum of air was obtained against an evacuated IR cell background which showed the absorption level for atmospheric carbon dioxide (Figure 7-6). Similarly, control experiments with a system containing phosphoric acid without hair fibres demonstrated the absorption scale for residual carbon dioxide present in the experimental setup (Figure 7-7). The ratio between these two absorption levels gave the minimum detection limit under these experimental conditions. The calculations are summarized below in Table 7-4.

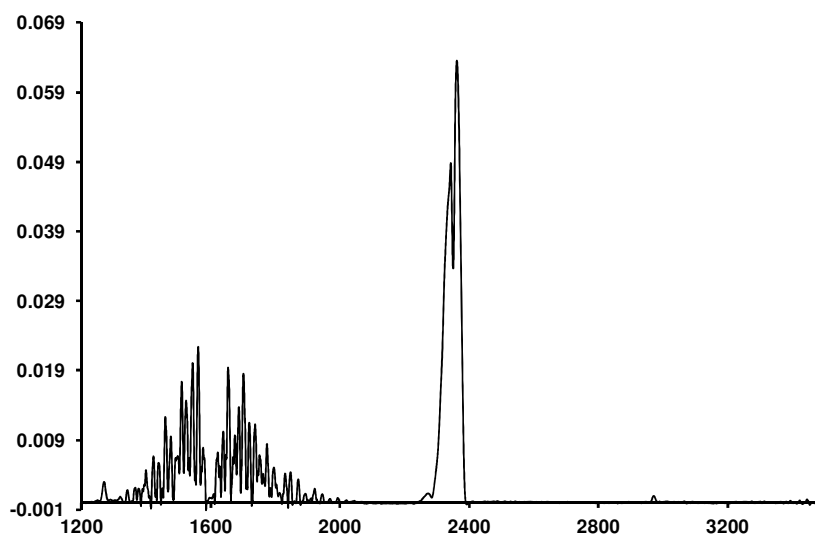


Figure 7-6: FT-IR spectrum of air.

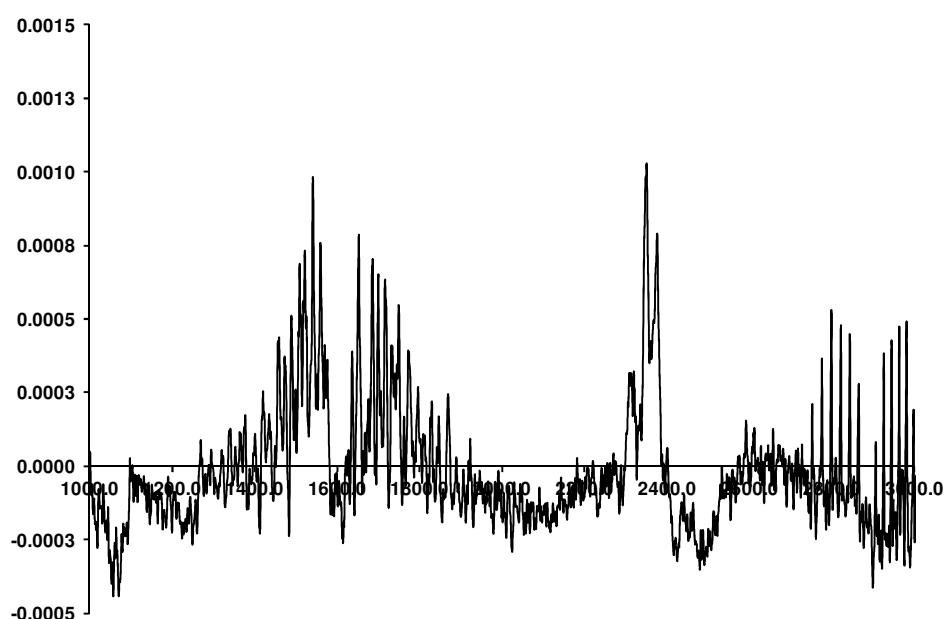


Figure 7-7: Control experiment using phosphoric acid and stirring bar without hair fibres or carbonate showing low level of absorption for carbon dioxide.

<b><i>Calculating the CO<sub>2</sub> detection limit for IR method</i></b>	
Carbon dioxide absorption level (AU) in air observed by recording IR spectrum of air	0.0635
Maximum absorption level (AU) for CO <sub>2</sub> in a control experiment	0.001
S/N ratio	$0.0635/0.001 = 63.5$
Amount of CO <sub>2</sub> in air (ppm)	394
Minimum detectable CO <sub>2</sub> concentration (ppm)	$394/63.5 = 6.20$

Table 7-4: Calculating CO<sub>2</sub> detection limit using IR method.

Previous studies using gas phase IR have described minimum detection limit for carbonate and carbon dioxide. This limit varies greatly depending upon experimental conditions such as IR cell path length, sample size and sample preparation.<sup>217</sup> An experimental setup employing multiple gas extraction traps may go to sub-ppb level for carbon dioxide for more precise and accurate quantifications.<sup>218, 219</sup> So, it is difficult to compare our detection limit in a simple set-up with the previously reported values.

### 7.3.4 Determining the amount of carbonate in hair fibres

A standard curve was first developed to quantify carbon dioxide in an unknown sample. Details are further discussed in experimental section 9.9.7.1. Next, IR spectra of hair samples containing bubbles were recorded under identical experimental conditions. The results (Figure 7-8) show an increase in absorption intensity for carbon dioxide with increasing bubble count level. Zero bubble count level showed absorption level comparable to the control experiment. Pulverised hair powder showed significantly higher absorption which might be due to greater surface area and accessibility of carbonate in powder specimen.

For quantitative measurements, absorption intensity at  $2360\text{ cm}^{-1}$  was used to calculate the level of carbonate. The results are given in Table 7-5.

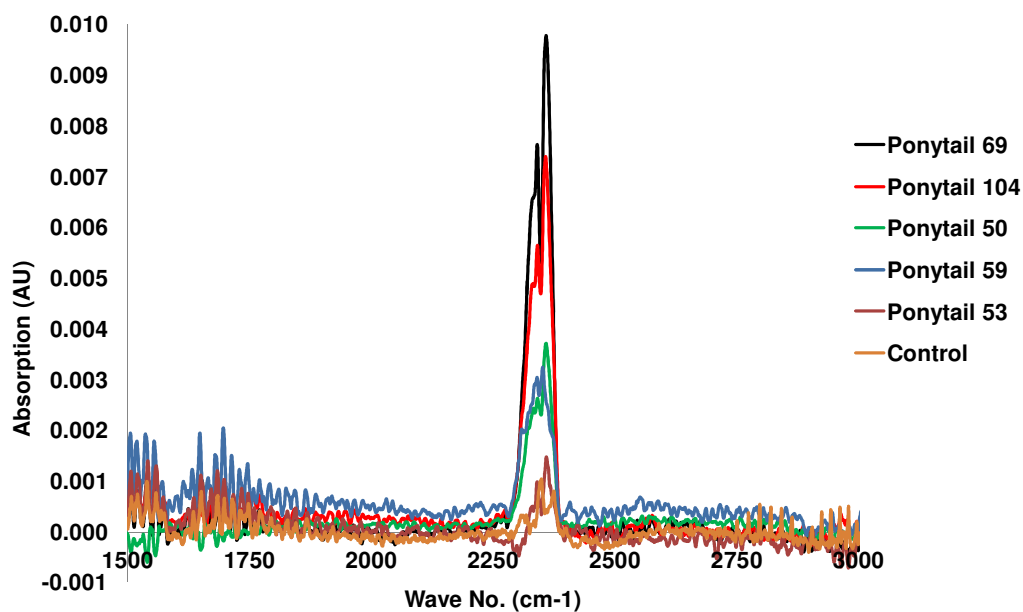


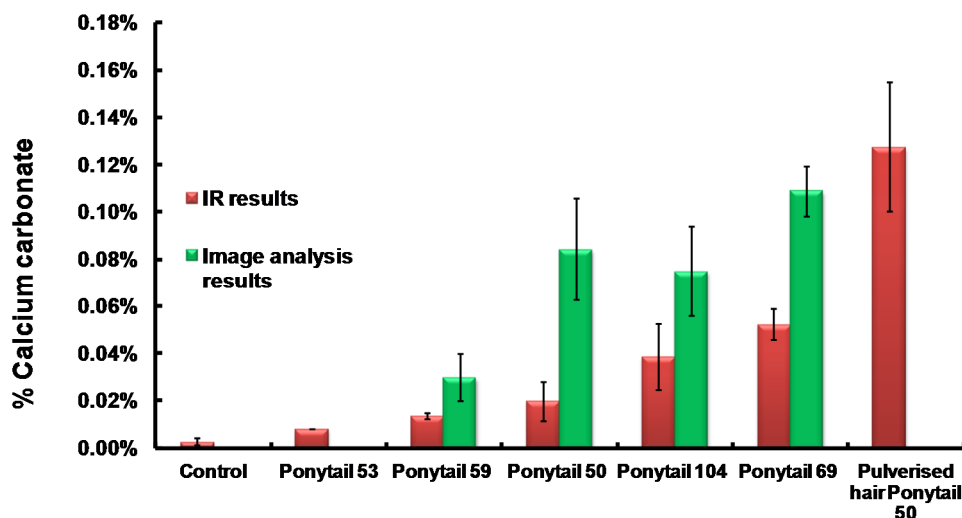
Figure 7-8: IR spectra for various samples of human hair fibres showing the absorption band for carbon dioxide produced.

Sample	Avg. Absorption for CO <sub>2</sub>	Amount of Calcium Carbonate (ppm)	Carbonate content (%)
Control	0.0005	24.7 ± 8.62	0.0025 ± 0.0009
Ponytail 53	0.0015	78.5	0.0079 ± 0.000
Ponytail 59	0.0025	134.2 ± 9.16	0.0134 ± 0.0009
Ponytail 50	0.0037	196.2 ± 37	0.0196 ± 0.004
Ponytail 104	0.0072	384.2 ± 81.2	0.0384 ± 0.007
Ponytail 69	0.0095	520.0 ± 46.5	0.052 ± 0.006
Pulverised hair powder (Ponytail 50)	0.0098	1270.1 ± 320	0.127 ± 0.026

Table 7-5: Carbonate levels (%) in various human hair samples with different bubble count level. Each ponytail sample analysed contained 350 mg hair fibre while for pulverised hair powder (ponytail 50), 100 mg hair fibres were used.

## 7.4 Defining the nature of bubble material

Comparing image analysis estimation and IR quantification for calcium carbonate helps to define the nature of unknown material present in the bubbles. The estimated level of unknown material from image analysis is 2-3 times higher than the actual level of calcium carbonate found from IR method (Figure 7-9). Although image analysis is only an approximation, the comparison with IR data still suggests that bubble material may not be solely calcium carbonate. It seems that some other unknown material may also be present along with calcium carbonate in the bubbles.



**Hair fibres with different bubble counts**

Figure 7-9: Comparing amount of calcium carbonate determined by image analysis and gas IR method.

Calcium level in hair varies significantly and it depends upon demographics, gender and hair condition. A recent report discussed a comprehensive study where hair fibre from various countries across the globe were analysed for their metal contents.<sup>220</sup> It reports an average of 5000 ppm of calcium from over 300 hair samples analysed. Assuming these values, it seems that total level of calcium carbonate found from IR method is only *ca.* 0.025% of total calcium present in hair fibre. This means that most of calcium present in the hair fibre is not calcium carbonate.

Previous reports in the literature have discussed the bubble formation as a result of harsh thermal treatments such as flat ironing and blow drawing. These thermal treatments can cause significant hair damage due to localised overheating specially in wet hair where temperature may rise very quickly due to steam inside hair fibre.<sup>221-223</sup> This may cause significant decrease in fibre tensile strength at various points along the hair shaft. It is possible that these damaged spots accelerate deposition of calcium based inorganic materials which grow over time with repeated exposure to hard water.

Daily hair cleansing formulations such as shampoos, shower gels and soaps contain different surfactants. Long chain fatty acids and alcohols are common

examples used.<sup>171, 224, 225</sup> It is possible that repeated washing cause deposition of calcium salts of these long chain organic acids on hair fibre. During the current study, attempts were made to induce and grow these bubbles by immersing non-chemically treated hair fibres in calcium sulfate and sodium carbonate solution. However, no bubble formation or increase in bubble numbers was observed. This also suggests that bubble formation mechanism may involve some other factors. Outermost layer of hair cuticles is lipophilic composed of lipids.<sup>13, 226</sup> It is possible that these lipid-based components add to calcium deposits and play a role in the bubble formation. Recent results from work at P&G also suggest the presence of long chain organic materials.<sup>181</sup> Further work is required to investigate these factors and determine the exact nature of these bubbles.

## **7.5 Conclusion**

Two analytical methodologies were employed to quantify the amount of calcium carbonate in hair. Image analysis of hair offered a good approximation where digital data were utilised to estimate the amount of calcium carbonate.

Quantitative chemical analysis was carried out to quantify calcium carbonate content in human hair fibre using a gas infrared spectroscopic method. The level of calcium carbonate increased with increasing bubble count level as observed in SEM analysis. The amount of calcium carbonate from IR method was 2-3 times less than the image analysis estimation. This suggests that calcium carbonate may not be the only material present in the bubble. The low level of calcium carbonate found in the hair also suggests that the bulk of calcium present in the hair is not in the form of calcium carbonate. Following these results, further work has been carried out at P&G, preliminary data also suggest the presence of calcium salt of fatty acids which may be residues of soap or other grooming treatments.<sup>181</sup>

## **Chapter 8: General conclusion and future work**

---

## 8 General Conclusion and future work

Copper(II) and Iron(III) ions decompose alkaline hydrogen peroxide via a Fenton-like reaction. The NPGA probe has been successfully used to monitor hydroxyl radical formation in both model solution and real hair colouring systems. Copper(II) ions are more active in decomposing alkaline hydrogen peroxide compared to iron(III) ions in a chelant-free system. Both metal ions form insoluble metal hydroxides which eventually precipitate in the reaction solution leading to the deactivation of the metal ions. The initial rate of decomposition of hydrogen peroxide and hydroxyl radical formation increases with an increase in initial concentration of copper(II) ions which suggests that higher amounts of copper ions in oxidative colouring may lead to higher amounts of hydroxyl radicals formed and hence more oxidative hair damage.

Adding chelants to copper(II) or iron(III) reaction solution greatly influenced the catalytic activity of these metal ions.

Most of the aminocarboxylate and phosphonate chelants studied here are effective in chelating copper(II) ions and suppressing the decomposition of alkaline hydrogen peroxide decomposition except HEDP chelant which decomposed a large amount of alkaline hydrogen peroxide. The current study highlights different behaviour of the different metal-chelant systems under alkaline pH conditions.

The presence of large excess of a calcium salt can influence the speciation plots. Adding a chelant to a binary metal system triggers a competition where metal ions compete to bind the chelant. Among the chelants studied here, EDDS displayed preference for binding copper(II) ions and hence was the best chelant to prevent or minimise the decomposition of hydrogen peroxide and hydroxyl radical formation. Our results demonstrate the advantage of using EDDS chelant under the alkaline hair colouring conditions.

In order to validate the results obtained with the model systems, hair fibres treated with copper were used as source of metal ions to decompose alkaline hydrogen peroxide. An increase in the rate of hydrogen peroxide decomposition and hydroxyl radical formation with increasing level of copper in the hair fibre

agrees with the earlier solution model systems. Just like in solution models, EDDS chelant showed strong preference and selectivity for binding copper(II) ions adsorbed on the hair fibres. This led to suppression of the hydroxyl radical formation suggesting that EDDS is a better Cu(II) chelant in real systems than other compounds such as EDTA and DTPMP. Hence, it can be utilised to minimise free radical induced protein hair damage during oxidative hair colouring. The selectivity of EDDS chelant for copper(II) ions was explained using speciation plots. These results guide in choosing the right chelant combination in hair colouring formulation for an improved colouring application.

Catalytic activity of copper(II) ions in decomposition of alkaline hydrogen peroxide was also examined in an oxidative permanent hair colouring system. The presence of aromatic primaries and couplers suppressed decomposition of alkaline hydrogen peroxide. PPD/MAP combination had a profound impact on the course of the reaction suppressing the decomposition. Their oxidation forms some unknown intermediates which chelate copper catalysts changing their chemical activity. Unfortunately, the nature of this intermediate could not be elucidated and requires further work. In the current study of PPD/MAP oxidation, only one product was synthesised and isolated, but the reaction involves formation of dimer and polynuclear species. These other species should be isolated and examined for their role in suppressing the decomposition reaction. Similarly, different other dyes could be synthesised and examined to draw a general conclusion about their catalytic activity in a Fenton-like reaction.

Among the chelants examined in the current study, HEDP is an exception as Cu<sup>2+</sup>-HEDP system rapidly decomposed alkaline hydrogen peroxide and the reaction stopped abruptly. It is believed that the decomposition proceeds via formation of an unknown active catalyst that degrades the chelant and eventually seeds formation of catalytically-inactive basic copper phosphate/carbonate nanoparticles. Various unsuccessful attempts were made to identify the nature of this catalyst. The copper based catalyst is likely to be short-lived and its steady state concentration is likely to be low. It may require a more sensitive analytical approach to detect it. One method for studying highly reactive, short-lived species is continuous-flow. This approach has been employed in mechanistic studies of the Fenton reaction. A similar setup might be useful to explain the reaction mechanism and identify active catalyst in the future.

In the current project, human hair samples were analysed to quantify the amount of calcium carbonate present in hair. Microscopic analysis of hair fibres previously revealed the presence of bubble-like features which were assumed to be composed of calcium carbonate. Our results show that the amount of calcium carbonate measured by the IR method was 2-3 times less than the estimated values by image analysis. This means that calcium carbonate may not be the only material present in the bubbles and some other unknown material may also be present along with calcium carbonate in the bubbles. Identifying the exact nature of bubble material is important in order to define new strategies to remove these bubbles. Recent studies have highlighted the negative impact of such bubbles or deposits on the cosmetic features of hair fibre such as shine, difficulty in daily grooming and styling.<sup>227</sup> Removing or minimising these bubbles may improve quality of hair fibre, its health and hence consumer perception. Apart from calcium carbonate, the bubbles may contain salts of long chain fatty acids or alcohols which are commonly used in personal care formulations. Ideally a direct technique should be used to determine the bubble composition in the future. One approach could be using IR or Raman imaging techniques.

## **Chapter 9: Experimental procedures**

---

## 9 Experimental procedures

### 9.1 Materials and chemicals

All chemicals were purchased from Sigma – Aldrich and used as received without further purification. Hydrogen peroxide (30%) was purchased from Fisher Scientific. Dialysis tubes for the purification of nanoparticles were bought from Medicell International Ltd dialysis membrane [14.3 mm diameter, 30 kD molecular weight cut off (MWCO)].

### 9.2 Instrumentation

- The pH measurements were recorded using Jenway-3505 pH meter.
- The UV-Visible spectra were recorded on Hitachi U-3000 spectrophotometer using quartz cell with 1cm path length.
- All NMR spectra were recorded on Bruker ECX 400 MHz and ECS 400 MHz machines.
- Mass spectrometry was performed on Bruker Micro-TOF with ESI mode at MS Excellence Centre, Department of Chemistry, University of York.
- The EPR spectra were recorded on Bruker EMX machine.
- Elemental analyses were carried out at Department of Chemistry, University of York.
- FT-IR spectra were recorded at Thermo Nicolet Avatar-370 FT-IR spectrophotometer.
- ICP-OES analysis of samples was conducted at analytical services lab, University of Manchester.
- TEM analysis was carried out at Centre of Cytometry and Imaging, School of Biology, University of York.
- Thin layer chromatography was carried out using aluminium sheets with silica gel 60 F<sup>254</sup>.

## 9.3 Experimental procedures for chapter 2

### 9.3.1 Synthesis of *N,N'*-(5-nitro-1,3-phenylene)bisglutaramide (NPGA) probe

The synthesis of *N,N'*-(5-nitro-1,3-phenylene)bisglutaramide (NPGA) was carried out as reported in the literature.<sup>121</sup>

#### 9.3.1.1 Step A: Synthesis of 3,5-diaminonitrobenzene

3,5-Dinitroaniline (25 mmol, 4.6 g) was dissolved in ethanol (50 mL) with stirring. Ammonium chloride (93 mmol, 5 g in 15 mL warm water) was added slowly. Sodium sulfide (64 mmol, 15.4 g in 15 mL warm water) was added drop wise to the stirred reaction mixture. The temperature was maintained at 65-70 °C during the addition. Water (100 mL) was added to the solution. The reaction mixture was filtered to remove unreacted material. The filtrate was allowed to cool at room temperature, leading to the formation of red needle like crystals. The crystals obtained were dried. The product was recrystallised from water and dried (Yield: 72%), M.P 143.6 °C (Lit<sup>121</sup>, 143.0 °C), <sup>1</sup>H NMR (400 MHz, DMSO): δ(ppm), 5.42 (NH<sub>2</sub>-Ar,s, 4H), 6.12 (Ar, t, 1H, J=1.8Hz), 6.6 (Ar, d, 2H, J=1.8Hz). (Lit: <sup>1</sup>H NMR (400 MHz, DMSO): δ, 5.4 (NH<sub>2</sub>- Ar, s, 4H), 6.2 (Ar, t, 1H), 6.8 (Ar, m, 2H).

#### 9.3.1.2 Step B: Synthesis of NPGA

3,5-Diaminonitrobenzene (0.25 g, 1.62 mmol) was dissolved in dry acetonitrile. Glutaric anhydride (0.77 g, 6.75 mmol) was added to the reaction mixture. The reaction mixture was refluxed under nitrogen for 2 hours. The chemical conversion was monitored by TLC. After 2 hours of reflux, the mixture was allowed to cool at room temperature; yellow crystalline solid was filtered and dried. The product was recrystallised from water (Yield: 73%) M.P 196.0 °C (Lit<sup>121</sup>, 195.0 °C), <sup>1</sup>H NMR(400 MHz, DMSO): δ, 1.81 (q, 4H, J=7.3Hz), 2.28 (t, 4H, J=7.3Hz), 2.39 (t, 4H, J=7.3Hz), 8.21-824 (Ar,m 3H), 10.4 (NHCO,s 2H). (Lit: <sup>1</sup>H NMR(400 MHz, DMSO): δ, 1.8 (q, 4H), 2.3 (t, 8H), 8.3 (Ar, m, 3H), 10.3 (NHCO, s, 2H). <sup>13</sup>C NMR(400 MHz, DMSO), δ (ppm), 20.6(C<sup>1</sup>), 33.2(C<sup>4</sup>), 35.5(C<sup>2</sup>), 108.14(C<sup>7</sup>, C<sup>11</sup>), 140.5(C<sup>8</sup>, C<sup>10</sup>), 148.2(C<sup>6</sup>), 171.48(C<sup>5</sup>), 174.4(C<sup>1</sup>).

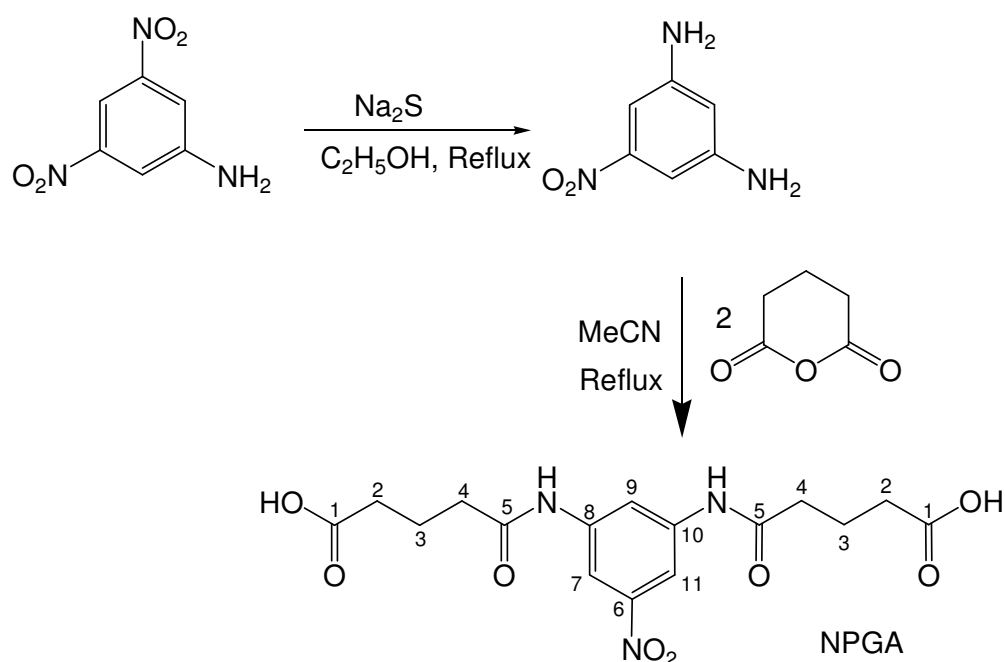


Figure 9-1: Synthesis of NPGA probe.

### 9.3.2 Monitoring hydroxyl radical formation with NPGA

A 3 mL reaction solution was carried out containing  $\text{Cu}^{2+}$  or  $\text{Fe}^{3+}$  metal ions (0.18 mM) and NPGA (1.0 mM) mixed in 20 mM ammonium hydroxide/ammonium chloride buffer solution. Hydrogen peroxide (0.98 M) was added to the reaction mixture in the UV-visible spectrophotometric cell and mixed quickly. The UV-visible spectra in the range of 200 – 600 nm were recorded immediately against the blank. The blank was prepared of the same composition except hydrogen peroxide.

Same procedure was used on adding the chelant (1.3 mM). Same approach was employed to monitor hydroxyl radical formation at different concentration levels of metal ions, different buffer composition and pH levels.

### 9.3.3 LC-MS separation of H-NPGA/NPGA

NPGA probe and its hydroxylated derivative were analysed using reverse phase HPLC. The column used was Dinosil (Manufacturer), Acclaim Polar Advantage II, C-18 polar with 3 micron packing and 2.1 x 150 mm dimensions. The solvent system contained acetonitrile mixed with 10mM ammonium formate buffer pH 7. Peaks obtained were identified by mass spectrometer.

Reaction solution contained copper(II) sulfate (0.18 mM) with NPGA probe (1 mM). Hydrogen peroxide (0.98 M) was added to start the hydroxylation reaction. At the 90<sup>th</sup> minute, reaction was quenched by adding a drop of catalase (10 times diluted solution). A sample of 10 microlitre was injected to the machine and separation was carried out.

Further isolation of H-NPGA derivatives was carried out using preparative TLC (R<sub>f</sub>: 0.35). The elution solvent used was dichloromethane and methanol (4:1) and a few drops of acetic acid.

## **9.4 Experimental procedures for chapters 3 & 4**

### **9.4.1 Determination of hydrogen peroxide**

Hydrogen peroxide concentration in the stock solutions was determined by iodometric titration method.<sup>228</sup>

### **9.4.2 Monitoring decomposition of hydrogen peroxide**

The decomposition of hydrogen peroxide in a Fenton-like reaction was determined by measuring the volume of oxygen gas evolved. The reaction was carried out in a thermostated closed reactor at 20 °C. The experimental set up has reaction vessel connected directly to a burette filled with water (Figure 9-2). The burette in turn was connected to a levelling funnel. The levelling funnel was adjusted accordingly to ensure that the pressure inside the burette was always constant (Atmospheric pressure). The decomposition of hydrogen peroxide generates oxygen gas which replaces water in the burette. The change in water level was recorded periodically as a measure of oxygen gas produced.

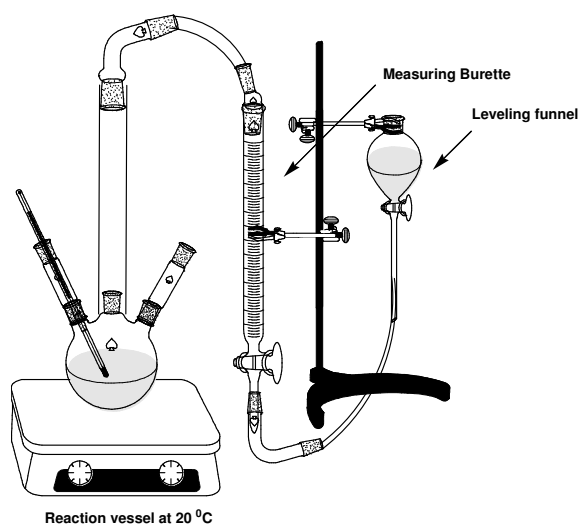


Figure 9-2: Experimental setup to monitor decomposition of hydrogen peroxide.

### 9.4.3 Decomposition of hydrogen peroxide in a chelant-free system

In a typical chelant-free reaction, copper(II) sulfate or iron(III) chloride (0.18 mM) was dissolved in 20 mM pH 10 ammonia/ammonium chloride buffer. Hydrogen peroxide (0.98 M) was injected in the closed reaction vessel and oxygen evolution was monitored over time. The volume of oxygen gas evolved was used to calculate hydrogen peroxide decomposition.

### 9.4.4 Decomposition of hydrogen peroxide in the presence of a chelant

The same setup was used by adding given chelant (1.3 mM) to monitor hydrogen peroxide decomposition in the presence of a chelant. The volume of the reaction varied from 10 – 500 mL depending upon the reactivity of the metal/chelant complex.

### 9.4.5 Decomposition of hydrogen peroxide in the presence of copper treated hair fibres

Decomposition of alkaline hydrogen peroxide in the presence of copper treated human hair fibres was also determined using the same gasometric setup.

The reaction solution (25 mL) contained 100 mg of hair fibres at pH 10 using 400 mM ammonia/ammonium chloride buffer solution. Hair fibres were cut to small pieces. Hydrogen peroxide (0.98 M) was added to the reaction solution and its decomposition was monitored.

Similar approach was used by adding chelant (1.3 mM) to the reaction solution and other experiments by changing the composition of the reaction solution.

#### **9.4.6 Hydrogen peroxide decomposition in binary metal system**

In copper-calcium binary metal system, copper(II) sulfate (0.18 mM) was mixed with calcium nitrate (125 mM) in 400 mM ammonia/ammonium chloride buffer solution. Hydrogen peroxide (0.98 M) was added to the reaction solution and its decomposition was monitored by measuring volume of oxygen gas evolved. Same setup was used on adding chelant (1.3 mM) to the reaction solution.

### **9.5 Monitoring hydroxyl radical formation in binary metal system**

Hydroxyl radical formation was monitored using NPGA probe as described in section 9.3.2. In binary metal system, two metal ions  $\text{Cu}^{2+}$  (0.18 mM) and  $\text{Ca}^{2+}$  (125 mM) were mixed in the quartz cell. Hydrogen peroxide (0.98 M) was added to the mixture in the cell and UV-vis spectra were recorded immediately against blank. Total volume of the reaction solution was 3 mL. Same setup was used on adding chelant (1.3 mM) to the reaction solution.

### **9.6 Monitoring hydroxyl radical formation in the presence of copper treated hair fibres**

To monitor hydroxyl radical formation in metal-treated hair fibre systems, a 3 mL reaction was carried out by mixing NPGA (1 mM) and hydrogen peroxide (0.98 M) and metal-treated hair fibres (50 mg) in ammonia buffer solution at pH 10 (0.4 M). The reaction aliquots (0.25 mL) were taken at regular intervals and

diluted 10-fold with ammonia buffer. The spectra were recorded immediately using UV-visible spectrophotometer against reagent blank. The same procedure was employed in the presence of chelants.

## **9.7 Experimental procedures for chapter 5**

### **9.7.1 Decomposition of hydrogen peroxide in Cu<sup>2+</sup>-HEDP systems**

Decomposition of hydrogen peroxide was determined using gasometric setup as described in section 9.4.2. Same experimental setup was used for series of experiments using different pH levels, composition of buffer solution and concentrations of copper and HEDP chelant.

### **9.7.2 Isolation & purification of nanoparticles**

Copper sulfate (1.3 mM) and HEDP chelant (1.3 mM) were dissolved in 20 mM pH 10 ammonia/ammonium chloride buffer. Hydrogen peroxide (0.98 M) was added to the reaction vessel (total reaction volume 1L). Addition of hydrogen peroxide immediate triggered the decomposition reaction. The reaction solution was stirred and temperature was maintained at 20 °C. After several minutes, yellow coloured solution was obtained and no further oxygen evolution was observed. A small amount of catalase (0.05 mL of aqueous suspension from Sigma, 20-50 mg/mL) was added to decompose remaining hydrogen peroxide and reaction solution was stirred for 30 minutes. Once all hydrogen peroxide was decomposed, reaction solution was concentrated under vacuum to obtain concentrated nanoparticle solution (200 mL). The nanoparticles solution was purified through dialysis for 24 hours using Medicell International Ltd dialysis membrane [14.3 mm diameter, 30 kD molecular weight cut off (MWCO)].

After the dialysis, the solvent was evaporated under vacuum and a solid residue of nanoparticles was obtained for further experiments.

### **9.7.3 Determination of copper and phosphorus**

Copper and phosphorus contents in nanoparticles residue were determined using atomic absorption spectroscopy (AAS) and inductively coupled plasma-

atomic emission spectroscopy. ICP-AES analysis was carried out at analytical services, University of Manchester.

Nanoparticles (5 mg) were dissolved in 5 M nitric acid (100 mL). A series of copper dilutions (5 – 50 ppm) were prepared in 5 M nitric acid using a standard copper solution from Sigma-Aldrich. These dilutions were analysed using AAS. A standard curve was obtained and concentration of copper in nanoparticle solution was determined. The same sample was then submitted for the quantification of copper and phosphorus to analytical services lab at University of Manchester.

#### **9.7.4 Determination of phosphate contents using molybdenum blue method**

Phosphate content in reaction solution and isolated nanoparticles was determined by molybdenum blue colorimetric method. All glassware was pre-rinsed with 2.5 M sulfuric acid to remove phosphate contamination. The colouring reagent was composed of

- a) Sulfuric acid 2.5 M
- b) Potassium antimonyl tartrate (0.27% solution)
- c) Ammonium molybdate (4% solution)
- d) Ascorbic acid (0.1 M)

The components B (5 mL), C (15 mL) and D (30 mL) were added to A (Sulfuric acid, 50 mL) step by step to form coloring reagent. The solution was thoroughly mixed on each addition.

A standard 1000 ppm phosphate solution was purchased from Sigma-Aldrich. A series of phosphate dilutions (0.25, 0.5, 0.75 & 1.0 ppm concentration levels) were prepared using deionised water. To each standard solution, 8 mL of the colouring agent was added and volume was made up to 100 mL with deionised water. The solution was left for 10 minutes to develop colour. After 10 minutes, spectra were recorded against reagent blank using UV-Vis spectrophotometer and absorption value at 880 nm was used to develop a standard curve.

### **9.7.5 Analysing phosphate contents in the reaction solution**

Copper(II) sulfate (0.18 mM) and HEDP chelant (1.3 mM) were dissolved in 20 mM ammonia/ammonium chloride buffer pH 10. Hydrogen peroxide (0.98 M, total reaction volume 25 mL) was injected to start the decomposition reaction. Sample aliquots (0.2 mL) were taken at regular time intervals and mixed with phosphate colouring reagent (8 mL). The volume of solution was made to 100 mL using deionised water. The solution was left for 10 minutes to develop colour. After 10 minutes, the spectrum was recorded using UV-Vis spectrophotometer against reagent blank.

### **9.7.6 Analysing phosphate in nanoparticles**

Solid residue of nanoparticles (1.9 mg) was directly dissolved in colouring reagent (8 mL). The mixture was stirred to make sure all the solid material was dissolved and subsequently volume was made up to 100 mL using deionised water. The spectrum was recorded against reagent blank. The % phosphate present in the sample was calculated.

### **9.7.7 Determination of carbonate content in nanoparticles**

Amount of carbonate in isolated nanoparticles was determined by IR spectroscopic method quantifying carbon dioxide evolution from nanoparticles. The experimental design involved mixing the nanoparticles with strong concentrated acid to generate carbon dioxide in a closed reaction vessel which was directly connected to gas IR cell of 10 cm path length.

For quantitative determination, a standard curve for carbon dioxide was obtained using a pre-dried anhydrous sodium carbonate mixed with silica. This mixture was mixed with phosphoric acid (85%). The absorption intensity for carbon dioxide at 2360  $\text{cm}^{-1}$  from different levels of sodium carbonate employed was used to obtain a standard curve. Similarly, nanoparticles (15.7 mg) were dissolved in concentrated phosphoric acid (0.5 mL) and gas evolved was analysed.

### **9.7.8 Determining the oxidation state of copper in nanoparticles**

Nanoparticles (2.0 mg) were dissolved in degassed concentrated hydrochloric acid (3 mL) under inert conditions. Experimental setup was degassed at Schlenk line. Solution was further diluted 8 times using degassed hydrochloric acid under inert conditions. UV-vis spectrum was obtained immediately against hydrochloric acid blank. Control experiments containing copper(I) chloride and copper(II) chloride were carried out under same inert conditions.

### **9.7.9 EPR study of copper-HEDP catalysed decomposition of hydrogen peroxide**

Decomposition reaction solution was carried out containing copper(II) sulfate (0.18 mM), HEDP (1.3 mM) in 20 mM pH 10 ammonia/ammonium chloride buffer with hydrogen peroxide (0.98 M) total reaction volume 25 mL. Aliquots (1.6 mL) were mixed with glycerol (0.4 mL) in a quartz EPR tube. The samples were frozen under liquid nitrogen and their spectra were recorded using Bruker EMX machine 120 K at different time intervals.

### **9.7.10 Identifying the active catalyst in copper-HEDP catalysed decomposition of hydrogen peroxide**

Copper(II) sulfate (0.05 mM) was mixed with HEDP chelant (0.05 mM) in 20 mM pH 10 ammonia/ammonium chloride buffer pH 10 in UV-vis quartz cell. Hydrogen peroxide (0.1 mM) was added and spectra were recorded immediately against reagent blank. Spectra obtained every 2 minutes over 120 minutes show changes in the reaction solution.

## **9.8 Experimental procedures for chapter 6**

### **9.8.1 Hydrogen peroxide decomposition the presence of dye primary/coupler or a combination of both**

Reaction was carried out containing copper(II) sulfate at different concentration levels (0.02 mM to 0.18 mM) in ammonia/ammonium chloride buffer. Dye primary or coupler (1mM) or combination both (1 mM each) were added. Reaction setup was completely sealed and closed to prevent any oxygen leakage. Solution was stirred for couple of minutes before adding hydrogen peroxide (0.98 M). Addition of hydrogen peroxide triggered the decomposition reaction and evolution of oxygen gas was monitored with the determined time interval to calculate hydrogen peroxide decomposition.

### **9.8.2 Hydrogen peroxide decomposition on adding pre-oxidised dye mixture**

Equal molar mixture of (25 mM) dye primary and coupler (e.g. PPD & MAP) were mixed together in ammonia/ammonium chloride buffer (25 mL) of pH 10 (400 mM) in a metal-free solution. Hydrogen peroxide (0.98 M) was added and reaction was stirred for 30 minutes. Addition of hydrogen peroxide instantaneously gave coloured solution.

In a separate vessel, a reaction (25 mL) was carried out using copper(II) sulfate (0.02 mM) and hydrogen peroxide (0.98 M). Hydrogen peroxide decomposition was monitored using gasometric setup. At a given time during the reaction, coloured solution made above paragraph (1 mL) was added to this reaction solution and change in oxygen evolution was monitored to determined hydrogen peroxide decomposition.

### **9.8.3 Reducing PPD-MAP oxidative dye using thioglycolic acid**

Dye primary PPD and coupler MAP (1 mM each) were mixed in ammonia/ammonium chloride buffer pH 10 (400 mM) in a round bottle for gasometric setup. Copper(II) sulfate (0.02 – 0.18 mM) was added to the reaction solution and stirred. Hydrogen peroxide (0.98 M) was added to the reaction

solution and subsequently stirred for 30 minutes. After 30 minutes, catalase was added to destroy remaining hydrogen peroxide. Reaction solution was stirred for 15 minutes. After 15 minutes, thioglycolic acid (0.7 M, 5%) was added and reaction solution was stirred for 30 minutes. Reaction solution was subsequently alkalinised to pH 8.0-9.0 by adding measured amount of ammonia (1 mL of 35% standard solution, 0.724 M ammonia).

A reagent blank was prepared containing same composition except dye precursors. Blank was prepared fresh and used immediately. Electronic spectrum was obtained at UV-visible spectrophotometer against reagent blank.

#### **9.8.4 Monitoring hydroxyl radical formation in the presence of dye precursors**

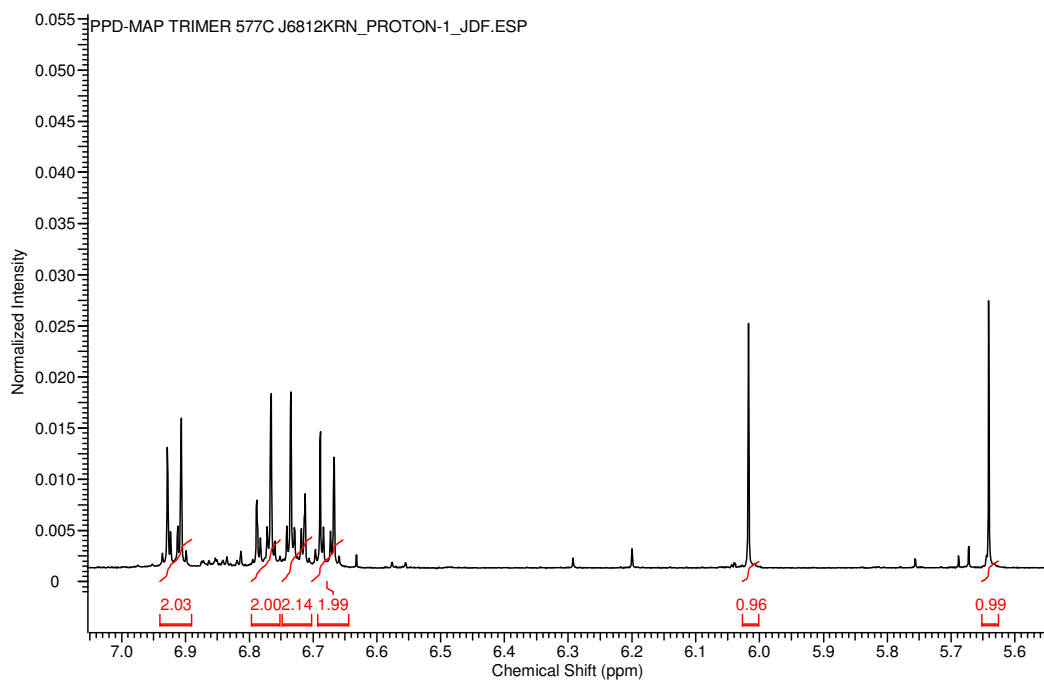
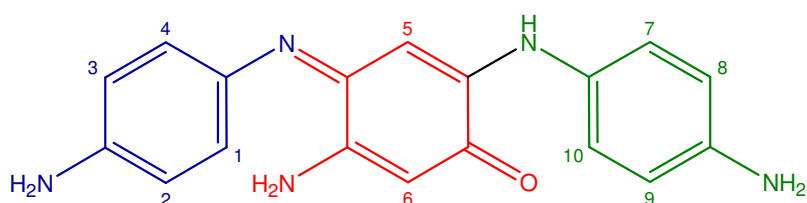
Dye primary PPD, coupler MAP and NPGA colorimetric probe (1 mM each) were mixed in ammonia/ammonium chloride buffer pH 10 (400 mM) in a round bottle of the gasometric setup. Copper(II) sulfate (0.02 – 0.18 mM) was added to the reaction solution and stirred. Hydrogen peroxide (0.98 M) was added to the reaction solution and subsequently stirred for 30 minutes. After 30 minutes, catalase was added to destroy remaining hydrogen peroxide. Reaction solution was stirred for 15 minutes. After 15 minutes, thioglycolic acid (0.7 M, 5%) was added and reaction solution was stirred for 30 minutes. Reaction solution was subsequently alkalinised to pH 8.0-9.0 by adding measured amount of ammonia (1 mL of 35% standard solution, 0.724 M ammonia).

A reagent blank was prepared containing same composition except NPGA probe. Blank was prepared fresh and used immediately. Electronic spectrum was obtained at UV-visible spectrophotometer against reagent blank.

#### **9.8.5 Synthesis of PPD-MAP tri-nuclear dye**

PPD (216.28 mg, 2.0 mmoles) and MAP (218.25 mg, 2.0 mmoles) were dissolved in ammonia/ammonium chloride buffer pH 10 (100mL). Copper(II) sulfate (0.5 mg) was added to the reaction mixture. Hydrogen peroxide (0.01 moles) was added and reaction was stirred for 30 minutes. After 30 minutes, catalase (0.1 mL of 3.4 protein/mL stock solution) was added to destroy remaining hydrogen peroxide. Reaction was left for 2 hours in ice bath and later

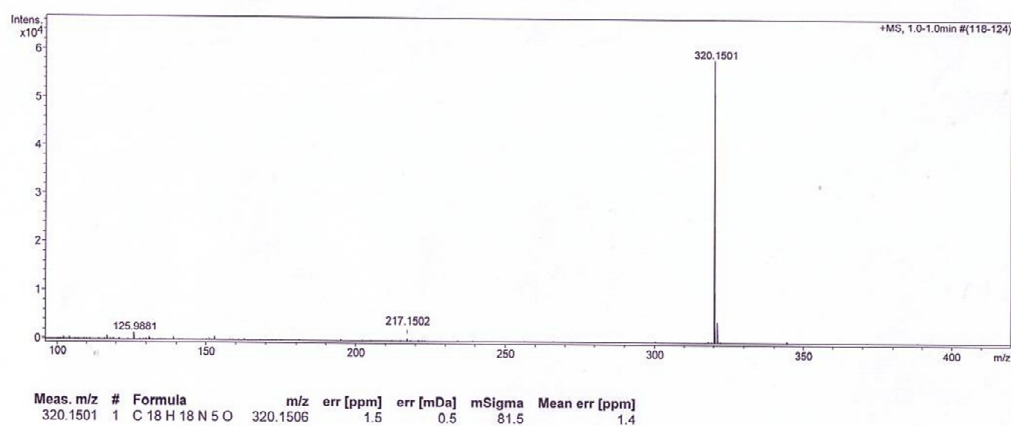
on was centrifuged. A solid residue was obtained, which was dried under vacuum overnight. TLC for the crude residue showed three spots. Two of them were very faint while third was intense brown black. Product was purified by prep-TLC plates using chloroform, ethyl acetate and ethanol (7:2:1). Brown black spot was erased and extracted using methanol and characterised by NMR and MS. The results show that isolated material is PPD-MAP tri-nuclear dye.  $^1\text{H}$  NMR (400 MHz,  $\text{CD}_3\text{OD}$ ):  $\delta$ = 6.95 – 6.89 (m, 2H, H1, H4), 6.80 – 6.65 (m, 6H, H2, H3, H7, H8, H9, H10), 6.02 (s, 1H, H5), 5.64 (s, 1H, H6). MS ESI  $[\text{M}+\text{H}^+]$ : 320.1501 Calc: 320.1506 m/z.



## Analysis Information

Analysis Filename vc41174kn\_1-f\_2\_01\_44520.d  
Method 400p\_meoh.m  
Submission Name vc41174kn  
Instrument micrOTOF  
ESI Positive

Acquisition Date 29/04/2013 10:09:48



### 9.8.6 Monitoring decomposition of hydrogen peroxide on adding PPD-MAP trinuclear dye

PPD-MAP trimer was dissolved in 1 mL ammonia/ammonium chloride buffer pH 10 400mM using sonicator. Despite sonicating for 15-20 minutes, it still contained some insoluble components demonstrating the low solubility of trimer.

Reaction solution (25 mL) contained copper(II) sulfate (0.02 mM) in a ligand-free system. PPD-MAP trimer solution (0.5 mL) was added (this gives approx 0.25mM trimer) to the reaction solution (25 mL). Solution was stirred for 15 minutes to make sure trimer is completely dissolved. Hydrogen peroxide (0.98 M) was added and its decomposition was monitored using gasometric setup.

### 9.9 Experimental procedures for chapter 7

All infrared spectra reported here were obtained in absorption mode using Thermo Nicolet Avatar-370 FT-IR spectrophotometer. A total of 16 scans were recorded for each analysis at 2 cm<sup>-1</sup> spectral resolution. A gas IR cell with 200 mL internal volume and sodium chloride windows was used throughout the study. Anhydrous sodium carbonate and phosphoric acid (85%) was purchased from Sigma-Aldrich, UK.

### 9.9.1 Image analysis

SEM images for the hair fibres were taken by P & G in Cincinnati, USA. Each image was processed individually using Google image program Picasa version 3.0. Picasa is accessible and can be downloaded free of cost from [www.google.com](http://www.google.com). The image pixel data were converted into measurements of height, width and diameter which were subsequently used to determine volume or area of the given object present in the image.

### 9.9.2 Calculating mass of human hair fibre from its SEM image

The dimensions of each fibre in the image were estimated using an SEM scale bar. Assuming the fibre is a cylindrical object; its volume was calculated using the following equation

$$\text{Volume of single hair fibre} = \pi r^2 h,$$

where  $r$  is radius and  $h$  is height from the SEM image.

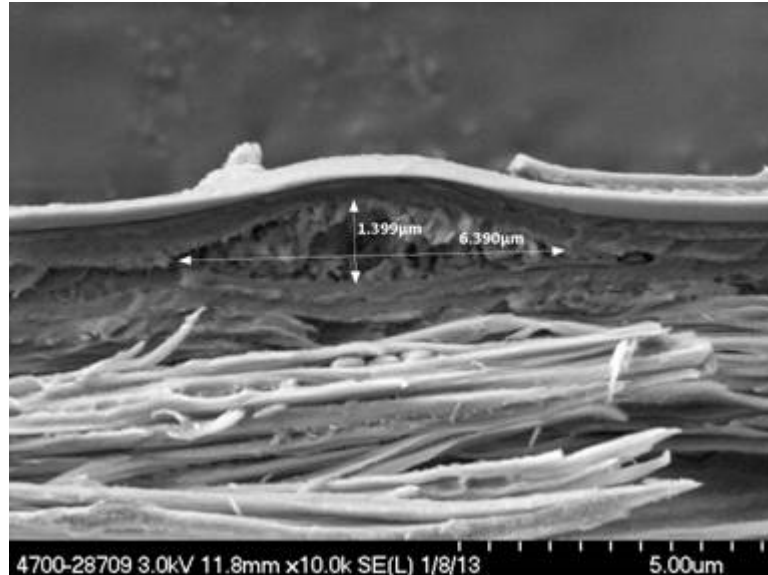


Figure 9-3: Cross-sectional SEM image of a human hair showing bubble underneath the cuticles.

Human hair density at 65% relative humidity reported in the literature<sup>229</sup> is  $1.32 \text{ g/cm}^3$ . So, the mass of the fibre was calculated as

$$\text{Mass} = \text{density} \times \text{volume}$$

This analysis was repeated for fifty images from all switches of various bubble count levels.

### **9.9.3 Calculating volume of a single bubble from SEM images**

SEM cross sectional images were obtained showing cross section of a single bubble. The imaging also showed the diameter and length of each bubble. These values were used to calculate volume of single bubble using the following equation. An average of 10 images was taken.

$$\text{Volume of disc cap} = 1/6 \pi h (3a^2 + h^2)$$

where  $a$  is radius and  $h$  is the height.

### **9.9.4 Characterising various hair switches and counting the number of bubbles per hair fibre**

Various hair switches were obtained using human hair from local consumers around Cincinnati, USA. Each switch contained two grams of hair fibres. SEM images of approximately fifty fibres were obtained for different hair switches chosen randomly. The image data characterised hair switches with different levels of bubbles and defined “hair bubble count” which is the number of hair fibres containing bubbles out of fifty fibres analysed under SEM.

### **9.9.5 Initial control experiments and designing new experimental setup**

A series of control experiments were carried out to optimise the Schlenk line evacuation time and pressure drop from IR cell. Initially carbon dioxide was collected and handled using syringes. However, they suffered with leakage and thus poor reproducibility was observed. To address this problem, a new reaction setup was designed where reaction vessel was connected directly to IR cell as show in Figure 9-4. The setup was evacuated for multiple times and flushed with nitrogen gas repeatedly in a cycle to make sure no residual air is present inside the reaction setup. It was followed by a two hour evacuation on a Schlenk line.

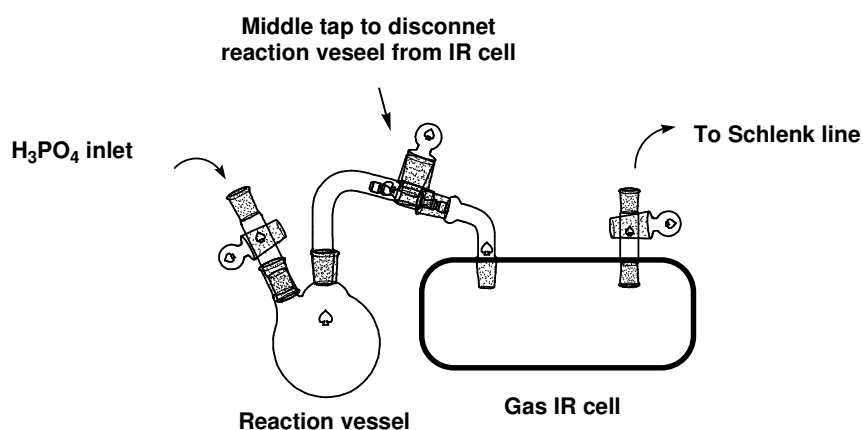


Figure 9-4: Schematic diagram of experimental setup for IR analysis of carbon dioxide.

The spectra were recorded immediately after evacuation of the cell. A delay of more than 10 minutes in recording the spectra resulted in increased interference from atmospheric carbon dioxide. Reaction vessel was always rinsed off with dilute hydrochloric acid followed by deionised water and dried in oven.

### 9.9.6 Recording IR spectra of atmospheric carbon dioxide

The above experimental setup was evacuated on a Schlenk line following the procedure described in the previous section. Empty evacuated cell was used to record the background spectra. IR cell taps were opened to release the pressure and the spectrum was obtained. Five spectra were collected and averaged.

### 9.9.7 Control experiment without using hair fibres

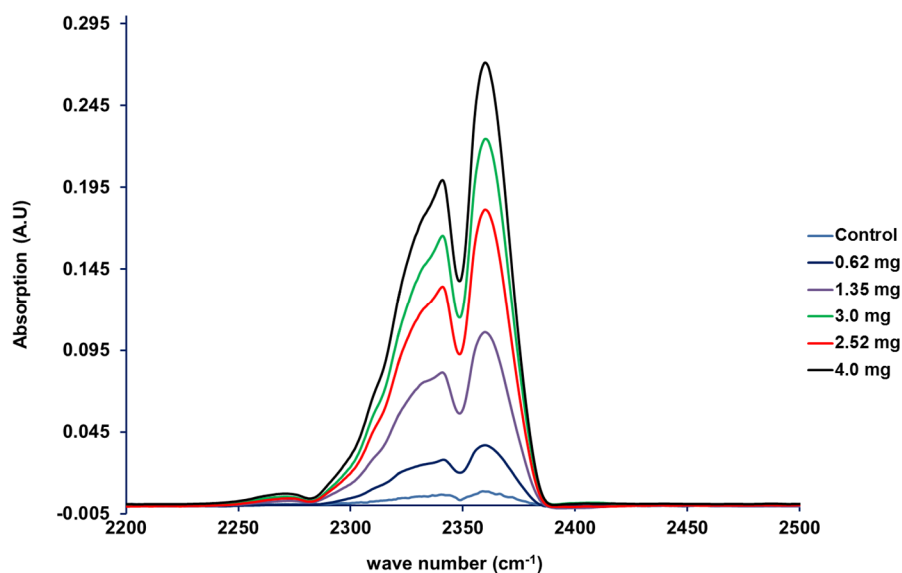
Reaction vessel containing teflon stirring bar was evacuated at schlenk line for two hours. The middle tap between the IR cell and reaction vessel in the experimental setup was closed and 10 mL of concentrated phosphoric acid was added to the reaction flask using syringe. Reaction vessel was immediately filled with nitrogen gas. Phosphoric acid was stirred for five minutes. After 5 minutes, reaction setup was placed in an IR spectrophotometer chamber. Empty evacuated cell was used to obtain the background spectrum. The middle tap was opened and gas from reaction vessel was drawn into IR cell due to negative pressure inside the IR cell. The tap was opened only for 10-15 seconds and

closed afterwards. The spectrum was recorded immediately. The experiment was repeated to obtain five spectra.

### 9.9.7.1 Developing a standard curve

Pre-dried sodium carbonate was mixed with silica gel (10% solid to solid mixture). The mixture was grounded using mortar and pestle to make sure the two solid components are uniformly mixed. This solid to solid mixture was standardised to determine actual amount of sodium carbonate by titration with methyl orange as indicator.

Accurately weighed amount of above mixture was taken in a reaction vessel. The setup was evacuated for two hours and phosphoric acid (10 mL) was added to the mixture. The reaction was stirred for five minutes and absorption spectrum for carbon dioxide was obtained against evacuated IR cell background. The experiment was carried out for five different concentrations. The absorption intensity of carbon dioxide at  $2360\text{ cm}^{-1}$  was plotted against amount of sodium carbonate to develop a standard curve which demonstrated a linear correlation following Beer-Lambert law.



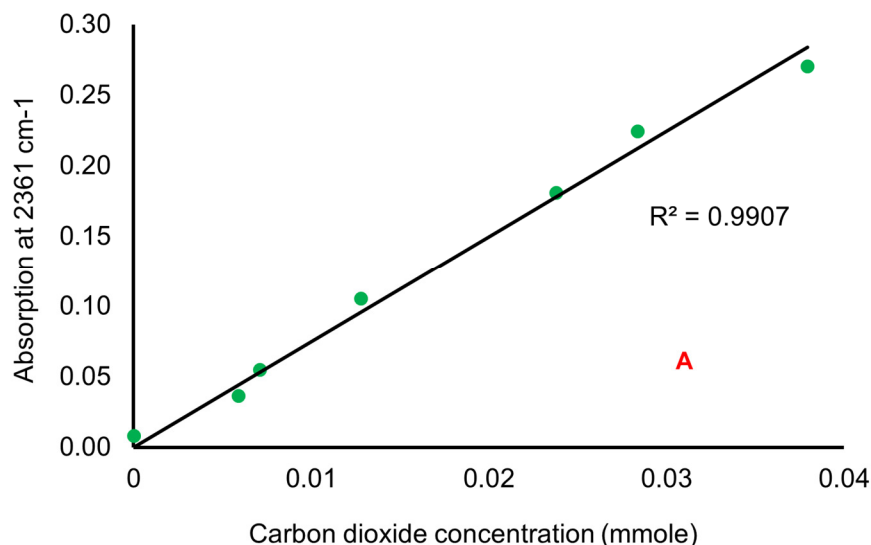


Figure 9-5: IR spectra for carbon dioxide from various concentration levels of sodium carbonate to develop a standard curve.

### 9.9.8 IR analysis of human hair fibres for calcium carbonate

Hair fibres (250 mg) were cut into small pieces and placed in the reaction vessel using the reaction setup described above. It was evacuated on a Schlenk line for two hours. On disconnecting the reaction vessel from IR cell, phosphoric acid (10 mL) was added to the reaction vessel. Ten millilitres of acid was enough to submerge all hair fibres. Reaction was stirred for five minutes. After recording the background spectrum for empty evacuated cell blank, middle tap was opened and spectrum of carbon dioxide evolved was recorded. At least a duplicate analysis was carried out for each switch of hair fibres. An average for carbon dioxide absorption intensity was obtained which was utilised to calculate the amount of calcium carbonate present in hair using standard curve. Standard deviation and standard error of mean were also calculated.

### 9.9.9 IR analysis of pulverised human hair fibres for calcium carbonate

Human hair fibres were pulverised under nitrogen environment. The ground hair powder (100 mg) was taken in the IR reaction vessel. The whole setup was evacuated using Schlenk line for two hours. On closing the middle tap to disconnect IR cell from the reaction vessel, phosphoric acid (10 mL) was added

to the reaction vessel. Reaction mixture was stirred for five minutes and spectrum of carbon dioxide evolved was obtained against empty evacuated cell blank.

# 10 Appendices

## 10.1 Appendix I

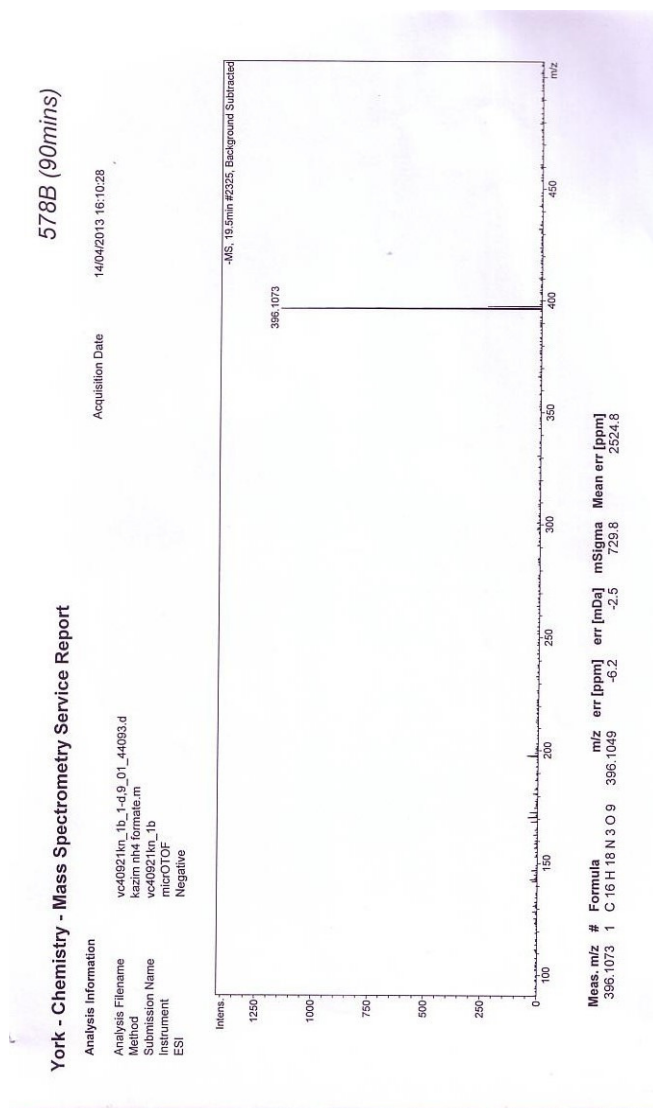


Figure 10-1: MS spectrum for H-NPGA in LC-MS analysis confirming the formation of H-NPGA derivative at 90<sup>th</sup> minute of hydroxylation. MS-ESI m/z [M-H]<sup>+</sup> Found 396.1060 (Calculated for C<sub>16</sub>H<sub>18</sub>N<sub>3</sub>O<sub>9</sub>: 396.1049)

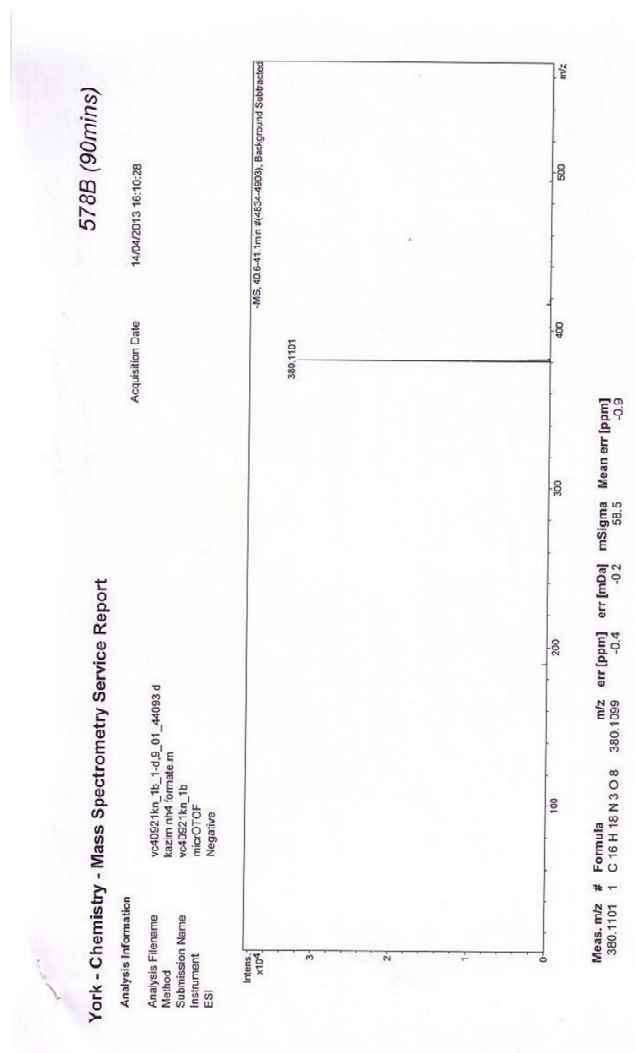


Figure 10-2: MS spectrum demonstrating presence of starting NPGA probe. MS-ESI m/z [M-H]<sup>+</sup> Found 380.1101 (Calculated for C<sub>16</sub>H<sub>18</sub>N<sub>3</sub>O<sub>8</sub>: 380.1099).

## 10.2 Appendix II

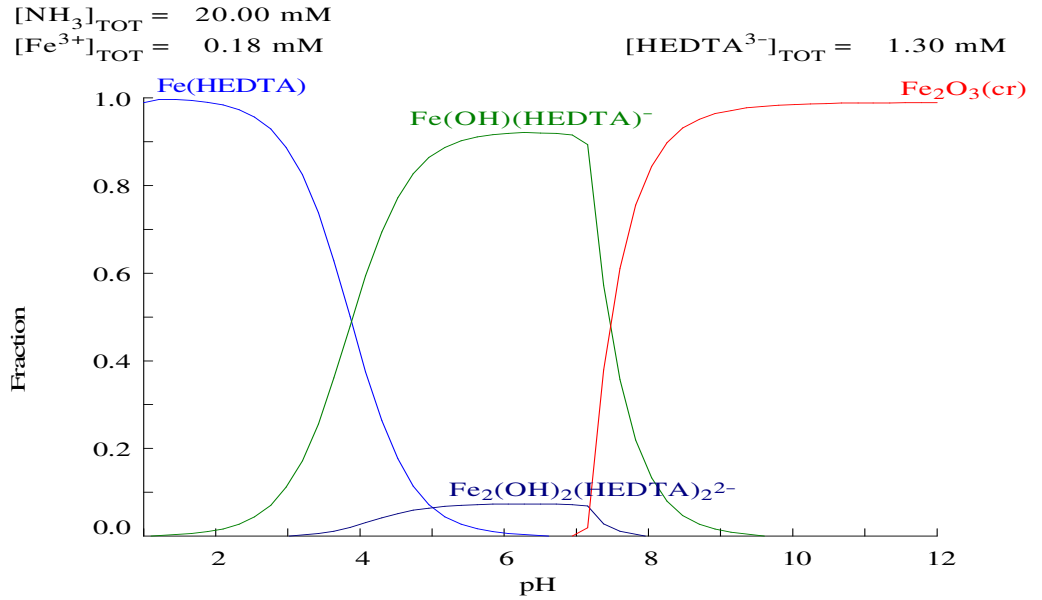


Figure 10-3: Iron(III) speciation in  $\text{Fe}^{3+}$ -HEDTA system.

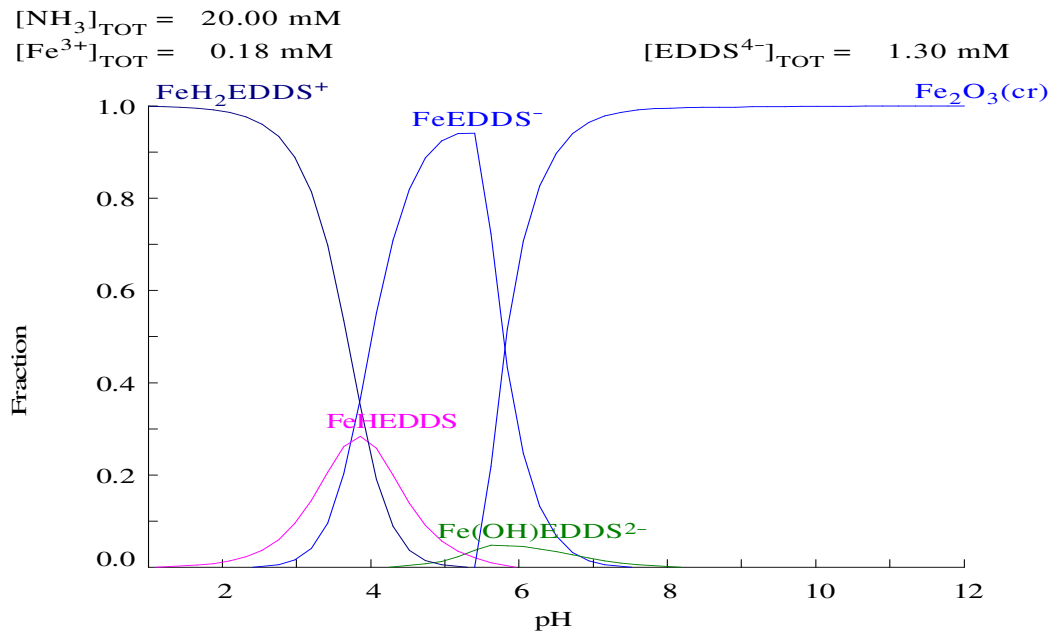


Figure 10-4: Iron(III) speciation in  $\text{Fe}^{3+}$ -EDDS system.

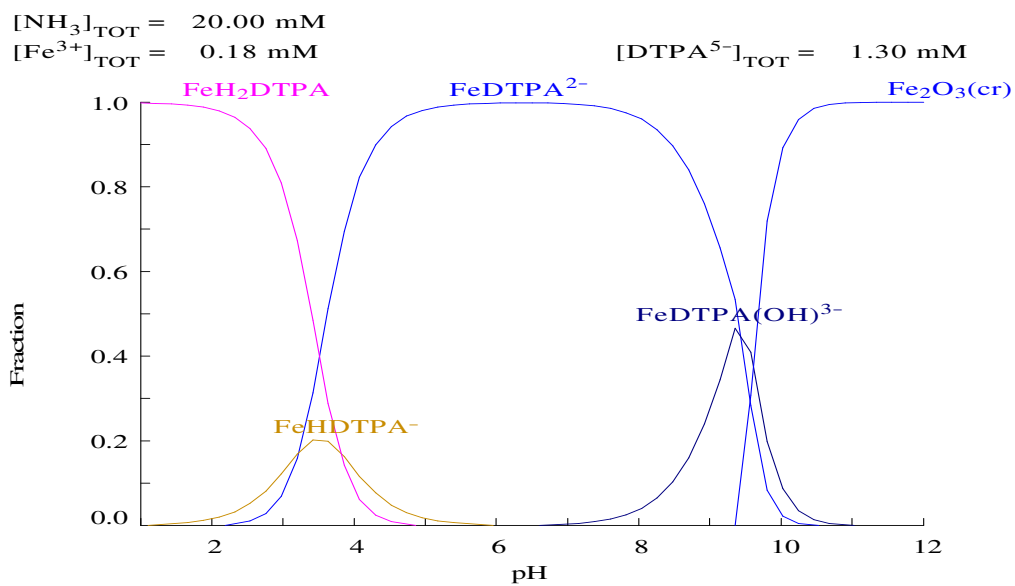


Figure 10-5: Iron(III) speciation in Fe<sup>3+</sup>-DTPA system.

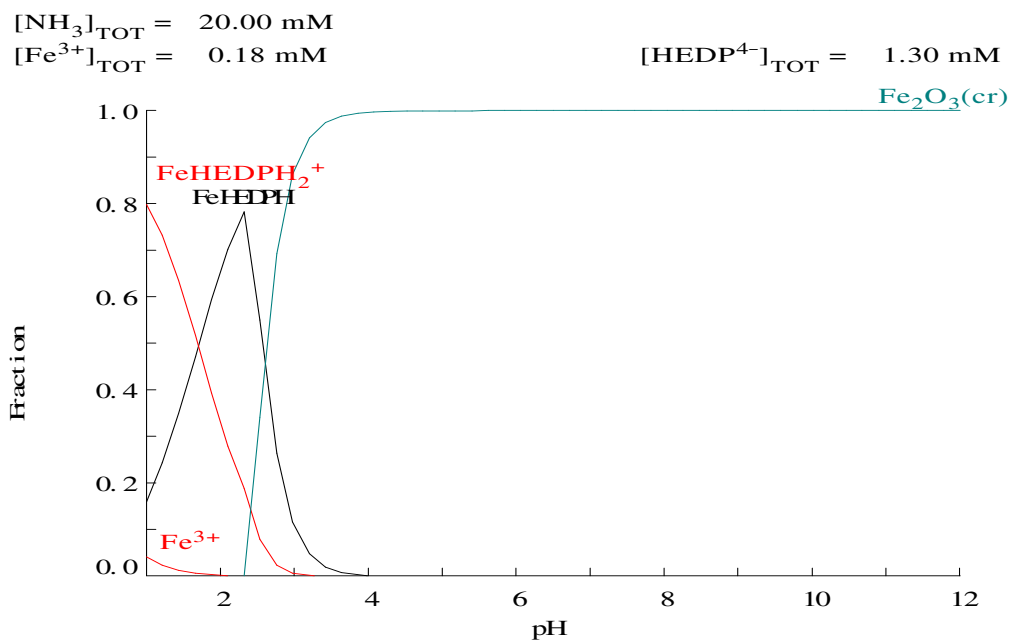


Figure 10-6: Iron(III) speciation in Fe<sup>3+</sup>-HEDP system.

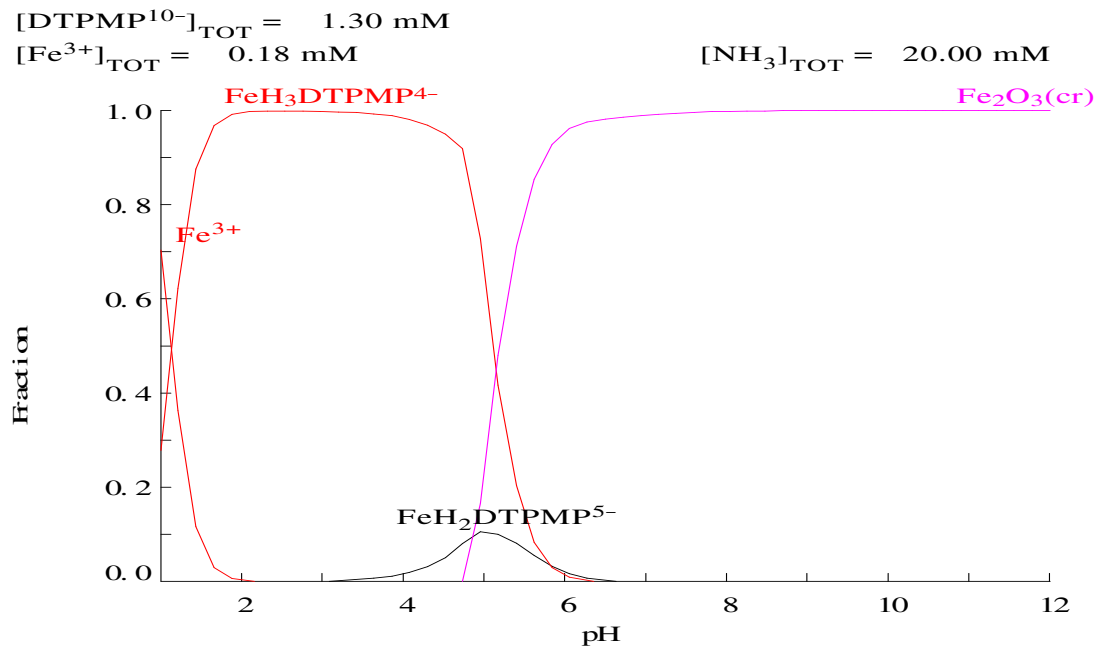


Figure 10-7: Iron(III) speciation in  $\text{Fe}^{3+}$ -DTPMP system.

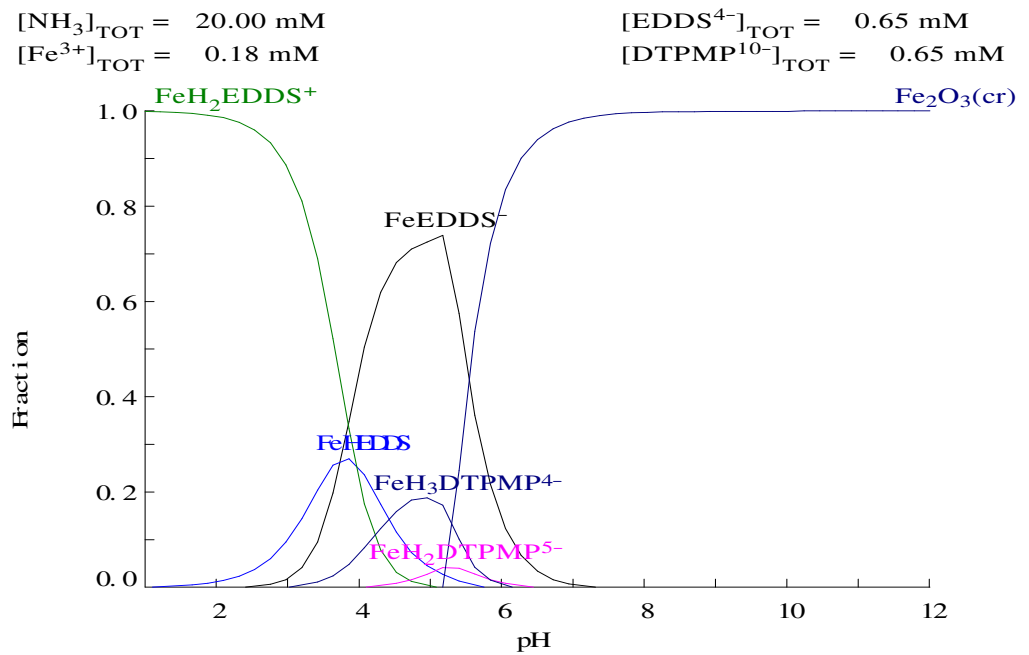


Figure 10-8: Iron(III) speciation in  $\text{Fe}^{3+}$ -EDDS/DTPMP mixed ligand system.

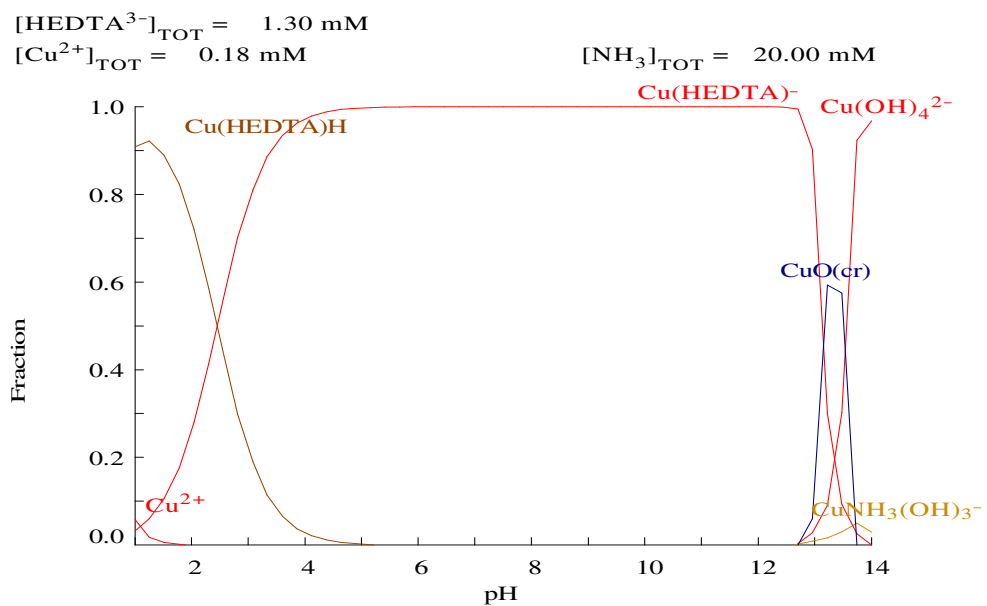


Figure 10-9: Copper(II) speciation in  $\text{Cu}^{2+}$ -HEDTA system.

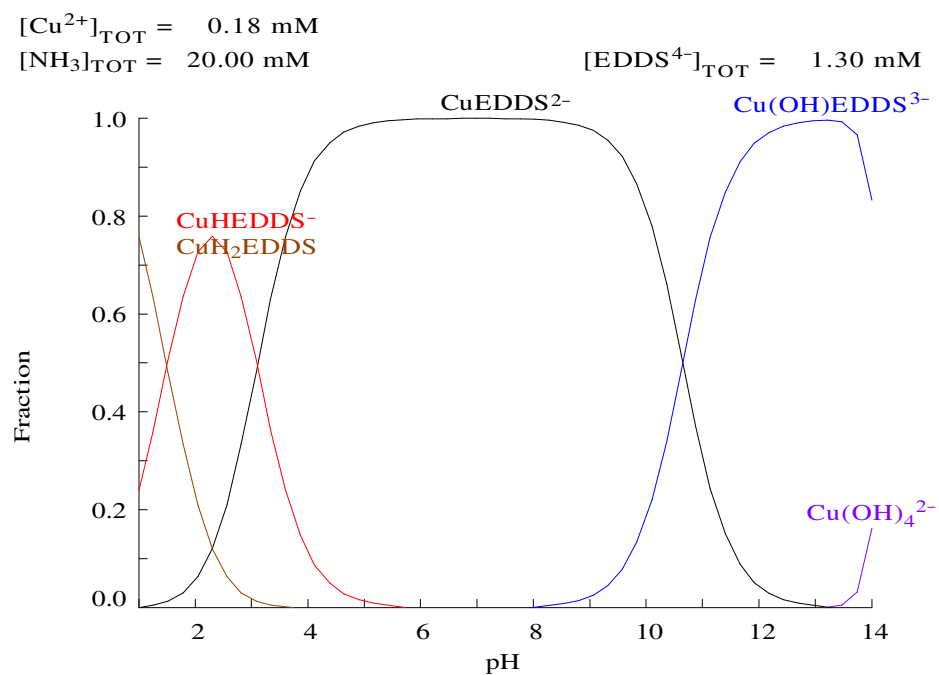


Figure 10-10: Copper(II) speciation in  $\text{Cu}^{2+}$ -EDDS system.

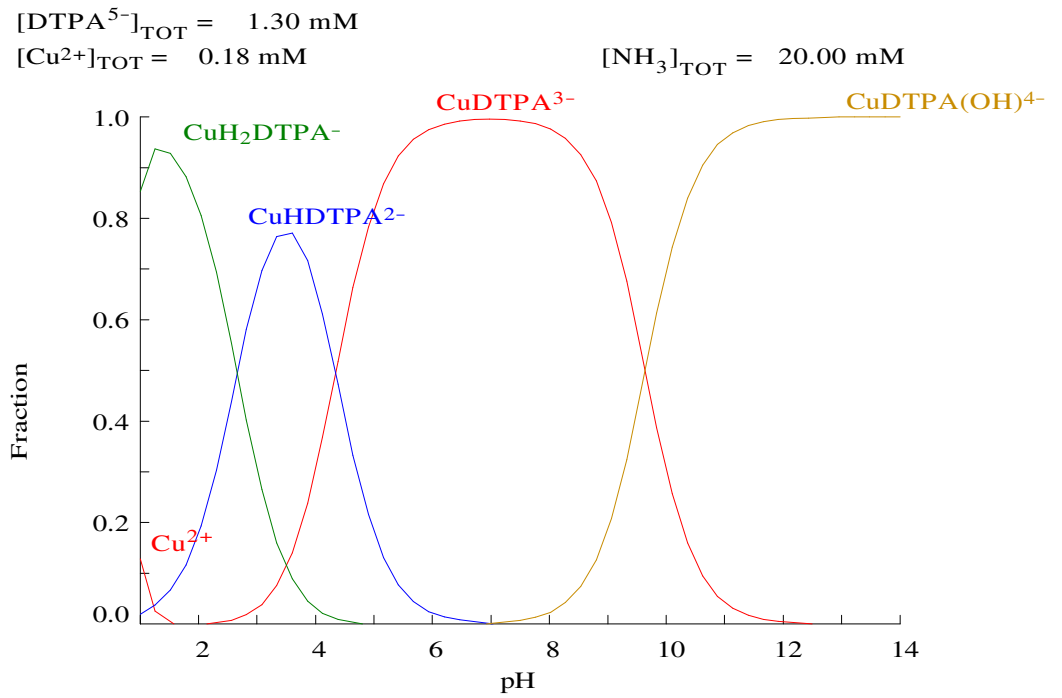


Figure 10-11: Copper(II) speciation in  $\text{Cu}^{2+}$ -DTPA system.

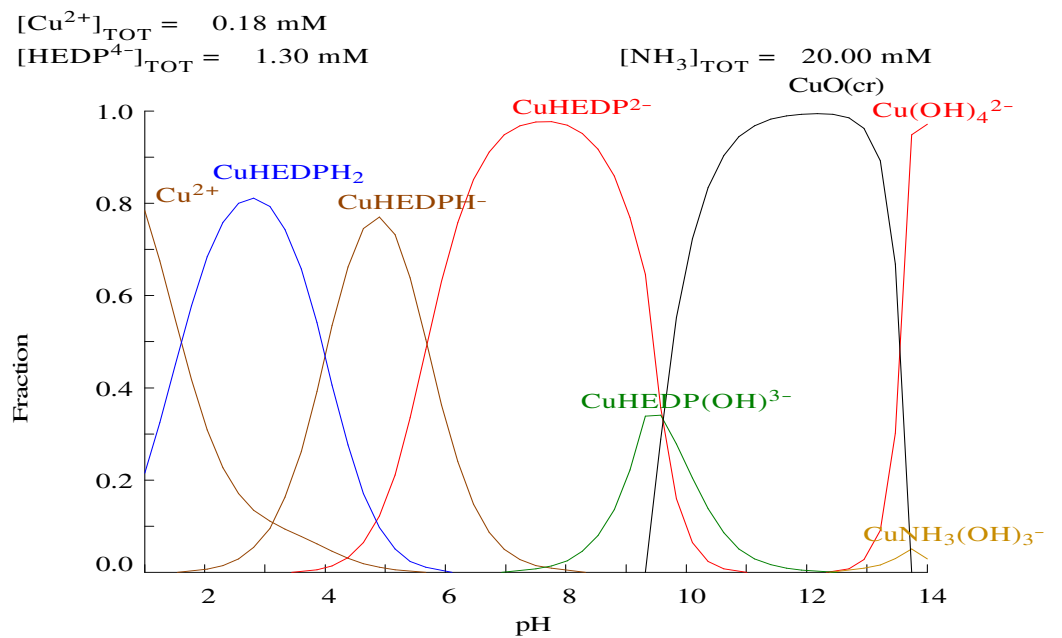


Figure 10-12: Copper(II) speciation in  $\text{Cu}^{2+}$ -HEDP system.

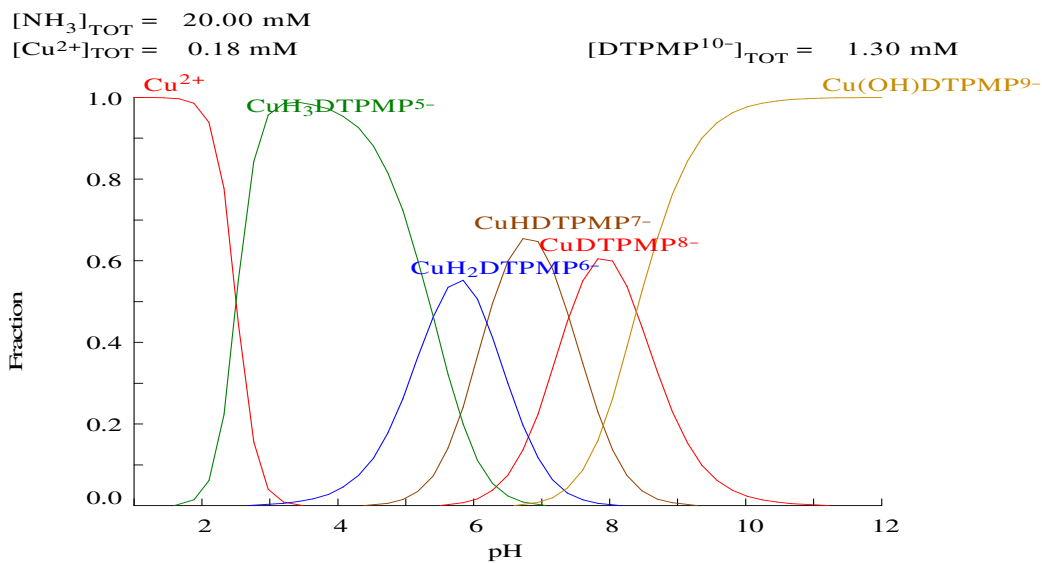


Figure 10-13: Copper(II) speciation in  $\text{Cu}^{2+}$ -DTPMP system.

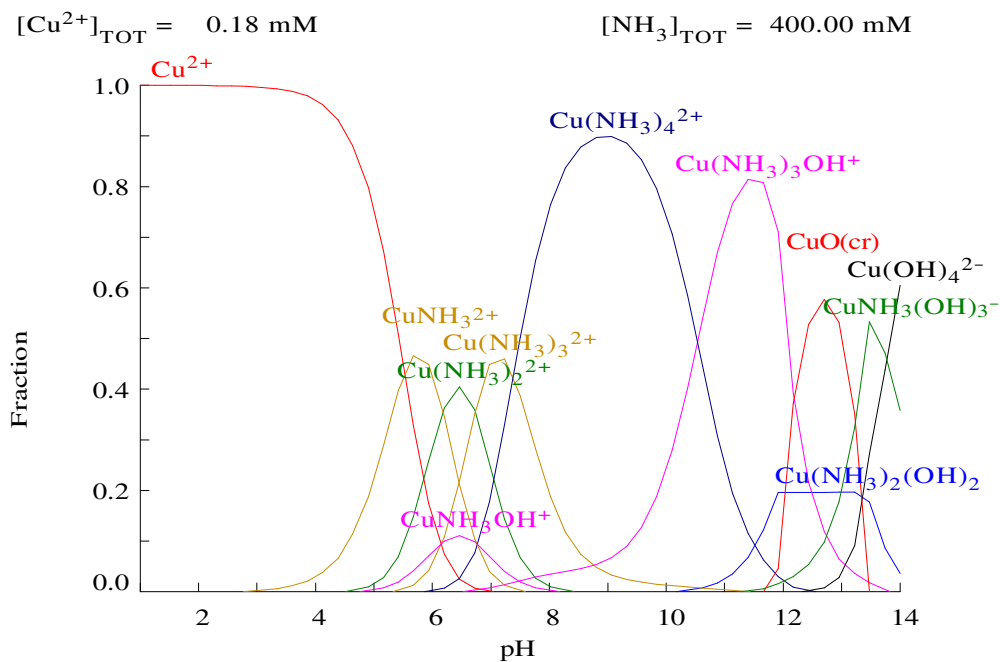


Figure 10-14: Copper(II) ions speciation at high ammonia level (400 mM) in the absence of calcium ions.

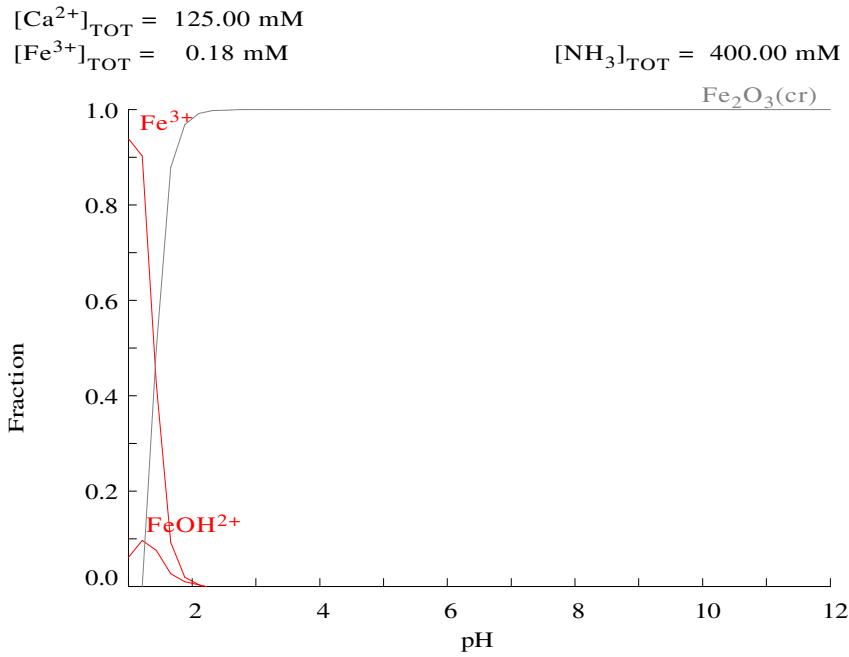


Figure 10-15: Iron(III) speciation in the presence of calcium in a chelant-free system.

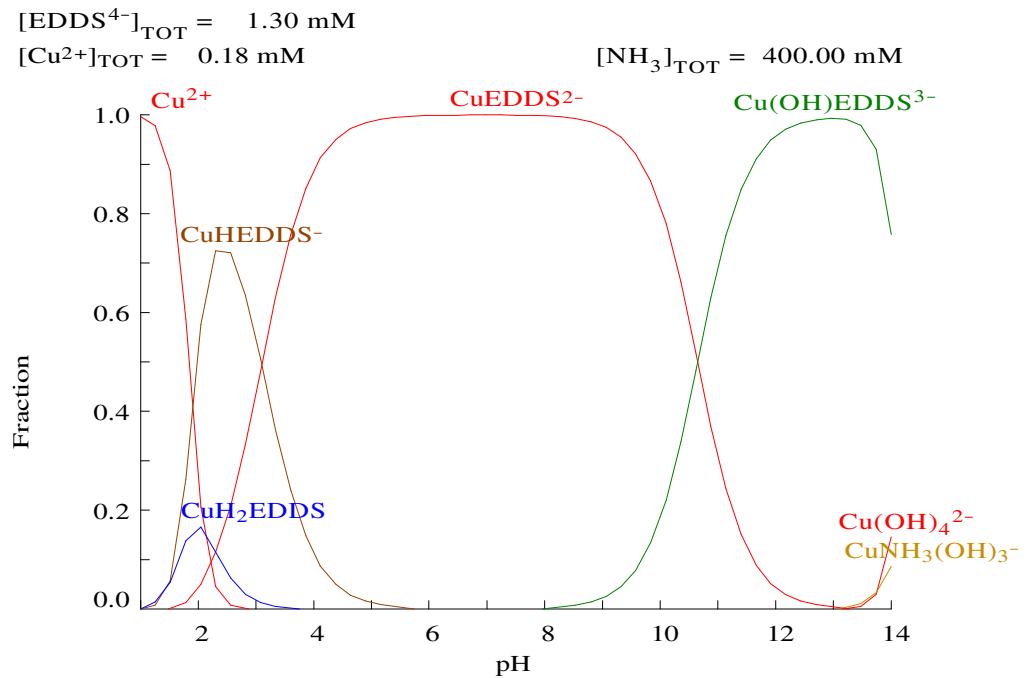


Figure 10-16: Copper speciation in EDDS system at higher ammonia concentration level (400 mM).

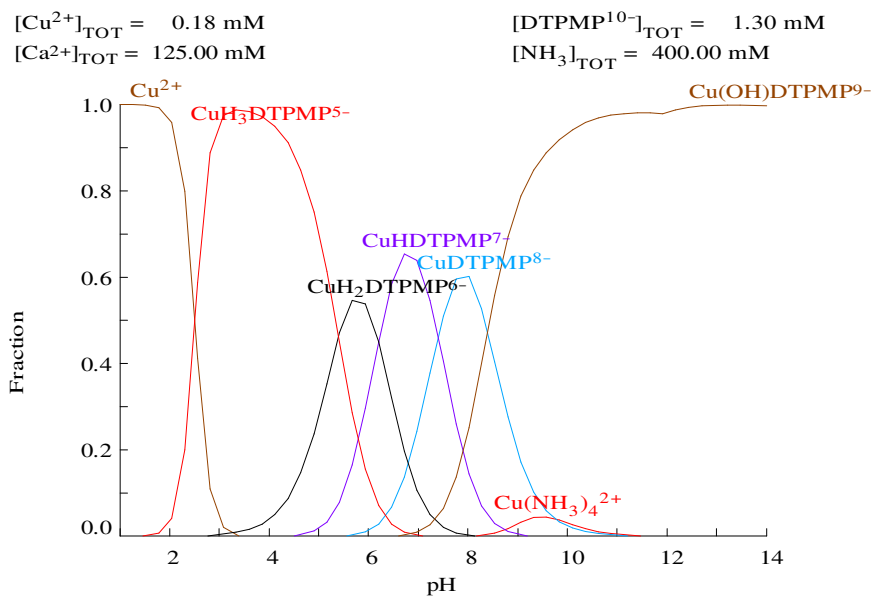


Figure 10-17: Copper ion speciation in DTPMP system in the presence of large excess of calcium ions.

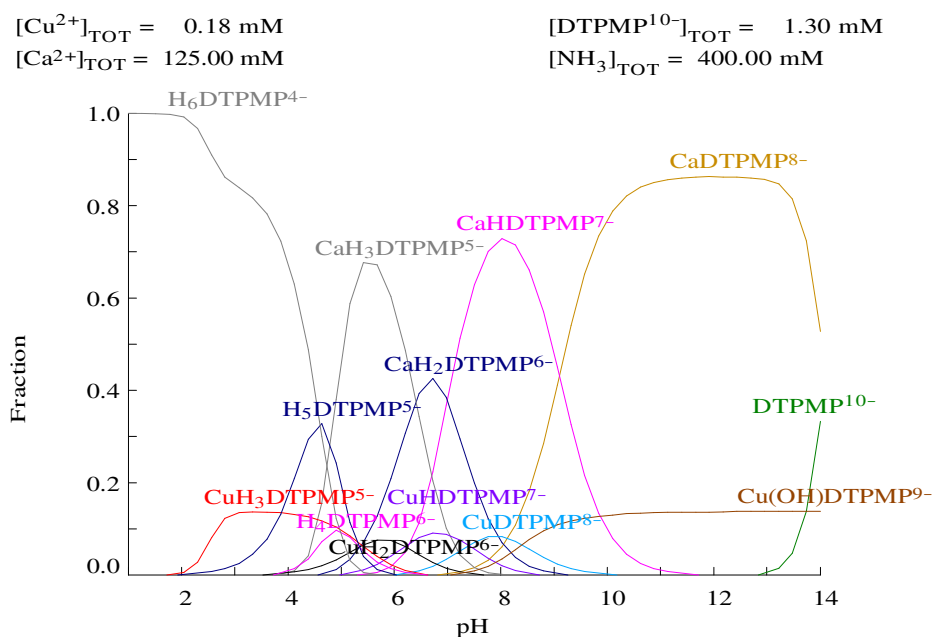


Figure 10-18: DTPMP speciation in copper-calcium binary system.

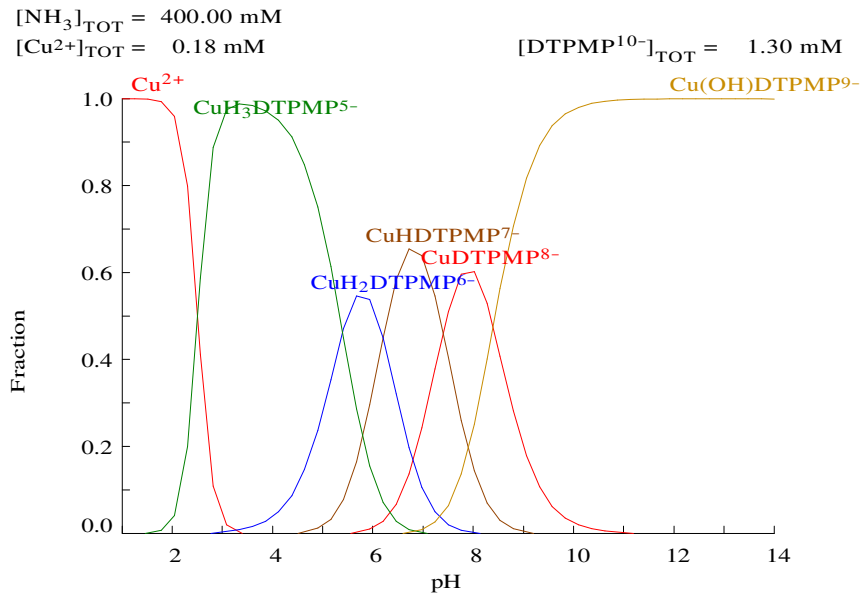


Figure 10-19: Copper speciation in DTPMP chelant system in the absence of calcium ions at higher ammonia level.

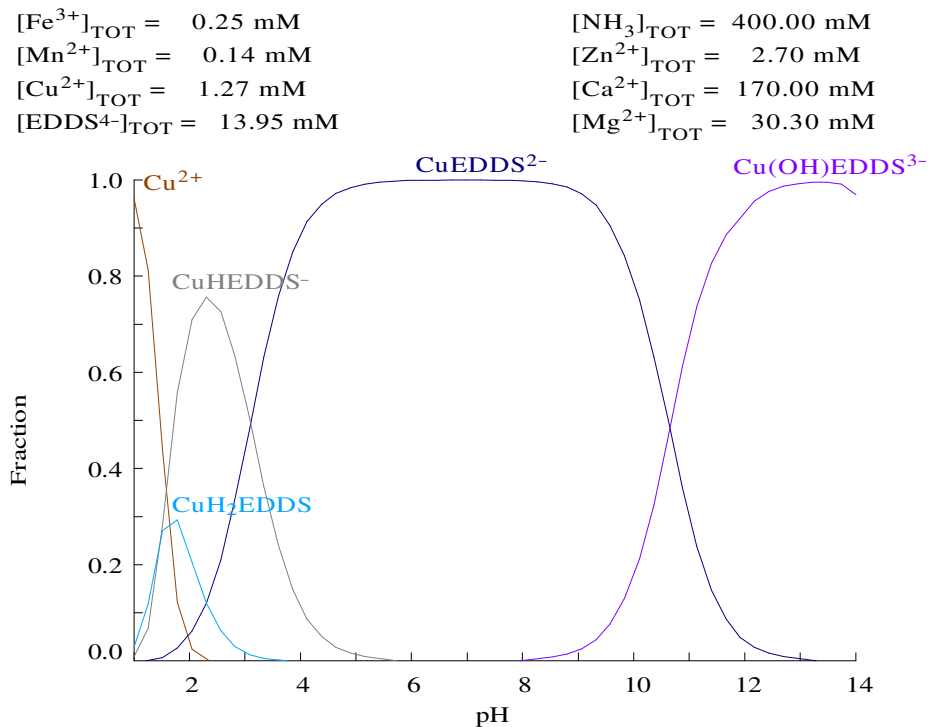


Figure 10-20: Copper speciation in Hair-EDDS chelant system using copper treated hair fibres.

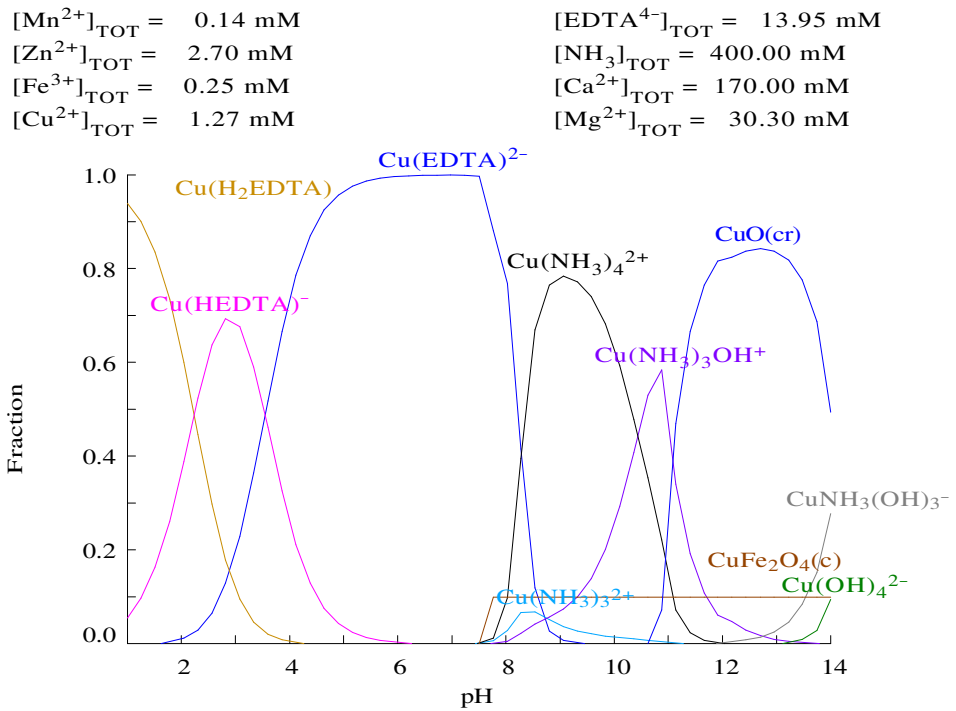


Figure 10-21: Copper speciation in Hair-EDTA chelant system using copper treated hair fibres.

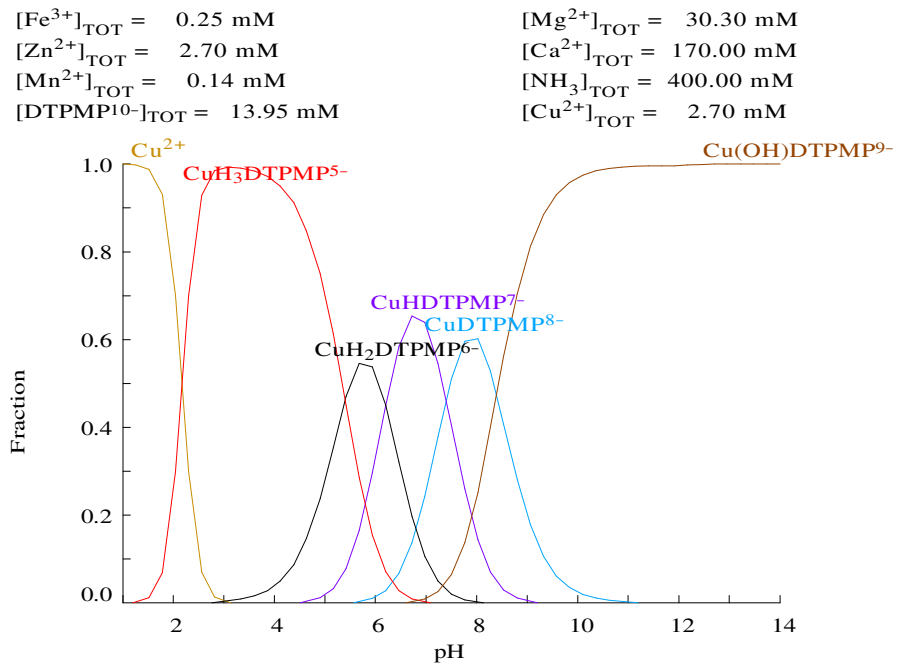


Figure 10-22: Copper speciation in Hair-DTPMP chelant system using copper treated hair fibres.

$[\text{Fe}^{3+}]_{\text{TOT}} = 0.25 \text{ mM}$                        $[\text{NH}_3]_{\text{TOT}} = 400.00 \text{ mM}$   
 $[\text{Mn}^{2+}]_{\text{TOT}} = 0.14 \text{ mM}$                        $[\text{Zn}^{2+}]_{\text{TOT}} = 2.70 \text{ mM}$   
 $[\text{Cu}^{2+}]_{\text{TOT}} = 1.27 \text{ mM}$                        $[\text{Ca}^{2+}]_{\text{TOT}} = 170.00 \text{ mM}$   
 $[\text{EDDS}^{4-}]_{\text{TOT}} = 0.93 \text{ mM}$                        $[\text{Mg}^{2+}]_{\text{TOT}} = 30.30 \text{ mM}$

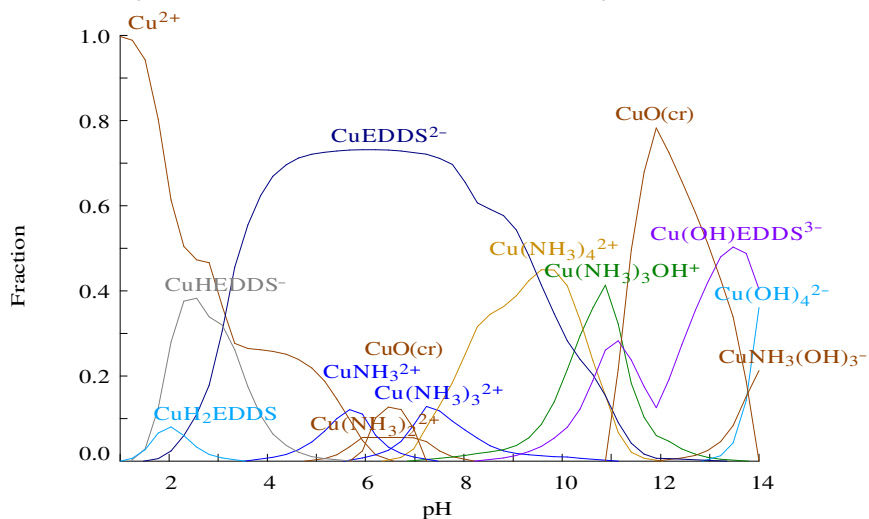


Figure 10-23: Copper speciation in hair-EDDS system using a low concentration of EDDS ligand.

$[\text{Mn}^{2+}]_{\text{TOT}} = 0.14 \text{ mM}$                        $[\text{EDTA}^{4-}]_{\text{TOT}} = 0.93 \text{ mM}$   
 $[\text{Zn}^{2+}]_{\text{TOT}} = 2.70 \text{ mM}$                        $[\text{NH}_3]_{\text{TOT}} = 400.00 \text{ mM}$   
 $[\text{Fe}^{3+}]_{\text{TOT}} = 0.25 \text{ mM}$                        $[\text{Ca}^{2+}]_{\text{TOT}} = 170.00 \text{ mM}$   
 $[\text{Cu}^{2+}]_{\text{TOT}} = 1.27 \text{ mM}$                        $[\text{Mg}^{2+}]_{\text{TOT}} = 30.30 \text{ mM}$

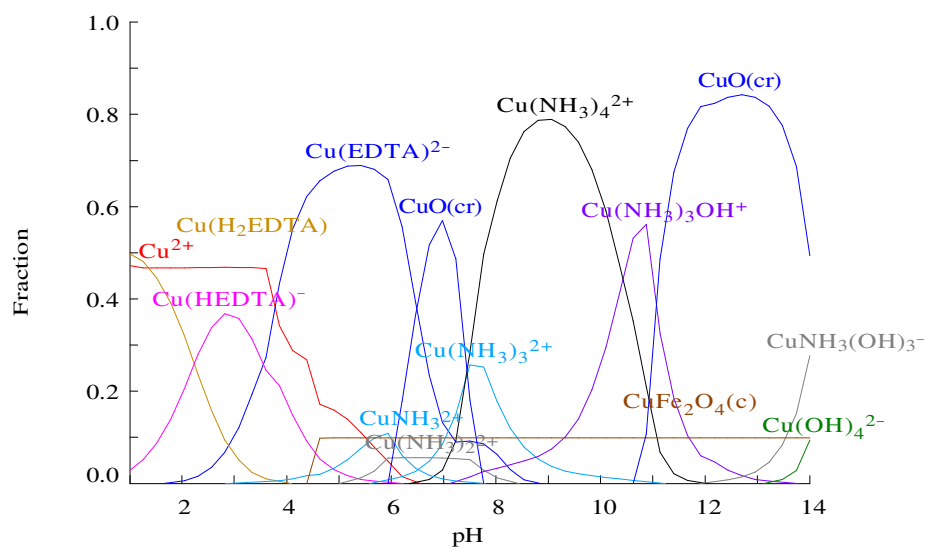


Figure 10-24: Copper speciation in hair-EDTA system using low concentration of EDTA ligand.

### 10.3 Appendix III

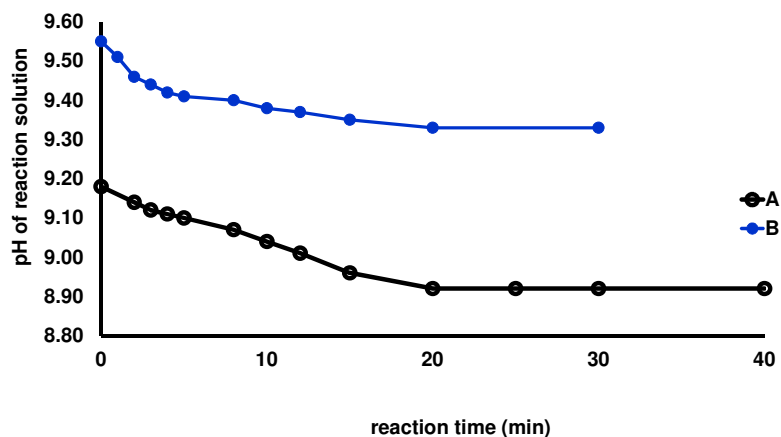
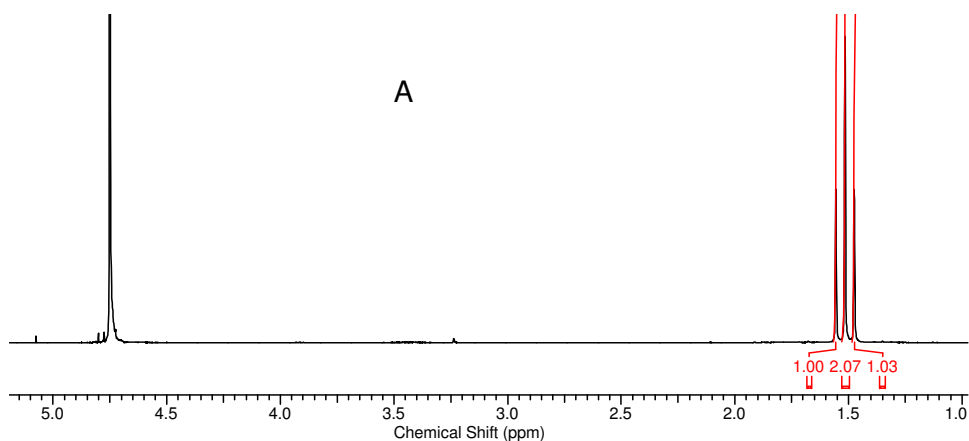


Figure 10-25: pH drop in  $\text{Cu}^{2+}$ -HEDP decomposition system. Reaction solution contained 0.18 mM  $\text{Cu}^{2+}$  ions and 1.3 mM HEDP chelant at pH 10 with 20 mM ammonia/ammonium chloride buffer. Hydrogen peroxide (0.98 M) was added to trigger the decomposition reaction. (A) Bench mark reaction solution (B) initial pH of the reaction solution adjusted to 9.55 using few drops of dilute ammonia solution.



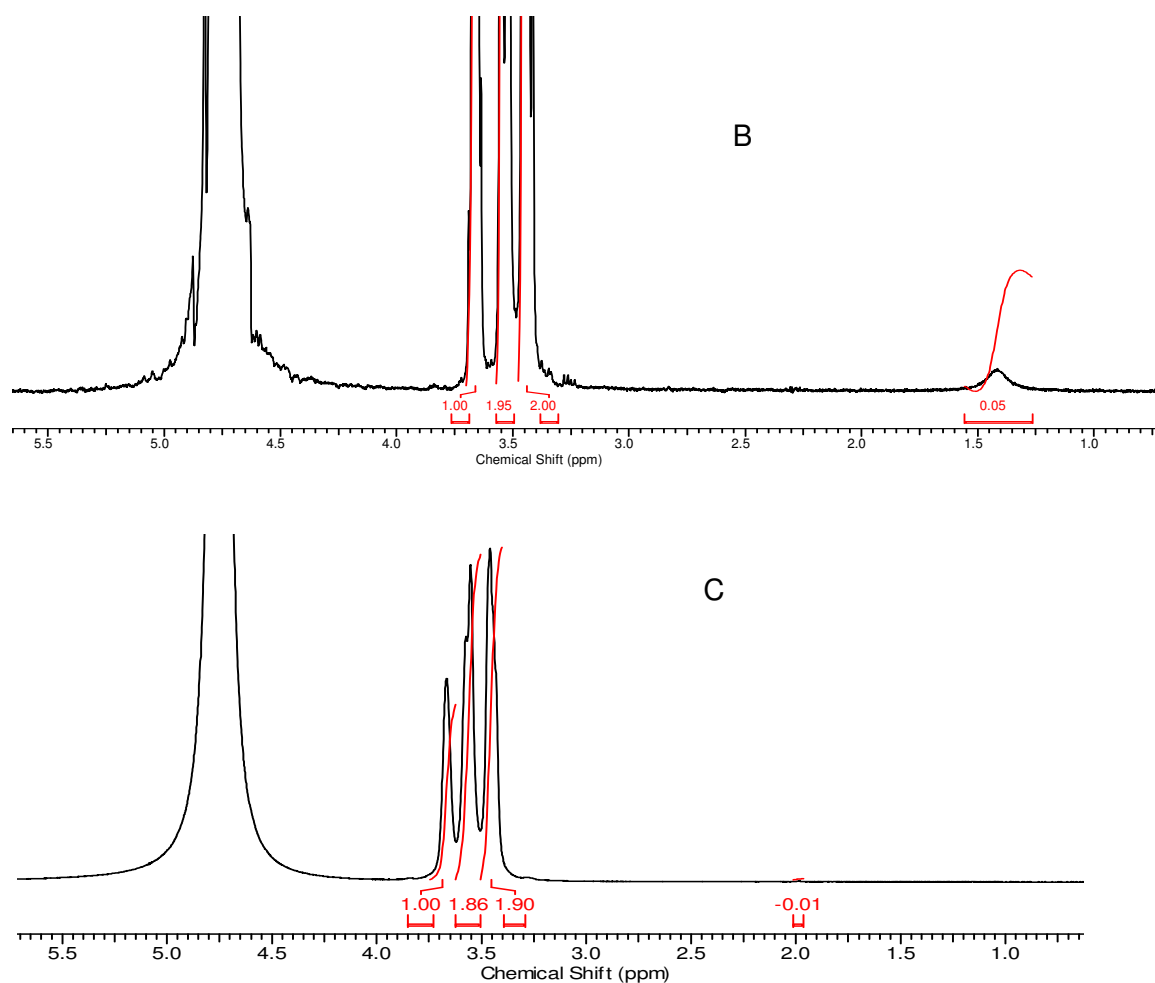


Figure 10-26: Monitoring HEDP degradation: <sup>1</sup>H NMR of isolated nanoparticles. (A) HEDP ligand in D<sub>2</sub>O (B) Cu/HEDP with glycerol (internal standard) in D<sub>2</sub>O, 0.18 mM Cu<sup>2+</sup>, 1.3 mM HEDP ligand dissolved in 20 mM pH 10 ammonia/ammonium chloride buffer (total reaction volume 25 mL). Solution was evaporated to remove buffer and solid residue was dissolved in D<sub>2</sub>O with a few drops of concentrated nitric acid and glycerol. The proton NMR at 400 MHz showed a broadened (due to Cu<sup>2+</sup>) peak for HEDP ligand (C) 5 mg nanoparticles dissolved in 0.4 mL of concentrated nitric acid and subsequently dissolved in D<sub>2</sub>O. Glycerol (0.1 g) was added and <sup>1</sup>H NMR was obtained at 400 MHz machine. The spectrum did not show signal for HEDP ligand.

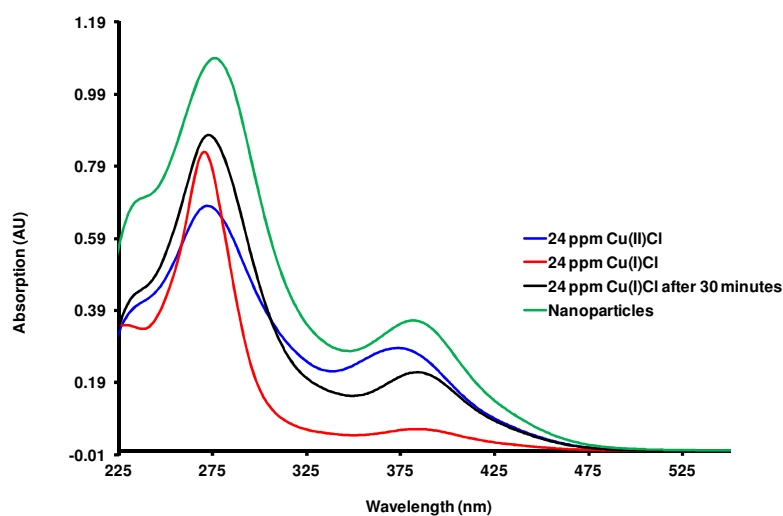


Figure 10-27: Colorimetric experiment to examine the oxidation state of copper in copper based nanoparticles.

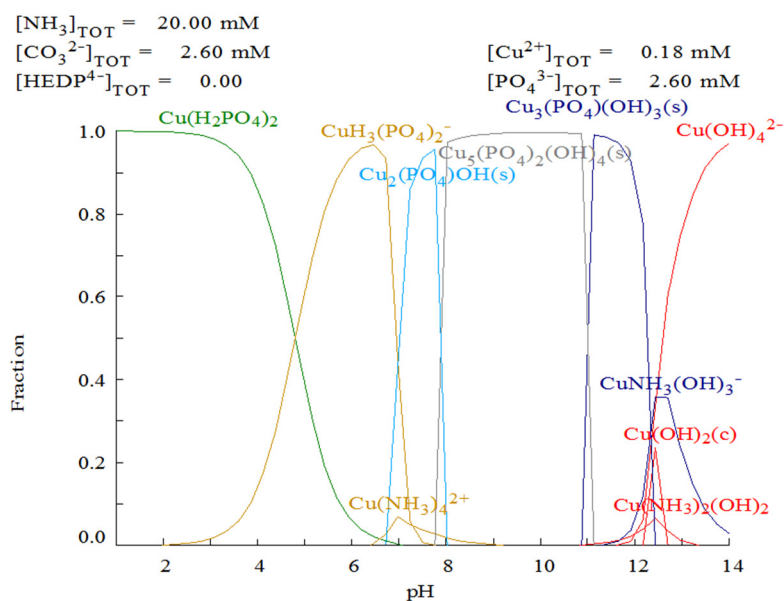


Figure 10-28: Changes in copper speciation in 20 mM ammonia/ammonium chloride buffer and subsequent changes after complete degradation of HEDP ligand.

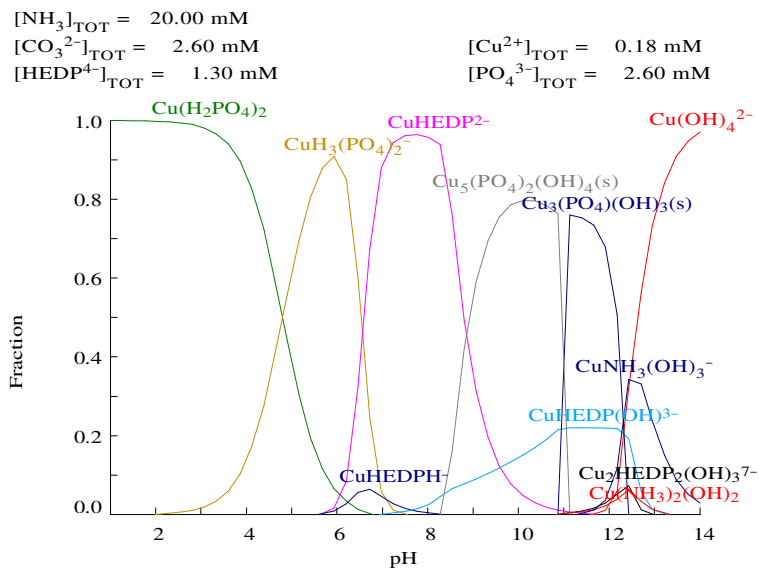


Figure 10-29: Changes in copper speciation in 20 mM ammonia/ammonium chloride buffer in the presence of HEDP chelant and phosphate & carbonate anions.

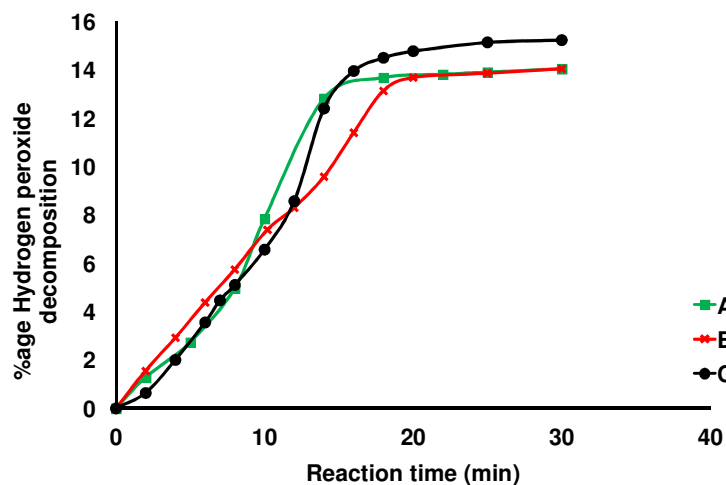


Figure 10-30: Hydrogen peroxide decomposition in  $\text{Cu}^{2+}$ -HEDP system with phosphate and carbonates added at the 6<sup>th</sup> minute to an ongoing decomposition reaction. (A) 0.18 mM of  $\text{Cu}(\text{II})\text{SO}_4$ , 1.3 mM of HEDP chelant dissolved in 20 mM pH 10 ammonia/ammonium chloride buffer with of hydrogen peroxide (0.98 M). Hydrogen peroxide decomposition was monitored over time. (B) To an ongoing reaction of A, 0.5 mL of 0.25 M phosphate buffer (disodium hydrogen phosphate-tri sodium phosphate) solution pH 10 was added at the 6<sup>th</sup> minute. (C) To another ongoing reaction A, 0.5 mL of 0.25 M ammonium carbonate was added at 6<sup>th</sup> minute using a syringe and hydrogen peroxide decomposition was monitored.

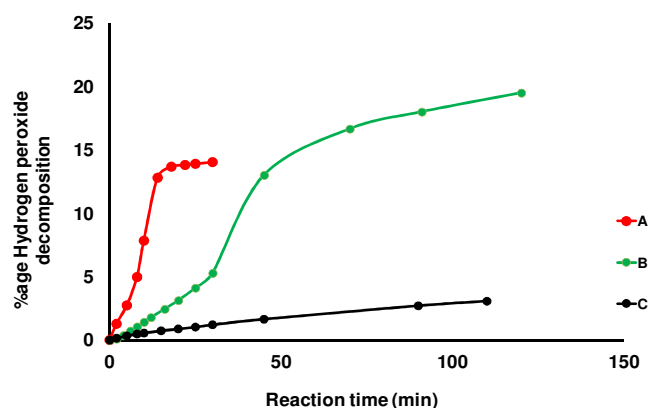


Figure 10-31: Copper-HEDP catalysed hydrogen peroxide decomposition using different buffer composition. (A) 0.18 mM of copper(II) sulfate, 1.3 mM of HEDP chelant dissolved in 20 mM pH 10 ammonia/ammonium chloride buffer and mixed with 0.98 M hydrogen peroxide. Hydrogen peroxide decomposition was monitored over time. (B) 0.18 mM of copper(II) sulfate, 1.3 mM of HEDP chelant dissolved in 20 mM pH 10 20 mM phosphate buffer with 0.98 M hydrogen peroxide. (C) 0.18 M of copper(II) sulfate in a chelant-free system dissolved in 20 mM pH 10 phosphate buffer with 0.98 M hydrogen peroxide.

Experiment	Reaction volume	Cu sulfate (II) Conc.			Buffer used	Stirring	result
A	25 mL	125 $\mu$ mol added slowly at 40 $^{\circ}$ C	250 $\mu$ mol $\text{Na}_2\text{HPO}_4$	125 $\mu$ mol $(\text{NH}_4)_2\text{CO}_3$	20 mM $\text{NH}_3/\text{NH}_4\text{Cl}$ buffer pH 10	Stirred 2 hours	Cloudy blue PPT
B	25 mL	125 $\mu$ mol added slowly at 40 $^{\circ}$ C	-	-	20 mM phosphate buffer pH 7	Stirred one hour	Cloudy blue
C	25 mL	4.5 $\mu$ mol added slowly at 50 $^{\circ}$ C	-	-	20 mM phosphate buffer pH 7	Stirred overnight	No NPs
D	25 mL	4.5 $\mu$ mol added slowly at 75 $^{\circ}$ C	-	-	20 mM phosphate buffer pH 9	Stirred overnight	No NPs, clear solution
<b>E</b>	<b>25 mL</b>	<b>12.5 <math>\mu</math>mol added slowly at 75 <math>^{\circ}</math>C</b>	-	<b>50 <math>\mu</math>mol <math>(\text{NH}_4)_2\text{CO}_3</math></b>	<b>20 mM phosphate buffer pH 9</b>	<b>Stirred overnight</b>	<b>NPs, UV &amp; TEM</b>

Table 10-1: Fabricating nanoparticles without using hydrogen peroxide under different conditions of reactions. Reaction E showed formation of nanoparticles.

## 10.4 Abbreviations

EDTA	Ethylenediaminetetraacetic acid
HEDTA	<i>N</i> -(Hydroxyethyl)-ethylenediaminetriacetic acid
DTPA	Diethylenetriaminepentaacetatic acid
EDDS	Ethylenediamine- <i>N,N'</i> -disuccinic acid
HEDP	1-Hydroxyethylidene 1,1-diphosphonic acid
DTPMP	Diethylenetriamine penta(methylene phosphonic acid)
PPD	<i>p</i> -Phenylenediamine
MAP	<i>m</i> -Aminophenol
AHT	4-Amino-2-hydroxy toluene
DTS	2,5-Toluenediamine sulfate
DMSO	Dimethylsulfoxide
DCM	Dichloromethane
EPR	Electron paramagnetic resonance
ESI	Electron spray ionization
g	Gram
MW	Molecular weight
MWCO	Molecular weight cut off
MS	Mass spectrometry
<i>m/z</i>	Charge to mass ratio
mL	Millilitre
mg	Milligram
min	Minute
NMR	Nuclear magnetic resonance
nm	Nanometre
ppm	Parts per million
TEM	Transmission electron microscopy
UV-Vis.	Ultraviolet visible

## 11 References

1. M. Feughelman, *Mechanical Properties and Structure of Alpha-keratin Fibres: Wool, Human Hair and Related Fibres*, UNSW Press, 1997.
2. M. Feughelman, *J. Appl. Polym. Sci.*, 2002, **83**, 489-507.
3. C. Zavik and J. Milliquent, in *The Science of Hair Care*, eds. C. Bouillon and J. Wilkison, Taylor & Francis Group, LLC, London, 2nd edn., 2005, pp. 29-35.
4. L. N. Jones, *Clin. Dermatol.*, 2001, **19**, 95-103.
5. R. J. M. Gold and C. R. Scriver, *Clinica Chimica Acta*, 1971, **33**, 465-466.
6. M. Feughelman, *J. Soc. Cosmet. Chem.*, 1982, **33**, 385-406.
7. C. R. Robbins and C. Kelly, *J. Soc. Cosmet. Chem.*, 1969, **20**, 555-564.
8. R. Dawber, *Clin. Dermatol.*, 1996, **14**, 105-112.
9. C. Popescu and H. Hocker, *Chem. Soc. Rev.*, 2007, **36**, 1282-1291.
10. W. Crewther, R. Fraser, F. Lennox and H. Lindley, *Adv. Protein Chem.*, 1965, **20**, 191-346.
11. H. Tanamachi, S. Tokunaga, N. Tanji, M. Oguri and S. Inoue, *J. Cosmet. Sci.*, 2010, **61**, 147-160.
12. L. N. Jones and D. E. Rivett, *Micron*, 1997, **28**, 469-485.
13. J. Rippon, *Wool dyeing. Bradford: Society of Dyers and Colourists*, 1992, 1-51.
14. P. W. Wertz and D. T. Downing, *Lipids*, 1988, **23**, 878-881.
15. C. R. Robbins, *Chemical and physical behavior of human hair*, 5th edn., Springer, 2012.
16. J. A. Swift, in *Practical Modern Hair Science*, eds. T. Evans and R. R. Wickett, Wissenschaftliche, 2012, pp. 1-37.
17. I. M. Kempson, W. M. Skinner and K. P. Kirkbride, *Environ. Sci. Technol.*, 2006, **40**, 3423-3428.
18. T. A. Hanners, W. J. Terrill, J. L. Kent and A. V. Colucci, *Environ. Health Perspect.*, 1974, **8**, 191-199.
19. J. L. Campbell, S. Faiq, R. S. Gibson, S. B. Russell and C. W. Schulte, *Anal. Chem.*, 1981, **53**, 1249-1253.

20. C. V. Monasterios, A. M. Jones and E. D. Salin, *Anal. Chem.*, 1986, **58**, 780-785.
21. E. DiPietro, D. Phillips, D. Paschal and J. Neese, *Biol. Trace Elem. Res.*, 1989, **22**, 83-100.
22. N. Worasith and B. A. Goodman, *Inter. J. of Cosmet. Sci.*, 2013, **35**, 424-429.
23. L. C. Bate, *Int. J. Appl. Radiat. Is.*, 1966, **17**, 417-423.
24. K. E. Smart, M. Kilburn, M. Schroeder, B. G. H. Martin, C. Hawes, J. M. Marsh and C. R. M. Grovenor, *J. Cosmet. Sci.*, 2009, **60**, 337-345.
25. A. O. Evans, J. M. Marsh and R. R. Wickett, *Inter. J. of Cosmet. Sci.*, 2011, 477-482.
26. N. Rudolf E, *Sci. Total Environ.*, 1999, **239**, 189-193.
27. Y. Liu, L. Hong, V. R. Kempf, K. Wakamatsu, S. Ito and J. D. Simon, *Pigm. Cell. Res.*, 2004, **17**, 262-269.
28. Y. Liu and J. D. Simon, *Pigm. Cell. Res.*, 2005, **18**, 42-48.
29. S. Ito, N. Suzuki, S. Takebayashi, S. Commo and K. Wakamatsu, *Pigment Cell Melanoma Res.*, 2013, **26**, 817-825.
30. P. Clanet, S. M. Deantonio, S. A. Katz and D. M. Scheiner, *Clin. Chem.*, 1982, **28**, 2450-2451.
31. C. Mérioux, F. Briki, F. Sarrot-Reynauld, M. Salomé, B. Fayard, J. Susini and J. Doucet, *Biochimica et Biophysica Acta (BBA) - General Subjects*, 2003, **1619**, 53-58.
32. J. M. Marsh, R. Iveson, M. J. Flagler, M. G. Davis, A. B. Newland, K. D. Greis, Y. Sun, T. Chaudhary and E. R. Aistrup, *Inter. J. of Cosmet. Sci.*, 2014, **36**, 32-38.
33. S. Godfery and J. M. Marsh, *Personal communication*, P & G, 2010.
34. S. McClean, E. O'Kane, D. J. M. Coulter, S. McLean and W. F. Smyth, *Electrophoresis*, 1998, **19**, 11-18.
35. W. Galas and J. Trzcionka, *Chem. Anal.*, 1997, **42**, 697-702.
36. A. A. Almeida, X. Jun and J. Lima, *Talanta*, 1999, **50**, 253-259.
37. J. Moreda-Pineiro, E. Alonso-Rodriguez, P. Lopez-Mahia, S. Muniategui-Lorenzo, D. Prada-Rodriguez, A. Moreda-Pineiro and P. Bermejo-Barrera, *Anal. Bioanal. Chem.*, 2007, **388**, 441-449.
38. C. Robbins, *J. Soc. Cosmet. Chem.*, 1971, **22**, 339-348.

39. C. Zavik and J. Milliquent, in *The Science of Hair Care*, eds. C. Bouillon and J. Wilkison, Taylor & Francis Group, LLC London, 2nd edn., 2005, pp. 246-268.
40. P. Prem, K. J. Dube, S. A. Madison and J. Bartolone, *J. Cosmet. Sci.*, 2003, **54**, 395-409.
41. S. Ito, *Pigm. Cell. Res.*, 2003, **16**, 230-236.
42. S. Ito and K. Wakamatsu, *Pigm. Cell. Res.*, 1998, **11**, 120-126.
43. S. Ito and K. Wakamatsu, *Photochem. Photobiol.*, 2008, **84**, 582-592.
44. J. D. Simon, D. Peles, K. Wakamatsu and S. Ito, *Pigment Cell Melanoma Res.*, 2009, **22**, 563-579.
45. A. Napolitano, A. Pezzella, M. R. Vincensi and G. Prota, *Tetrahedron*, 1995, **51**, 5913-5920.
46. P. Meredith and T. Sarna, *Pigm. Cell. Res.*, 2006, **19**, 572-594.
47. S. Ito and K. Wakamatsu, in *The Pigmentary System: Physiology and Pathophysiology*, eds. J. J. Nordlund, R. E. Boissy, V. J. Hearing, R. A. King, W. S. Oetting and J. P. Ortonne, Wiley, 2006, pp. 282-310.
48. J. M. Marsh, *Personal communication*, P & G, 2012.
49. L. J. Wolfram, K. Hall and I. Hui, *J. Soc. Cosmet. Chem.*, 1970, **21**, 875-900.
50. W. Edman and M. Marti, *J. Soc. Cosmet. Chem*, 1961, **12**, 133-145.
51. C. Robbins, *Text. Res. J.*, 1967, **37**, 811-813.
52. B. Bhushan, *Biophysics of Human Hair: Structural, Nanomechanical, and Nanotribological Studies*, Springer, 2010.
53. M.-S. Jeong, C.-M. Lee, W.-J. Jeong, S.-J. Kim and K.-Y. Lee, *The Journal of Dermatology*, 2010, **37**, 882-887.
54. Y. Z. Hessefort, B. T. Holland and R. W. Cloud, *J. Cosmet. Sci.*, 2008, **59**, 303.
55. C. Robbins and Y. Kamath, 2nd International Conference on Applied Hair Science, Princeton, NJ, 2006.
56. C. Robbins and Y. Kamath, *J. Cosmet. Sci.*, 2007, **58**, 629-636.
57. J. M. Marsh, C. J. Clarke, K. Meinert and R. M. Dahlgren, *J. Cosmet. Sci.*, 2007, **58**, 319-327.
58. J. M. Marsh, C. J. Clarke, K. Meinert and R. M. Dahlgren, *J. Cosmet. Sci.*, 2007, **58**, 621-627.

59. G. H. Xu and M. R. Chance, *Chem. Rev.*, 2007, **107**, 3514-3543.
60. H. Yin, L. Xu and N. A. Porter, *Chem. Rev.*, 2011, **111**, 5944-5972.
61. J. Marsh, C. Gummer and R. M. Dahlgren, *J. Cosmet. Sci.*, 2007, **58**, 88-89.
62. *USA Pat.*, US 7,179,302,B2, 2007.
63. P&G, *Hair colour research update*, 2010.
64. W. H. Koppenol, *Free Radical Biol. Med.*, 1993, **15**, 645-651.
65. P. Wardman and L. P. Candeias, *Radiat. Res.*, 1996, **145**, 523-531.
66. H. Fenton, *J. Chem. Soc., Trans.*, 1894, **65**, 899 - 910.
67. S. Goldstein, D. Meyerstein and G. Czapski, *Free Radical Biol. Med.*, 1993, **15**, 435-445.
68. G. Chen, *Angew. Chem. Int. Ed.*, 2010, **49**, 5413-5415.
69. F. Haber and J. Weiss, *Proc. R. Soc. London, Ser. A*, 1934, **147**, 332-351.
70. S. Croft, B. C. Gilbert, J. R. L. Smith, J. K. Stell and W. R. Sanderson, *J. Chem. Soc.-Perkin Trans. 2*, 1992, 153-160.
71. W. H. Koppenol and J. Butler, *Adv. Free Radical Bio.*, 1985, **1**, 91-131.
72. W. Freinbichler, L. Bianchi, M. A. Colivicchi, C. Ballini, K. F. Tipton, W. Linert and L. Della Corte, 13th International Conference on Biological Inorganic Chemistry, Vienna, Austria, 2007.
73. W. C. Bray and M. H. Gorin, *J. Am. Chem. Soc.*, 1932, **54**, 2124-2125.
74. M. L. Kremer, *Phys. Chem. Chem. Phys.*, 1999, **1**, 3595-3605.
75. H. B. Dunford, *Coord. Chem. Rev.*, 2002, **233-234**, 311-318.
76. J. D. Rush and W. H. Koppenol, *J. Am. Chem. Soc.*, 1988, **110**, 4957-4963.
77. W. Freinbichler, K. F. Tipton, L. Della Corte and W. Linert, *J. Inorg. Biochem.*, 2009, **103**, 28-34.
78. B. Ensing, F. Buda and E. J. Baerends, *J. Phys. Chem. A*, 2003, **107**, 5722-5731.
79. S. Rachmilovich-Calis, A. Masarwa, N. Meyerstein, D. Meyerstein and R. van Eldik, *Chem. Eur. J.*, 2009, **15**, 8303-8309.
80. J. Prousek, *Pure Appl. Chem.*, 2007, **79**, 2325-2338.
81. I. A. Salem, M. El-Maazawi and A. B. Zaki, *Int. J. Chem. Kinet.*, 2000, **32**, 643-666.

82. W. Koppenol, in *Free radical damage and its control*, eds. C. A. Rice-Evans and R. H. Burdon, Elsevier, 1994, vol. 28, pp. 3-24.
83. A. N. Pham, G. Xing, C. J. Miller and T. D. Waite, *J. Catal.*, 2013, **301**, 54-64.
84. T. Ozawa and A. Hanaki, *J. Chem. Soc., Chem. Commun.*, 1991, 330-332.
85. M. H. Robbins and R. S. Drago, *J. Catal.*, 1997, **170**, 295-303.
86. J. F. Perez-Benito, *Mon. Chem.*, 2001, **132**, 1477-1492.
87. J. F. Perez-Benito, *J. Inorg. Biochem.*, 2004, **98**, 430-438.
88. C. Walling, R. E. Partch and T. Weil, *Proc. Natl. Acad. Sci. USA*, 1975, **72**, 140-142.
89. A. Brausam and R. van Eldik, *Inorg. Chem.*, 2004, **43**, 5351-5359.
90. S. Fujii, C. Tsueda, K. Yamabe, K. Nakajima and H. Sakai, *Inorg. Chim. Acta.*, 2008, **361**, 1207-1211.
91. A. Brausam, J. Maigut, R. Meier, P. A. Szilagyi, H. J. Buschmann, W. Massa, Z. Homonnay and R. van Eldik, *Inorg. Chem.*, 2009, **48**, 7864-7884.
92. M. D. Engelmann, R. T. Bobier, T. Hiatt and I. F. Cheng, *Biometals*, 2003, **16**, 519-527.
93. M. C. R. Symons and J. M. C. Gutteridge, *Free radicals and iron: chemistry, biology, and medicine*, Oxford University Press, 1998.
94. P. Bautista, A. F. Mohedano, J. A. Casas, J. A. Zazo and J. J. Rodriguez, *J. Chem. Technol. Biotechnol.*, 2008, **83**, 1323-1338.
95. W. A. Pryor, *Annu. Rev. Physiol.*, 1986, **48**, 657-667.
96. H. Sies, *Eur. J. Biochem.*, 1993, **215**, 213-219.
97. B. M. Aveline, I. E. Kochevar and R. W. Redmond, *J. Am. Chem. Soc.*, 1996, **118**, 10113-10123.
98. M. P. DeMatteo, J. S. Poole, X. Shi, R. Sachdeva, P. G. Hatcher, C. M. Hadad and M. S. Platz, *J. Am. Chem. Soc.*, 2005, **127**, 7094-7109.
99. P. Wardman, *Rep. Prog. Phys.*, 1978, **41**, 259.
100. C. W. Jones, *Applications of Hydrogen Peroxide and Derivatives*, Royal Society of Chemistry, 1999.
101. M. S. Bharara and D. A. Atwood, in *Encyclopedia of inorganic chemistry*, J. Wiley, 2nd edn.
102. E. G. Janzen, *Acc. Chem. Res.*, 1971, **4**, 31-&.

103. E. Finkelstein, G. M. Rosen and E. J. Rauckman, *Arch. Biochem. Biophys.*, 1980, **200**, 1-16.
104. E. G. Janzen, C. M. DuBose and Y. Kotake, *Tetrahedron Lett.*, 1990, **31**, 7395-7398.
105. R. A. Meyers, *Encyclopedia of Analytical Chemistry*, Wiley, 2012.
106. A. Press, J. C. Lindon, G. E. Tranter, J. L. Holmes and J. L. Aaa, *Encyclopedia of Spectroscopy and Spectrometry*, Elsevier Science & Technology, 2000.
107. J. L. Clement, B. C. Gilbert, A. Rockenbauer and P. Tordo, *J. Chem. Soc.-Perkin Trans. 2*, 2001, 1463-1470.
108. R. V. Lloyd, P. M. Hanna and R. P. Mason, *Free Radical Biol. Med.*, 1997, **22**, 885-888.
109. A. E. Dikalova, M. B. Kadiiska and R. P. Mason, *P. Natl. Acad. Sci. USA*, 2001, **98**, 13549-13553.
110. M. Donoghue, X. Xu, D. Bernlohr and E. Arriaga, *Anal. Bioanal. Chem.*, 2013, 1-8.
111. L. Villeneuve, L. Alberti, J. P. Steghens, J. M. Lancelin and J. L. Mestas, *Ultrason. Sonochem.*, 2009, **16**, 339-344.
112. M. Saran and K. H. Summer, *Free Radic. Res.*, 1999, **31**, 429-436.
113. X. F. Yang and X. Q. Guo, *Analyst*, 2001, **126**, 928-932.
114. L. X. Li, Y. Abe, Y. Nagasawa, R. Kudo, N. Usui, K. Imai, T. Mashino, M. Mochizuki and N. Miyata, *Biomed. Chromatogr.*, 2004, **18**, 470-474.
115. F.-C. Cheng, J.-F. Jen and T.-H. Tsai, *J. Chromatogr. B*, 2002, **781**, 481-496.
116. M. G. Steiner and C. F. Babbs, *Arch. Biochem. Biophys.*, 1990, **278**, 478-481.
117. R. C. Scaduto Jr, *Free Radical Biol. Med.*, 1995, **18**, 271-277.
118. J. Schiller, J. Arnhold, J. Schwinn, H. Sprinz, O. Brede and K. Arnold, *Free Radic. Res.*, 1999, **30**, 45-57.
119. J. M. Schulman and S. G. Schulman, in *Chemiluminescence in Analytical Chemistry*, ed. A. M. Garcia-Campana, Taylor & Francis, 2001, pp. 105-122.
120. É. Mahé, P. Borno, E. Briot, J. Chevalet, C. Comninellis and D. Devilliers, *Electrochim. Acta*, 2013.
121. S. Singh and R. C. Hider, *Anal. Biochem.*, 1988, **171**, 47-54.

122. H. K. Porter, in *Organic Reactions*, John Wiley & Sons, Inc., 2004.
123. I. G. R. Gutz, *Curtipot*, <http://www2.iq.usp.br/docente/gutz/Curtipot.html>, (2010), Sao Paulo, Brazil.
124. D. Kocar, M. Strlic, J. Kolar and B. Pihlar, *Anal. Bioanal. Chem.*, 2002, **374**, 1218-1222.
125. V. S. Selih, M. Strlic, J. Kolar and B. Pihlar, *Polym. Degrad. Stabil.*, 2007, **92**, 1476-1481.
126. I. Puigdomenech, *Medusa, Chemical Equilibrium Diagrams* (2010), Stockholm.
127. D. F. Shriver, P. W. Atkins and C. H. Langford, *Inorganic Chemistry*, 2nd edn., Oxford University Press, 1994.
128. C. E. Housecroft and A. G. Sharpe, *Inorganic Chemistry*, Pearson Education Limited, UK, 2005.
129. G. A. Lawrance, *Introduction to coordination chemistry*, John Wiley & Sons Ltd, 2010.
130. J. Barrett, *Inorganic Chemistry in Aqueous Solution*, Royal Society of Chemistry, 2003.
131. *Lecture 17. Jahn-Teller distortion and coordination number four, Department of Chemistry & Biochemistry, University of North Carolina at Wilmington, USA.* (<http://uncw.edu/chem/>), 2013.
132. *NIST critical stability constants of metal complexes database*, 2004.
133. K. C. Francis, D. Cummins and J. Oakes, *J. Chem. Soc., Dalton Trans*, 1985, 493-501.
134. C. Walling, M. Kurz and H. J. Schugar, *Inorg. Chem.*, 1970, **9**, 931-937.
135. S. Godfery, *P&G Personal communication*, 2012.
136. C. Clarke and J. M. Marsh, *Personal communication: Hair dosage protocol*, 2011.
137. L. G. Sillén and A. E. Martell, *Stability Constants of Metal-ion Complexes*, Chemical Society, 1971.
138. J. M. Marsh, *Molecular modelling EDTA vs EDDS for calcium vs copper: Unpublished data*, P & G, 2014.
139. D. R. Lide, ed., *CRC Handbook of Chemistry and Physics*, 90th edn., CRC press, 2010.
140. M. E. T. Sillanpää, T. Agustiono Kurniawan and W.-h. Lo, *Chemosphere*, 2011, **83**, 1443-1460.

141. A. Masarwa, S. Rachmilovich-Calis, N. Meyerstein and D. Meyerstein, *Coord. Chem. Rev.*, 2005, **249**, 1937-1943.
142. B. Hobel and C. von Sonntag, *J. Chem. Soc., Perkin Trans. 2*, 1998, 509-514.
143. B. Balci, M. A. Oturan, N. Oturan and I. Sirés, *J. Agric. Food Chem.*, 2009, **57**, 4888-4894.
144. K. A. Barrett and M. B. McBride, *Environ. Sci. Technol.*, 2005, **39**, 9223-9228.
145. J. Murphy and J. P. Riley, *Anal. Chim. Acta*, 1962, **27**, 31-36.
146. S. Tsang, F. Phu, M. M. Baum and G. A. Poskrebyshev, *Talanta*, 2007, **71**, 1560-1568.
147. R. P. Mihajlovic, V. M. Kaljevic, M. P. Vukasinovic, L. V. Mihajlovic and I. D. Pantic, *Water SA*, 2007, **33**, 513-517.
148. *standard method for the examination of water and wastewater*, American Public Health Association, American Water Works Association, Water Environment Federation, 1999.
149. D. R. Clary and G. Mills, *J. Phys. Chem. C*, 2011, **115**, 1767-1775.
150. A. Kumar, A. Saxena, A. De, R. Shankar and S. Mozumdar, *RSC Advances*, 2013, **3**, 5015-5021.
151. D. Meyerstein, *Inorg. Chem.*, 1971, **10**, 2244-2249.
152. A. Casitas and X. Ribas, *Chem. Sci.*, 2013, **4**, 2301-2318.
153. A. E. Martell and R. D. Hancock, *Metal complexes in aqueous solutions*, Plenum Press, New York, 1996.
154. T. Osako, K. Ohkubo, M. Taki, Y. Tachi, S. Fukuzumi and S. Itoh, *J. Am. Chem. Soc.*, 2003, **125**, 11027-11033.
155. T. Osako, S. Nagatomo, T. Kitagawa, C. Cramer and S. Itoh, *J. Biol. Inorg. Chem.*, 2005, **10**, 581-590.
156. L.-M. Zheng, H.-H. Song, C.-Y. Duan and X.-Q. Xin, *Inorg. Chem.*, 1999, **38**, 5061-5066.
157. L. M. Mirica, X. Ottenwaelder and T. D. P. Stack, *Chem. Rev.*, 2004, **104**, 1013-1046.
158. D. Maiti, J. S. Woertink, A. A. N. Sarjeant, E. I. Solomon and K. D. Karlin, *Inorg. Chem.*, 2008, **47**, 3787-3800.
159. K. D. Karlin, C. X. Zhang, A. L. Rheingold, B. Galliker, S. Kaderli and A. D. Zuberbühler, *Inorg. Chim. Acta.*, 2012, **389**, 138-150.

160. E. I. Solomon, J. W. Ginsbach, D. E. Heppner, M. T. Kieber-Emmons, C. H. Kjaergaard, P. J. Smeets, L. Tian and J. S. Woertink, *Faraday Discuss.*, 2011, **148**, 11-39.
161. E. A. Lewis and W. B. Tolman, *Chem. Rev.*, 2004, **104**, 1047-1076.
162. A. M. Kirillov, M. N. Kopylovich, M. V. Kirillova, M. Haukka, M. da Silva and A. J. L. Pombeiro, *Angew. Chem.-Int. Edit.*, 2005, **44**, 4345-4349.
163. C. Zavik and J. Milliquent, in *The Science of Hair Care*, eds. C. Bouillon and J. Wilkison, Taylor & Francis Group, LLC, London, 2nd edn., 2005, pp. 296-327.
164. O. J. X. Morel and R. M. Christie, *Chem. Rev.*, 2011, **111**, 2537-2561.
165. K. Hunger, ed., *Industrial dyes, Chemistry, properties, applications*, Wiley.com, 2007.
166. C. Zavik and J. Milliquent, in *The Science of Hair Care*, eds. C. Bouillon and J. Wilkison, Taylor & Francis Group, LLC, London, 2nd edn., 2005, pp. 269-295.
167. H. Tucker, *J. Soc. Cosmet. Chem.*, 1971, **22**, 379-398.
168. K. Venkataraman, *The chemistry of synthetic dyes*, Academic Press, 1971.
169. G. M. Wis-Surel, *Inter. J. of Cosmet. Sci*, 1999, **21**, 327-340.
170. J. F. Corbett, *J. Soc. Cosmet. Chem*, 1984, **35**, 297-310.
171. J. F. Corbett, *J. Soc. Dyers. Colour.*, 1976, **92**, 285-303.
172. G. R. Bhat, E. R. Lukenbach, R. R. Kennedy and R. M. Parreira, *J. Soc. Cosmet. Chemist*, 1979, **30**, 1-8.
173. J. F. Corbett, *Rev. Prog. Color. Relat. Top.*, 1973, **4**, 3-7.
174. J. F. Corbett, *Rev. Prog. Color. Relat. Top.*, 1985, **15**, 52-65.
175. J. F. Corbett, *J. Soc. Dyers. Colour.*, 1968, **84**, 556-560.
176. R. Smith, Department of Chemistry, University of York, UK, Victor Chechik group, 2013.
177. X.-G. Li, M.-R. Huang, W. Duan and Y.-L. Yang, *Chem. Rev.*, 2002, **102**, 2925-3030.
178. M.-R. Huang, H.-J. Lu and X.-G. Li, *J. Mater. Chem.*, 2012, **22**, 17685-17699.
179. Y.-L. Min, T. Wang, Y.-G. Zhang and Y.-C. Chen, *J. Mater. Chem.*, 2011, **21**, 6683-6689.

180. R. Tang, Q. Li, L. Ding, H. Cui and J. Zhai, *Environ. Technol.*, 2012, **33**, 341-348.
181. J. M. Marsh, *P&G Personal communication*, 2014.
182. V. Valkovic, D. Miljanic, R. M. Wheeler, R. B. Liebert, T. Zabel and G. C. Phillips, *Nature*, 1973, **243**, 543-544.
183. J. M. Marsh, P&G unpublished SLR report., December 2010.
184. J. Loebel, *Image analysis: principles and practice*, Joyce Loebel, 1985.
185. W. G. Kropatsch and H. Bischof, *Digital Image Analysis: Selected Techniques and Applications*, Springer, 2001.
186. C. Petibois, *Anal. Bioanal. Chem.*, 2010, **397**, 2051-2065.
187. P. Coppin, I. Jonckheere, K. Nackaerts, B. Muys and E. Lambin, *Int. J. Remote. Sens.*, 2004, **25**, 1565-1596.
188. B. W. Pogue, S. C. Davis, X. Song, B. A. Brooksby, H. Dehghani and K. D. Paulsen, *J. Biomed. Opt.*, 2006, **11**, 033001-033016.
189. D. Van Neste and R. Trüeb, *J. Eur. Acad. Dermatol.*, 2006, **20**, 578-583.
190. U. Blume-Peytavi, K. Hillmann and M. Guarrera, in *Hair Growth and Disorders*, Springer, 2008, pp. 125-157.
191. J. H. Baek, S. Y. Lee, M. Yoo, W. S. Park, S. J. Lee, Y. C. Boo and J. S. Koh, *Inter. J. of Cosmet. Sci.*, 2011, 1-6.
192. B. Fink, F. Neuser, G. Deloux, S. Röder and P. J. Matts, *J. Cosmet. Dermatol.*, 2013, **12**, 78-84.
193. R. McMullen and J. Jachowicz, *J. Cosmet. Sci.*, 2002, **54**, 335-351.
194. C. Robbins, P. Mirmirani, A. G. Messenger, M. P. Birch, R. S. Youngquist, M. Tamura, T. Filloon, F. Luo and T. L. Dawson, *Brit. J. Dermatol.*, 2012, **167**, 324-332.
195. S. P. Gurden, V. F. Monteiro, E. Longo and M. M. C. Ferreira, *J. Microsc.-Oxf.*, 2004, **215**, 13-23.
196. N. Chen and B. Bhushan, *J. Microsc.*, 2006, **221**, 203-215.
197. J. A. Swift and J. R. Smith, *Scanning*, 2000, **22**, 310-318.
198. ASTM, ASTM International, 2002.
199. ASTM, ASTM International, 2007.
200. P. L. Buldini, S. Cavalli and A. Trifirò, *J. Chromatogr. A*, 1997, **789**, 529-548.

201. B. J. Wildman, P. E. Jackson, W. R. Jones and P. G. Alden, *J. Chromatogr. A*, 1991, **546**, 459-466.
202. B. López-Ruiz, *J. Chromatogr. A*, 2000, **881**, 607-627.
203. M. Mecozzi, E. Pietrantonio, M. Amici and G. Romanelli, *Analyst*, 2001, **126**, 144-146.
204. M. Tatzber, M. Stemmer, H. Spiegel, C. Katzlberger, G. Haberhauer and M. H. Gerzabek, *Environ. Chem. Lett.*, 2007, **5**, 9-12.
205. P. Agarwal and K. A. Berglund, *Crystal Growth & Design*, 2003, **3**, 941-946.
206. A. Cassella, R. De Campos, S. Garrigues, M. De La Guardia and A. Rossi, *Fresenius J. Anal. Chem.*, 2000, **367**, 556-561.
207. J. V. Rau, S. N. Cesaro, D. Ferro, S. M. Barinov and I. V. Fadeeva, *J. Biomed. Mater. Res. A*, 2004, **71B**, 441-447.
208. D. Tsikas and K. Chobanyan-Jürgens, *Anal. Chem.*, 2010, **82**, 7897-7905.
209. A. M. Beccaria, G. Poggi and G. Castello, *J. Chromatogr. A*, 1987, **395**, 641-647.
210. D. W. T. Griffith and I. M. Jamie, in *Encyclopedia of Analytical Chemistry*, John Wiley & Sons, Ltd, 2006.
211. F. Rouessac and A. Rouessac, in *Chemical Analysis: Modern Instrumentation Methods and Techniques*, Wiley, 2013, pp. 207-234.
212. D. H. Williams and I. Fleming, *Spectroscopic methods in organic chemistry*, McGraw-Hill, 1995.
213. R. M. Silverstein, F. X. Webster and D. J. Kiemle, *Spectrometric identification of organic compounds*, John Wiley & Sons, 2005.
214. P. Griffiths and J. A. De Haseth, *Fourier Transform Infrared Spectrometry*, Wiley, 2007.
215. P. W. Atkins, *The Elements of Physical Chemistry*, Oxford University Press, 2001.
216. *Carbon dioxide information analysis centre, US Department Of Energy, USA*. <http://cdiac.ornl.gov/> Date Accessed: 13th April 2013.
217. F. Cadet, S. Garrigues and M. Guardia, *Encyclopedia of Analytical Chemistry*, 2000, 1-26.
218. S. A. Huber and F. H. Frimmel, *Anal. Chem.*, 1991, **63**, 2122-2130.
219. T. Noguchi, M. Hatta, T. Yamanaka and K. Okamura, *Anal. Sci.*, 2013, **29**, 9.

220. S. Godfrey, W. Staite, P. Bowtell and J. Marsh, *Inter. J. of Cosmet. Sci*, 2013, **35**, 264-271.
221. R. McMullen and J. Jachowicz, *J. Soc. Cosmet. Chem.*, 1998, **49**, 223-244.
222. R. McMullen and J. Jachowicz, *J. Soc. Cosmet. Chem.*, 1998, **49**, 245-256.
223. S. Ruetsch and Y. Kamath, *Inter. J. of Cosmet. Sci*, 2004, **26**, 217-217.
224. F. J. Mottram, in *Poucher's Perfumes, Cosmetics and Soaps*, ed. H. Butler, Springer Netherlands, 1993, pp. 170-194.
225. R. G. Harry and M. M. Rieger, *Harry's Cosmeticology*, 8th edn., Chemical Publishing Company Incorporated (NY), 2000.
226. L. J. Wolfram, *J. Am. Acad. Dermatol.*, 2003, **48**, S106-S114.
227. A. O. Evans, J. M. Marsh and R. R. Wickett, *J. Cosmet. Sci.*, 2011, **62**, 383-391.
228. G. H. Jeffery, J. Bassett, J. Mengham and R. C. Denny, *Vogel's textbook of quantitative chemical analysis*, 5th edn., Longman Scientific & Technical, Essex, UK, 1989.
229. C. R. Robbins, *Chemical and physical behavior of human hair*, 4th edn., Springer-Verlag, New York, 2002.